The modelling of electronic effects in molecular dynamics simulations

Szymon Daraszewicz

Department of Physics and Astronomy &
London Centre for Nanotechnology
UCL University College London
s.daraszewicz@physics.org

Thesis submitted for the degree of
Doctor of Engineering (EngD) of University College London

November 2013

I, Szymon Daraszewicz, confirm that the work presented in this thesis is my own. Where information has been derived from other sources, I confirm that this has been indicated in the thesis.

Szymon Daraszewicz
November 2013

Rev. 21st May 2014

Abstract

This thesis describes the development and applications of the continuum-atomistic molecular dynamics (MD) model in the context of radiation damage. By extending the classical MD method to incorporate the electronic excitations represented as an electron fluid and coupled to the ions in the two-temperature (2T) formalism, we have been able to correctly capture the physics governing the atomistic dynamics under huge electronic excitations. The integrated 2T-MD model has been specifically adapted to study three types of non-equilibrium scenarios: laser excitations, swift heavy ion impacts and large-scale high energy collision cascades.

Using the 2T-MD model we have estimated the impact of the electron-phonon coupling and the electronic stopping power on the primary radiation damage yield in bcc iron. We have found that the cascade dynamics and the resultant damage from 50-100 keV primary knock-on atom impacts is highly sensitive to the electronic stopping treatment at low projectile velocities, which represents the first rigorous study of this type.

By examining the temporal evolution of the structure factor of laser-irradiated gold thin films, we have been able to directly compare the 2T-MD results with Bragg peaks measured by ultrafast electron diffraction and have achieved an excellent agreement between theory and experiment with no fitting parameters. This has enabled us to elucidate the melting dynamics following laser irradiation at a picosecond resolution for the first time and also to validate the two-temperature approach.

To simulate semiconductors under electronic excitations, the continuum part of the 2T-MD model, which represents electrons, has been replaced by two continuum equations: one for carrier density and one for their energy, to account for the finite band-gap effects. We have applied such extended method to simulate ion tracks, which result from swift heavy ion impacts. We have achieved a very good agreement with the experimental results on the ion track radii, provided that we are free to adjust the strength of the electron-phonon coupling.

We propose future studies in the field of non-equilibrium atomistic modelling. In particular, we discuss *ab initio* methods and further improvements to hybrid MD to study the effects of the interatomic potential changes in response to high electronic excitations.

List of Publications

Parts of the work presented in this thesis have formed a basis for the following publications:

1. E. Zarkadoula, S. L. Daraszewicz, D. M. Duffy, M. A. Seaton, I. T. Todorov, K. Nordlund, M. T. Dove and K. Trachenko, 'Electronic effects in high-energy radiation damage in iron', J. Phys.: Condens. Mat. **26**, 085401 (2014)

2. A. A. Leino, S. L. Daraszewicz, O. H. Pakarinen, F. Djurabekova, K. Nordlund, B. Afra and P. Kluth, 'Structural analysis of simulated swift heavy ion tracks in quartz', Nucl. Instr. Meth. Phys. Res. B, REI 2013 conference paper, accepted for publication (2013)

3. S. L. Daraszewicz, Y. Giret, N. Naruse, Y. Murooka, J. Yang, D. M. Duffy, A. L. Shluger and K. Tanimura, 'Structural dynamics of laser-irradiated gold nanofilms', Phys. Rev. B **88**, 184101 (2013)

4. Y. Giret, N. Naruse, S. L. Daraszewicz, Y. Murooka, J. Yang, D. M. Duffy, A. L. Shluger and K. Tanimura, 'Transient atomic structure determination of laser-excited materials from time-resolved diffraction data', Appl. Phys. Lett., accepted for publication (2013)

5. E. Zarkadoula, S. L. Daraszewicz, D. M. Duffy, M. A. Seaton, I. T. Todorov, K. Nordlund, M. T. Dove and K. Trachenko, 'The nature of high-energy radiation damage in iron', J. Phys.: Condens. Mat. **25**, 125402 (2013)

6. S. L. Daraszewicz and D. M. Duffy, 'Hybrid continuum–atomistic modelling of swift heavy ion radiation damage in germanium', Nucl. Instr. Meth. Phys. Res. B **303**, 112–115 (2013)

7. D. M. Duffy, S. L. Daraszewicz and J Mulroue, 'Modelling the effects of electronic excitations in ionic-covalent materials', Nucl. Instr. Meth. Phys. Res. B **277**, 21–27 (2012)

8. S. L. Daraszewicz and D. M. Duffy, 'Extending the inelastic thermal spike model for semiconductors and insulators', Nucl. Instr. Meth. Phys. Res. B **269**, 1646–1649 (2011)

Unpublished (including currently reviewed) work is not listed.

Acknowledgements

I am extremely grateful to my primary supervisor, Dorothy Duffy, whose help and encouragement was indispensable in the completion of this work. I am exceptionally thankful for the intellectual (and travel) freedom I enjoyed during these fruitful four years.

I also owe many thanks to Yvelin Giret, Alexander Shluger and Katsumi Tanimura, who have taken me on board their project and have been very supportive of the collaboration we have thus created. In particular, I should thank Yvelin Giret, whose electronic structure insights have saved the projects on several occasions.

I am, furthermore, indebted to Olli Pakarinen, Aleksi Leino and Kai Nordlund for hosting me at the University of Helsinki and the excellent debates on ion track physics, which are continuing to date. Further thanks should go to Alfredo Correa and Tadashi Ogitsu for their continuous encouragement, inspiration and time they have devoted teaching me electronic structure theory during my stay at Lawrence Livermore National Laboratory (LLNL).

I would also like to acknowledge the outstanding technical help with the DL_POLY code development I have received from Ilian Todorov and Michael Seaton. I should thank Ilian Todorov for his involvement with the modified Tersoff (MOD) potential implementation.

Finally, I extend my gratitude to two brave proofreaders, who have been effectively blackmailed to read parts of this thesis and who have transformed it into a human-readable form: Tomek Blusiewicz and Richard Ainsworth. I also acknowledge the help of Panagiotis Grammatikopoulos and Joe Staines with the final editorial corrections. I wish to thank Su Shan, who has unintentionally forced me to revise my notion of statistical significance and, last but not least, my mother - the only non-physicist, who has promised to read this thesis in full.

This work would not be possible without the financial assistance of Culham Centre for Fusion Energy (Sergei Dudarev), as well as of the M3S Industrial Doctorate Centre (via EPSRC) headed by Nora de Leeuw. I acknowledge the use of the supercomputing resources of HECToR, funded by the UK's HPC Materials Chemistry Consortium via EPSRC (EP/F067496), and the UCL Legion High Performance Computing Facility.

Table of Contents

List of Figures

List of Tables

Abbreviations

Term	Meaning
2T	Two-temperature (model)
BC	Boundary conditions
BCA	Binary collision approximation
CIT	Coarse-grained ionic temperature (cell)
CET	Coarse-grained electronic temperature (cell)
DFT	Density functional theory
DT	Deuterium-Tritium
DOS	Density of states
dpa	Displacements per atom
DWF	Debye-Waller factor
EAM	Embedded atom model
eiTS	Extended inelastic thermal spike (model)
EoM	Equation(s) of motion
EoS	Equation of state
e-p	Electron-phonon (coupling)
e-s	Electronic stopping
ETD	Electronic temperature dependent (potential)
FEG	Free electron gas
FP	Frenkel pair
FWHM	Full width at half maximum
iTS	Inelastic thermal spike (model)
RT TD-DFT	Real-time time-dependent density functional theory
TDE	Threshold displacement energy
MD	Molecular dynamics
MSD	Mean-square displacement
nn	Nearest-neighbour
NVE	Constant particle number (N), volume (V), energy (E) ensemble
NPT	Constant particle number (N), pressure (P), temperature (T) ensemble
PES	Potential energy surface
PDF	Pair density function

Term	Meaning
pka	Primary knock-on atom
RCS	Replacement collision sequence
SHI	Swift heavy ion
UED	Ultrafast electron diffraction
WDM	Warm dense matter
W-S	Wigner-Seitz (method)

Chapter 1

General introduction

1.1 Rationale and scope

Understanding and predicting radiation damage in materials and, in general, the ultrafast dynamics processes in solids will have immediate implications for both fundamental science and technology. The most pertinent application example is the design of efficient radiation-resistant materials, which are subject to high-energy neutron irradiation. These are required for future fusion and next-generation fission reactors.

Fusion power has the potential to become the main alternative for a sustainable, safe and virtually limitless energy source in the near future, assuming its current commercial and materials challenges can be tackled. In brief, a fusion nuclear reaction occurs when deuterium (D) and tritium (T) nuclei overcome Coulomb repulsion and react at extremely high temperatures ($\sim 10^8$ K) producing alpha particles and 14.1 MeV energy neutrons (with a spread of 0.5 MeV). These high-energy neutrons generated in the fusion reaction leave the plasma; their kinetic energy is absorbed by the reactor wall and then it is transferred to the coolant. Similarly, fission neutrons of energies from few keV to several MeV are captured by fission reactor materials.

Why model radiation damage? The current irradiation facilities make it all but impossible for scientists to perform longitudinal radiation damage studies. In particular, the existing sources of 14.1 MeV neutrons (for fusion reactor materials development) have a low intensity and are hence incapable of providing a suitable damage accumulation in a reasonable time. The current experimental strategy is to mimic the 14.1 MeV neutrons radiation with fission neutrons, high-energy protons or heavy ions. Results obtained in this way need thus to be extrapolated for the fusion conditions and the accuracy of this procedure raises several concerns. In particular, it is difficult to separate out the effects of particle type, particle energy, temperature, accumulated damage and hence to predict the overall damage rates. The planned construction of the International Fusion Materials Irradiation Facility (IFMIF), which will enable testing of long-term behaviour of materials under fusion-like neutron flux, can alleviate some of these problems. Nonetheless, it is difficult to envisage that a "brute-force" approach, which would test for every possible material composition under the required irradiation condi-

tion, will be successful. As a result, a bottom-up theoretical and a reliable, predictive modelling effort is the key to ensure the correct design and the initial selection of materials for fusion power plants and other applications.

In general, radiation damage is a complex and inherently multi-scale phenomenon. It begins typically with the primary damage production through "billiard ball"-like collisions of atoms[1] at the picosecond timescale to years of damage evolution. Initially, the atomic collision cascades create point defects (vacancies and interstitials) and larger clusters, which then evolve into secondary defects such as voids and dislocation loops. The primary and secondary radiation damage effects result in a change in the bulk properties of a material, which in general can include changes in chemical/physical composition, decrease of electrical/thermal conductivity, embrittlement and dimensionality changes (such as swelling). This challenge calls for multi-scale simulation methods with each step responsible for different spatiotemporal regimes. Therefore, an accurate prediction of the primary radiation damage yield is paramount, as it is used as input for the methods describing long-term structure evolution. In this thesis we focus on the primary radiation damage processes occurring on the picosecond time- and nanometre length-scales. This is one of the first links in this multi-scale modelling chain, second only to *ab initio* studies, which deal with defect energetics.

The future success of fusion power is dependent on the performance of materials against the adverse radiation effects, both insulators (forming divertor plates, mirrors and diagnostics) and first-wall steels [9–13]. However, there is a plethora of potential application of radiation damage modelling in areas other than neutron or fission fragment damage for nuclear applications. These include the damage caused by the most energetic and heaviest particles, namely swift heavy ions (SHIs), which are of typical specific energies of several MeV/u. These penetrate matter interacting mainly with electrons of the target atoms, which is in contrast to fission and fusion neutrons that interact mainly through atomistic collisions. Application areas where predictive radiation damage modelling of SHIs would be beneficial include nanotechnology (modification of nanostructures [14], formation of nm-sized channels called track etch membranes [15], changes in quantum wells and dots [16]), optoelectronic components for space missions [17] and heavy-ion therapy in medicine [18].

The scope of this thesis is also driven by the requirement for an increased theoretical understating of irradiation-induced structural changes not only in metals, but also in band-gap materials. Such materials are interesting to study for three reasons: (i) they are typically more sensitive to radiation damage than metals, (ii) they have plenty of industrial applications and (iii) they are very difficult to model and the current theoretical description is incomplete. In fact, even low radiation doses can have a strong effect on an insulator's functional properties. Indeed, insulators can be heavily affected by doses less than 1 dpa (displacements per atom), whole structural steels can typically withstand 10 dpa. From an applied physics point of view, understating the SHI radiation in band-gap materials in particular will enable us to tune the refractive index of materials such as quartz [19] and $LiNbO_3$ [20] at the microscale.

[1] In the case of most types of fission and fusion neutron irradiation - this point will be addressed in this thesis.

Finally, because of the presence of the band-gap, the standard modelling methods, such as the two-temperature approach, most certainly do not capture the correct carrier dynamics and therefore alternative (and most likely more complex) modelling methods are highly sought for.

The study of the initial stages of radiation damage is connected to the larger research field of ultrafast dynamics. Both deal with electron-ion non-equilibrium scenarios at a sub- and picosecond timescale and invoke the same physics concepts. (However, traditionally, ultrafast dynamics deals with laser-excitation of solids, rather than with particle irradiation.) Consequently, a comprehensive understanding of atomistic dynamics at high electronic excitations from the ultrafast dynamics perspective will help to build and validate models of radiation damage. In this thesis, we discuss the ultrafast dynamics of thin-film gold thereby testing some of the theoretical concepts for radiation damage.

In a larger picture, the rationale behind studying ultrafast dynamics is twofold. First, as the atomic motions, chemical reactions, and electron-ion interactions and radiation damage cascades occur at such short timescales, advances in ultrafast science can realise the long-standing dream of the scientific community to observe matter transformation as these processes happen. Creating such a "molecular movie", instead of conventional time-averaged studies, is of interest across all science domains, but primarily in reaction chemistry, solid-state physics and materials science. Secondly, through recent advances in ultrafast science, not only tracking but also controlling the electronically excited state of matter, and thereby modifying macroscopic materials properties is now becoming a real possibility. This can eventually realise another ultimate scientific aim, namely being able to adjust materials properties at will. Currently, resolving ultrafast dynamics at the atomic scale is the common challenge in the fields of photo-induced phase transitions and primary radiation damage modelling.

The recent rapid development of optical pump-probe experiments has revolutionised physics by enabling scientists to probe the non-equilibrium processes at a sub-picosecond timescale following an ultrashort (sub-picosecond) laser pulse excitation (i.e. a pump). Indeed, photo-excitation has been shown to cause transient and dramatic changes in the physical properties of solids caused by phenomena purely driven by electronic excitations. The excited electron system can lead to macroscopic phase changes of the ionic system, leading to new metastable phases of matter. They are also called "hidden" phases of matter, as they exist (typically transiently) on the electronic excitations scale and hence are not thermally accessible. Examples of such purely electronic phase transformations induced by optical excitations include metal to insulator, magnetic to non-magnetic, formation of highly coordinated liquids, solid-to-solid phase transitions and others. The landmark discovery in the field led to a Nobel Prize in Chemistry in 1999 (A. Zewail) for tracking of the interatomic potential changes of a photo-excited molecule. In the future, developments in this area will likely lead to light-switching functionality of the materials and thus enable ultrafast information processing.

The progress in gaining insight into the radiation damage processes or even observing ultrafast dynamics at the atomic scale is conditional upon developing transferable, large-scale, predictive and rigorously justified models, which are free of adjustable parameters. The ap-

proach presented in this thesis builds on the emerging field of augmented molecular dynamics (MD) by including a concurrent physical description of the electron-ion coupled dynamics and excited-state interatomic interactions providing a large-scale atomistic description of the effects of electronic excitations. In short, this thesis explores the electron-ion coupled dynamics relaxing the assumption of a local electron-ion thermal equilibrium at the MD spatiotemporal scales that are accessible to the pump-probe experiments and relevant for radiation damage processes.

1.2 Including electronic effects (technical details)

This project makes use of, validates and extends a set of unique simulation tools capable of tackling the problem of primary radiation damage and ultrafast dynamics. These tools bridge the regimes that are currently inaccessible to *ab initio* methods (due to spatiotemporal scale) and to classical MD (due to lack of accuracy), by implementing and extending an augmented two-temperature (2T-MD) strategy in DL_POLY package. This scheme is based on a fluid description of electronic excitations, which is coupled with MD. It therefore enables us to take into account explicit dynamic electronic excitations and electron-ion energy transfer on the MD spatiotemporal scale. This augmented method can access scales beyond the orders of one hundred million atoms and one hundred picoseconds, provided it is efficiently parallelised for memory-distributed architectures, thus enabling a direct experimental comparison.

We rigorously parameterise this large-scale augmented 2T-MD strategy, using input from *ab initio* methods. Crucially, the model can include the interatomic potentials dependent on the excitation levels (electron temperature). Therefore, augmented MD is also able to capture photo-induced structural transformations resulting from collective atomic motion due to the modified equilibrium positions and thus non-thermal expansion. Finally, in the case of semiconductors the simple electron fluid description is replaced with an explicit solver for carrier density and energy to take into account some of the finite band-gap effects in semiconductors.

1.3 Thesis overview

The current chapter introduces the general problem of radiation damage in the context of materials research for future fusion reactors. It also discusses the related research area of ultrafast dynamics and the outstanding challenge of the development of accurate atomistic models of phase transitions. The chapter provides a motivation behind the inclusion of the electronic effects in molecular dynamics simulations, and outlines the scope and the aims of this thesis.

The core sections of the thesis can be divided roughly into two parts: theory (chapters 2-4) and results (chapters 5-7). In chapter 2 we introduce the key theoretical concepts, which we use throughout this work. Chapter 3 summarises and discusses the current literature (both modelling and experimental results) on three types of problems: radiation damage cascades, laser photo-excitation and swift heavy ion tracks. In chapter 4 we provide the technical details

on how we have extended DL_POLY package to incorporate the effects of electronic excitations at the level of the 2T-MD model and the typical simulations setups required for each simulation type.

In the results chapters we discuss the exact parameterisation of the models and present the modelling results in the context of the previous findings and experimental data for three above-mentioned classes of problems: radiation damage cascades (chapter 5), laser photo-excitation (chapter 6) and swift heavy ion tracks (chapter 7). The aims of the consecutive results chapters are as follows.

Chapter 5: analysis of the impact of the electronic stopping and electron-phonon coupling implementation on the primary radiation damage production through 2T-MD cascades simulations in Fe.

Chapter 6: characterisation of the structural changes of laser-excited Au by comparing the calculated and experimental time-evolution of Bragg peaks.

Chapter 7: development of a method based on the 2T-MD formalism for simulation of band-gap materials. Testing and validation of this development in the case of swift heavy ion tracks in semiconductors, such as Si and Ge.

Finally, chapter 8 provides a summary of the thesis and gives recommendations for the future research avenues and ideas for further augmented molecular dynamics development.

Chapter 2

Models of electronic excitations in radiation damage

2.1 Theoretical description of radiation damage mechanisms

2.1.1 General concepts

The physics of slowing down of a projectile that is penetrating a target medium is characterised by the so-called stopping power. It is defined as the energy loss (E) of a particle per distance (x) travelled along its path

$$S = \frac{dE}{dx}. \tag{2.1}$$

It is an effective quantity as it encompasses all of the different projectile-target processes, through which a projectile loses its energy travelling through a medium. These effects include (after [21]): emission of radiation, chemical/nuclear reactions, elastic atomistic collisions (i.e. transfer of kinetic energy and momentum) and changes in the electronic state of the target and projectile atoms through electronic excitations and ionisation. For convenience, the stopping powers relating to the elastic ion-ion collisions and inelastic ion-electron events are separated out and called nuclear S_n and electronic S_e stopping powers, respectively, so that

$$S = S_n + S_e. \tag{2.2}$$

Depending on the energy of the imparting particle, different stopping power regimes can be distinguished. When a particle's energy is relatively small, typically up to several keV, the nuclear stopping power dominates over the electronic one, implying that ion-ion collisions are a predominant effect. The nuclear stopping power peaks for the projectile energies between the keV and MeV. Also, in this range, S_e rises sharply, but it remains smaller or comparable with the atomistic stopping ($S_e < S_n$). At higher projectile energies, the probability of a direct atomistic projectile-target collision becomes virtually zero and the projectile produces a trail of electronic excitations along its path and so $S_e \gg S_n$. In this thesis, we are studying the radiation damage dynamics in two regimes: (i) $S_e < S_n$, in the case of fusion neutron primary knock-on (pka) atoms (pka is an atom of the target material that was first to interact with the

impinging projectile); (ii) $S_e \gg S_n$, in the case of swift heavy ions (SHIs), where the explicit atom-atom collisions are not considered. These two regimes are highlighted schematically in Fig. 2.1.

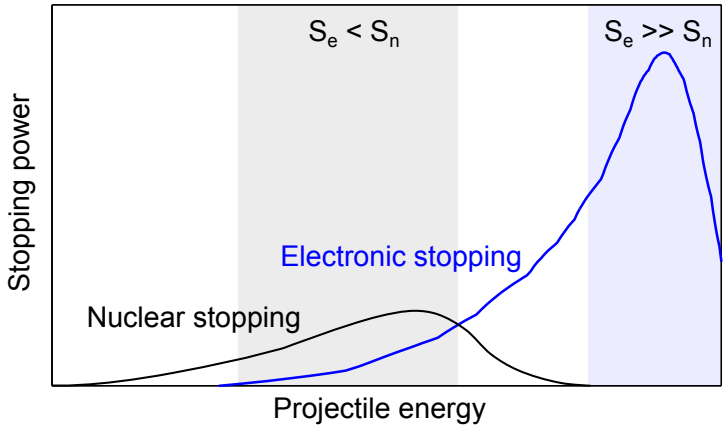

Figure 2.1: Typical electronic and nuclear stopping in a target as a function of projectile energy. In the $S_e < S_n$ regime, the atom-atom collisions are dominant, but electronic effects are not negligible, while in the $S_e \gg S_n$ range direct atomistic collisions are highly improbable.

The physics of interaction between the projectile and the target electrons is classified conveniently into two regimes: electronic stopping (a ballistic projectile one, where electronic stopping dominates) and the electron-phonon coupling one - applicable to small atomic perturbations. These two processes have the same underlying physics, i.e. a response of electrons to atomic motion through ionisation and excitation. However, the electron-phonon coupling occurs when small harmonic atomic vibrations dominate and the electronic stopping is derived for a single atom moving in an electron medium, colliding inelastically with electrons. In the former case, the ionic temperatures, and thus phonons can be determined and the electron-phonon provides an energy transfer mechanism from electrons to atoms and vice versa. This is in contrast to the electronic stopping power, which deals with the energy transfer from the projectile to the electrons only. We discuss both of these processes in turn.

2.1.2 Electronic stopping

The two most popular binary collision models build specifically to derive the electronic stopping power are due to Firsov [22] and Lindhard and Scharff [23]. The first comprehensive approach to stopping theory in amorphous media (expanding on Lindhard and Scharff [23]) was published by Lindhard, Scharff and Schiott [24] and is commonly referred to as the LSS theory. The Lindhard and Scharff expression is derived from elastic scattering of free electrons of the target atoms from a screened point charge of the projectile. Firsov's model is derived from the momentum exchange of projectile and target atoms when the electron clouds of both overlap. Both formalisms predict the electronic stopping power to be proportional to the projectile velocity, $S_e \propto v$. Also, both of these models are applicable to slow and heavy particles only. Slow ions in this context means $v < v_o Z_1^{2/3}$, where $v_0 = \alpha c = e^2/4\pi\epsilon_0\hbar$ is the Bohr velocity

of an inner shell electron in a hydrogen atom, Z_1 is projectile atomic number and α denotes the fine-structure constant; heavy implies $Z_1 \gtrsim 20$. In this regime the projectile ions are considered not to be fully stripped of electrons (nor neutral) with inner shells not contributing to the stopping power. On the other hand, the high speed regime considers bare nucleus ions and the stopping power is explained by the so-called Bethe-Bloch formula, which predicts $S_e \propto (1/v^2)\ln(v^2)$. A comprehensive review of the vast subject of the electronic stopping models applicable to different velocities and the atomic numbers of a projectile can be found in [25].

2.1.3 Electron-phonon coupling

There are two ways in which ions interact with electrons. First, the static ions give a periodic potential to the conduction electrons. Secondly, when ions vibrate they can scatter off the electrons (and likewise the electrons can scatter off the phonons) - this is the essential physics behind the electron-phonon (e-p) coupling. Many analytical frameworks, which consider explicit calculations of scattering rates of electrons in particular states of phonons, exist. However, a theoretical e-p coupling derivation is beyond the scope of this thesis. Excellent theoretical accounts on the subject can be found in [26] with a more formal treatment in [27]. In a simple picture we adapt in this thesis, the e-p coupling process is an effective interaction parameter G transferring the energy between the electrons and ions in a two-temperature (2T) state formalism, where different effective temperatures are assigned to electrons and ions. This is due to the fact that in the models studied here, phonons and electrons are not explicitly represented.

There are numerous experimental measurement techniques (summarised, for instance, in [28]) and *ab initio* theoretical attempts [29–31] to calculate G and its strong dependence on the electronic temperature. It is also considered that it depends on the local structure and ionic temperature [32]. For most materials, the value of G is not known or known with a high uncertainty. Furthermore, the limited studies point to a strong variation of the e-p coupling across materials. As a result, in theoretical or modelling work a range of G values is usually sampled (as we do for swift heavy ions in chapter 7).

In the ultrafast science of laser excitation and in thermal models of swift heavy ion irradiation, e-p coupling is mainly responsible for the energy transfer from the excited electrons to the colder ions. In molecular dynamics (MD) cascade simulations this process is also (and under certain conditions even primarily) responsible for cooling of hot ions. The most pertinent and difficult challenge is to determine when the process of e-p coupling is applicable in a collision cascade. In the radiation community, the effects of e-p coupling are considered when a ballistic motion of an atom through a medium is no longer applicable. This can occur under a particular energy threshold. Other arguments can involve a sufficient thermalisation of the ionic system, which allows for an ionic temperature to be defined. When modelling radiation damage cascades in chapter 5, we explore both of these options.

2.1.4 Time scales of electronic effects

We have thus-far analysed how the electrons get excited (i.e. gain an effective high electronic temperature) through the electronic stopping and electron-phonon coupling processes. We now discuss the relevant processes, and their timescales, in an electronically excited solid. This is usually presented in the context of short pulse (sub-picosecond) laser excitation, but it is also relevant in studying radiation damage and particularly SHIs, which also excite mainly the electrons. In a recent review on non-thermal transitions in semiconductors [33] four different types of carrier (electron-holes) and ionic processes were identified (see Fig. 2.2). Most of these are also applicable to metallic materials, where the processes involve electrons rather than carriers. These processes are carrier excitation and removal, thermalisation and thermal effects. Most of these can be accounted for in the models based on the two-temperature approach discussed in Sec. 2.2. Carrier excitations cover single and multi-photon absorption of photons from a laser-pulse, or excitation from SHIs. Impact ionisation also contributes to carrier generation in the case of semiconductors. The thermalisation processes, which is realised by the carrier-carrier scattering, occurs within 10-100 fs and forces the carriers into a Fermi-Dirac distribution. Therefore, on the picosecond timescale of the relevant models, it is usually assumed to occur immediately, thus allowing the definition of an effective electronic temperature. The other thermalisation effect is the electron-phonon (carrier-phonon) scattering, which acts on a typical timescale of picoseconds and is responsible for driving the electronic and ionic temperatures to an eventual equilibrium. In semiconductors, Auger or other recombination effects (discussed in Sec. 2.2.2.2) can additionally remove carriers. The thermal effects, such as ablation and thermal diffusion, usually occur at timescales greater than 10 ps. Collapse of the crystal structure due to electron-phonon coupling can occur at a minimum time of around a picosecond, which is around the frequency of a phonon. Resolidification mediated by phonon thermal conductivity occurs much later at a timescale of nanoseconds. However, it can occur quicker if the excited electrons transport away some of the energy from a locally molten region.

2.2 Continuum models

Continuum models, and particularly the ones based on the two-temperature (2T) formalism, were among the first attempts to simulate the conditions of local electron-ion non-equilibrium. We concentrate on the 2T-based inelastic thermal spike model (iTS) developed to describe swift heavy ion (SHI) irradiation, and its band-gap extension, called the extended iTS model (eiTS).

2.2.1 Two-temperature and the inelastic thermal spike models

In the iTS model, the energy of an incoming particle is deposited in the electrons of the target material. This energy then gets transferred to the lattice through the electron-phonon interaction on a timescale of a few picoseconds. If the melting point is exceeded within the propagating thermal spike, local (and transient) lattice melting and/or sputtering can occur.

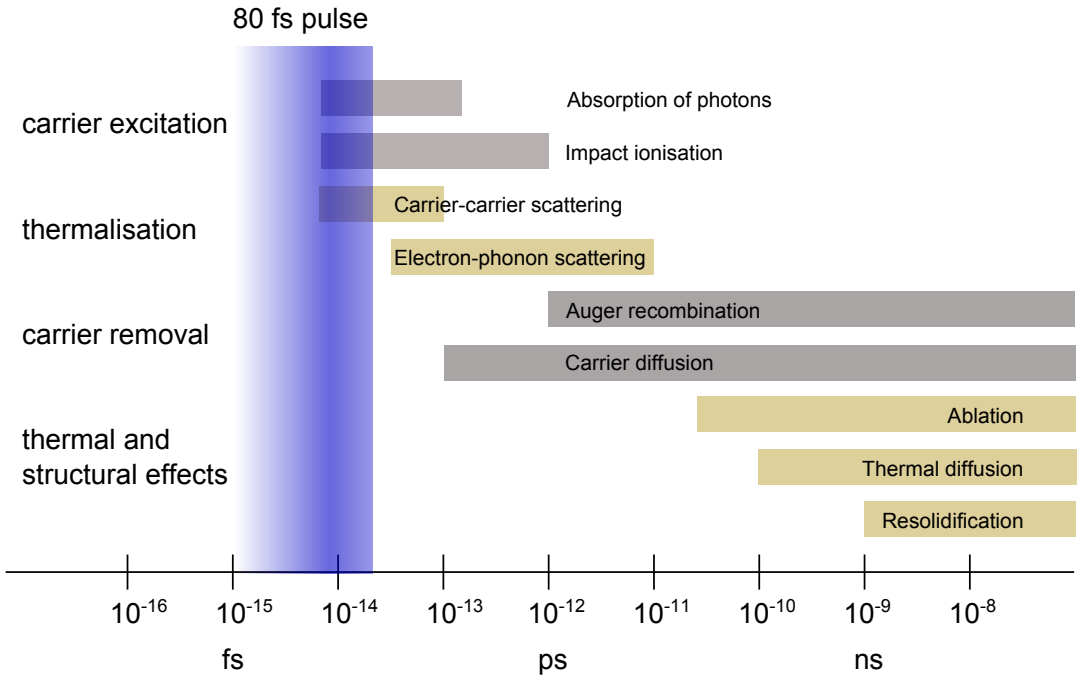

Figure 2.2: Relative timescale of electronic effects in excited solids in the case of semiconductors. Impact ionisation and carrier recombination processes are irrelevant for metals, but the relative timescales of carrier (or electron) excitation, carrier-phonon coupling and thermal effects are still applicable. Short thermalisation of the electronic system enables us to define an effective electronic temperature which is distinct from the ionic one, and therefore apply the two-temperature formalism.

The subsequent cooling and recrystallisation usually leaves residual defects and/or modified crystal structure localised around the path of the impinging ion. A continuous modified structure created in that way is called an ion or latent track. The idea of a thermal spike following ion irradiation was originally proposed by Desauer [34].

The model was later revisited by Lifshitz, Kaganov and Tanatarov [35] (and in [35–37]) who developed the two-temperature formalism. This approach assumes two separate temperatures for electrons (T_e) and ions (T_i), not necessarily in a mutual equilibrium. The model further states that the energy exchange rate is proportional to both the electron-phonon coupling strength (G) and the temperature difference between the systems ($T_e - T_i$). It treats the electronic and atomistic systems as continuous media with the time-evolution of heat flows in both governed by a heat diffusion equation (obtained from Fourier's law). It can therefore be expressed as a set of two coupled non-linear differential equations describing the spatiotemporal evolution of effective electronic and ionic temperatures

$$C_e(T_e)\frac{\partial T_e}{\partial t} - \nabla \cdot [\kappa_e \nabla T_e] = -G(T_e - T_i) + A(r[v_{ion}], t) \tag{2.3a}$$

$$C_i(T_i)\frac{\partial T_i}{\partial t} - \nabla \cdot [\kappa_i \nabla T_i] = G(T_e - T_i). \tag{2.3b}$$

Here $C_{e,i}$, $\kappa_{e,i}$ are the specific heats and the thermal conductivities of the electronic (subscripted e) or atomistic/ionic lattice (subscripted i) systems, respectively. Parameterisation of the

energy source term $A(r[v_{ion}], t)$ is discussed in Sec. 2.2.3.1. In Eq. 2.3a, r denotes the lateral (perpendicular to the ion's path) initial energy deposition radius, v_{ion} is the impacting ions's velocity and t is time. In the present model, there is only one energy source (i.e. $A(r[v_{ion}], t)$), as we assume an electronic stopping power regime (i.e. $S_e \gg S_n$), where the contribution from S_n is negligible.

Both equations (Eq. 2.3a and Eq. 2.3b) are typically solved numerically because of the complex temperature dependence of most of the parameters involved. A standard numerical solution scheme is outlined in Sec. 4.3.2. The application of the model and its recent successes and criticism are reviewed in Sec. 3.3.2.2.

The two-temperature approach is also commonly used for ultrashort (sub-picosecond) laser irradiation studies with the modification of the source term in Eq. 2.3a described in Sec. 2.2.3.2. This formalism applies because of the shorter characteristic time of electron-electron (or in general carrier-carrier) scattering (10-100 fs) and the ultrashort laser pulse width ($<$ 100 ps) as compared with the timescale of the electron-phonon coupling (0.1-10 ps; see Fig. 2.2). These timescales enable us to define an electronic temperature on the picosecond timescale and the relatively slow electron-phonon coupling process results in a state of electron-ion temperatures non-equilibrium. The existence of a two-temperature state was later confirmed in experiments [38, 39], but it wasn't until a combined theoretical and experimental study [3] (see chapter 6) that the 2T model was quantitatively verified for metals.

2.2.2 Extended inelastic thermal spike model

The development of the extended inelastic thermal spike (eiTS) method [7, 8, 40, 41] is driven by the premise that band-gap materials behave differently to metals following strong electronic excitation. Specifically, the number of conduction electrons is constant in a metal, but it varies in space and time in a band-gap material. This variation can be accounted for by including an additional conservation equation for the carrier density.

2.2.2.1 Theory

The theory behind the extended iTS model is based on a formulation of Boltzmann transport equations for carrier and energy transport in semiconductors, which first appeared in [42]. This approach was later revisited in [43] (and later in [44] with errors in the formulation of the carrier current) and applied to solve carrier dynamics following ultrafast laser excitation. The model remained widely used to describe the lattice dynamics following short-pulse laser excitation (exemplar recent applications can be found in [45–48]) and it was not applied to describe ion irradiation until the publication by Klaumänzer [41]. In [41] the provision for the iTS extension based on Boltzmann transport equations for band-gap materials was critically reviewed. This continuum model of carrier dynamics has also been recently linked with MD [49], forming an augmented continuum-atomistic technique. The core of the continuum model forms a set of three coupled differential equations corresponding to conservation of carrier

density (N), carrier energy (U) and ionic temperature (T_i). These are expressed as follows

$$\frac{\partial N}{\partial t} - \nabla \cdot J = G_{e-h} - R_{e-h} \tag{2.4a}$$

$$\frac{\partial U}{\partial t} - \nabla \cdot W = -\frac{C_{e-h}}{\tau_{ep}}(T_e - T_i) + A(r[v_{ion}], t) \tag{2.4b}$$

$$C_i(T_i)\frac{\partial T_i}{\partial t} - \nabla \cdot [\kappa_i \nabla T_i] = \frac{C_{e-h}}{\tau_{ep}}(T_e - T_i), \tag{2.4c}$$

where G_{e-h} and R_{e-h} are carrier generation and recombination terms, J and W are carrier current and carrier energy flux density and A is the initial energy given to the carriers. These terms are discussed in turn. Following [43, 45], the sink term (Eq. 2.4a) in the carrier density equation ($-R_{e-h}$) is expressed as

$$-R_{e-h} = -\gamma N^3 + \delta(T_e)N, \tag{2.5}$$

where γ is the Auger recombination and δ is the impact ionisation coefficient. There might be other sink terms for different materials (see Sec. 2.2.2.2 for a discussion), however only these two terms are relevant in Si, results for which are presented in chapter 7. Simulations of Ge neglect the impact ionisation, leaving the Auger recombination term only. The source term (G_{e-h}) is the number of carriers generated after an electronic excitation event. The energy absorption and carrier generation rates from photon absorption are well-known for lasers. Carrier density generation in the case of SHI irradiation is assumed to take a fraction ($\sim \frac{1}{3}$) of the total energy deposited, $A(r[v_{ion}], t)$. In Eq. 2.4a, J, is the carrier-pair current, which is related to the carrier density (N), electronic temperature (T_e) and band-gap (E_g) by

$$J = -D(T_i)\left(\nabla N + \frac{2N}{k_B T_e}\nabla E_g + \frac{N}{2T_e}\nabla T_e\right), \tag{2.6}$$

with D being the ambipolar diffusivity - diffusion of a bound electron-hole carrier dependent on lattice temperature (T_i). This formulation renders the model to be charge-neutral. Since we treat electron-holes as bound carries, their respective temperatures are also assumed to be the same (i.e. $T_e = T_h$). For simplicity, in the context of eiTS we stick to the T_e notation to denote the bound carrier temperature (T_{e-h}). A locally non charge-neutral model requires an additional term for the electron-hole electrostatic interaction (see [41]). The carrier energy flux density (W) is related to J by

$$W = (E_g + 4k_B T_e)J - (\kappa_e + \kappa_h)\nabla T_e, \tag{2.7}$$

with κ_e and κ_h being the thermal conductivities of electrons and holes, respectively. The W term is composed of two parts: one dependent on the carrier flow (J) and a carrier temperature gradient part. The thermal conductivities in Eq. 2.7 are related to the experimentally measured carrier mobility values by the generalised Wiedemann-Franz law [50]; mobility values need typically to be adjusted for lattice and electronic temperatures (see Sec. 7.2.2). The total energy, U, of the electron-hole carrier consists of a potential and kinetic part

$$U = NE_g + 3Nk_B T_e. \tag{2.8}$$

The energy source term, $A(r[v_{ion}], t)$, in Eq. 2.4b corresponds to the initial deposition of energy in the system, which would be different for a laser pulse or a SHI impact. In the case of SHI, as mentioned earlier, we assume that a fraction of the energy from the source term is required to create carriers (NE_g) and the remaining part goes to their kinetic energy ($3Nk_BT_e$). The carrier energy and atomistic lattice coupling $\dot{U}_{ep}$ is phenomenologically realised by

$$\dot{U}_{ep} = \frac{C_{e-h}}{\tau_{ep}}(T_e - T_i), \tag{2.9}$$

where τ_{ep} is the electron-lattice relaxation time and C_{e-h} is the electronic (electron-hole) specific heat given by

$$C_{e-h} = \frac{\partial U}{\partial T_e} = N\frac{\partial E_g}{\partial T_e} + 3Nk_B, \tag{2.10}$$

with the first term being typically neglected. An alternative *ab initio* parameterisation of C_{e-h} linked with this model for Si is presented in [51]. The relaxation time is related to the electron-phonon coupling (G) by [52]

$$\tau_{ep} = C_{e-h}/G, \tag{2.11}$$

where G is dependent on electronic and lattice temperatures, but assumed to be a constant in eiTS. Eq. 2.11 is derived from the energy transfer rate ($\dot{U}$) in the two-temperature formalism (see Eq. 2.3), which can be expressed as $\dot{U} = C_e\frac{\partial T_e}{\partial t} = -C_i\frac{\partial T_i}{\partial t} = -G(T_e - T_i)$ in the absence of the heat transport term [52]. Assuming a constant e-p coupling and $T_e \gg T_i$, the energy decrease in time is a exponential with a characteristic time, $\tau_{ep} = C_{e-h}C_i/(G \cdot (C_{e-h} + C_i))$. Since $C_i \gg C_{e-h}$, Eq. 2.11 follows. We note that in the two-temperature formalism, the electron-phonon relaxation time τ_{ep} is different to the electron-phonon and electron-electron scattering times determining the transport time τ_e in the Drude's model of conduction. These scattering times are determined by momentum-changing collisions of electrons and phonons. On the other hand, the relaxation time τ_{ep} describes the energy exchange between electrons and phonons. It thus follows that the τ_{ep} parameter cannot be directly connected to the mean free path of electrons (i.e. transport time, τ_e) and hence materials transport properties such as heat conductivity.

Finally, similarly to the iTS continuum model, the last equation in the set (Eq. 2.4c) governs the heat flow in the atomistic lattice with C_i and κ_i being the experimentally measured specific heat and thermal conductivity, respectively.

A numerical solution of the equation set (Eq. 2.4) behind the eiTS model is nontrivial and there exists a separate publication devoted to this problem [53]. We describe our finite difference method solution in Sec. 4.3.2 and Sec. 4.3.4.

2.2.2.2 Carrier processes

In the simulations for Si and Ge (which are presented in chapter 7), it is necessary to consider only the Auger recombination and impact ionisation effects as sink/source terms in the equation for the carrier density, Eq. 2.4a. In band-gap materials, the Auger effect is a three-body

interaction phenomenon in which an electron-hole combines and an electron from a higher energy level takes up the recombination energy and gets promoted in to the conduction band. Impact ionisation can be viewed as the inverse of the process. An electron or a hole with sufficient kinetic energy can knock an electron out of its bound state in the valence band and promote it to a state in the conduction band thus creating a carrier pair. From energy-momentum considerations the initial energy in an impacting carrier must be greater than $\frac{3}{2}E_g$, where E_g is the material band-gap. Recombination and impact ionisation processes allow the carriers to achieve equilibrium at a particular electronic temperature, T_e. Also, neither of the these phenomena represent source or loss terms for total carrier energy and are non-radiative processes. However, it needs to be noted that Auger recombination increases the rate of carrier energy transfer to the lattice by converting the carrier ionisation energy into thermal energy, which is lost to the lattice rapidly, since the systems' coupling strength is proportional to temperature difference between ions and electrons. Impact of the Auger recombination R^A_{e-h} on carrier density can be significant in the initial stages following an electronic excitation. Since $R^A_{e-h} \propto N^3$, once the energy deposition is finished and the carriers have diffused, Auger recombination becomes unimportant. Impact ionisation was shown to have minimal effect on carrier generation. However, it is not certain if recombination effects can be included before a Fermi-Dirac distribution of carrier pairs is achieved, which occurs in 10-100 fs (see Fig. 2.2).

Figure removed due to third party copyright restriction

Figure 2.3: Schematic representation of various carrier and lattice processes in band-gap materials following electronic excitation (after [33]). VB and CB stand for valence band and conduction band, respectively; red/yellow arrows depict phonons/photons. (a) Carrier de-excitation by phonon emission (b) Direct Auger recombination, (c) Impact ionisation, (d) Radiative recombination, (e) Indirect non-radiative recombination, (f) Shockley-Read-Hall recombination. *Figure reproduced from [7].*

Other sink terms are possible and may be dominant/significant in other types of materials [33, 41]. These are listed below and a few more are presented in Fig. 2.3.

1. Radiative recombination (Fig. 2.3.d) is the inverse of the optical excitation process, where the excess of carrier energy is given out in a form of a photon. This de-excitation by

photon emission transports the energy out of the excited region, since the probability of reabsorption is very low.

2. Direct recombination is particularly important for direct semi-conductors (such as GaAs), where instead of photon emission, the energy is directly transferred to (many) phonons. This process is extremely improbable in defect-free materials. Furthermore, Si is an indirect band-gap material and hence is not affected by this process.

3. When defects and impurities are present, which have electronic states in the middle of the band-gap, another type of recombination process can arise. These so-called 'trapped' states catalyse recombination and are characterised by the Shockley-Read-Hall recombination rate (Fig. 2.3.f). The recombination energy is $\sim E_g$ and is transferred to the phononic system. Currently, this process is neglected in the continuum model as it contains no information about defect and impurities, and in the MD-coupled scheme due to complexity.

4. In a wide band-gap insulator with low atomic density, electrons and holes attract each other electrostatically so strongly that they form an excited state in the middle of the band-gap. This so called 'self-trapped exciton' is strongly bound and immobile. This process does not affect Si and cannot be modelled in eiTS, as it does not consider charged carriers.

5. In-surface recombination the excess energy is given to a surface state. Currently, surface effects are not considered.

2.2.3 Energy deposition

Accuracy of any of the models depends critically on the correct choice of the geometry of the initial energy deposition on electrons. Although transfers of energy and carrier currents, as well as the electron-phonon coupling, complicate the situation at later stages, it is still important to know the initial electronic energy deposition in the carrier excitation and/or ionisation stage. In most media this is referring to the events occurring at a femtosecond timescale. We, in turn, describe the energy source terms in the cases of a SHI event and laser photo-excitation.

2.2.3.1 Swift heavy ion

In swift heavy ion (SHI) simulations, the stopping power S_e for a given ion energy is calculated with SRIM [54], which uses a combination of experimental data and empirical fits to describe ion stopping in matter. However, the density of the deposited energy along the direction perpendicular to the ion path depends on the velocity of the projectile ion (this is the so-called velocity effect) and the target medium. The experimentally verified [55] velocity effect implies that the ions of the same stopping power, but greater velocity, produce a sharper electronic excitation distribution.

Table 2.1: Mean deposition radii for different specific ion energies in silicon and silica.

Specific ion energy E'	Velocity v_{ion}	r'_{ion} silicon	r'_{ion} Silica
5 MeV/u	$2.20{\cdot}10^7$ m/s	6.24 nm	0.81 nm
1 MeV/u	$9.82{\cdot}10^6$ m/s	2.79 nm	0.36 nm
0.5 MeV/u	$6.95{\cdot}10^6$ m/s	1.97 nm	0.26 nm
0.07 MeV/u	$2.60{\cdot}10^6$ m/s	0.74 nm	0.096 nm
0.04 MeV/u	$1.96{\cdot}10^6$ m/s	0.56 nm	0.072 nm

We assume that a SHI deposits a carrier energy density $A(r[v_{ion}], t)$ of cylindrical symmetry in the central column of the simulation cell. It is further assumed that the spatial energy generation on electrons (integrated in time) is distributed normally in the radial direction r from the ion path centre, r_0:

$$D(r[v_{ion}]) = \frac{S_e}{\sqrt{2\pi\sigma^2}} \exp\left[-\frac{(r-r_0)^2}{2\sigma^2}\right], \tag{2.12}$$

with a standard deviation denoted by σ. Two regimes appear in the energy deposition: the core, within the mean absorbtion radius r'_{ion}, where most of the energy is deposited and the so-called crown, where deposited energy density over a large volume is typically small. It was noted in [55] that due to the differences in the time-averaged energy densities between these two regions, it can be assumed that the core is the driving force in the latent track formation. For an assumed Gaussian distribution, the major challenge is the determination of r'_{ion} (assuming here $r'_{ion} = \sigma$) for a particular medium and a projectile ion specific energy.

The mean absorption radius r'_{ion} can be obtained by applying Bohr's principle of adiabatic invariance [41]. For non-relativistic ions it can be expressed as

$$r'_{ion} = b_{max} = \frac{\hbar v_{ion}}{2E_g}, \tag{2.13}$$

where v_{ion} is the velocity of the imparting ion, E_g is the band-gap of the material at 300 K and $\hbar$ is the reduced Planck constant. It is derived as follows. The impact parameter is denoted b, hence the transit time ($\sim 2b_{max}/v_{ion}$) must be smaller than or equal to the reaction time ($\sim \hbar/\epsilon$) of the electron to which energy (ϵ) is transferred from the incident particle. The deposition radius (b_{max}) is assumed to be the maximum impact parameter. As the minimum estimate for the lowest electronic excitation energy in a band-gap material is $\epsilon \sim E_g$, hence Eq. 2.13 follows. The screening of the projectile can be safely ignored in a solid material with a relatively large band-gap [41]. There is also a simple relativistic correction to the above formula in [56]. Since we are be dealing with SHI of typical speeds $\sim 0.01c$ the non-relativistic formulation in Eq. 2.13 can still be applied. Exemplar r'_{ion} radii for specific ion velocities in silicon and silica are shown in Tab. 2.1.

Following [57], we consider $A(r[v_{ion}], t) = AD(r[v_{ion}])\alpha e^{-\alpha t}$ with $\alpha = 1/\tau_d$, where τ_d is a characteristic deposition time taken to be 1 fs . Normalisation of $A(r[v_{ion}], t)$ is constrained so that the spatial and temporal integration equal the assumed electronic stopping power (S_e);

in cylindrical coordinates

$$S_e = \int_{t=0}^{5\tau} \int_{r=0}^{r_{max}} 2\pi A(r[v_{ion}], t) r dr dt, \tag{2.14}$$

where r_{max} is the maximum range of carriers projected in the lateral direction and is assumed to be 5σ. A more sophisticated method of calculating the exact energy deposited in the electronic structure (which can also be applied to metals) is presented by Waligórski, Hamm and Katz [58] and has been recently reviewed in [59].

2.2.3.2 Laser pulse

We assume the laser source term $S(t, z)$ to be a Gaussian in time [60]:

$$S(t, z) = \frac{F}{\sqrt{2\pi\sigma^2}} \exp\left[\frac{(-4\ln 2)\cdot(t - t_0)^2}{t_p^2}\right] \cdot \frac{\exp\left[-z/L_p\right]}{L_p}, \tag{2.15}$$

where t is time, t_0 is the time zero (arrival of the peak of the laser pulse), z is the depth of the sample, F is the absorbed laser fluence, L_p optical penetration depth and t_p is the duration of the pulse taken at the FWHM, linked to σ through

$$t_p = \sigma \cdot (2\sqrt{2\ln 2}). \tag{2.16}$$

Note that the laser source term $S(t, z)$ describes the attenuation in the z-direction only. Lateral energy distribution will be linked to the spot shape and size of a particular laser beam.

2.3 Atomistic models

Continuum models (Sec. 2.2) were developed to describe the relaxation times of electron-ion non-equilibrium. These models were traditionally used to model ultrashort pulse laser illumination and later swift heavy ion impacts. On the other hand, primary radiation damage description (caused, say, by high-energy neutrons) requires atomistic models and specifically the knowledge of the number of defects produced after an irradiation event. The first modelling attempts to calculate this involved the binary collision approximation (Sec. 2.3.1). This method was later slowly taken over by classical molecular dynamics, which offered a better parameterisation of the atomistic interactions. However, it wasn't until the beginning of the century when the electron-ion non-equilibrium ideas and molecular dynamics were merged into hybrid (also called augmented) models (Sec. 2.3.2). More sophisticated modelling developments in radiation damage involve incorporation of the electron-ion non-equilibrium caused by irradiation by simulating the electron and ion dynamics explicitly (Sec. 2.3.3).

2.3.1 The binary collision approximation

The binary collision approximation (BCA) model simulates a cascade event, initialised by an energetic pka, simply as a series of collisions involving two atoms only. Atoms are assumed to travel in straight lines at constant velocity between the collisions. When atoms come within a

given distance, they interact and their new directions and kinetic energies are determined from scattering theory. In the BCA model, since there are only four types of possible scattering outcomes (after [21]), which depend on the kinetic energy transferred to the target (E^t), remaining kinetic energy of the projectile atom (E^p), spherically-averaged threshold displacement energy (TDE) E_d (i.e. the energy required to permanently displace an atom from its lattice site) and a small energy cutoff E_{cut}:

1. $E^t > E_d$, $E^p > E_{cut}$: The projectile atom continues colliding and the target atom joins the cascade,

2. $E^t > E_d$, $E^p < E_{cut}$: The projectile atom scatters off the target atoms, which remains on its lattice position,

3. $E^t < E_d$, $E^p > E_{cut}$: The projectile atom replaces the target at its lattice site, and the target atom joins the cascade instead,

4. $E^t < E_d$, $E^p < E_{cut}$: The projectile atom becomes a local interstitial, while the target atoms remains on its lattice position.

The SRIM [54] package is an example program, which uses the above algorithm to calculate the range of a pka in a given target. Additionally, TRIM [61], which is at the core of SRIM and precedes it, gives the resultant distributions of ions and damage yield. Another popular code, MARLOWE [62] is commonly used in BCA simulations in crystalline, rather than amorphous, targets. Later version of the codes additionally included the effects of electronic stopping in the formalism of Firsov [22], and Lindhard and Scharff [23].

The BCA model has been used to study collision cascades [63, 64] and sputtering yields [65, 66]. This method was the basis for the famous "NRT" (after Norgett, Robinson and Torrens [67] and Kinchin and Pease [68]) empirical formula, which related the number of Frenkel pairs N_{FP} to the damage energy in a linear fashion (equivalent here to the pka energy E_{pka} as the electronic effects are neglected):

$$N_{FP} = \frac{0.8 E_{pka}}{2 E_d}. \tag{2.17}$$

The method, despite setting a standard for a long time, omits a lot of relevant physics. First of all, it does not include the many-body effects, which at higher pka energies would most certainly happen. Because of that it does not predict a local transient melt phase or a thermal spike in cascade collisions. Secondly, because of a lack of any atomistic dynamics apart from the simple binary collision algorithm, it cannot describe defect diffusion and recombination occurring at the primary radiation damage formation stage.

2.3.2 Molecular dynamics

An explicit representation of ions and inclusion of many-body effects in MD marks a significant improvement over the BCA model. Due to the growth in computational power and development of parallel MD codes, studying primary radiation damage with MD has gradually become more

popular. Earliest MD studies (with low pka energies of 400 eV) date back to 1960s (Gibson, Goland, Milgram and Vineyard [69]) and were among the first applications of MD - the first use of the MD technique was reported in 1959 [70]. However, it wasn't until the 1990s when large-scale simulations with complex many-body potentials became affordable that MD became a standard tool for primary radiation damage study.

The current achievement of classical cascade MD simulations, as applied to radiation damage problems has been extensively reviewed, for instance, in [71–73]. In brief, cascade MD simulations have shown that (after [71]): (i) cascade recombination effects absent in the BCA reduce the amount of the residual damage to a fraction (0.3) of the NRT predictions, (ii) high-energy cascades break up into sub-cascades and this branching process boosts recombination, (iii) large clusters of SIA can already be formed by primary radiation damage processes.

Below we concentrate on the MD-based modelling methods, which relax the assumption of local electron-ion non-equilibrium and attempt to include a degree of electronic excitation effects.

2.3.2.1 Augmented molecular dynamics

The augmented MD methods aim to include the effects of electronic stopping and electron-phonon coupling as additional damping and driving terms in the atomistic equations of motion. The electronic stopping effect for slow and heavy particles can be included in molecular dynamics as an additional friction force proportional to the projectile velocity using the fact that $S_e \propto v$. Caro and Victoria [74] and Finnis, Agnew and Foreman [75] have pioneered the idea of viscous MD with a non-directional damping term applied to all ions above an energy cutoff E_c - an *ad hoc* value that prevents an equilibrium system (or later stages of a cascade simulation) from being artificially damped. This approach has become almost a standard method of extracting the energy due to electronic stopping in molecular dynamics cascades and has been used extensively since.

Such an approach assumes that the local electronic temperature rise does not have an impact on the dynamics and that this energy is not fed back to the atoms. The original approach by Caro and Victoria [74] also included an additional sink term for the atoms that represented the electron-phonon coupling. The sink was linked to a target temperature and neglected any local heating effects. The local effects of electron-phonon coupling were pioneered by Duffy and Rutherford [76] via the so-called inhomogeneous Langevin thermostat mechanism. Such inhomogeneity necessitated the inclusion and concurrent tracking of a local electronic temperature in a two-temperature formalism.

The effect of electron-phonon coupling on primary radiation damage was touched upon in several papers ([77–79] and more recently in [80]). It was concluded that the strength of the e-p coupling has a significant effect on the primary damage formation - it can increase [78] or, under some circumstances, decrease the number of defects [81]. Nonetheless, it is still uncertain how to include the effect of electron-phonon coupling in molecular dynamics in a precise physical manner. The method we adapt here, which broadly follows [76], is presented in Sec. 4.3.

2.3.2.2 Including excited state interatomic potentials

Molecular dynamics with its augmented applications to non-equilibrium dynamics is built on the assumption that the interatomic potentials remain unmodified by the strong local electronic excitations. This can be a good approximation to some extent and we will revisit this point in chapter 6. However, in general excitations of the order of several eV can cause bond weakening, bond breaking and other more complex effects on the potential energy surface (some of which are discussed in Sec. 3.3.2.3).

Some early attempts at including the change in the bonding character involved transient and local removal of the attractive part of the potential [82, 83]. This has obvious limitations, as the resulting excited-state potential is entirely phenomenological and not constructed to reproduce any particular property. An empirical fitting procedure for potentials dependent on an effective electronic temperature was presented in [84] for tungsten and in [85] for silicon. An alternative scheme based on the force-matching technique [86] was applied to construct a T_e-dependent potential for gold [87]. To date, only three T_e-dependent potentials have been published.

In general, these potentials have provided us interesting insights in non-equilibrium dynamics. For instance, the increase of the lattice parameter at high T_e was responsible for non-thermally accelerated melting (or "phase explosion"), which was found in the case of laser-excited Si [51] and Au [3]. Such change of the lattice parameter was also a contributing factor in the mechanism of laser-induced ablation in Au [87, 88]. Other notable application areas of such potentials are SHI sputtering studies [83] (see also Sec. 3.3.2.3).

2.3.3 Incorporating electrons explicitly

We briefly overview selected methods to study radiation damage that incorporate the effects of electronic excitations explicitly, rather than as an effective medium. These are based on the Ehrenfest dynamics, where atoms follow trajectories based on quantum mechanical description of electrons. Such methods include time-dependent tight-binding (with explicit electrons) [89] and real-time time-dependent density functional theory (RT TD-DFT), which includes an accurate *ab initio* electronic structure [90, 91].

The above models were used to provide with theoretical calculations of the electronic stopping power [92, 93]. The models point to a complex dependence of the S_e on both the local environment (for instance non-directionality of the drag force [94]) and the ion velocity and can give useful insights into the thus-far assumed electron-stopping power cutoff E_c [91]. Because of the spatiotemporal scales that the RT TD-DFT model can access, the studies are performed with high-energy pka's that are allowed to channel only (and hence no direct atomistic collisions occur). Tight-binding can typically access thousands of atoms and allows for low energy pka (~ 1 keV) studies.

Both of the above modes are useful to evaluate the non-adiabatic effects on radiation damage, allowing for an energy transfer from ions to the electrons. Therefore these can capture the electronic stopping power, however cannot fully account for the electron-phonon coupling

effect, which can transfer the energy from the excited electrons to ions too. This is because Ehrenfest dynamics schemes do not take into account phonon emission as they do not treat the ions quantum-mechanically. The correlated electron ion dynamics method which allows to simulate very few atoms [95–98] could be a potential solution to evaluate and gain an understanding of the electron-phonon coupling process from *ab initio*.

2.4 Summary

In summary, we have presented some basic theoretical concepts in radiation damage and have outlined the timescale of the effects of electronic excitations. We have outlined the theory behind the continuum models, based on the two-temperature approach, which is used to model electron-ion non-equilibrium conditions caused by swift heavy ions and ultrashort laser pulses. We have also discussed how electronic effects can be included in the atomistic MD-based models and the electron-ion dynamics insights that more sophisticated models, which include electrons explicitly, can provide.

Given a trade off between the computational complexity and the physics accuracy, an augmented molecular dynamics scheme can remain very popular in the years to come. This is because it can simulate the evolution of a microstructure of a studied material, providing with an effective model of electronic excitation effects, which can be parameterised more accurately from *ab initio*. For these reasons, it is a model of choice for the problems tackled in this thesis.

Chapter 3

Literature review

3.1 Overview

In this chapter we review the recent progress and current challenges in the field of cascades, swift heavy ions and laser radiation damage modelling. We start by introducing the notion of a collision cascade and consider the stages of its evolution, highlighting the role of electronic effects and the energy domain where these are important. Subsequently, we discuss the so-called warm dense matter (or cold plasma) - a state with hot electrons, but cold nuclei in the context of the recent pump-probe experiments. We also focus on the current advancements in theory and modelling techniques in the ultrafast dynamics field. Finally, we move onto the swift heavy ion irradiation topic, where we describe the experimental evidence for track formation, overview the most commonly used models, and outline the current research directions and challenges.

3.2 Radiation damage cascades

3.2.1 Introduction

In most cases the majority of the radiation energy absorbed by a material is ultimately converted to the kinetic energy of its atoms. This has obvious applications in the nuclear industry, where the kinetic energy from the fission products is converted to thermal energy of the reactor core and subsequently to electricity. Also, future commercial fusion reactors would harvest the energy from highly intense neutron radiation (with the energy spectrum peak at 14.1 MeV). However, radiation, in general, can have a deteriorating effect on material's mechanical and transport properties thereby degrading them to a point where they lose their key functional purpose. In the initial stages, this happens as the incoming energetic particles (radiation) displace atoms from their crystalline positions, and/or create high electronic excitations, creating in turn high structural disorder. Radiation damage is thus an important research subject with implications for both science and technology. The prominent example is fusion energy, with its commercial viability largely depending on the development of advanced materials that would withstand radiation damage created in fierce reactor conditions [9–13].

In a typical radiation damage scenario an incoming atom with a high velocity (but not high enough to predominantly interact inelastically with electrons) displaces other atoms around its path elastically. Such a set of energetic collisions resulting in a region of high topological disorder is often referred to as a "collision cascade". Experiments cannot access typical spatial and temporal scales of a collision cascade event. For example, for a primary knock-on atom (pka) in the energy range of 10-100 keV the duration of the cascade is typically several ps and its size is several tens of nm [99]. Therefore, molecular dynamics simulations, which access such spatiotemporal domains, are invaluable when bridging the gap between theory and experiment. Examples where MD was used as a complementary tool to radiation damage experiments can be found in [99] and in references therein (in particular [100–103]).

In general, radiation damage modelling is a multi-scale problem. It begins with the primary damage production through collision cascades occurring at the picosecond timescale to thousands of years of damage evolution for long-lived radioactive waste encapsulation models (example in [104]). This challenge is tackled in a multi-scaled way with different simulation methods responsible for different spatiotemporal regimes. Accurate and precise prediction of the primary radiation damage yield is thus of cardinal importance, as it forms the starting point for the methods higher up in the multi-scale hierarchy. Since it has been shown that the models of long-term damage evolution are consistently sensitive to the primary radiation damage input [105–107], state-of-the-art (i.e. which gradually include more physical effects, such as electronic excitations) and systematic (i.e. of detailed statistics) MD studies are still required. All in all, cascade simulations enable us to gain insight into the physical phenomena behind radiation damage accruing at ps and nm scales as well as to investigate their effects on materials properties though multi-scale modelling.

3.2.2 The evolution of a radiation damage cascade

The idea of a displacement cascade and an associated term of a thermal spike (explained later in Sec. 3.2.2.2) were developed in the 1950s (after [72]). Shortly after, the first attempts to simulate a collision cascade were made. These used tools such as binary collision approximation and molecular dynamics and the former set the reference calculations in the field until the 1970s. By the end of the 1980s molecular dynamics was slowly taking over, however simulations were carried out using pair-potentials and concentrated primarily on fcc metals. In the late 1980s the first MD simulations employing many-body potentials for sputtering and then cascades were conducted and the first paper [108] focussing on cascades in α-Fe using this advanced potential form was published.

3.2.2.1 The initial stages and channelling

A typical MD radiation damage simulation scenario starts with an atom given a high initial velocity. It is referred to as the primary knock-on atom (pka) and its initial condition represents an interaction with an imparting energetic particle, which is not simulated explicitly. The initial velocity of the pka depends on the type of the imparting particle: its mass and energy

spectrum. The pka displaces atoms elastically as it travels though the material. During this process, if any atom is given an energy greater than the threshold displacement energy (TDE), it can be displaced permanently and, as a result, form a crystalline defect. The TDE value is around 40 eV for iron, as measured experimentally [72] (and references therein) and a majority of the MD interatomic potentials reproduce this value quite well. In general, the dynamics of the ensuing collision cascade is strongly dependent on the energy spectrum of the imparting particle (and hence its pka energy) as well as the properties of the target material.

A pka or any other atom emerging from the collision cascade with sufficient energy may travel at a low-angle scattering direction across the lattice thus avoiding collisions with other atoms. As a result it can permeate large distances in comparison with the displacements associated with typical collision cascades, as the energy losses due to elastic collisions are small. Such process is called channelling, since the atom moves across particular crystallographic directions (i.e. channels) guided by the repulsion from the neighbouring atoms. This phenomenon has been verified experimentally - for instance an implantation of a 40 keV radioactive ^{125}Xe ions into crystalline tungsten (which allows for channelling to occur) gave penetration depths up to ten times greater compared to amorphous tungsten [109]. Furthermore, theories exist regarding the critical angle of incidence required for channelling with values of $3-5^{\circ}$ reported [110, 111]. A channelling process occurring in a exemplar 100 keV pka cascade simulation is illustrated in Fig. 3.1.

3.2.2.2 Displacement and thermal spikes

Once the cascade atoms slow down and arrive at the kinetic energy which maximises the elastic collision cross-section, atomistic collisions start to occur very frequently. This process is referred to as the displacement spike phase, during which a phenomenon called replacement collision sequence (RCS) can occur. Here an energetic atom displaces its neighbour and occupies the lattice site, which is now made vacant. In turn, the displaced atom interacts with its next neighbour and so on, thus creating a mechanism for a defect to travel large distances away from the initial site [69]. This process is more efficient in closed-packed directions and it can be visible in the cascade simulations as large displacements along these (see Fig. 3.1).

The displacement phase is usually followed by a thermal spike, where the kinetic energy is redistributed along the neighbouring atoms forming a hot (and sometimes molten) region. It is also manifested as a "spike" in the ionic temperature evolution and relatively equilibrated kinetic and potential energies (i.e. thermalisation).

3.2.2.3 Sub-cascade branching

When an atom recoils after a collision with sufficient energy to channel a significant distance before colliding with others at a high incidence angle, the so-called cascade branching may occur. It is characterised by the formation of non-overlapping pockets of damage, called sub-cascades, in the displacement/thermal spikes and later stages (see Fig. 3.1). This phenomenon occurs at relatively high pka energies, around 20 keV for $\alpha-$Fe [71]. It has been historically argued

that because of branching high energy cascades are effectively a set of smaller 20 keV cascades, and therefore the smaller sub-cascades provide all the primary radiation defect information required. However, it has been discovered that the defect production with cascade energy is different in the > 20 keV pka range than in ≤ 20 keV [71] implying that the sub-cascade damage picture is not complete. Furthermore, the increasing importance of the electronic effects with the pka (electronic effects dominate above 700 keV pka for iron projectile in α-Fe; see Fig. 3.3) means that the cascade behaviour is likely to be non-linear with the pka energy.

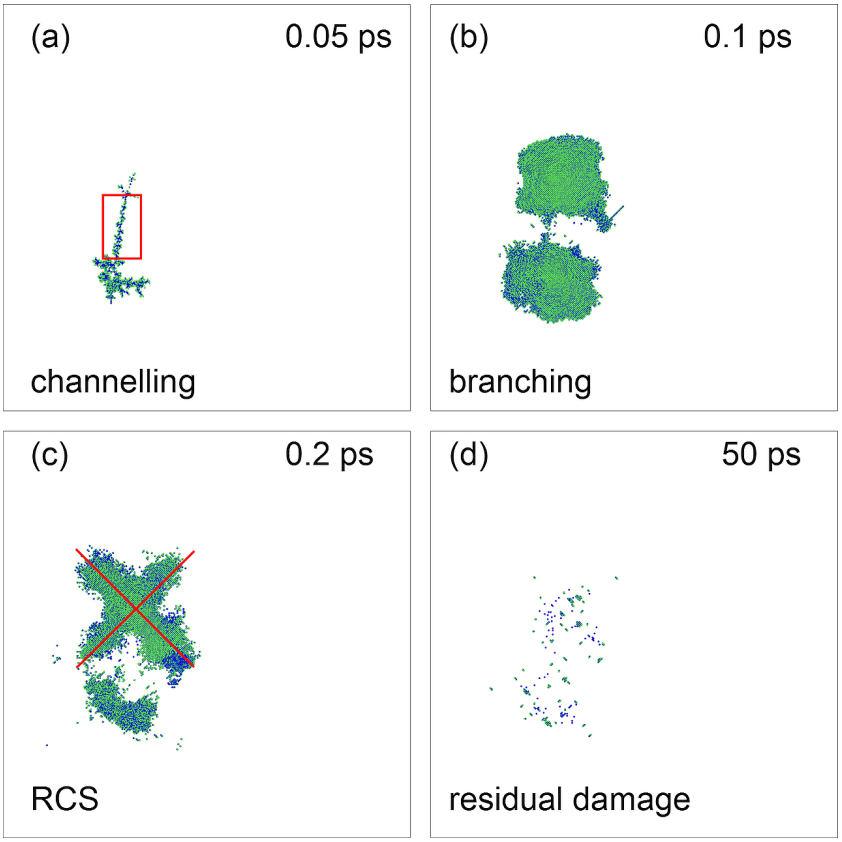

Figure 3.1: Selected stages of a radiation damage collision cascade for an exemplar 100 keV pka event. Channelling (a) enables two separate sub-cascades, i.e. branching (b), to occur; at later stages replacement collision sequence (RCS) occurs (c) along closed-packed directions (red lines); residual damage is shown in (d). The time scales of the depicted processes are approximate as based on one particular event.

3.2.2.4 Primary radiation damage

After the thermal spike a cooling phase ensues, which depending on the type of material (its electronic thermal conductivity, strength of electron-phonon coupling, band-gap, etc.) can last up to hundreds of picoseconds. It is during this phase where the majority of the defect recombination occurs, although some will remain as residual (or primary) radiation damage and continue to migrate or coalesce.

Once the resultant damage stabilises in the simulation we typically compute the residual

point defects: vacancies (vacant lattice sites), interstitials (lattice sites occupied by more than one atom) which are collectively called Frenkel pairs (FP). Defect clusters are also of huge interest - these are a collection of point defects occupying neighbouring lattice sites. The evolution of these is cardinal in the analysis of the deterioration rate of materials properties.

3.2.3 Current achievements

The application of molecular dynamics to study primary radiation damage formation, through so-called cascade simulations introduced in this chapter, is widespread and well established. The method has been extensively applied to study iron, other metals such as Fe-C, Fe-Cu and Ce-Cr, and ceramic materials relevant to nuclear industry. In particular, the primary radiation damage in iron, which is the core component of structural alloys in fission and future fusion reactors, is well characterised and there is a large volume of work published on the subject. The recent modelling progress has been reviewed in [71] and [72], with the former giving a more general overview of the subject and the later focussing on defect clustering in iron.

3.2.4 Current challenges

There are, however, several areas in cascade simulations that require further research. Some of these are somewhat technical considerations, such as the interatomic potential choice and the joining process of the equilibrium potential to the short-ranged screened Coulomb interaction. Another constraint is limited computations resources, which constrained the scientists' ability to explore the impact of rare-events (such as unusually large defect clusters) in the cascade processes, as well as to perform cascade simulations beyond 100 keV. Final considerations are due to the inherent limitations of classical MD modelling, such as the explicit inclusion of magnetic degrees of freedom or, most importantly, the interaction between the electronic and ionic systems. We aim to briefly describe each of these limitations in turn.

3.2.4.1 Technical considerations

It is necessary to join the equilibrium interatomic potentials to short-ranged screened Coulomb interaction to describe the short-range interactions (see Sec. 4.1.4.3 for details), which are likely to occur in a ballistic phase of a cascade simulation that the equilibrium potential would otherwise fail to do. This joining process, also called potential stiffening, can significantly affect the critical aspects of the simulation, such as defect formation and cascade evolution. A systematic study of that effect [72] has been published; however there is still no agreed standard on the potential 'stiffening' process. Furthermore, the equilibrium potential choice has been shown to have relatively little effect on the final Frenkel pair (FP) distribution (see [112] for instance), though it does usually affect the final defect configurations and size distribution. The choice of the best potential is not evident and the vast volume of previous work reporting data using different potentials makes the cascade simulation comparison very problematic.

The impact and the probability of occurrence of rare-events in the cascade processes is understudied, as typically around ten runs for each pka energy are carried out. This is due

to the finite computational resources available. Such rare-events could include formation of abnormally large defect clusters, deviating significantly from the mean FP number found at a particular pka energy. Quantifying the number of such large defects is paramount in prediction of long-term (and/or large dose) damage accumulation [71]. An example of a systematic study with a large number (one hundred) of cascade runs at 50 keV, and hence detailed defect statistics, can be found in [113]. This study found a 223 FP defects and a 153 vacancy loop in one of the runs, in cascades which produced an average of 130 FP, which illustrates that the statistical spread of defects produced at a particular pka energy is relatively high. In another study, a thousand cascades in the pka range of 1-5 keV were run [114]. It was concluded that the defect distribution even at such low energies is of large variance. It is thus paramount to perform sufficient runs at each pka energy and simulation condition to obtain statistically sound findings.

Figure removed due to third party copyright restriction

Figure removed due to third party copyright restriction

Figure 3.2: ITER's (International Thermonuclear Experimental Reactor) and selected fission reactor pressure vessels (FFTF, HFIR, PWR) simulated neutron (left panel) and normalised pka spectra (right panel). *Figure reproduced from [115].*

Limited computational resources have also constrained the maximum cascade energies to about a 200 keV pka, and therefore left the physics behind the high pka energy simulations (defined here as 200 keV pka and above) unexplored. Thus far, there are very few simulations reported for 200 keV pka impacts in iron; a mere 9 simulations were published in [71] with significantly more cascade data available for 100 keV. A paper describing a 250 keV simulation appeared recently in [116]. This lack of simulation data is perhaps not unexpected, as a typical MD cascade of 200 keV requires ∼20M atoms, while a 500 keV one necessities a cell of approximately 100M atoms (note that these estimates are dependent on the simulation details, such as the use of a boundary thermostat, for instance). Whilst larger single MD simulations have already been performed (5.2bn atoms in 2000 [117], 310bn in 2006 [118], and the one trillion atom milestone was reached in 2008 [119]), these used short-ranged pair-potentials, such as Lennard-Jones. For reliable cascade simulations, many-body potentials are used and this greatly raises the computational expense. However, the recent developments in high-performance computing are lifting the simulation size constraint and enable scientists to

run high pka energy simulations. This is due to the availability of massive parallel computing facilities, such as UK Hector Phase 3 [120] and scalable molecular dynamics codes, such as DL_POLY [121] based on domain decomposition strategy, which is able to perform some of the data analysis "on the fly" (such as defect and displacement analysis) to save storage space.

Studying such high knock-on energies is not merely a computational challenge, but it is vital in the context of materials development for fusion, and the next generations of fission reactors. The main difference between the fission and the fusion (Deuterium-Tritium (DT) cycle) neutron spectra is that the fusion neutron energy peaks at 14.1 MeV and produces a high flux of neutrons of energies above 1 MeV. This translates to a very similar behaviour of pka energy spectra for both fission and fusion reactors at low energies; with significant differences at energies above 100 keV pka. Notably, the fusion pka spectrum can reach the energies above 1 MeV, with an average pka energy of about 0.5 MeV (see Fig. 3.2) [71, 115]. There is, therefore, a clear need to perform high energy cascade simulations, given that the assumption of extrapolating of the low energy results has not been put to test and thus the low energy results could potentially miss important cascade features occurring in high energy cascades. Also, it is argued that an appropriate spatiotemporal modelling scale must always be chosen to reflect the size of the problem at hand [122].

3.2.4.2 Magnetism

Other considerations are due to the inherent limitations of classical MD modelling. One of such constraints in simulations of metals, such as iron or chromium, is magnetism and its effect on the primary stage of radiation damage as well as stable defect evolution. The magnetic effects are presumed to be low in the ballistic stage of the cascade, though magnetic excitations would very likely influence the structure and clustering of stable defects in steels and iron-based alloys. Furthermore, magnetism is responsible for the relative stability of phases (a classical example is the magnetic α- to γ-iron transition), high temperature mechanical properties and defect configuration. Preliminary work on interatomic potentials, which incorporate magnetic effects has begun with the first such potentials now published [123, 124]. Explicit incorporation of magnetic degrees of freedom in MD for the purpose of cascade simulations, built for instance on the spin-lattice-electron (i.e. three-temperature) model proposed in [125, 126], is a significant computational challenge yet to be addressed. To summarise, thus far, magnetism is an almost unstudied area in radiation damage community.

3.2.4.3 Electronic effects

Another intensive area of research is the interaction between atomistic and electronic systems, through the mechanisms of electronic stopping (e-s) and electron-phonon (e-p) coupling. Accompanying problems are the energy storage and redistribution and hence the correct the parameterisation of electronic specific heat and thermal conductivity. These processes represent possibly the biggest unsolved problem in primary radiation damage modelling with the MD simulations pushed to improve on the classical "billiard ball" description [127].

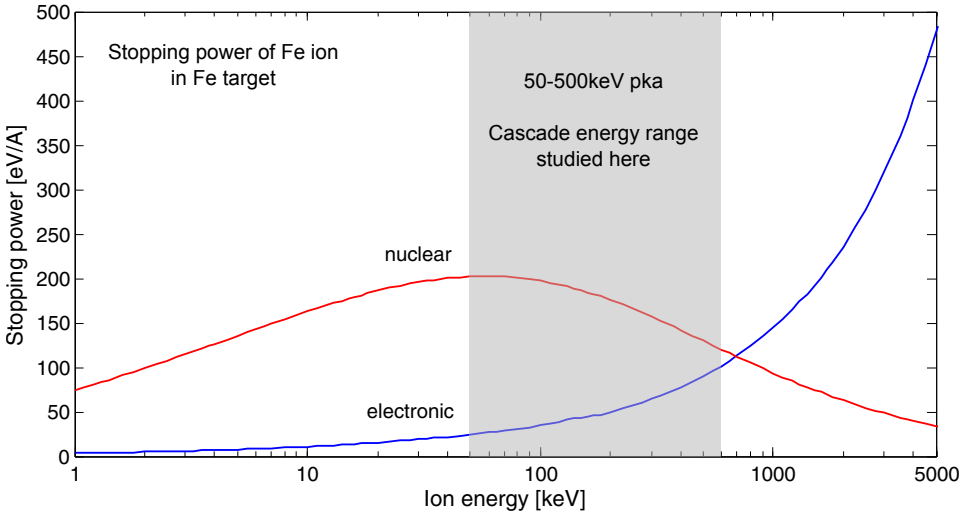

Figure 3.3: Stopping power of an Fe ion in an Fe target. At low ion energies ($\lesssim$ 50 keV) the nuclear stopping dominates, whilst the contribution from the electrons becomes non-negligible above that cutoff. The crossover between these energy loss channels occurs at around 700 keV, above which the electronic stopping contribution sharply increases over the nuclear one. Data obtained from the SRIM code [54].

The electronic stopping strength is well characterised (the theory behind it is discussed in Sec. 2.1.2) and can readily be obtained through SRIM [54] calculations. Electronic stopping is usually assumed to be effective above a certain threshold beyond which atoms are able to scatter inelastically. This threshold is subject to an on-going debate and there are numerous values of that parameter assumed: 0.6 eV [128], 1-5 eV [129], 8.2 eV [76] and 10 eV [130]. Molecular dynamics implementing electronic stopping as a viscous drag term was first suggested in the late eighties [74] and it has become almost a standard simulation technique for cascades since.

The current challenge is not the inclusion of the effects of e-s, but also of the e-p coupling. Research in this field intensified with two recent publications [76, 81], where the authors used, for the first time, the hybrid continuum-atomistic two-temperature model, representing both the e-p coupling and the e-s through modified MD equations of motion. The subsequent cooling of a thermal spike is be achieved via electron-phonon coupling and this can have a profound effect on the primary radiation damage produced (as remarked on in [71]), as defect could be rapidly 'quenched' before they have a chance to recombine. A strong effect of the strength of the e-p coupling on the number of stable defects has already been demonstrated in 10 keV cascades (see [81]). While the two-temperature model remains the most sophisticated approach to cascade simulations, several issues remain.

The majority of the issues pertain to (i) 'activation' (i.e. conditions under which it is effective) of the e-p coupling process, (ii) e-p coupling strength in ground-state and its parameterisation under strong non-equilibrium conditions, (iii) the interplay between the e-s and the e-p coupling processes. The subject of the e-p coupling is even more controversial, as it cannot be distinguished experimentally from the electronic stopping in an irradiation scenario, perhaps apart some partial evidence coming from the ion beam mixing experiments [129].

The conditions under which e-p occurs in a thermal spike are uncertain. As this process involves interaction between phonons and electrons, its strength in liquid-like or defect-rich structures (which are likely to occur in cascades) is also all but unknown. From a theoretical standpoint, the electronic stopping is effective when atoms move ballistically through the target medium, whilst e-p is effective when atoms oscillate around their equilibrium positions. Electronic stopping is derived for a single atom moving in electron gas, which doesn't interact with the correlated motion of other atoms in a cascade. Unlike the e-p coupling process, which occurs between thermalised systems of electrons of phonons, and does not interact with ballistic atoms, as these are not a part of the phononic system. Nonetheless, the underlying physical processes of the electron-ion scattering (i.e. both the e-p and the e-s interactions) are the same [21, 25] and hence the boundary between these is ill-defined. It is thus extremely difficult to switch from one regime to another in a cascade simulation. It is not obvious whether below a particular kinetic energy cutoff, the projectile atom is immediately thermalised and oscillating around its equilibrium position, thus taking part in the e-p interaction. An insight from sophisticated models based on the Ehrenfest dynamics, such as RT TD-DFT [91, 92] may improve our theoretical understanding in the future. The value of the electron-phonon coupling (at standard conditions, i.e. at $T_i = 300$ K and $T_e \sim T_i$) is typically obtained through low fluence laser irradiation experiments, where the issues connected with the loss of crystallinity and high electronic or ionic temperatures can be neglected. To complicate matters further, such experiments are rare and there is usually a high degree of error associated with the e-p coupling measurements.

All in all, while some progress has been made in the area of electronic excitations in cascade simulations, there is a clear need for more rigorously parameterised models and more research into the question of the impact of the e-p and e-s processes. The results presented in chapter 5 aim to shed some light onto these issues.

3.3 Swift heavy ions

3.3.1 Introduction to ion tracks

Swift heavy ions (SHI), which are of typical specific energies (E') of several MeV/u, penetrate matter interacting mainly with the electrons (inelastically) and less with the nuclei (elastically) of a target. This is in stark contrast to cascade simulations, where the dominant effect of elastic scattering is assumed. In some materials SHIs of sufficient energy are able to produce cylindrical regions of structural modification also commonly known as ion tracks. Formation of such poses a challenging theoretical and modelling problem as tracks originate from a transient and a highly non-equilibrium state of matter. During the last two decades there has been a growing interest in gaining insight into the exact mechanisms governing high electronic excitation in metals as well as band-gap materials. However, the analysis of ion irradiation-induced structural modification of matter is not only interesting from a fundamental, but also from an applied physics point of view. Potential application areas, where predictive radiation damage

modelling from SHI would be beneficial, include primarily nanotechnology, but also materials selection in nuclear and space industry. Ion irradiation can modify nanostructures [14, 131], form nm-sized channels called track etch membranes [15], create changes in quantum wells and dots [16] and induce anisotropy in etching [132]. Furthermore, in quartz [19] and $LiNbO_3$ [20] the refractive index changes due to SHI radiation (SHI irradiation causes significant decrease in light refraction at the end of the ion track thus creating an optical barrier). Therefore, being able to predict the exact structural response (damage distribution) induced by SHI would find applications in nano-fabrication technologies of optical devices.

SHI modifications in a material's structure have different morphologies: from spheres, discontinuous and inhomogeneous tracks to homogeneous cylinders around the path of the incident ion depending on the projectile particle specific energy, E', and velocity v_{ion}. Such effects occur when the deposited energy on the electronic system exceeds a stopping power threshold, S_{th}. Ion tracks (also referred to as latent tracks) are continuous damage regions: μm long with diameters of up to several nm. These are produced with SHIs of $E' \sim$ MeV/u and are primarily observed in insulating materials. However, with increasing beam energies in the MeV range, there is also recent evidence that they are formed in metals at very high stopping powers [133–136], alloys [137] and semiconductors [136, 138]. Examples of such elongated features in insulators are presented in Fig. 3.4.

3.3.2 Track formation models

The discussion of the structural modifications resulting from SHI bombardment has been, at least historically, relying only on the energy losses caused by elastic recoil of the projectile particle and the nuclei of the material. Such energy losses are characterised by the nuclear stopping power, S_n, and typically lead to direct atomic displacements, i.e. a collision cascade introduced in Sec. 3.2. However, if this process was a complete physical picture describing the SHI radiation damage a similar defect structure in metals and band-gap materials would be observed (similar arguments were reviewed here: [111, 139, 140]). It is well-known that SHI tracks are created relatively easily in insulating materials, which suggests that electronic effects, such as ionisation and electronic excitation, play a crucial part in the process. The electronic energy losses are characterised by the electronic stopping power (S_e) and are increasingly dominant over S_n with increasing incident ion energy (see Fig. 3.3). It is now understood that $S_e >> S_n$ for SHIs, and only the electronic stopping component is usually considered.

In contrast to metallic materials, properties of insulators are very sensitive to radiation damage. Structural steels can typically withstand doses of 10 dpa (displacements per atom), while insulators can be already affected by less than 1 dpa. Moreover, thermal conductivity and dielectric properties in insulators may be modified by as low as 10^{-3} dpa [9]. Construction of a modelling framework for insulating materials is therefore of particular interest, as such materials are affected by radiation most.

The physics of ion track formation is still a subject of an on-going debate. This is due to the fact that all the models put forward to date suffer from either severe theoretical, or technical limitations, or are unable to reproduce the vast data set on track sizes available

Figure removed due to third party copyright restriction

Figure removed due to third party copyright restriction

Figure 3.4: First observations of ion tracks in matter (1958). Tracks of fission fragments in mica (left panel); etched fission tracks in LiF (right panel). *Images reproduced from [141, 142].*

in the literature. The most predominant models can be divided into three main categories: Coulomb explosion, variations of the inelastic thermal spike (iTS) and *ab initio*-based structural relaxation methods. This thesis focuses on the potential applications and the extension of the iTS model to semiconductors (with the theory behind outlined in Sec. 2.2.1). In this chapter, we describe iTS in various polymorphs and their applications found in literature. As for the Coulomb explosion and structural relaxation methods, we provide here with both a very brief theoretical introduction and a literature review of their applications.

3.3.2.1 Coulomb explosion

The Coulomb explosion model proposed by Fleischer, Price and Walker [143] in 1965 was the first theoretical attempt at explaining the formation of ion tracks in minerals. It was argued that the radiation defects result principally from the removal of the electron following an energetic particle passage. As an incident ion such as SHI penetrates the lattice it ionises the atoms around its path, thus creating a narrow cylinder filled with positive ions. These ions repel each other and when the repulsive energy becomes greater than the binding energy, the ions are ejected (hence the name Coulomb explosion). However, the major concern with the model is the charge neutralisation time (which can be approximated as $\tau_c = \epsilon/\sigma$, where ϵ is electrical permittivity and σ is the conductivity [144]), which needs to be greater than 10 fs [145] to induce significant atomic displacements. However, the relaxation time for most metals is of the order of a femtosecond (Al: 0.3 fs, Cu: 0.2 fs, Ni: 0.8 fs W: 5 fs [144]) - too short to explain track formation in metals. In band-gap materials due to the lack of free electrons, charge neutralisation is slower (for instance, in Si it is $\tau_c \sim 1.0$ ps) and could contribute to the track formation mechanism (see [146] for a recent simulation study in Si), but the development of an atomistic model based on Coulomb explosion assumptions is challenging and has not been performed in a comprehensive manner to date.

The Coulomb explosion model produces few quantitative results. It was mainly successful in explaining multi-charge ions emission from the surface (due to a local charge imbalance)

following an intense radiation event [147, 148] and aspects of radiation damage effects in polymers [149].

3.3.2.2 Inelastic thermal spike and its polymorphs

The original version of the inelastic thermal spike (iTS) model is described mathematically by distinct electronic (T_e) and ionic temperatures (T_i) evolved by two coupled diffusion equations. The model, with its mathematical formulation and the assumptions behind it, is introduced detail in Sec. 2.2.1. Here we briefly describe its variants present in literature and its successes in reproducing the experimental data as well as its notable limitations.

In brief, the iTS model assumes that the energy of an incoming particle is deposited to the electrons and then converted to lattice phonons through the electron-phonon interaction. This subsequently can result in local melting of the lattice. Defect generation or sputtering occurs when the deposited energy density exceeds the melting (or vaporisation as argued in [150]) threshold within the propagating thermal spike. These processes are highly dependent on the interplay between the e-p coupling strength and the speed with which the energy can be dissipated by the electrons. The subsequent cooling off and recrystallisation usually leaves residual defects and/or modified crystal structure.

The model was extensively used to simulate SHI irradiation in metals [136], alloys [137], and more recently in semiconductors [150–153] and insulators [154, 155]. Its applicability to band-gap materials remains very controversial [41], however despite that it remains widely used. This can be attributed to the model's relative mathematical simplicity and thus a small set of parameters required (either known or fitted). Also, the iTS has a long success history of reproducing the experimental latent track radii dependence on the stopping power and it is able to account for the so-called velocity effect [55], where ions of the same stopping power, but greater velocity, produce smaller tracks.

The models based on thermal spike formulation are however problematic for a very simple reason. So far, little correlation has been found between track formation and the thermal properties of the materials [156]. Also, this model fails to reproduce results above amorphisation threshold and therefore cannot account for the cumulative nature of radiation damage in insulators, as pointed out in [140].

Furthermore, obtaining correct iTS model parameters in insulators is particularly controversial. The model parameters for metals (i.e. the electronic specific heat C_e and electronic thermal conductivity κ_e) can be estimated from theoretical considerations, or obtained from experimental measurements. However, the theory of free electron gas cannot be applied to band-gap materials, and electronic conductivity in a thermal spike in an insulator is unknown from both experimental and theoretical viewpoint. Nonetheless, the arguments that hot electrons in an insulator behave like in a metal (which is true to some extent) dominate the iTS literature [59, 150, 157], but do not provide accurate and precise parameters. Most recent developments are based on Monte Carlo methods (described in [158–161]), which provide with source term for the 2T models. Lastly, the applicability of the heat diffusion equations to such local huge non-equilibrium conditions on a nm-space and ps-time scale can be questioned [162].

Historically, the iTS model was solved in continuum. However, such implementation neglects several physical phenomena such as: lattice straining, emission of shock waves, and does not take into account the volume change due to phase transitions. More sophisticated continuum-only methods were later introduced and incorporated extra variables for the transport of energy, momentum, and mass [163]. These were used to describe the sputtering processes from SHI impacts.

Accessing atomistic behaviour via trajectory of the atoms in MD has several advantages to continuum models and it was made possible due to advancements in computing power and parallel codes development. First of all, it was shown that in an SHI irradiation event that the strong localised superheating may not lead to track formation [164]. Also, a detailed atomistic evolution of the SHI irradiated system allows for a direct and more precise comparison with the experiments [2], which can measure the density changes or defect channels in a latent track. Such hybrid continuum-atomistic approaches (usually synonymous with 2T-MD) evolved from static electronic energy depositions in MD [165]. Such a method was later improved by a time-dependent energy deposition, which eventually lead to the development of methods that solved the electronic temperature and the MD part of the model concurrently.

3.3.2.3 Structural relaxation methods

The lattice (structural) relaxation model is built on the assumption that the potential energy surface (PES) is strongly modified in the regions of high electronic temperature. Such modifications can cause the PES to become weakly bonding (sometimes enough for the thermal fluctuations to overcome the cohesive energy), or even non-bonding (i.e. with no PES minima), which immediately leads to strong repulsive forces (see Fig. 3.5). A plethora of other effects such as a shift of the PES minima and an associated dynamical instability, or other changes in the bonding character (and thereby induced phase-changes, coherent phonons, etc.) are also possible. Particularly interesting examples of the PES effect at high T_e are photo-induced phase transitions, which were recently presented in a comprehensive topical review [166]. The amount of energy transferred to the lattice by this mechanism would crucially depend on the lifetime and distribution of the local excitations. Structural rearrangements resulting from PES changes are non-thermal, as they don't involve the electron-phonon coupling and are a result of electronic structure changes. However, electron-phonon scattering (which is a "thermal" process) would typically accompany the non-thermal processes.

The main disadvantage of this method is its complexity of parameterising the PES effects at high T_e into a set of MD-ready potentials. A mere three potentials have been parameterised with respect to T_e to date, namely for W [84], Si [85] and Au [87]. While *ab initio* MD (in the Born-Oppenheimer scheme) is able to provide atomistic information at high T_e it is limited to hundreds of atoms and the most important processes, such as sputtering or latent tracks, require spatiotemporal scales of MD.

A simpler approach, yet of significantly lower accuracy, is to approximate the PES changes at high T_e by modifying or even removing the bonding part of the MD potential [82]. Such

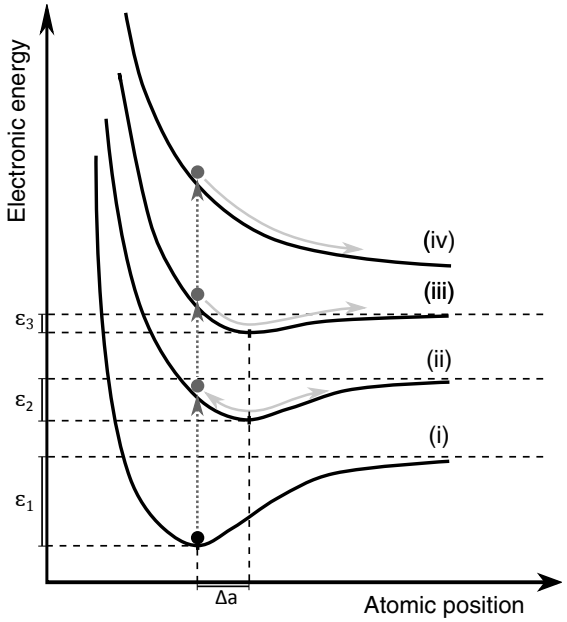

Figure 3.5: Structure relaxation model: the possible PES changes at high T_e. (i) Ground-state PES; (ii) PES at low T_e: shift of the PES minima by Δa and a lower cohesive energy (ϵ_2). The excitation results in weakening of the bonds and increased kinetic energy of the ions as they "roll down" towards a modified PES minimum; (iii) Intermediate T_e: the PES is still bonding (i.e. has a minimum), however the kinetic energy given to ions is enough to overcome the cohesive energy, ϵ_3; (iv) High T_e: the PES becomes is non-bonding. Typical structure relaxation scenario involves four stages: electronic excitation, where the PES changes from (i) to (ii)-(iv). This is followed by structure relaxation, where atoms move in response to the PES changes. Later electronic de-excitation occurs and structure relaxes again to (i).

approach was somewhat successful in describing the creation of ions tracks as a non-thermal process [82], or sputtering processes occurring under SHI bombardment [83].

3.3.3 Final remarks

In brief, despite its limitations, the iTS and particularly its MD-coupled variant, remains the most popular model for SHI track simulation. Its modelling power for direct experimental comparison has been recently demonstrated even in a case of a wide band-gap insulator (SiO_2 quartz) [131]. This MD-variant has also provided scientists with invaluable track morphology insights, where the discrepancy between the experimental techniques measuring defect-rich channels (Rutherford backscattering spectrometry) or local density changes (small angle X-ray scattering) can be resolved [2].

The main criticism of iTS stems from the difficulty of parameterising the electronic structure. For metals, the iTS models contains effectively one fitting parameter namely the e-p coupling, while the behaviour of electronic thermal conductivity at varying T_i and T_e is poorly known. The situation in band-gap materials is even more complicated. Here, both the diffusivity D and the e-p coupling G are all but unknown and effectively fitted to, usually very sparse, experimental data. It usually not clear if a particular choice of D or G is a one-to-one

mapping to the experimental data (a point investigated in chapter 7), not to mention the complex outcome possibilities when these parameters are allowed to be functions of both T_e or T_i, which they most likely are. Furthermore, this effective model neglects several crucial carrier dynamics processes.

On the other hand, the extended models (eiTS), the development of which we focus on in this thesis, contains the correct carrier physics, which is a great leap forward from a theoretical standpoint in SHI modelling. However, from a practical point of view, its main drawback is the number of parameters required and their behaviour in a highly non-equilibrium scenario. Since several of these are poorly known this may lead to over-fitting to the experimental data. Owing to this fact the eiTS extension to wide band-gap materials, where the parameter uncertainty is even greater, is challenging.

Non-thermal models (such as the structural relaxation methods) are perhaps more justified on the physics grounds at levels of excitations induced by SHIs. The degrees to which the thermal (i.e. e-p coupling) and non-thermal processes are important is not resolved in the SHI scenario. However, we show later that even at low to moderate excitation levels ($T_e' = 0.8$ eV) the interatomic potential changes significantly in a metal. We can therefore safely assume that the SHI irradiation, which induces local excitations in excess of $T_e = 10$ eV, to have a huge impact on the resultant interatomic forces even in wide band-gap materials.

However, technical problems persist, as there are currently no *ab initio* codes, which implement localised and dynamic electronic excitations. Because of the nm scale of the resultant SHI tracks, such models are computationally intractable in any case, even if they existed. A solution is to design potentials, which are dependent on the electronic temperature. However such an option, while possible, is an extremely tedious optimisation process and prone to typical errors associated with the interatomic potential construction. Nonetheless, it is currently the only viable method.

Experimental (track size variation with the initial target temperature) and theoretical work (relaxation time of the electron-phonon coupling) work points to a thermal component in the SHI track formation. However, the degree to which the electronic excitations and the e-p energy transfer contribute is uncertain. This interplay is most likely to be the next hot topic in the field, once the technical constraints are lifted. It is believed that the current theoretical research direction would be aimed at resolving the thermal and non-thermal contributions in SHI track formation, with *ab initio* methods (and probably additional related developments) playing a larger part in the process. As there is currently a large uncertainly in the initial distribution of the energy of the track (the results from [58] are extrapolated from proton in water studies), inclusion of the non-thermal effects combined with further work on the initial carrier dynamics (exemplar studies in [158–161, 167]) could be very insightful.

3.4 Laser illumination

The rationale behind studying ultrafast dynamics, defined here as the study of processes occurring at a sub-picosecond timescales, is two-fold. Firstly, the field of photo-induced transitions,

which are triggered and subsequently probed by ultrashort light pulses, is driven by the aim of looking at the atomistic dynamics as it happens. Secondly, ultrafast science offers the possibility to create photo-excited exotic (and yet undiscovered) states of matter. One of the most exciting prospects in the field deals with the opportunity of both tracking and controlling photo-induced transitions, where the electronic excitations lead to different properties of matter at the macroscopic level [168, 169]. In this chapter we outline the recent advancements in ultrafast dynamics, predominantly in the field of transient photo-induced phase transitions, discuss the physics behind the so-called warm dense matter (WDM) state, and finally review the current theoretical work on gold, which remains the most studied metal in this context.

3.4.1 Ultrafast dynamics

A typical ultrafast dynamics experiment, involves a laser pulse to excite the matter, which is followed by a series of delayed probe signals. It is also referred to as a pump-probe experiment. Recent advancements in the short pulse laser generation (pump) and ultrafast probing techniques, such as electron diffraction, have enabled the study of phase transitions that occur at < 100 fs. This time is less than a typically frequency of a phonon ($t \sim$ ps) and therefore in principle a molecular movie can thus be generated. The most commonly used techniques for probing the matter are: time-resolved ultrafast X-ray diffraction (tr-XD) [33], ultrafast electronic dynamics (UED) [170], and time- and angle-resolved photoelectron spectroscopy [171]. The UED is currently the most advanced diffraction method, which offers greater scattering cross-section over the conventional tr-XD. Also, by using relativistic electron pulses (thus minimising the space-charge effect) relativistic UED technique can offer even higher intensities per pulse. This enables < 100 fs diffraction time-resolution, without compromising on the electron intensity required for high-quality diffraction images [172]. On the pump side, Terahertz pulses can now induce atomic oscillations directly [173] by generating frequencies resonant with these of optical phonons. Progress has been achieved not only on the experimental side, but also on the diffraction data analysis aimed at structure determination [174] (even for disordered materials [175]) and accompanying modelling, which we discuss later.

The landmark discovery in the ultrafast dynamics field was the work on femtochemistry by A. Zewail, which was awarded a Nobel Prize in 1999, where a change in the interatomic potential of a photo-excited molecule was tracked. Since then several notable advances have been made in the field, such as the observation of neutral-ionic instability [176], and photon-induced phonon instability in semiconductors [177] and semi-metals [178] (Where it was shown that the collective oscillation modes in bismuth are mechanical and the resulting dynamics are isentropic.) The current research avenues include femtomagnetism, transient photo-induced phase-transitions (insulator to conductor, or non-magnetic to magnetic) and others [169]. The prospect of transforming the material to another phase, which is not achievable at thermal equilibrium, is particularly appealing from a theoretical standpoint. Such “hidden phases” are proposed in [179, 180].

3.4.2 Warm dense matter

The ultrafast optical-excitation typically leads to a transient exotic state, which is referred to as warm dense matter (WDM). Creation of WDM exploits the physics that the pump photon energy is absorbed primarily by the electrons and that the electronic excitations it creates thermalise at the 10-100 fs timescale, leaving the ionic system cold. This is due to the relatively slow electron-phonon coupling process (relaxation time of 1-10 ps), which is responsible for the eventual equilibration of the electron and ion temperatures. Simply put, WDM is a two-temperature state with excited-state ("hot") electrons and cold unperturbed ions.

We emphasise that the WDM is an in-between state of plasma and "regular" condensed matter, on the electronic excitation scale. It is therefore very difficult to achieve a theoretical understanding of it, as it is inherently non-equilibrium, different to thermal equilibrium modelling and too strongly excited to apply any perturbative approach from the ground state. Due to the complexity it is a remaining theoretical bridge in our understanding between "regular" matter and plasma physics. This problem of a gap in theoretical understanding of WDM behaviour is shown in the example of equation of state calculations for Cu [181].

3.4.3 The case of thin film gold

From an experimental standpoint, thin films are chosen to achieve homogeneity of the system excitation along the "depth" axis, as the ballistic electron transport in Au is around 100 nm [182, 183]. Furthermore, the homogeneity in the lateral directions is ensured by the laser spot size, which is typically much larger than the probed region. Since gold nanofilms are easy to manufacture and don't oxidise easily, they remain preferable in the ultrafast experiments, leading to a volume of experimental and also theoretical work.

From the modelling perspective, *ab initio* and classical MD, and a combination of both methods are most suitable (and prevalent in literature) to describe the experiment data on ultrafast dynamics, due to the compatible spatiotemporal timescales of both. Also, solutions to the two-temperature model in continuum with various additions can be found [172].

The theoretical work on photo-induced PES changes in Au started with the paper of Mazevet *et al.* [184], who observed bond-hardening in the phonon spectra at elevated electronic temperatures at isochoric conditions though *ab initio* calculations. The conclusion of this study, under the given conditions, is not disputed. However, bond-hardening was shown to occur when the system no longer has free energy minima [3], and therefore the notion of bonds can be controversial. Besides, a high degree of electronic excitation leads to a shift in the free energy minima due to the reduction of screening [3]. This implies that atoms would experience a huge repulsive force to move them into the modified equilibrium positions. At the modified equilibrium positions, however, the bonds, as indicated by the *ab initio* calculations, are softened, rather than hardened. Which effect would have a stronger weight on the ensuing photo-excited gold dynamics, bond hardening [172], or the shift in the PES minima (and accompanying softening) is currently debated [3].

The coupled two-temperature molecular dynamics (2T-MD) using ground-state potentials was pioneered and applied to photo-excited lasers by Zhigilei [60, 185, 186] and his colleagues in 2002. Since then, this method was also applied to study Ag-film Cu-substrate systems [187], as well as Ni [188], Cr [189], Al [190] and other metals. Subsequently the effects of electronic pressure [87, 191], as well as the T_e-dependent potentials were employed [87] and investigated in the context of ablation. Electronic parameters derived from *ab initio* calculations [29] were also incorporated at a later stage. Monocrystalline free-standing films remain most commonly studied, but larger-systems with grain-boundaries are also simulated [192]. The work of Zhigilei *et al.* was of crucial importance, as it predicted the heterogeneous and homogeneous melting processes in Au [193–195], before it was verified in a combined experimental-theoretical study [3]. The most recent success of the 2T-MD is the theoretical description of nano-bumps formation in a photo-excited thin-metal film [196].

Photo-excited gold topic is still controversial and there are several unsolved questions regarding the ultrafast dynamics of such a relatively simple system as monocrystalline nanofilm gold in the WDM state. In particular the following aspects (and the excitation limits within which these occur) are currently under investigation and debated in literature:

1. Strong electronic excitations leading to a change in the bond character (bond softening versus hardening, modification of the lattice parameter),
2. Non-thermal and thermal melting processes interplay,
3. The physical processes behind ablation dynamics (thermal versus non-thermal and the role of electronic pressure).

3.5 Summary

The common thread in scientific literature among the topics of laser illumination, cascades and swift heavy ions is the successful use of the two-temperature model to simulate the non-equilibrium conditions between the electrons and ions. What differentiates all these studies is the use of different initial conditions and setups in the 2T-MD scheme, but the physics behind the model is largely applicable to study a range of phenomena, as the literature survey suggests. Although the input from *ab initio* is required when studying non-thermal effects, the ground-state 2T-MD method will most likely remain the standard simulation technique for low-level electronic excitations for some time due to its success history, appropriate spatiotemporal scale and robustness of parameters. Limitations of the method will be most apparent when the ground-state potentials will no longer be a good approximation. For instance, when photo-induced phase transitions are expected, but are not captured at the level of the interatomic potential.

Chapter 4

Simulation techniques

4.1 Classical molecular dynamics

Classical molecular dynamics (MD) is an atomistic simulations method which aims to solve Newton's equations of motion (EoM), given a suitable interatomic potential U and a set of initial conditions. For a system of N atoms that make up the simulated material indexed i with masses m and position vectors $\mathbf{r_i}$ the classical EoM are a set of second-order non-linear differential equations:

$$m_i \frac{d^2\mathbf{r}_i}{dt^2} = \mathbf{F}_i = -\nabla_{\mathbf{r}_i} U(\mathbf{r}_1, \mathbf{r}_2, ..., \mathbf{r}_N), \tag{4.1}$$

where $\mathbf{F}_i$ are the classical forces. The numerical solution to Eq. 4.1 is the essence of MD and enables one to track the evolution of the individual atoms. It is a well-known N-body problem, which in three dimensions can be solved exactly only for $N = 2$ (and $N = 3$ in a special case). The direct output of an MD simulation are particle trajectories ($\mathbf{r}_i$) and velocities ($\mathbf{v}_i$) as a function of time, t. The evolution of the thermodynamic and structural properties of the simulated microstructure can be obtained from these.

In fact, there are two main types of MD. The one explored here treats atoms as classical particles, the dynamics of which are determined by an interatomic potential. In fact, classical MD makes extensive use of the adiabatic approximation. In the timescales of MD, the electrons are "stationary" and factored in at a level of the static interatomic potential only. On the other hand, the *ab initio* MD solves the degrees of freedom of ions and electrons with the latter described by their wavefunctions.

We will first review some of the key concepts of classical MD (Sec. 4.1) and subsequently move onto the hybrid MD schemes, where provisions for the electronic excitations are introduced to simulate non-equilibrium processes (Sec. 4.2 and Sec. 4.3). We later outline some methods helping with the MD data analysis (Sec. 4.4).

4.1.1 Key concepts

Simulations in MD, which represent bulk conditions, are typically performed in a parallelepiped supercell with periodic boundary conditions. This means that the atom leaving the supercell

in the $-z$ direction, say, re-enters to the other side of the simulation, namely from $+z$. The minimum image convention is usually applied when calculating the forces on atoms. This means that two atoms of positions $\mathbf{r}_1$ and $\mathbf{r}_2$ interact with each other along the shortest distance possible, which may be across the periodic boundary conditions.

When calculating the forces on atoms from an interatomic potential, typically a force cutoff distance is used, r_{cut}. This removes the long-range interactions, which tend to zero and are therefore negligible. Making the forces short-ranged, reduces the computational complexity when evaluating the pairs of interacting atoms. Instead, of a double loop over all particles with time complexity of $\mathcal{O}(N^2)$, neighbour linked lists can be constructed (and updated less frequently than the time-step) reducing the time complexity to $\mathcal{O}(N)$.

Knowing how to calculate the forces on all the atoms, we can start propagating a system by solving Eq. 4.1 numerically. We require symplectic integrators, i.e. ones which conserve the phase-space volume of Hamiltonian dynamics (Liouville's theorem) and are in effect time-reversible and conserve the total energy. An example of the simplest such integrator is Velocity Verlet (see Sec. 4.1.3). There exists are plethora of other (not necessarily symplectic) classes of MD integrators, such as Beeman, Verlet, Leapfrog, Runge-Kutta and predictor-corrector, most of which can be extended to include higher orders in Taylor's expansion in small time-step sizes, Δt, reducing the local truncation error and hence the global error, yet at a computational cost.

The typical time-step for MD is about $\Delta t \sim 1$ fs, which will depend on the masses of the atoms involved as well as the how "hot" the atoms are. Due to advancements in both parallel codes and increase of computational power, MD can now easily simulate up to 10^8 atom systems for around 10 ns, although significantly larger and longer simulations have been already reported.

The biggest challenge in MD is obtaining the correct interatomic potentials, which determine the forces on all atoms and in effect all physics of the simulated system. The potentials can be empirical, such as the famous Lennard-Jones one. However, to effectively simulate real systems, one needs to often parameterise much more complex potentials forms (for instance with 3-, 4-body terms) and fit their free parameters to the known properties of the material to be simulated. An important issue when developing a potential is a questions of transferability. Potentials are typically trained (i.e. fitted) to reproduce a set of parameters, such as elastic constants or lattice parameter. A highly transferable potential is one that will reproduce the parameters that it was not originally fitted to, quite well.

When solving the Eq. 4.1 with a symplectic integrator, the corresponding atomistic dynamics evolve in a constant particle number, constant volume and energy (NVE) ensemble. One typically appends the EoM with a thermostat, or a barostat, effectively emulating constant temperature and constant pressure ensembles, called NVT and NPT, respectively.

4.1.2 DL_POLY code

DL_POLY [121] is the UK flagship molecular dynamics code, of which extensions are used throughout this work. It is a Fortran 90 code which employs the domain decomposition

parallelisation strategy (using the MPI library) effectively redistributing the atomistic data across compute nodes and the linked-cell method allowing for quick computation of the sum of the interatomic forces. The code is, therefore, perfectly suited for memory distributed parallel systems. Version 4.01 is the basis for the developments described in this thesis.

4.1.3 Integration algorithm

We will be using the simplest second-order (i.e. with the global error in position and velocity of $\mathcal{O}(\Delta t^2)$) symplectic integrator, namely the Velocity Verlet scheme. It can be derived as follows. Let's start with the Taylor expansion of the atomic position $\mathbf{r}_i$ forward in time, $t+\Delta t$:

$$\mathbf{r}_i(t+\Delta t) = \mathbf{r}_i(t) + \Delta t\ \dot{\mathbf{r}}_i(t) + \frac{1}{2}(\Delta t)^2\ \ddot{\mathbf{r}}_i(t) + \frac{1}{6}(\Delta t)^3\ \mathbf{r}_i^{(3)}(t) + \mathcal{O}(\Delta t)^4. \tag{4.2}$$

Similarly, replacing $+\Delta t$ with $-\Delta t$:

$$\mathbf{r}_i(t-\Delta t) = \mathbf{r}_i(t) - \Delta t\ \dot{\mathbf{r}}_i(t) + \frac{1}{2}(\Delta t)^2\ \ddot{\mathbf{r}}_i(t) - \frac{1}{6}(\Delta t)^3\ \mathbf{r}_i^{(3)}(t) + \mathcal{O}(\Delta t)^4. \tag{4.3}$$

We can now cancel the odd power terms by adding Eq. 4.2 and Eq. 4.3. After some rearrangement and recalling that $\ddot{\mathbf{r}}_i(t) = \mathbf{F}_i/m_i$:

$$\mathbf{r}_i(t+\Delta t) = -\mathbf{r}_i(t-\Delta t) + 2\mathbf{r}_i(t) + (\Delta t)^2\ \mathbf{F}_i/m_i + \mathcal{O}(\Delta t)^4. \tag{4.4}$$

Note that the algorithm above (also called simply Verlet) does not require the explicit knowledge of velocities. The Velocity Verlet variant gives the velocity at time t as follows:

$$\mathbf{v}_i(t) = \frac{\mathbf{r}_i(t+\Delta t) - \mathbf{r}_i(t-\Delta t)}{2\Delta t} + \mathcal{O}(\Delta t)^2. \tag{4.5}$$

In practice, in the Velocity Verlet algorithm we follow four algorithm steps. We first calculate updated positions ($\mathbf{r}_i(t+\Delta t)$) from positions, velocities and accelerations at the previous time-step

$$\text{step 1}: \mathbf{r}_i(t+\Delta t) = \mathbf{r}_i(t) + \mathbf{v}_i(t)\Delta t + \frac{1}{2}\frac{\mathbf{F}_i(t)}{m_i}(\Delta t)^2. \tag{4.6}$$

We then compute the half step velocities $\mathbf{v}_i(t+\frac{1}{2}\Delta t)$ from forces at time (t), i.e.

$$\text{step 2}: \mathbf{v}_i(t+\frac{1}{2}\Delta t) = \mathbf{v}_i(t) + \frac{1}{2}\frac{\mathbf{F}_i(t)}{m_i}\Delta t. \tag{4.7}$$

With the new atomic positions we can now update the forces, as we now have the new atomistic positions

$$\text{step 3}: \mathbf{F}_i(t+\Delta t) \leftarrow \mathbf{F}_i(t), \tag{4.8}$$

and then the velocities at $(t+\Delta t)$:

$$\text{step 4}: \mathbf{v}_i(t+\Delta t) = \mathbf{v}_i(t+\frac{1}{2}\Delta t) + \frac{1}{2}\frac{\mathbf{F}_i(t+\Delta t)}{m_i}\Delta t. \tag{4.9}$$

This completes the computation of all quantities $(\mathbf{r}_i, \mathbf{v}_i, \mathbf{F}_i)$ at $(t+\Delta t)$ and the algorithm starts again from Eq. 4.6. The half-step velocity can be eliminated and step 2 and 4 combined to

$$\mathbf{v}_i(t+\Delta t) = \mathbf{v}_i(t) + \frac{1}{2}\left[\frac{\mathbf{F}_i(t)}{m_i} + \frac{\mathbf{F}_i(t+\Delta t)}{m_i}\right]\Delta t. \tag{4.10}$$

4.1.4 Force field methods

In the work presented in this thesis, we are dealing with two types of interatomic potentials, namely the embedded atom model (EAM) and Tersoff potentials. These formalisms are applicable for metals and materials with directional bonds (such as semiconductors), respectively. Both types of potential are described in detail below. Subsequently, we also discuss the Ziegler-Biersak-Litmark (ZBL) short-range potential form.

4.1.4.1 Embedded Atom Model

The embedded atom model (EAM) is an efficient formalism to describe metallic systems, which was developed in [197] following on from earlier work on effective medium theory [198]. It was put forward to overcome the limitation of two-body potentials, which do not contain any information on the bond strength as function of the local coordination, in an attempt to capture some additional physics behind metallic bonds. The general form of the EAM total energy, U, is as follows:

$$U = \frac{1}{2}\sum_{i}^{N}\sum_{i\neq j}^{N} V_{ij}(r_{ij}) + \sum_{i}^{N} F(\rho_i), \tag{4.11}$$

where N is the total number of atoms and r_{ij} is the interatomic separation of atoms of indices i and j. The EAM is composed of three, generally non-analytical parts, which are fitted to when constructing a potential. These are namely: pairwise potential $V(r_{ij})$, the embedding functional of the local electron density, $F(\rho_i)$, and the local electron density experienced by an atom i, ρ_i, that is defined as:

$$\rho_i = \sum_{j,i\neq j}^{N} \phi_j(r_{ij}). \tag{4.12}$$

The electron density is effectively a superposition of densities $\phi_j(r_{ij})$ from all neighbouring atoms of atom i. The two terms in Eq. 4.11 represent a two-body core-core (electrostatic) contribution, $V_{ij}(r_{ij})$, and a cohesive term, $F(\rho_i)$, which is "embedding" an atom i in the local electron density. The non-linearity of the embedding functional, F, is essential to tackle the two-body potential limitations. It is easy to observe that if F was linear with respect to ρ_i, i.e. $F(\rho_i) \propto \rho_i$, the EAM potential formulation would be equivalent to a two-body one.

4.1.4.2 Tersoff and modified Tersoff

The Tersoff [199–201] and the modified Tersoff (MOD) [202] potentials belong to a class of bond-order potentials, which have the capability of describing the different bonding states of an atom depending on its environment. More specifically, these contain two- and three- body terms with the bond-order (or bond stiffness) included as an angular term. It is widely used as a formalism for systems with covalent bonds, such as Si, Ge and C. In the original Tersoff potential the energy is expressed as:

$$U = \frac{1}{2}\sum_{i}\sum_{j,i\neq j} \Phi_{ij}(r_{ij}), \tag{4.13}$$

where r_{ij} is, as usual, the interatomic separation. The potential function is given as:

$$\Phi_{ij} = f_c(r_{ij})[\overbrace{A\exp(-\lambda_1 r_{ij})}^{\text{repulsive}} + \overbrace{b_{ij}B\exp(-\lambda_2 r_{ij})}^{\text{attractive}}], \tag{4.14}$$

where $f_c(r_{ij})$ is a smooth cutoff function. The two terms in square brackets correspond to attractive and repulsive parts of the potential, respectively. The cutoff function is written as:

$$f_c(r_{ij}) = \begin{cases} 1 & R_1 \leq r_{ij} \\ \frac{1}{2}\left[1 + \cos\left(\pi \frac{r_{ij}-R_1}{R_2-R_1}\right)\right] & R_1 < r_{ij} < R_2 \\ 0 & r_{ij} \geq R_2, \end{cases} \tag{4.15}$$

and the values of R_1 and R_2 are chosen as to include only the first nearest neighbours. The angular-dependency, the key feature of this potential, is included in the b_{ij} term. It is expanded as follows:

$$b_{ij} = (1 + \xi_{ij}^{\eta})^{-\delta} \tag{4.16}$$

$$\xi_{ij} = \sum_{k \neq i,j} f_c(r_{ij})\ g(\theta)\ \exp[\alpha(r_{ij} - r_{ik})^{\beta}] \tag{4.17}$$

$$g(\theta) = a\left[1 + \frac{c^2}{d^2} + \frac{c^2}{d^2 + (h - \cos(\theta))^2}\right], \tag{4.18}$$

where $\theta = \theta_{ijk}$ is the angle between r_{ij} and r_{ik}. The following are the parameters that are fitted to: A, B, λ_1, λ_2, η, δ, α, β, a, c, d, h, R_1, R_2, while in the original formulation of the Tersoff potential β and $\eta \cdot \delta$ are set.

As for the physical interpretation of the terms in Eq. 4.16, the $(1 + \xi_{ij}^{\eta})$ term represents the effective coordination of atom i with the ij bond is counted as one. As in the original formulation $\eta \cdot \delta = 0.5$ the strength of the bond is smaller with the greater coordination number of atom i. The effective coordination represented by ξ_{ij} is comprised of two terms: (i) $\exp[\alpha(r_{ij} - r_{ik})^{\beta}]$ the difference in the bond length of ij and ik, and (ii) $g(\theta)$ the angle between the ij and ik bonds. In the angular term, the parameters c and d determine the strength of the overall angular dependence and the bond angle, respectively.

The modified Tersoff potential (MOD) [202] is a slightly revised version of the bond-order Tersoff potential for silicon, specifically its T3 version (third and the most popular revision of Tersoff potential for silicon [201]). Incidentally, MOD was formulated in such a way that the T3 is its special case. It has been reviewed to be superior to T3 and at least as good as the alternative and very popular Stillinger-Weber potential [203]. There are four major changes that are required to arrive at the MOD from T3: (i) modifications to the cutoff function $f_c(r_{ij})$, (ii) change to the form of the $g(\theta)$ function, (iii) lifting a constraint in the effective coordination number exponent and finally (iv) changes to the form of $\omega_{ik} = \exp[\alpha(r_{ij} - r_{ik})^{\beta}]$ function (this is only particular to the DL_POLY implementation, which can handle constant ω_{ik} only). This potential has recently been incorporated in DL_POLY with the help of the present author. For

derivatives of the MOD potential and further implementation notes, see the DL_POLY manual [204]. The MOD changes are listed below.
(i) Modified cutoff function proposed by Murty [205] to ensure continuous second-order derivatives. In the range of $R_1 < r_{ij} < R_2$ it has the form:

$$f_c(r) = \frac{1}{2} + \frac{9}{16}\cos\left(\pi\frac{r - R_1}{R_2 - R_1}\right) - \frac{1}{16}\cos\left(3\pi\frac{r - R_1}{R_2 - R_1}\right), \tag{4.19}$$

where we simplify the notation and use $r = r_{ij}$.
(ii) Modified angular-dependent term $g(\theta)$:

$$\begin{aligned} g_{mod}(\theta) &= c_1 + g_0(\theta)g_a(\theta) \\ g_0(\theta) &= \frac{c_2(h - \cos(\theta))^2}{c_2 + (h - \cos(\theta))^2} \\ g_a(\theta) &= 1 + c_4\exp(-c_5(h - \cos(\theta)^2)) \end{aligned}$$

where c_i and h are additional fitted parameters.
(iii) Lifted the constraint on $\eta \cdot \delta = 0.5$ such that the original T3 expression

$$b_{ij} = (1 + \xi_{ij}^{\eta})^{-\delta} \tag{4.20}$$

is not only limited to the following form:

$$b_{ij} = (1 + \xi_{ij}^{\eta})^{-\frac{1}{2\eta}}. \tag{4.21}$$

4.1.4.3 ZBL short-range interaction

Both the Tersoff and EAM potentials are equilibrium potentials and are bound to fail on physics (and technical) grounds when two atoms very get close to each other, i.e. at distances $r \lesssim 1$ Å. Such close-range interactions are typically given by a Coulomb potential times a screening function $\phi(r)$ of the electrons, i.e.

$$U(r) = \frac{Z_1 Z_2}{r}\phi(r), \tag{4.22}$$

where $Z_{\{1,2\}}$ are the nuclear charges on the interacting atoms and r is the interatomic separation, respectively. The screening function has historically many forms, such as Bohr screening function of $\phi(r) = \exp(-r/a)$, where a is a constant screening radius. In the Ziegler-Biersack-Littmark (or ZBL for short) [206] formulation the screening radius is given by:

$$a = \frac{0.8853 a_B}{\left(Z_1^{2/3} + Z_2^{2/3}\right)^{1/2}}, \tag{4.23}$$

where a_B is the Bohr's radius. It is a common practice to join the ZBL potential with an equilibrium potential to describe close-range collisions effectively. However, this joining process (particularly to more complex potential forms) is not straightforward from a technical standpoint, as one needs to match the potential and its derivative at the joining points correctly. Hence, this procedure can have an impact on the equilibrium part of the potential, which was shown in turn to impact the result in cascade simulations [72]. Nonetheless, ZBL remains the standard short-range potential in radiation damage community.

4.2 Damped MD

The 'electronic friction' due to ionisation and excitation effects is particularly important in high-energy cascade simulations, where substantial energy losses due to inelastic interactions occur. Using the fact the electronic stopping is proportional to the ballistic ion velocity for slow heavy ions [22, 23], the losses can be represented in the MD EoM as a simple friction term, as follows [74, 76]

$$m_i \frac{d^2\mathbf{r}_i}{dt^2} = \boldsymbol{F}_i - \gamma_i \boldsymbol{v}_i, \tag{4.24}$$

where $\boldsymbol{v}_i$ and m_i are, as usual, velocity and mass of atom i. $\boldsymbol{F}_i$ is the force acting on atom i (at the time t) due to the interaction potential. The energy loss is represented by a friction coefficient, γ_i, which is linked to the electronic stopping power [76] and constructed in the following way

$$\gamma_i = \gamma_{es} \quad \text{for } v_i > v_{cut} \tag{4.25}$$

$$\gamma_i = 0 \qquad \text{otherwise,} \tag{4.26}$$

where v_{cut} is a cutoff velocity of a projectile. It is in essence a free parameter and it is usually quoted as the cutoff kinetic energy instead $E_c = \frac{1}{2} m v_{cut}^2$.

4.3 Two-temperature molecular dynamics

Two-temperature molecular dynamics (2T-MD) is an augmented MD method, which as the name suggests will use the idea of the two-temperature state introduced in the section on continuum models, Sec. 2.2. There are two components for the 2T-MD scheme, notably the modified EoM for the ions and the continuum electronic temperature (T_e) part. Ionic motions can be damped or subject to additional force coming from the electronic stopping, or the electron-phonon coupling effects. We incorporate these effects at the level of the inhomogeneous thermostat (Sec. 4.3.1). Subsequently, we describe the continuum solver implementation, i.e. the finite difference solution scheme used, for the extended and the inelastic thermal spike models.

4.3.1 Inhomogeneous Langevin thermostat description

We start by describing the MD equations of motion following the standard Langevin dynamics, which is used to keep the MD simulation at a constant temperature thus emulating an NVT ensemble. (It technically speaking imposes Brownian dynamics or stochastic Langevin dynamics on the system). The Langevin dynamics EoM is as follows

$$m_i \frac{d^2\mathbf{r}_i}{dt^2} = \overbrace{\boldsymbol{F}_i}^{(1)} - \overbrace{\gamma_i \boldsymbol{v}_i + \tilde{\boldsymbol{F}}_i}^{(2)}, \tag{4.27}$$

where $\boldsymbol{r}_i$ and m_i are the position and mass of atom i. The first part (labelled (1)) is the force, $\boldsymbol{F}_i$, acting on atom i due to the interaction potential. The second part (2) comprises of an

energy loss term represented by a friction coefficient γ_i and an energy gain term represented by a stochastic force $\tilde{\boldsymbol{F}}_i$. The latter has a random magnitude and orientation with $\tilde{\boldsymbol{F}}_i = \sqrt{\Gamma_i}\tilde{\boldsymbol{R}}_i$, where $\tilde{\boldsymbol{R}}_i$ is a three-dimensional vector with components randomly distributed in the $[-1, 1]$ set. In this formulation, $\Gamma_i = 6\chi m_i k_B T_T$, where $\chi = \gamma_i/m_i$ is an assumed time constant, T_T is the target temperature of the thermostat and k_B is the Boltzmann's constant. The following set of equations must also be satisfied by the stochastic force term. It must not represent a sink or a source term

$$\langle \tilde{\boldsymbol{F}}_i(t) \rangle = 0. \tag{4.28}$$

Moreover, it can neither exhibit any spatial (for atoms labelled i and j) nor temporal correlation (at different times, t and t') and it has to satisfy the fluctuation-dissipation theorem, i.e.

$$\langle \tilde{\boldsymbol{F}}_i^{\alpha}(t) \cdot \tilde{\boldsymbol{F}}_j^{\beta}(t') \rangle = 2k_B T_T m_i \chi \delta'_{\alpha\beta} \delta'_{ij} \delta(t - t'), \tag{4.29}$$

where superscripts denote Cartesian indices, δ' is the Kronecker's delta and δ is Dirac delta function.

The inhomogeneous Langevin thermostat developed by Rutherford and Duffy [81] is a mechanism for energy transfer between the continuum electronic part and the ionic MD part. It takes the electronic temperature (T_e) rather than the target one (T_T) as an argument, in effect thermostating the system to the electronic temperature with the energy given to the atomistic lattice by a stochastic force term. We cast the Langevin thermostat into the following (inhomogeneous) form $\Gamma_i = 6\gamma_i k_B T_e^j$ in order to force it to scale with the local electronic temperature of the system at a finite volume element j, T_e^j (called synonymously a voxel, or a coarse-grained cell). The random force can thus be represented as

$$\tilde{\boldsymbol{F}}_i = \left(\frac{6\gamma_i k_B T_e^j}{\Delta t} \right)^{1/2} \tilde{\boldsymbol{R}}_i, \tag{4.30}$$

where Δt is the MD time-step. Note that γ is no longer an empirical parameter relating to the thermostating "strength". It is now related to the electron-phonon coupling strength G [81] and hence renamed γ_{ep}

$$\gamma_{ep} = \frac{V}{N} \frac{m}{3k_B} G, \tag{4.31}$$

where N and V are the number of atoms in a finite volume element T_e^j and its volume, respectively. Further changes to γ are necessary to incorporate the electronic stopping (energy loss due to the inelastic electron scattering of ballistic atoms) in the same manner as in the damped MD schemes. This can be achieved as follows for γ_i (now indexed i as it is in principle different across atoms labelled i even when their masses are the same)

$$\gamma_i = \gamma_{ep} + \gamma_{es} \quad \text{for } v_i > v_{cut} \tag{4.32}$$

$$\gamma_i = \gamma_{ep} \quad \text{for } v_i \leq v_{cut}, \tag{4.33}$$

where v_{cut} is an assumed cutoff velocity.

Care should be taken when simulating the ionic velocities, $\boldsymbol{v}_i$, as these should take into account the random (i.e. thermal motion) only, $\boldsymbol{v}'_i$, particularly in the case of the electron-phonon interaction. Therefore, we usually discount for the centre of mass velocity, $\boldsymbol{v}_i^{CoM}$, in a volume element, V, i.e. $\boldsymbol{v}'_{\boldsymbol{i}} = \boldsymbol{v}_i - \boldsymbol{v}_i^{CoM}$. Note that the local lattice temperature (T_i) is computed from the kinetic energy of atoms in a voxel j (denoted $j \in V$) and no requirements are made regarding the distribution of the velocities, i.e.

$$T_i^j = \frac{\sum_{j \in V} m_j (\boldsymbol{v}'_j)^2}{3Nk_B}. \tag{4.34}$$

Alternative and similar 2T-MD schemes were used by Zhigilei and Ivanov [60], Duvenbeck [207–209], which were prototyped by Caro and Victoria [74]. We briefly discuss the approach by Zhigilei *et al.* who expressed the electron-phonon coupling as an additional (non-stochastic) force, which is proportional to the electron-phonon coupling strength, G, and the temperature difference between the ionic and electronic system, as follows:

$$m_i \frac{\partial \boldsymbol{v}_i}{\partial t} = \boldsymbol{F}_i + \xi m_i \boldsymbol{v}_i. \tag{4.35}$$

Here, $\boldsymbol{F}_i$ is the classical Newtonian force on the atom i and $\xi m_i \boldsymbol{v}_i$ is the 2T driving term related to the electron-phonon coupling via

$$\xi = \frac{V\ G \cdot (T_e - T_i)}{\sum_{j \in V} m_j (\boldsymbol{v}'_j)^2}, \tag{4.36}$$

where subscript j runs over all atoms in a voxel of volume V. A full derivation of this method can be found in [60]. The main advantage of this approach is its simplicity making it relatively easy to implement. However, a non-equilibrium Langevin thermostat reflects not only the statistical nature of the electron-ion scattering, but also allows for selective phonon excitations in future implementations, through changes to the random force spectrum, $\tilde{\boldsymbol{R}}$.

4.3.2 Finite difference scheme

The continuum electronic part of the 2T model (Eq. 2.3a) remains almost unchanged and can be cast into the following equation:

$$C_e \frac{\partial T_e}{\partial t} - \nabla \cdot [\kappa_e \nabla T_e] = G(T_e - T_i) + G_{es} T'_i. \tag{4.37}$$

Here, G is the coupling constant for the electron-phonon interaction and G_{es} is related to the rate of electronic stopping. Note the added extra term ($G_{es}T'_i$) - this represents a source term to balance the energy lost by the ionic system through electronic stopping with T'_i representing the temperature of the subsystem with velocities $v_i > v_{cut}$. We discuss the finite difference scheme solutions to Eq. 4.37, which is of a form of a heat diffusion equation.

Robust algorithms allowing us to solve the heat equation are central to the framework described. In the continuum model, for the original iTS (two-temperature) method, two coupled heat equations need to be solved for temporal and spatial dependence, while the extended iTS

is expressed by three conservation equations, which can be recast to heat diffusion equation forms. The simplest implementation is based on a standard forward in time, centred in space, finite difference method using explicit time-stepping (also known as Euler's method). Following [210] we define the thermal diffusivity as $\alpha \equiv \frac{\kappa}{C}$, where κ is the thermal conductivity and C is the heat capacity. We further denote the heat sink or source term as $\dot{q}$ and rewrite the heat equation as follows:

$$\frac{\partial T}{\partial t} - \alpha \nabla^2 T = \frac{\dot{q}}{C}. \tag{4.38}$$

This equation (Eq. 4.38) is closed and first order in time and second order in space and hence requires one boundary condition in time and surrounding boundary conditions in space. Based on the even space-time discretisation (equal spacing of space points x_i with intervals of size $\Delta x = x_{i+1} - x_i$ and time-steps t_n at intervals $\Delta t = t_{i+1} - t_i$) we can write the derivative approximations as:

$$\frac{\partial T}{\partial t} \mid_{x_i, t_{n+1/2}} \simeq \frac{T_i^{n+1} - T_i^n}{\Delta t} \tag{4.39a}$$

$$\frac{\partial T}{\partial x} \mid_{x_{i+1/2}, t_n} \simeq \frac{T_{i+1}^n - T_i^n}{\Delta x}. \tag{4.39b}$$

By taking the differences of the derivative approximations one can arrive at the expression for the second derivative:

$$\frac{\partial^2 T}{\partial x^2} \mid_{x_i, t_n} \simeq \frac{\frac{\partial T}{\partial x} \mid_{x_{i+1/2}, t_n} - \frac{\partial T}{\partial x} \mid_{x_{i-1/2}, t_n}}{\Delta x} \simeq \frac{T_{i-1}^n - 2T_i^n + T_{i+1}^n}{(\Delta x)^2}. \tag{4.40}$$

Inserting this into the heat equation (Eq. 4.38) for 1-D conduction we obtain:

$$\frac{T_i^{n+1} - T_i^n}{\Delta t} - \alpha \frac{T_{i-1}^n - 2T_i^n + T_{i+1}^n}{(\Delta x)^2} = \frac{\dot{q}}{C}. \tag{4.41}$$

Finally, we can solve this for the temperature at a new time-step (T_i^{n+1}), i.e.

$$T_i^{n+1} = T_i^n + \Delta t \left[\alpha \frac{T_{i-1}^n - 2T_i^n + T_{i+1}^n}{(\Delta x)^2} + \frac{\dot{q}}{C} \right]. \tag{4.42}$$

This is the core of the so-called forward time integration algorithm. It is an explicit time-stepping algorithm, meaning that each new temperature at $n+1$ is calculated independently. Note the algorithm's simplicity in that (ignoring the source term) the new temperature is the weighted average of the old temperature at the point T_i^n and its neighbours $T_{i\pm1}^n$.

For the α parameter independent of any other parameters (such as temperature) it is convenient to define the Fourier mesh number, which permits further simplification of Eq. 4.42.

$$F = \alpha \frac{\Delta t}{(\Delta x)^2}. \tag{4.43}$$

The Fourier number can be thought of as the ratio of time-step size to the time required to equilibrate one space interval of size Δx. The Fourier mesh also defines the stability of the solution. In the 1-D case for $F > \frac{1}{2}$ leads to exponentially unstable solutions.

Extending the grid into 3-dimensions with j, k indices denoting y, z axes respectively, Eq. 4.42 becomes

$$T^{n+1}_{i,j,k} = F \cdot (T^n_{i-1,j,k} + T^n_{i+1,j,k} + T^n_{i,j-1,k} + T^n_{i,j+1,k} + T^n_{i,j,k-1} + T^n_{i,j,k+1} - 6T^n_{i,j,k}) + \Delta t \frac{\dot{q}}{C}, \tag{4.44}$$

with the modified stability criterion requiring now that $F \leq \frac{1}{6}$. In order to design a simulation one needs to choose a mesh in space first and then choose Δt to satisfy the stability criteria of Fourier mesh, i.e. $\Delta t \leq \frac{(\Delta x)^2}{6\alpha}$.

In this discussion we have assumed that α is temperature independent, thus $\nabla \cdot [\alpha \nabla T] = \alpha \nabla^2 T$ simplification was made. This however will not be the case in general, particularly at phase transitions (changes in heat capacity) and for the Laplacian pre-factors found in the extended thermal spike model. The procedure for finite difference solutions of this class of problem is roughly as follows. We freeze the coefficients by considering the problem locally [211] and proceed as in the constant coefficient case. Simply put, α will be different for each of the interactions of the $T^n_{i+1,j,k}$ site with its neighbours and hence α will take the average value of the variable of interest between the interacting cells as the argument. An explicit finite difference scheme for the updated site $T^{n+1}_{i,j,k}$ which results from the interaction between $T^n_{i,j,k}$ and $T^n_{i+1,j,k}$ of $\alpha = \kappa(T)/C(T)$ strength is given by

$$T^{n+1}_{i,j,k} = \frac{\Delta t}{(\Delta x)^2} \frac{\kappa\left[\frac{1}{2}(T^n_{i+1,j,k} + T^n_{i,j,k})\right]}{C(T^n_{i,j,k})} \cdot (T^n_{i+1,j,k} - T^n_{i,j,k}) + \ldots + \Delta t \frac{\dot{q}^n_{i,j,k}}{C(T^n_{i,j,k})}. \tag{4.45}$$

Use of this algorithm was employed is similar simulations in the past to simulate low-energy electronic excitation in atomic collision cascades (for instance by Duvenbeck and Wucher [207]). Similar schemes were devised in [45, 53].

Using this formulation a stability condition can be derived [211]. This condition will depend on the frozen coefficients involved and the key idea is to choose the most conservative time-step, covering all possible values of the frozen coefficient. The variable coefficient dependencies are quite complicated and hence bounds for the coefficients could only be estimated for a given time-step (at most a short time period) in the simulation. Therefore an adaptive time-stepping is the only practical solution. In 2T-MD both the ionic and the electronic systems are solved with adaptive (variable) time-steps, Δt_{MD} and Δt_{FD}, respectively, and therefore the FD time-step is constrained to be an integer multiple of the MD time-step.

4.3.3 Note on boundary conditions

There are three types of boundary conditions (BC) that are used in the continuum and the hybrid MD variant of the simulations, namely: Dirichlet (infinite source/sink), Neumann (zero-flux) and Robin's (variable flux), which follows Newton's law of cooling. Zero-flux BC is important for trial runs, as it confines the evolved quantity in the simulation region, therefore enabling stability tests, i.e. checking for any 'drifts' of the evolved quantity, to be performed.

In production runs, variable flux is the BC of choice, as it can approximate the conduction into bulk. To summarise:

1. Dirichlet (infinite flux) BC ($T|_{\partial\Omega} = T_0$), where T is the evolved scalar quantity, $\partial\Omega$ is the boundary (i.e. a halo/ghost cell) and T_0 the target scalar quantity,

2. Neumann (zero flux) BC ($\dot{T}|_{\partial\Omega} = 0$); can be implemented by copying the edge cells to the halo region every time-step,

3. Robin's (variable flux) BC ($\dot{T}|_{\partial\Omega} = -k(T - T_0)$) fills the halo cells with a constant fraction ($k \in [0, 1]$) of the quantity held in the edge cells, in accordance with the Newton's law of cooling.

4.3.4 Extended iTS implementation

The three equations (Eq. 2.4a, Eq. 2.4b, Eq. 2.4c) that we attempt to solve within the extended iTS model, which includes finite band-gap effects, are a set of coupled diffusion-like equations with variable coefficients (or Laplacian pre-factors) and source terms. These (Eq. 4.46, Eq. 4.47) can be cast into a form similar to heat diffusion equation, while Eq. 2.4c is already in the suitable form:

$$\begin{aligned}\frac{\partial N}{\partial t} &- \nabla \cdot [D(T_i)\nabla N] \\ &- \nabla \cdot \left[D(T_i) \left(\frac{2N}{k_B T_e} \right) \nabla E_g \right] \\ &- \nabla \cdot \left[D(T_i) \left(\frac{N}{2T_e} \right) \nabla T_e \right] \\ &= \underbrace{G_{e-h}}_{\text{source}} - \underbrace{R_{e-h}}_{\text{sink}}\end{aligned} \tag{4.46}$$

$$\begin{aligned}\frac{\partial U}{\partial t} &- \nabla \cdot [\zeta(T_i, T_e, E_g)\nabla N] \\ &- \nabla \cdot \left[\zeta(T_i, T_e, E_g) \left(\frac{2N}{k_B T_e} \right) \nabla E_g \right] \\ &- \nabla \cdot \left[\zeta(T_i, T_e, E_g) \left(\frac{N}{2T_e} \right) \nabla T_e \right] \\ &- \nabla \cdot [(\kappa_e + \kappa_h)\nabla T_e] \\ &= \underbrace{A(r[v_{ion}], t)}_{\text{source}} - \underbrace{\frac{C_{e-h}}{\tau_{ep}}(T_e - T_i)}_{\text{sink/source}}\end{aligned} \tag{4.47}$$

where $\zeta(T_i, T_e, E_g) = D(T_i) \cdot (E_g + 4k_B T_e)$. The contributions from each component (i.e. ∇N, ∇E_g and ∇T_e) can be solved within the Euler scheme separately and subsequently summed over.

Another difference when solving the extended model over the combined 2T-MD is that in the current Langevin thermostat formalism the energy exchange $\dot{U}_{ep} = \frac{C_{e-h}}{\tau_{ep}}(T_e - T_i)$ necessitates a different form of γ parameter to ensure the conservation of energy and link with τ_{ep}, i.e. $\gamma_{ep} = \frac{V}{N}\frac{mN_{e-h}}{\tau_{ep}}$ at each iteration time-step, where N_{e-h} is the number of carriers and N is the number of atoms of mass m contained in a temperature voxel.

Another challenge is the determination of the Dirichlet boundary conditions for the system. Van Driel [43] employed the following:

$$\begin{aligned} N(\boldsymbol{x} \to \infty, t) &= N_{eq} \simeq 10^{-9}\text{nm}^{-3} \\ T_e(\boldsymbol{x} \to \infty, t) &= 300 \text{ K} \\ T_i(\boldsymbol{x} \to \infty, t) &= 300 \text{ K}, \end{aligned}$$

where $\boldsymbol{x}$ is a point in a three-dimensional space. The choice of T_e and T_i is standard. However, in the current method we are solving for spatiotemporal dependence of U, N and T_i and not explicitly for T_e. Using $U = NE_g + 3Nk_BT_e$, we can thus determine the carrier energy sink. For instance, for Si $E_g = 1.16$ eV at 300 K we obtain $U(\boldsymbol{x} \to \infty, t) = 1.19 \cdot 10^{-9}$ eV.

4.3.5 Energy conservation

It can be shown by the means of stochastic calculus that for non-equilibrium Langevin thermostat the average energy transferred from the electrons to the ions is $\Delta E = 3N\Delta t k_B T_e \gamma_{ep}/m$, treating T_e as fixed. The energy transferred from the atoms, both by the electron-phonon and electron stopping processes, is $\Delta E = (-3k_B\Delta t/m) \cdot (NT_i\gamma_{ep} + N'T_i'\gamma_{es})$. Here, N' and T_i' are the number and the "temperature" of ballistic atoms with $v > v_{cut}$.

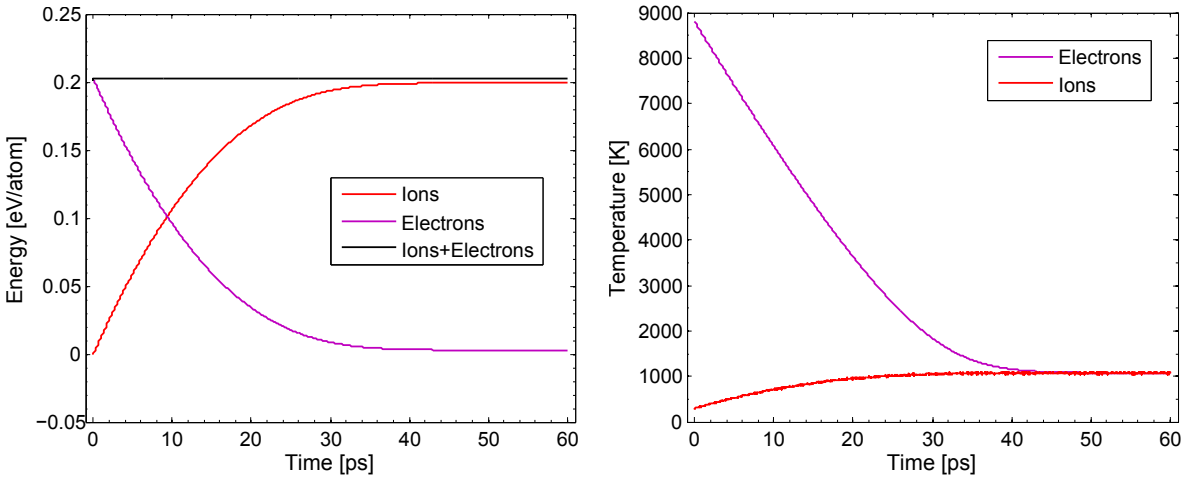

Figure 4.1: Normalised electronic and ionic energies (left panel) and the electronic and ionic temperatures relaxation (right panel) evolutions under homogeneous electron excitation of Cu. This simulation is a part of PARCAS MD code test-case suite.

It is argued in [212] that since the new electronic temperature are calculated assuming an average energy transfer, small total energy, E_{tot}, drifts are unavoidable. Note that the total energy $E_{tot} = E_i + E_e$, is total kinetic and potential energy of the ions, E_i, and the

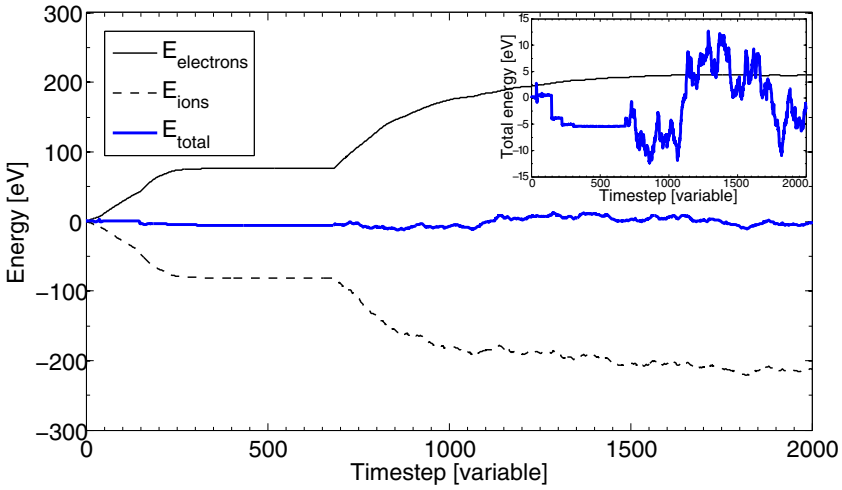

Figure 4.2: Energy conservation for an exemplar 1 keV pka cascade simulation in Fe. Ionic energies are reset to zero at the start of the simulation.

electron fluid energy, E_e. In reality, at each time-step the energy transferred can be smaller or larger and this discrepancy would correct for itself if $T_T = T_e = const.$. However, in the inhomogeneous Langevin thermostat T_e varies not only temporally but also spatially, allowing for the total energy to drift in a random walk fashion. This can be corrected for by calculating the exact energy exchange at each time-step (instead of a fixed average) according to the method described in [212].

Furthermore, in the current implementation small drifts in the total energy are possible, when G is made to depend on electronic temperature $G(T_e)$ and when the time-step in the electronic temperature solver (Δt_{FD}) is smaller than the MD time-step (Δt_{MD}). This is due to the fact that the $G(T_e)$ is updated every Δt_{FD} in the FD solver, but $G(T_e)$ is updated less frequently at Δt_{MD}, thus leading to slightly different averaged values of $\pm G(T_e)$ over a full Δt_{MD} time-step.

The total energy conservation and T_e, T_i evolution results for a sample 2T-MD simulation of a 4k Cu atoms system under isochoric laser heating with the electronic system parameters, such as $C_e(T_e)$, $G(T_e)$ and κ_e taken as that of Au from [184] are presented in Fig. 4.1. Since the initial excitation is homogeneous and the energy is "trapped" in the electronic and ionic system (i.e. periodic boundary conditions are used for ions and Neumann for electrons), almost perfect total energy conservation can be achieved[1]. In simulations of strong T_e and T_i inhomogeneity (Fig. 4.2) the total energy drift is more pronounced. However, it is still is negligible as it never exceeds 1% of the total energy over tens of picoseconds.

4.3.6 Simulations setups

There are three main simulation types that are now possible with the 2T-MD method as implemented in DL_POLY (local version 4.01). We use the acronyms CET and CIT to describe the coarse-grained electronic and ionic temperature cells (voxels), respectively. The temperature

[1]This simulation example in PARCAS MD code uses Zhigilei's [60] method of coupling electrons to ions.

cells are cubes with side sizes typically around 1 nm due to two competing requirements. A cell must contain enough atoms so that the thermal fluctuations of ions are negligible and a temperature can be defined. Also, the cell must be small enough to reflect the geometry of the initial energy deposition. Variable CET/CIT meshing (different sizes in all three dimensions) is sometimes used. In particular, in the SHI simulations, one would typically require small cells in the lateral directions, but long enough in the direction of the ion impact to contain a sufficient number of atoms. Such variable meshing is available in both DL_POLY and PARCAS [213–215]. The simulation setups (with their code names in bold) for each of these simulation classes are as follows:

1. **Cascades**: No initial energy deposition in the electronic system (i.e. $S_e = \frac{dE}{dx} = 0$), but an ion initialised with very high velocity; CETs extend further than CITs in all dimensions and boundary conditions are open (Dirichlet) or semi-open (Robin) in all dimensions to represent thermal electronic conduction into the bulk. Stochastic boundary conditions can be applied in the ionic system to damp the shock-wave generated by the displacement spike; see Fig. 4.3,

2. **Swift heavy ions (SHIs)**: $\frac{dE}{dx} \neq 0$ with Gaussian spatial and Gaussian or decaying exponential ($\propto \exp(-t)$) temporal distribution in T_e; The size of $\mathrm{CET}_z = \mathrm{CIT}_z$, while CET_{xy} extend over the corresponding CIT_{xy}; Boundary conditions: no flux going out in z-direction, x-y BCs open or semi-open. Stochastic boundary conditions can be applied in the ionic system in the lateral direction only to represent a non-negligible phononic thermal conductivity components in semiconductors into the bulk. Similarly, the electronic thermal conduction in the lateral directions is allowed, while in the normal to the SHI impact is not. This reflects the fact that the simulation represents a small cross-section of the evolution of a μm sized track; see Fig. 4.4,

3. **Lasers**: $\frac{dE}{dx} \neq 0$; homogeneous spatial and Gaussian temporal distribution of T_e; electronic system matching the ionic one in size, zero flux BCs in all directions. This represents a homogeneous laser excitation with the simulated part being a small section of a larger photo-excited sample; see Fig. 4.5

The overview of the added code structure as well as the additional functionality along with keywords that are now available in the local branch of DL_POLY (version 4.01) are reviewed in Appendix C.

4.3.7 Model testing

As a test and validation of the two-temperature model development in DL_POLY we have reproduced the 2T-MD results of photo-excited gold films reported by [184] and [60]. Specifically, we were able to reproduce the electronic and ionic temperatures evolution using the same parameters for both the electronic and ionic systems.

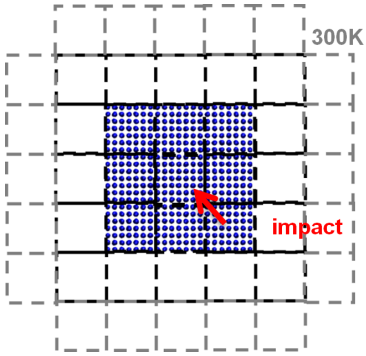

Figure 4.3: Schematic cascade simulation setup. The electronic temperature cells extend over the ionic (MD) simulation cell to simulate the electronic energy dissipation. The boundary conditions of the T_e part are set to converge towards 300 K to represent conduction into the bulk.

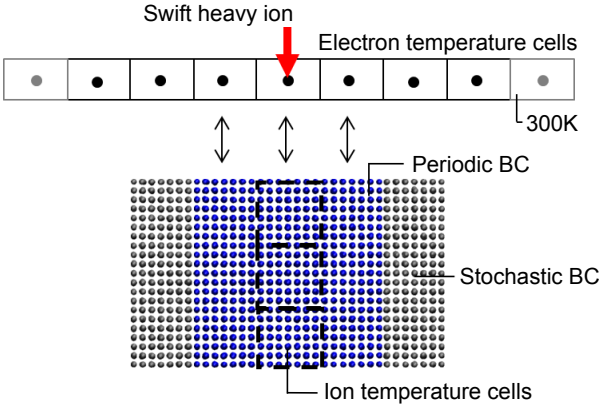

Figure 4.4: Simulation setup for swift heavy ion impact.

4.4 Molecular dynamics data analysis

4.4.1 Direct structure factor calculations

One way of representing real space atomic correlation is through the pair density function (PDF), which depends on the relative atomic distances. It is defined as:

$$\rho(r) = \frac{1}{4\pi N r^2} \sum_{i}^{N} \sum_{j,j\neq i}^{N} \delta(r - r_{ij}) = \frac{1}{2\pi N r^2} \sum_{i}^{N} \sum_{j<i}^{N} \delta(r - r_{ij}) \tag{4.48}$$

where N is the total number of atoms in the simulation box, r_{ij} are interatomic distances and δ is the Dirac delta function. In our implementation of the PDF, a top-hat function representation for the Dirac delta is taken, with the width corresponding to the numerical discretisation of space in the radial distance (Δr), which was chosen to be $\Delta r = 0.01$ Å. Since periodic boundary conditions are typically used in MD, the real space correlations can be evaluated up to a maximum radius r_{max}, which should satisfy $r_{max} < L/2$, where L is the shortest edge of the MD simulation box, in order to avoid introduction of false periodicity. The PDF calculation scales as $\mathcal{O}(N^2)$ with the system size due to the presence of the double sum, which can

Figure removed due to third party copyright restriction

Figure 4.5: Simulation setup for laser irradiation. *Figure reproduced from [3].*

become very computationally expensive for larger systems[2]. However, simple parallelisation schemes to evaluate the double sum in Eq. 4.48 exist. One such scheme utilising the OpenMP library is outlined in Appendix A.

A pair density function can be very efficiently transformed to a static structure factor $S(Q)$, where Q is the magnitude of the scattering vector. The structure factor is a valuable simulation characteristic as it can be measured directly in diffraction experiments. Computing $S(Q)$ from a PDF requires a simple one-dimensional sine Fourier transform on the positive radial distance (r) axis:

$$S(Q) = 1 + 4\pi \int_0^\infty r^2 \rho(r) \frac{\sin(Qr)}{Qr} W(r) dr \tag{4.49}$$

where $W(r)$ is a damping modification function to suppress artificial ripples with a period of $\Delta = \frac{2\pi}{r_{max}}$ resulting from a cutoff of r_{max} applied in the evaluation of the PDF. The damping function $W(r)$ prevents a discontinuous jump in the derivative at r_{max} by smoothing out the PDF at large radial distances thereby forcing the PDF to reach zero at the cutoff distance. Several methods were proposed to dampen these spurious ripples (see refs in [194]). We use a Lorch modification function of the following form:

$$W(r) = \frac{\sin(\pi r / r_{max})}{\pi r / r_{max}} \tag{4.50}$$

The impact of the modification function W(r) is presented in Fig. 4.6 for an equilibrated system of 180k Au atoms ($12.2 \times 12.2 \times 20.39$ nm^3) with $r_{max} = 60$ Å. While at an equilibrium situation the peaks are easily distinguishable even without such a correction, at higher degrees of disorder the peak intensities would be diminished and it would be impossible to discern these from spurious 'noise' ripples. Another way of improving the quality of the S(Q) peaks is to increase the cutoff distance r_{max} used for the calculations. This has obvious limitations, as

[2] A typical calculation for a configuration containing 180k atoms takes approximately 30 min on an Intel Pentium T4400 2.20GHz processor.

an increased r_{max} requires a larger MD simulation box. The effect of increased cutoff distance on the quality of S(Q) is presented in Fig. 4.7. There is an insignificant signal improvement from $r_{max} = 80$ Å to 100 Å as the peaks become well-defined beyond $r_{max} = 80$ Å. Therefore a sufficiently large MD simulation box, for the analysis to be valid, is constrained to a minimum size of $\sim 16 - 20$ nm.

The scheme presented here assumes a random sample orientation scattering (i.e. in the case of a crystalline powder), or equivalently probing from random directions [216]. Therefore the computed diffraction patterns would allow for additional reflections to appear in comparison to the ones measured in an experimental setup from a particular beam axis (i.e. zone axis) on a mono-crystalline sample.

It needs to be noted that direct computations of the structure factor from atomic configurations exists. One such formulation can be expressed as follows:

$$S(Q) = 1 + \frac{2}{N} \sum_{j}^{N} \sum_{i<j}^{N} \frac{\sin(Qr_{ij})}{Qr_{ij}}. \tag{4.51}$$

Nonetheless, such methods are more computationally expensive. This is mainly because of the requirement for repetitive calculation for each value of Q and the computation of the sine function [194].

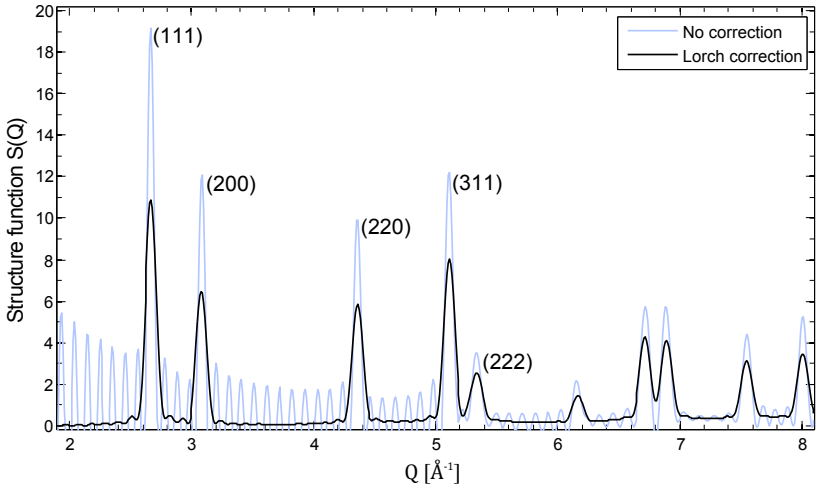

Figure 4.6: The effect of the truncation of the pair distribution function at $r_{max} = 60$ Å on the structure function in Au. Elimination of the spurious ripples (i.e. Fourier ringing) of a period of $\Delta = 2\pi/r_{max}$ is achieved by an addition of the Lorch damping function $W(r)$ in the Fourier transform. A Lorch damping correction (black) shows significant improvement to signal quality over uncorrected results (blue), where Fourier ringing can obscure smaller peaks. The results are presented for an fcc Au ($12.2 \times 12.2 \times 20.4$ nm^3) system equilibrated at 300 K. Selected Bragg peaks are labelled.

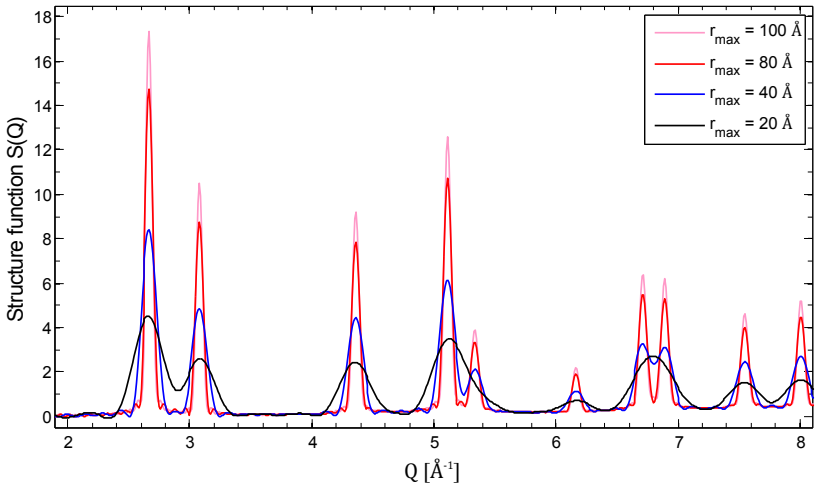

Figure 4.7: The effect of the cutoff radius r_{max} on the structure functions for Au ($20.4 \times 20.4 \times 20.4$ nm^3) system equilibrated at 300 K. Failure of capturing of the long-range correlations under 40 Å results in the merge of some peaks. Peaks become sharp with well defined positions around 80 Å, with only insignificant signal improvements between 80 Å and 100 Å.

4.4.2 Bragg peaks fitting

An X-ray or electron probe pulse can measure the time evolution of the diffraction patterns. Bragg peaks in the diffraction pattern probe only the average structure characterising the long-range order, while diffuse scattering probes the local deviations, which characterise the short range order.

It needs to be noted that Bragg peaks are affected by the Debye-Waller factor (DWF) (see Sec. 4.4.3) and thermal diffuse scattering - both result from thermally excited lattice vibrations. An increase in the DWF manifests itself in the reduction of Bragg peak heights, while thermal diffuse scattering appears as an increase of the background "noise" and the emergence of the peak corresponding to the liquid phase. So the information contained in Bragg peaks is long-range order (degree of heating, which induces disordering), while in diffuse scattering it is the local periodic structure and deviations from the average structure (i.e. degree of disordering). Uniaxial expansion, on the other hand, changes the crystal symmetry. This is manifested by the emergence of additional peaks in the diffraction pattern (i.e. peak splitting), corresponding to the "new" symmetry. However, if the expansion is uniform all Bragg peaks would shift their position, but would not split.

In order to effectively compare the experimental diffraction pattern with theoretical work which assumes single scattering events, the experiment should be free of inelastic multiple electron effects, which manifest themselves as (000)-order attenuation [217]. When the extinction distance is smaller than the sample thickness, the diffraction pattern requires analysis employing dynamical theory of electron diffraction. In the case of nanofilms and a 3.0 MeV electron probe, the multiple diffraction effects are negligible, as the extinction distance for (200)-peak is 186 nm [218].

The computed Bragg peak pattern was analysed with a customised Interactive Peak Fitter code (version 2.2) [219] in Matlab (version R2012B). In the experiment, discussed in chapter 6, the beam axis (i.e. the zone axis - the axis along which the probe is located) was placed normal to the (001) surface and therefore any splitting due to (001) expansion was not detected. However, in the computed pattern peak splitting was visible as the analysis assumed a random sample orientation (i.e. crystalline powder diffraction). Therefore, peak splitting is neglected in the subsequent data analysis. We use linear background subtraction to factor out the diffusive thermal scattering effects and noise. We perform Lorenzian or Gaussian fits (whichever yields a smaller fit error). An example fit is presented in Fig. 4.8.

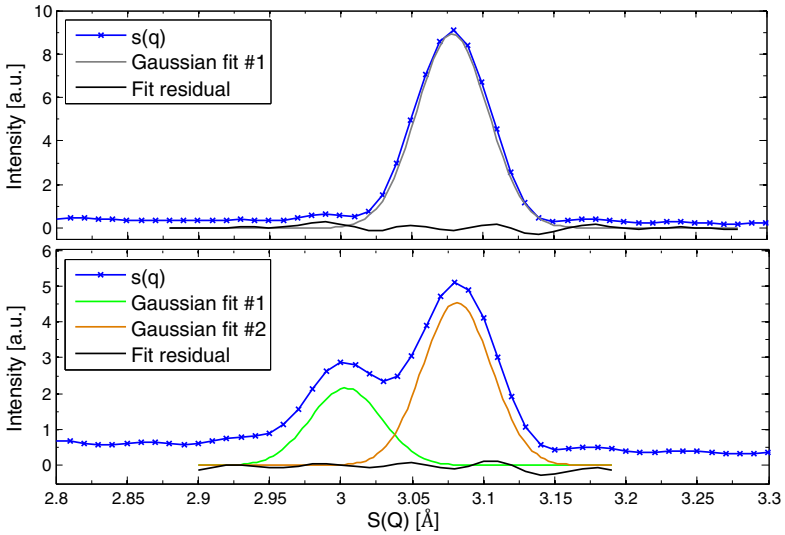

Figure 4.8: Examples of Bragg diffraction peak fitting procedure.

4.4.3 Debye-Waller factor calculations

The thermal contribution to the Bragg peaks "smearing" is typically described by the Debye-Waller factor (DWF), $W_I = e^{-2M}$, where M is a time-dependent quantity [194]. The reduction of Bragg peak heights can be attributed to the Debye-Waller effect. The DWF can be expressed as a function of mean-square atomic displacements (MSD, denoted u) and the scattering vector Q [220]:

$$W_I = e^{-2(\frac{1}{2}\langle(\boldsymbol{u}\cdot\boldsymbol{Q})^2\rangle)} = e^{\frac{1}{3}\langle u^2\rangle Q^2}, \tag{4.52}$$

where $\langle ... \rangle$ denotes time averaging. Note that the $\frac{1}{2}\langle(\boldsymbol{u}\cdot\boldsymbol{Q})^2\rangle$ expression is derived assuming harmonic approximation [220]. The factor of $\frac{1}{3}$ in Eq. 4.52 arises from spherical averaging. The DWF contribution can easily be predicted from the MD simulations, as MSD can be readily obtained from the atomistic trajectories as follows

$$u(t) = \frac{1}{N}\sum_{i}^{N} |\mathbf{r_i}(t) - \mathbf{r_i}(t_0)|, \tag{4.53}$$

where N is the number of atoms labelled i at positions $\mathbf{r_i}$ and measured from a given initial time, t_0.

4.4.4 Local order parameter

To distinguish solid-like from liquid-like environments for a particular atom i, we used the centro-symmetry parameter, defined as [192, 221, 222]:

$$\Phi_i = \frac{1}{6}\frac{1}{a_0^2}\sum_{j=1}^{6} |\boldsymbol{d}_j + \boldsymbol{d}_{-j}|^2 \,, \tag{4.54}$$

where $\boldsymbol{d}_j$ and $\boldsymbol{d}_{-j}$ are vectors connecting atom i to its opposite nearest neighbours j, $-j$; a_0^2 is the equilibrium lattice parameter. The values of the centro-symmetry parameter are hence dimensionless through a_0^2 normalisation. For an fcc lattice, sufficient sensitivity of the method is obtained when six such vector pairs (four for bcc), corresponding to the first nearest-neighbour (nn) shell, are chosen. In practice, a cutoff distance r_{cut} is selected (which is larger than the first nn shell distance) within which the six shortest vector pairs j and $-j$ are selected.

To reduce the thermal noise in the analysis one can average the values of Φ_i over a particular time period, over the nn values, or use a velocity damping technique [192]. In the case of fcc Au we are averaging the Φ_i parameter over the twelve nn values.

The centro-symmetry parameter provides us with a quantitative measure of a degree of crystallinity; it is zero for atoms in perfect crystalline surroundings and sharply increases as the local atomistic environment become disordered. It can also be used to detect defects, dislocations and indicate free surfaces.

4.5 Summary

In this chapter we described the evolution of the atomistic simulation techniques from classical molecular dynamics (Sec. 4.1), through damped MD (Sec. 4.2) to the more sophisticated non-equilibrium two-temperature MD (Sec. 4.2). We looked at some of the post-processing analyses methods, which help to visualise the phase transitions (Sec. 4.4.4) and relate the MD data to the experimentally measurable quantities (Sec. 4.4.1).

The common thread in the MD "evolution" presented here is a step-by-step inclusion of the non-equilibrium electron-ion interactions. Damped MD includes the electronic stopping power, while the two-temperature MD adds an effective description of the electron-phonon coupling. Beyond that, three-temperature models include a temperature to account for the spin degree of freedom in magnetic materials. We envisage that further non-equilibrium effects will be successively added in the future, such as selective electronic excitations (with a separate temperature describing each), selective phonon excitations and most importantly T_e-dependent interatomic potentials.

Chapter 5

Radiation damage cascades

□ **Attribution:** The 200-500 keV pka cascade simulations were performed in collaboration with researchers at Queen Mary, University of London. Parts of the simulation setup, parameter selection, the subsequent defect statistics and clustering analysis were conducted by the present author. The second batch of the simulations, in the range of 50-100 keV pka, was designed, run and analysed independently by the present author.

The parallel two-temperature DL_POLY code development was carried out by M. Seaton (Daresbury Laboratory) and was based on a serial version provided by the present author, which was in turn built from a provisional development by A. Rutherford. Extensive acceptance testing performed before the code was released to our collaborators, as well as the code documentation was the assumed responsibility of the present author.

Parts of the research presented here were published in [1, 5, 223].

5.1 Introduction

The aim of this chapter is to investigate the effects of the electronic stopping and electron-phonon coupling on the primary radiation damage formation in α-iron using the two-temperature molecular dynamics model (2T-MD). An extensive comparison to 'standard' cascades, which do not include the interactions between the ions and the electrons, as well as literature data, is made. A method to separate e-s and e-p processes at the simulation level is presented and the impacts of each of these energy transfer channels on the evolution of the damage cascade are quantified. The results summarised here are particularly timely, since the impact of the electronic effects (particularly the strength of the e-p coupling) in cascade simulations has recently been investigated for low energy pka impacts (10 keV) [81, 224] and the requirement to include these processes has been emphasised in recent reviews (see also Sec. 3.2). Nonetheless, a detailed and rigorous comparison of the impact of the e-p and e-s effects against 'stand-

ard' cascades is still missing. Furthermore, the results reported here provide detailed defect number statistics for higher, more representative and hence realistic, 50-500 keV pka impact simulations. Modelling of such high energies was enabled by the progress achieved in building a massively parallel 2T-MD code.

This chapter concentrates on the simulations performed for α-iron, as it is a candidate for primary components of steels and alloys for the future nuclear reactors. Furthermore, α-iron is, by far, the most commonly studied material through cascade simulations, which makes the comparison with the vast amount of literature data possible.

Secondary aims of the chapter include detailed characterisation of the Frenkel pair (FP) distribution, for 50 keV and 100 keV pka impacts, over a large number of cascade runs. This is to investigate the possibility of rare-events - infrequent generation of very large defects clusters or exceptionally high FP numbers in comparison to the mean FP expected at a particular cascade energy[1]. Local defect structures and defect cluster distribution along with remarks on global morphology trends for 50, 100, 200 and 500 keV cascades are presented and analysed in the context of previous research findings. We note that the 500 keV cascade results presented here represent the highest energy cascade simulation in iron published to date.

5.2 Model parameters for Fe

5.2.1 Electronic thermal conductivity and specific heat

The success of the 2T-MD model largely depends on the correct parameterisation of the electronic structure system. Parameters, such as electronic thermal conductivity or electronic specific heat are well-known under 'standard conditions', however for high electronic excitations, parameterisation with respect to the electronic and ionic temperatures is required. We start our parameters discussion with the electronic specific heat (C_e), defined as the amount of energy (U_e) required to raise the electronic temperature, $C_e = \partial U_e / \partial T_e$.

In general, the electron specific heat capacity would depend on the derivative of the Fermi function and the form of electron density of states (DOS), $g(\varepsilon)$ [29, 225]:

$$C_e = \int_{-\infty}^{\infty} g(\varepsilon) \frac{\partial f(\varepsilon, \mu, T_e)}{\partial T_e} \varepsilon d\varepsilon, \tag{5.1}$$

where ε and μ are the energy level and chemical potential, respectively. The Fermi function is defined as $f(\varepsilon, \mu, T_e) = 1/[e^{\beta(\varepsilon-\mu)} + 1]$ with $\beta = 1/(k_B T_e)$. At low electronic temperatures ($k_B T_e \ll \varepsilon_F$),where ε_F is the Fermi energy, the Sommerfeld expansion is typically used to obtain a linear electronic heat capacity T_e dependence (after [225]):

$$C_e = \Gamma T_e, \tag{5.2}$$

where Γ is the electronic heat capacity coefficient and is given by

$$\Gamma = \frac{\pi^2}{3} k_B^2 g(\varepsilon_F). \tag{5.3}$$

[1]Cascade energy or damage energy is the pka energy minus any inelastic losses to the electrons.

The expression can also be rewritten for free electron gas (FEG)

$$\Gamma = \frac{\pi^2}{2} k_B^2 n_e / \varepsilon_F, \tag{5.4}$$

where n_e is the number density of free electrons. Values of Γ have been calculated experimentally for various metals and several of these are collected in [225]. The value of C_e at higher temperatures approaching the binding (or cohesive) energy ($k_B T_e \sim \varepsilon_{coh}$, where $\varepsilon_{coh} = 4.28$ eV/atom $\sim 50,000$ K for Fe) can be approximated as that of an ideal gas with the heat capacity of $\frac{3}{2}k_B$ per electron [226]. For Fe with two electrons in the 4s band, C_e would thus saturate at around $3k_B$ until core electrons are excited at even higher temperatures.

At intermediate (0 K $\ll k_B T_e < \varepsilon_B$) and very high temperatures ($k_B T_e > \varepsilon_B$), however, the C_e can vary in a non-monotonic fashion and therefore the DOS and the $\frac{\partial f(\varepsilon,\mu,T_e)}{\partial T_e}$ terms should be computed directly from Eq. 5.1. Such computations were performed in [29] for eight transitions metals (several more, such as fcc and bcc iron can be found in [227]) using density functional theory (DFT). While the precise details of the calculations can be found in [29], we note here that the evaluation of the $\frac{\partial f(\varepsilon,\mu,T_e)}{\partial T_e}$ term requires prior knowledge of the chemical potential ($\mu(T_e)$) as a function of the electronic temperature. It can be obtained through the conservation of the total number of electrons (N_e), i.e.

$$N_e = \int_{-\infty}^{\infty} g(\varepsilon) f(\varepsilon, \mu(T_e), T_e) d\varepsilon. \tag{5.5}$$

In the following work we use the $C_e(T_e)$ *ab initio* parameterisation for non-magnetic bcc iron published in [29, 227], as for the high electronic excitations produced in cascade simulations, the Sommerfeld approximation (derived for low T_e) is no longer valid. The different models of temperature dependence of C_e for Fe are presented in Fig. 5.1, with the *ab initio* results presented in more detail in Fig. B.1.

In general, thermal conductivity is a measure of heat transfer and is defined as the proportionality constant between the heat flux and temperature gradient. It has two components, a phononic (κ_l) and an electronic one (κ_e). In metals, the electronic part dominates over the phononic component, due to the availability of current carriers in the conduction band, by about an order or two in magnitude (for instance, in tungsten κ_l/κ_e has been measured to be 0.25 [228]). It is the κ_e component that enters the electronic (continuum) system equation in 2T-MD, whilst κ_l is handled by the molecular dynamics part. The thermal conductivity is well known in low-temperature equilibrium states and in plasma. In the former, it is usually related to the electronic conduction (σ) via the Wiedemann-Franz law for metals ($\kappa = LT\sigma$), where L is the Lorentz number. In dielectrics its temperature dependence is described by the Debye model of phonons, whereas in the case of semiconductors both conductivity components are significant. In a plasma, thermal conductivity is described by the Coulomb collisions between atoms which results in a $\propto T_e^{5/2}$ temperature dependence. For metals, such as Fe, in an equilibrium situation κ_e temperature dependence is well characterised experimentally and $\kappa \propto (T_i)^{-1}$. However, an effective non-equilibrium parameterisation of electronic thermal conductivity, in the so-called warm dense matter (WDM) state with relatively cold ions and hot

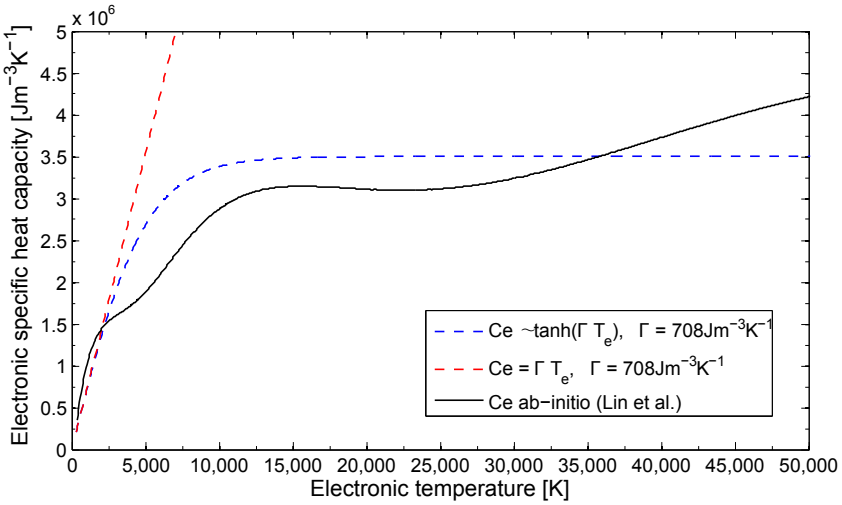

Figure 5.1: Electronic specific heat capacity for bcc Fe as a function of electronic temperature. Low temperature linear approximation (red dashed line) is valid up to 3,000 K, whilst a $\propto \tanh(\Gamma T_e)$ fit (blue dashed) assuming that the heat capacity saturates at $3k_B$ (contribution of two electrons per atom) follows the *ab initio* results (black) [29, 227] well up to 35,000 K, above which more than two electrons contribute. The most accurate *ab initio* results are used for the cascades simulations.

electrons or with hot ions and cooler electrons, is a more complicated task. This is because the different scattering contributions to the thermal conductivity (described below) can no longer be described by one temperature. Therefore for an effective non-equilibrium description of κ_e, the ionic and electronic temperature contributions should ideally be decoupled and quantified separately.

The thermal conductivity can be related to the electron velocity v, electronic specific heat capacity C_e, and the electron characteristic scattering time τ_e according to the Drude model:

$$\kappa_e = \frac{1}{3} v_F^2 C_e \tau_e. \tag{5.6}$$

The velocity of the electrons is typically approximated by the Fermi velocity (v_F) below the plasma temperature limit. The electron scattering time (i.e. transport time) has two contributions: electron-electron (τ_{e-e}) and electron-phonon scattering (τ_{e-p}), of which characteristic times are related by $1/\tau_e = 1/\tau_{e-e} + 1/\tau_{e-ph}$. We can assume that the electron-phonon scattering time depends on the number of phonons only and therefore on their temperature [229], thus $1/\tau_{ep} = 1/(BT_i)$, where B is a constant. This relationship is valid in the $T_i > T_D$ regime, where T_D is the Debye temperature (Fe, T_D = 470 K). Furthermore, $1/\tau_{e-e} = 1/(AT_e^2)$ for $T_e \ll \epsilon_F/k_B$, where A is a constant. In iron and other conductors, the electron transport time would be dominated by the electron-phonon scattering and therefore the AT_e^2 term can be neglected for $T_e \ll \epsilon_F/k_B$. Ivanov *et al.* [60] made a further assumption of a linear electronic heat capacity and arrived at the following simple expression for electronic thermal conductivity:

$$\kappa_e = \frac{1}{3} v_F^2 C_e \tau_e = \frac{1}{3} v_F^2 \frac{\Gamma T_e}{AT_e^2 + BT_i} \approx K_0 \frac{T_e}{T_i}, \tag{5.7}$$

which assumes negligible contribution from the electron-electron scattering. In the following 2T-MD cascade simulations in Fe, we expect to deposit enough energy in the electronic system to notice significant deviations from the linear specific heat (ΓT_e) with respect to the *ab initio* one. In fact, the maximum electronic temperature recorded in 2T-MD cascades of 50 keV/100 keV pka was of the order of 8,000 K/10,000 K (see Fig. 5.15). Furthermore, since we neglect the electron-phonons scattering dependency on the ionic temperature in the electron-phonon estimation (see Sec. 5.2.2), for consistency we should neglect it in the expression for the electronic thermal conductivity, assuming these quantities are related. These approximations can be accounted for in the equation for thermal conduction as follows:

$$\kappa_e = \kappa_0 \frac{C_e(T_e)}{C_e(300\ \mathrm{K})}. \tag{5.8}$$

A limitation of this approach is that it would result in wrong κ_e under equilibrium conditions (i.e. $T_i = T_e$) at $T_e > 300$ K, unlike the expression in Eq. 5.7. In the simulations presented here we have used $\kappa_0 = 80.2$ W/(K m) for Fe. The conductivity would reach its peak at around the Fermi energy ($T_e \sim \epsilon_F/k_B$), when the contribution from the electron-electron scattering becomes dominant. The thermal conductivity would subsequently decrease as the collision frequency would decrease as $1/\tau_{e-e} \propto T_e^{-3/2}$. However, the high Fermi energy of iron ($\epsilon_F = 11.1$ eV) means that this limit is unlikely to be reached and therefore Eq. 5.8 remains valid in the temperature regime considered in the cascades investigated here. An alternative expression for κ_e in the $T_e < \epsilon_F/k_B$ limit, based on the higher order corrections in the Sommerfeld theory, is presented in [229].

For completeness, we briefly describe an expression which would describe the electronic thermal conductivity above the Fermi energy in a situation when electron gas becomes non-degenerate, i.e. in a low density plasma limit. Such an expression was described further in [60, 230] and given as

$$\kappa_e = C \frac{(\vartheta_e^2 + 0.16)^{5/4}(\vartheta_e^2 + 0.44)\vartheta_e}{(\vartheta_e^2 + 0.092)^{1/2}(\vartheta_e^2 + b\vartheta_i)}, \tag{5.9}$$

where C and b are experimentally determined constants, $\vartheta_e = T_e/T_F$, and $\vartheta_i = T_i/T_F$. This expression correctly reproduces the low (Eq. 5.8) and the high temperature limits ($\kappa_e \propto T_e^{5/4}$).

The most commonly used formula for κ_e in the two-temperature laser-matter interaction studies is Eq. 5.7. It is also argued that this form leads to better theoretical predictions of desorption for laser heating experiments [231]. Due to the complexity of some of the expressions and uncertainties involved (none of these expressions can be directly verified by experiments), some authors used the simplest approach and employed a constant electronic conductivity value (as in [76]). Nonetheless, it needs to be noted that a non-equilibrium thermal conduction theory describing a two-temperature state has not been developed yet.

5.2.2 Electron-phonon coupling and electronic stopping

The electronic stopping is a measure of energy loss of a ballistically travelling ion to the electronic excitations per unit distance. This process is agnostic to the motion of other atoms

in a cascade and assumes only small trajectory deviations in electron-ion encounters. The projectile interaction cross-section is predicted to be proportional to its velocity in the Firsov [22] and Lindhard and Scharff [23] models. This feature makes electronic stopping very easy to implement in the MD equations of motion, as it can be represented by a simple damping term proportional to the ionic velocity. The value of this damping term can be estimated from the SRIM [54] code. In the case of iron projectile in iron the damping time (τ_{es}) is obtained from the stopping strength of $\lambda = 0.1093$ eV/Å via $1/\tau_{es} = \chi_{es} = \lambda(\frac{m}{2})^{1/2}$ and is set to $\tau_{es} = 0.984$ ps, where λ is the constant of proportionality [76] in the Firsov [22] ($S_e = \lambda E^{1/2}$) or Lindhard and Scharff [23] ($F = \lambda(m/2)^{1/2}v$) models.

The electronic stopping cutoff energy, E_C, is a practical way of preventing over-damping of the ionic system. In particular, for a system at equilibrium ($T_i = T_e$) the ionic temperature in damped MD would tend to zero. It is therefore assumed that below a certain cutoff the motion of atoms is too correlated to be represented as a projectile through an electron sea and that the electron-phonon coupling (which allows for two-way energy transfer) is dominant. Since there is no theoretical justification for the value of the cutoff, rather than a practical one, it is here assumed to be 8.4 eV [76], 4.2 eV and 0.6 eV [128]. Recently, approximation to Ehrenfest time-dependent tight-binding [128], and real-time time-dependent density functional theory (RT TD-DFT) [91] have not conclusively shown that such a well-defined cutoff exists.

The evaluation of the electron-phonon coupling is more difficult. A value for e-p is typically obtained through low energy laser excitations experiments by fitting the temperature relaxation data to the two-temperature models. Here, we are using the electron-phonon coupling constant reported by Zhigilei *et al.* [29, 227]:

$$G_0 = 5.5 \cdot 10^{18} \text{ W m}^{-3}\text{K}^{-1}, \tag{5.10}$$

and we can translate it to the electron-phonon relaxation time (analogously to Eq. 2.11)

$$\tau_{ep} = C_e(300 \text{ K})/G_0 = 1.404 \text{ ps}. \tag{5.11}$$

The value of $G_0 = G(300 \text{ K})$ is kept constant throughout the simulations for simplicity. In general, it will depend quite strongly on T_e and less on T_i. However, due to electron-phonon coupling inherent uncertainty even at equilibrium conditions ($T_i = T_e = 300$ K) the addition of further complexity in the model is unnecessary. The G_0 dependence on T_e for iron was characterised in [29].

5.2.3 Interatomic potential

We chose a potential based on the many-body embedded atom model (EAM). Details of this potential form are described in Sec. 4.1.4.1. The EAM parameterisation used here was optimised [232] to reproduce the defect energetics, as well as other bulk properties of bcc-iron. It is therefore a suitable and a widely chosen interatomic interaction model for cascade simulations (see 'M07' in [233] for a comparison). The EAM potential was joined to a ZBL form [206] at short distances (< 1 Å). This joining process was calibrated against the threshold

displacement energies [233], which the joined ZBL+EAM potential form reproduces well [72, 234]. The details on the ZBL form are presented in Sec. 4.1.4.3.

5.2.4 Assumptions of the two-temperature model revisited

The electronic stopping process occurs when the ionic projectile travels ballistically, whereas the e-p coupling applies to small displacement motion of ions. However, the exact boundary between these processes is not clearly defined from the modelling perspective. In the two-temperature theory, the e-p coupling should be effective assuming both electronic and ionic systems are thermalised, i.e. have achieved equipartition of energy and have a defined, roughly uniform, temperature. The electron-electron scattering time is very short, of the order of $\tau_{e-e} = 10$ fs, and so an electronic temperature can be assumed at all times. However, the thermalisation time of the ionic system in a cascade scenario is not known *a priori*. We have looked at the convergence of the kinetic and potential energies of the ionic system for two exemplar simulations (with friction) at 200 keV (see Fig. 5.2). We note that the ionic system thermalises at around 0.3 ps, and it is past that time that the e-p should presumably become effective. There are several other assumptions of the 2T model, as applied to cascade simulations, which can be challenged, however handling the non-thermalised ions remains the most significant one. Others include the usual 2T model criticism, such as the applicability of the diffusion processes on a nanometre space-scale and to such high electronic temperatures.

The ionic system thermalisation time of 0.3 ps for a 200 keV pka cascade remains an estimate and it is still not clear which of the following modelling options describes the physical process correctly:

1. Apply e-s above an energy cutoff and e-p when both systems locally (i.e. in a temperature voxel) thermalise. This is tricky to implement, as it is hard to obtain an exact condition for thermalisation for several tens of atoms in a temperature voxel. Also, as different criteria are used for the e-s and e-p both could be active at the same - it is debatable if this is a physical scenario. A simpler alternative to this could be a global time cutoff thermalisation time, which can be tuneable parameter,

2. Apply e-s above an energy cutoff and e-p below it. This is computationally easy to implement and excludes e-s and e-p processes overlap.

In this chapter, we will be exploring the effect of e-p and e-s using both methods on the residual radiation damage in α-Fe.

5.3 Simulation considerations

5.3.1 The simulation setup

All simulations were performed with NPT pre-equilibrated (Nose-Hoover NPT ensemble at 300 K, 1 atm for a minimum of 30 ps) bulk iron with periodic boundary conditions. A variable time-step, Δt_{MD}, with a maximum of $\Delta t_{MD} = 1$ fs was used to simulate the atomic part of

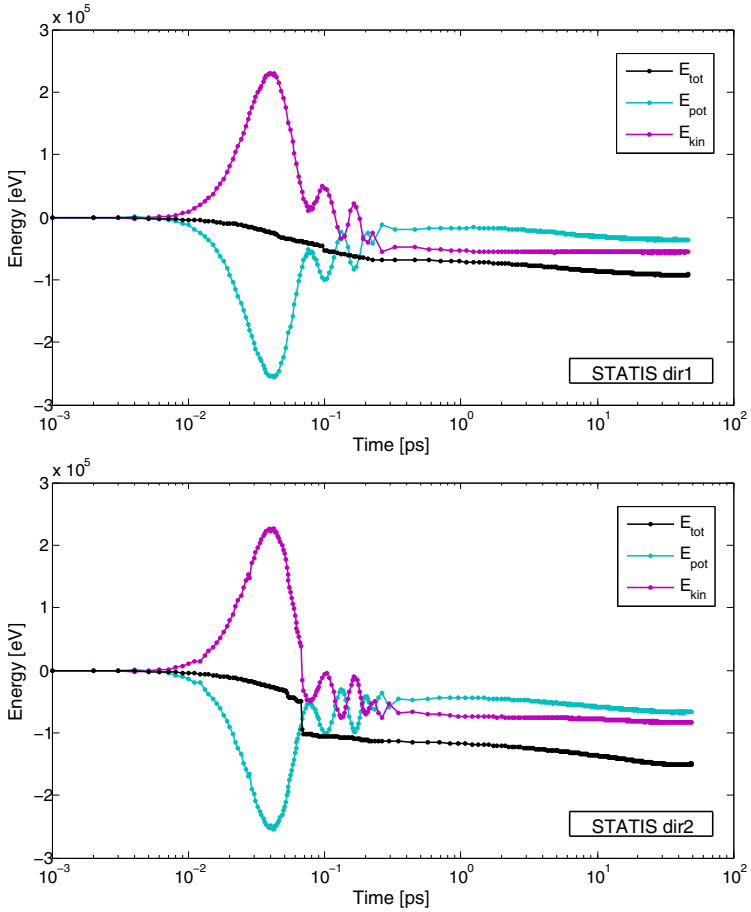

Figure 5.2: Kinetic and potential energies evolution in two exemplar 200 keV pka events. The 'global' thermalisation time for both can be assumed to be $\tau_{i-i} \sim 0.3$ ps.

the cascade, to correctly account for the initial large velocities in the system. The electronic system was evolved with a variable time-stepping algorithm too, which depended on the local T_e gradients. The time-step of the finite difference solver (Δt_{FD}) was typically a few times smaller than for the ionic one. All simulations were run for 55k steps, which corresponded approximately to a simulation time of $t = 45$ ps.

The following sets of simulations were performed, each of which consisted of 20 or 16 runs for 50 and 100 keV pka conditions, respectively.

1. 2M atoms, 50 keV pka, 6× friction MD variations (3× reduced impact energy, 3× friction E_c cutoffs),

2. 4M atoms, 50 keV pka, 9× different 2T-MD conditions (various friction E_c and thermalisation τ_{i-i} cutoffs),

3. 8M atoms, 50 keV pka, 3× different types of boundary conditions for NVE runs (periodic, 2× variation on the thickness of the boundary thermostat),

4. 16M atoms, 100 keV pka, 5× simulations types (1× NVE, 2× friction MD runs, 2× 2T-MD runs).

The projectile was initialised to travel in random directions (randomly generated set of vectors, which were identical across the simulation sets). The projectile was selected to be the middle atom of the simulation cell for 50 keV runs, and around the 2/3 point on the diagonal of the simulation cell in the case of 100 keV runs (in which case the projectile was fired in a random direction into one of the octants). It needs to be noted that only a few of the collision cascades would occasionally wrap around the simulations cell (typically less than 1 in 10 runs), which shows that the simulation cell was of a suitable size to contain the events.

The 200 keV and 500 keV simulation runs (both friction and standard NVE ones) were composed of 100M and 500M atoms, respectively. Stochastic boundary conditions of 10 Å thickness and set to 300 K were used. Only four crystallographic directions were simulated: <1.2,1.2,1.8>, <1.3,1.2,1.8>, <1.6,1.7,1.8> and <1.6,1.9,1.0>. These were manually selected to avoiding channelling, unlike in the previous case.

In the two-temperature runs, the electronic system was three times bigger than the ionic one in all directions, so that the ions are effectively embedded in the sea of electrons, and thus the electrons can effectively carry away the energy outside of the MD cell. For instance, in the 16M atom simulation (554 Å box size), we used 55 T_i and 165 T_e voxels across each dimension. Robin's boundary conditions (see Sec. 4.3.3) at 300 K were applied on all sides of the continuum T_e solver. Such a configuration is schematically presented in Fig. 4.5.

5.3.2 Measuring defects, displacements and defect clusters

To analyse the damage produced in a collision cascade we keep track of the time evolution of defects and displacements. Displacements (N_{disp}) are atoms that move a certain distance (d) from their initial position at time $t = 0$, in this case taken to be $d = 0.75$ Å. This method quantifies the overall (cumulative) damage introduced; however some of it can recover on the picosecond and longer timescales due to recombination effects. Hence, we also consider 'defects' (N), which are either interstitial or vacancies. Note that in this notation $N = 2N_{FP}$, where N_{FP} is the number of Frenkel pairs. In the model, interstitials are defined as atoms that are closer to any of the crystalline positions, which are already occupied, by a distance d. Analogously, a vacancy is a crystalline position, for which no atoms exists closer to it than $d = 0.75$ Å. Keeping track of both displacements and defects allows us to quantify the maximum damage, defect recombination dynamics and the resultant primary radiation damage formation.

While taking $d = 0.75$ Å as a 'sphere' cutoff value is arbitrary, we note that the dynamics recovery is not very sensitive to d, provided that it is in a sensible range. Too small ($d \sim 0.2$Å) would be affected by thermal fluctuations, while too large ($d > 1.0$ Å) would not identify the defect atoms correctly, as this value would be too close to the nearest neighbour distance. However, two complications arise when using a method with an arbitrary and non-standardised cutoff for defect analysis. Firstly, the value of d can vary across different materials, as it is related to the crystal structure and the lattice parameter. It also differs across literature even for the same materials, making a meaningful comparison with previous modelling results next to impossible [72]. Secondly, while a cutoff works fine for point defects, it identifies crowdions (a

long chain of atoms along a lattice direction containing an additional atom - a single net point defect) incorrectly, as a line of interstitials, whilst in reality it is just one 'net' defect inserted into a particular crystal direction. Furthermore, the gross number of defects (i.e. the sum of both vacancies and interstitials in a cluster) reported for a crowdion is highly dependent on the cutoff d chosen. More sophisticated methods, such as Wigner-Seitz (W-S) decomposition, exist (see Fig. 5.3). However, while W-S correctly computes 'net' defects, there is significantly more computational expense associated with it.

Clusters are composed of defects that are closer than two nearest-neighbour (2nn) distance (plus a 0.2 perturbation), $d = 3.44$ Å in α-Fe. This criterion (2nn) is very common across literature [71, 235], however other criteria, particularly for vacancy clustering, have been reported (from 1nn to 4nn) [72]. Defect clustering and related analysis was performed with an in-house built code.

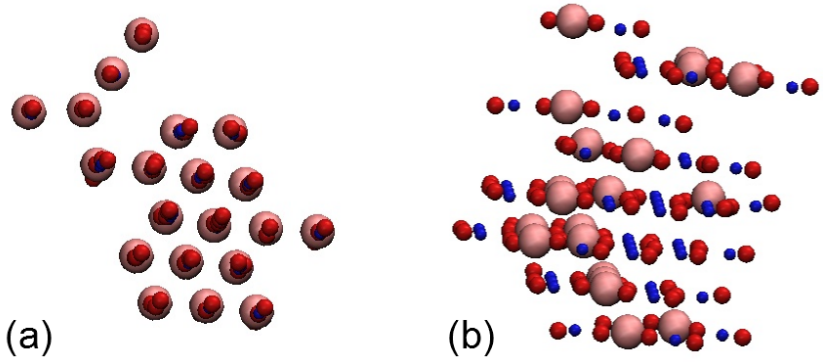

Figure 5.3: Comparison of Wigner-Seitz and sphere defects analysis methods on an exemplar defect structure (a set of crowdions) at two projections: (a) (-111) and (b) (-1-11). Interstitials (vacancies) identified by the sphere method are indicated in red (blue), while the W-S interstitials are in pink.

5.4 Results for 50-500 keV cascades in Fe

5.4.1 Stable defect distribution

5.4.1.1 Trends with cascade energy (50-500 keV)

We first analyse the point defect production for 50-500 keV cascades run with the friction cutoff of $E_c = 8.4$ eV. We compare the trends in FP production to the data available for NVE runs [71], where the electronic effects are taken into account at the level of reduced cascade energy. While some simulation differences exist between these data sets (different cell sizes, boundary conditions, initial temperature and potentials) three interesting points can be noted. Firstly, the N_{FP} production yield is comparable with the 100 keV runs producing the same number of FPs, despite the differences in the simulations. However, the defect production trend (50-200 keV) with the cascade energy is significantly different, with the friction MD simulation runs producing defects at a higher rate with cascade energy than the NVE runs

(see Fig. 5.4). This could be attributed to the differences in the available damage energy in both cases; however the exact processes require further investigation. Finally, the trend at the highest energy achieved (500 keV) is different - defect production rate slows down with cascade energy. This could be attributed to the reduced sub-cascading occurring at such pka energies, yet further studies (including a quantitative measure of sub-branching) are needed to verify such a conclusion.

We also examine the maximum cluster sizes (counting the net defects only) for 200 keV and 500 keV runs and compare this data to [233]. While the defect clusters that are produced in 200 keV runs are greater than the ones reported in literature for lower energies (< 100 keV), we notice no significant trend with the cascade energy (see Fig. 5.5). In fact, the maximum cluster sizes seem to saturate at around 200 keV, however such conclusion would need to be validated with better statistics, as such large clusters are rare-events and one would need typically a large number of runs to examine such trends. Some example figures of defect structures found are shown in Appendix B.

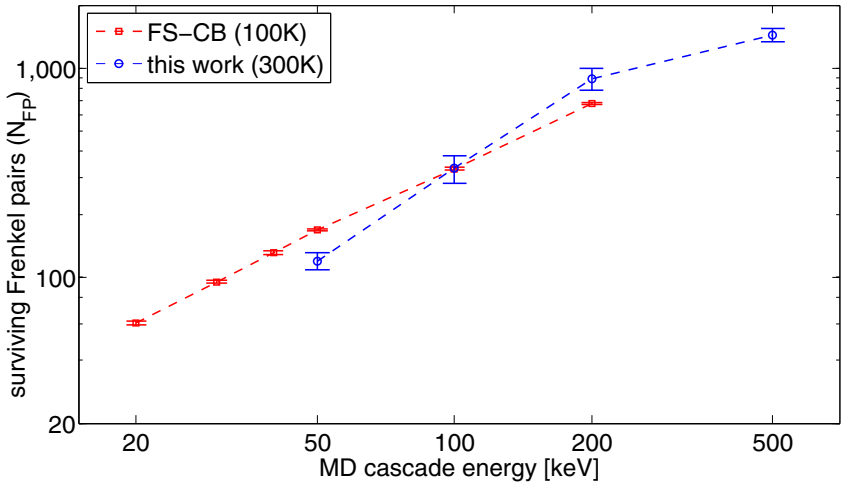

Figure 5.4: Number of FPs as a function of cascade energy; a comparison of trends for two types of runs: (i) (red) Finnis-Sinclair potential with no friction [71] and (ii) (blue) the current work with a friction term and $E_c = 8.4$ eV. The friction simulation runs give much steeper increase in defect production with cascade energy and the 500 keV data show a change of a trend. Notable differences in the simulation setups exist, however both produce comparable results, particularly around 100 keV pka.

5.4.1.2 The impact of electronic stopping (50-100 keV)

We have analysed the impact of the electronic stopping (e-s) cutoff on the number of residual Frenkel Pair (FP) defects and defect clustering. Despite vast cascade data for Fe in literature, such rigorous parameter sensitivity study has not been performed to date.

We have simulated twenty 50 keV impacts from random directions from the centre of the cell at three different electronic stopping cutoffs: 8.4 eV, 4.2 eV and 0.6 eV in a 2M atom MD cell. The first two cutoff values are related to the cohesive energy of iron ($\varepsilon_{coh} = 4.28$ eV), and were used in [65, 236]. The 0.6 eV value was proposed by le Page *et al.* [128]. We compare

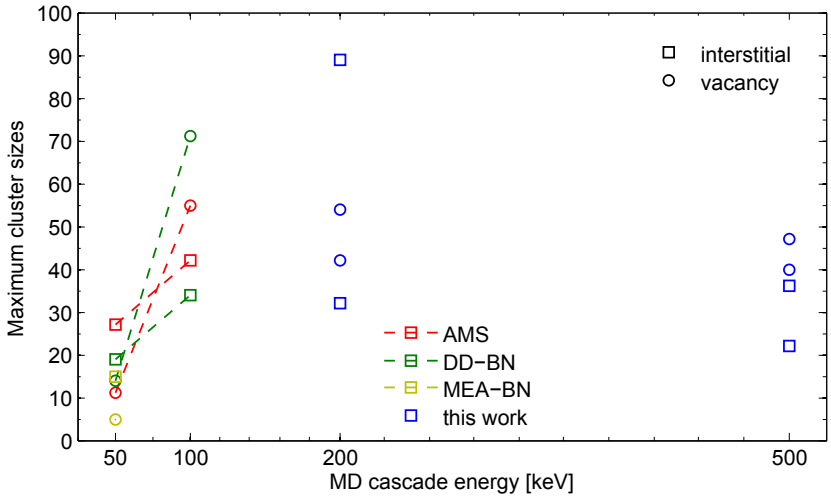

Figure 5.5: Maximum cluster sizes as a function of cascade energy. 200 and 500 keV runs do produce slightly greater clusters, however no significant trends can be seen, which could also be attributed to the poor statistics due to the rare-event nature of the large cluster generation. AMS, DD-BN and MEA-BN data are obtained from [235] (the same notation).

these results to twenty 50 keV 'standard' NVE ensemble cascades and cascades with reduced pka energies of 45 keV and 34 keV. These correspond to the atomistic stopping power values obtained from SRIM and the Robinson's approximation to the LSS theory [24, 71] for a 50 keV impact, respectively. We emphasise that each simulation used the same set of twenty random directions for a meaningful comparison.

Figure 5.6 shows the average residual FPs number for the different stopping power cutoffs considered. An almost perfectly inverse linear relationship between the defect number and the e-s cutoff is apparent. This is due to the fact that lower e-s cutoff cascade lose more energy to the electronic system, which means that the transient thermal spike temperature is lower and thus defect recombination (annealing) is reduced. This can be confirmed by examining the temporal evolution of the global average (ionic) temperature evolution (treating it as a proxy for the local temperature evolution) for a set of exemplar simulations (Fig. 5.7). Indeed, lower cutoffs lead to quicker reduction of the ionic temperature and subsequent equilibration to a lower temperature value, with the former effectively quenching the defect structures thereby inhibiting recombination. All simulations equilibrated to temperatures higher than 300 K prior to impact. Defect annealing can be calculated from the difference between the peak number of FP recorded at any time-step and the number of FP in the final configuration. Table 5.1 presents defect recombination averaged over all 20 runs and points to a lower recombination rate for lower e-s cutoffs, as expected.

Another interesting feature apparent from Fig. 5.6 is that the 8.4 eV and 4.2 eV cutoff friction MD runs produce approximately the same number of defects as 45 keV cascades run in an NVE ensemble. The energy losses from these two friction MD simulations (see Tab. 5.1) are approximately 8 keV. It is around the 5 keV assumed to be lost to electrons as calculated with SRIM.

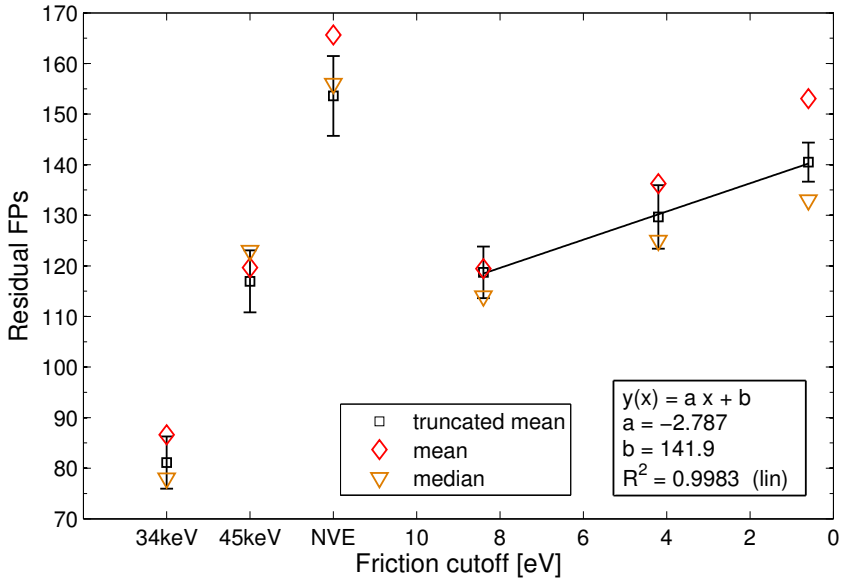

Figure 5.6: Average residual FP defect number versus electronic stopping friction cutoff. 45 keV corresponds to the atomic stopping power from SRIM for a 50 keV pka, while 34 keV corresponds to the one obtained via LSS theory (Robinson's approximation). Residual Frenkel pair number increases linearly with decreasing friction cutoff, however no friction condition (i.e. NVE, where cutoff $E_c \to \infty$) produces the largest number of defects in the set. The linear fit was performed on the truncated mean, which removes two outliers (10%) from a given data set. The error bars indicate standard error in the truncated mean.

The effect of local quenching of the cascade, and hence more efficient defect production, seems more dominant than the reduced damage energy. This is illustrated by the simulation runs with 0.6 eV cutoff, where as much as 20.5 keV is lost to the electrons (Tab. 5.1) and the defect yield is significantly higher than in the runs with 8.4 eV and 4.2 eV e-s cutoffs. However, should this amount of the energy be subtracted from the initial impact ion (approximately the case of 34 keV pka), the damage efficiency can be almost halved. This difference is due to the very low defect recombination rate for a heavily damped system at the e-s cutoff of 0.6 eV. This clearly illustrates that the correct treatment of the electronic energy losses is cardinal for a predictive primary radiation damage framework.

Following this line of argumentation, NVE cascade simulations should produce an even lower number of defects than for the 8.4 eV cutoff, while in fact more FPs are produced for NVE than for 0.6 eV. This could occur for two reasons: (i) significantly more energy is deposited in the NVE than in the friction MD case. Thus, despite higher transient temperatures, which favour recombination, more damage is effectively produced. This is somewhat in conflict with the dominant effect of ionic temperature on defect recombination discovered for friction MD runs; (ii) since the initial projectile atoms motion is not damped, atoms travel farther. This leads to increased peak damage production and thus increased primary damage creation efficiency. The latter hypothesis can be validated by computing the radius of gyration of cascades. Since branching, which occurs in the NVE case more often, does not favour recombination it seems that the hypothesis (i) is more likely.

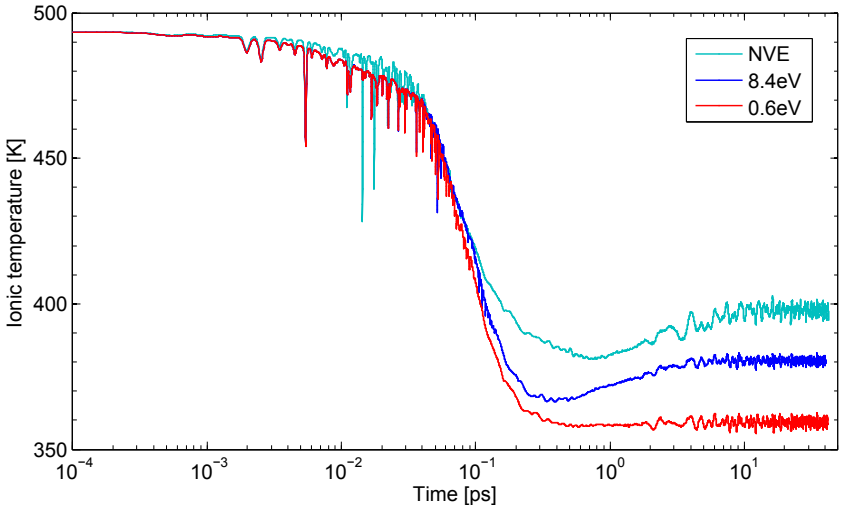

Figure 5.7: Temporal ionic temperature evolution for an exemplar 50 keV cascade with varying friction cutoffs. NVE denotes no cutoff.

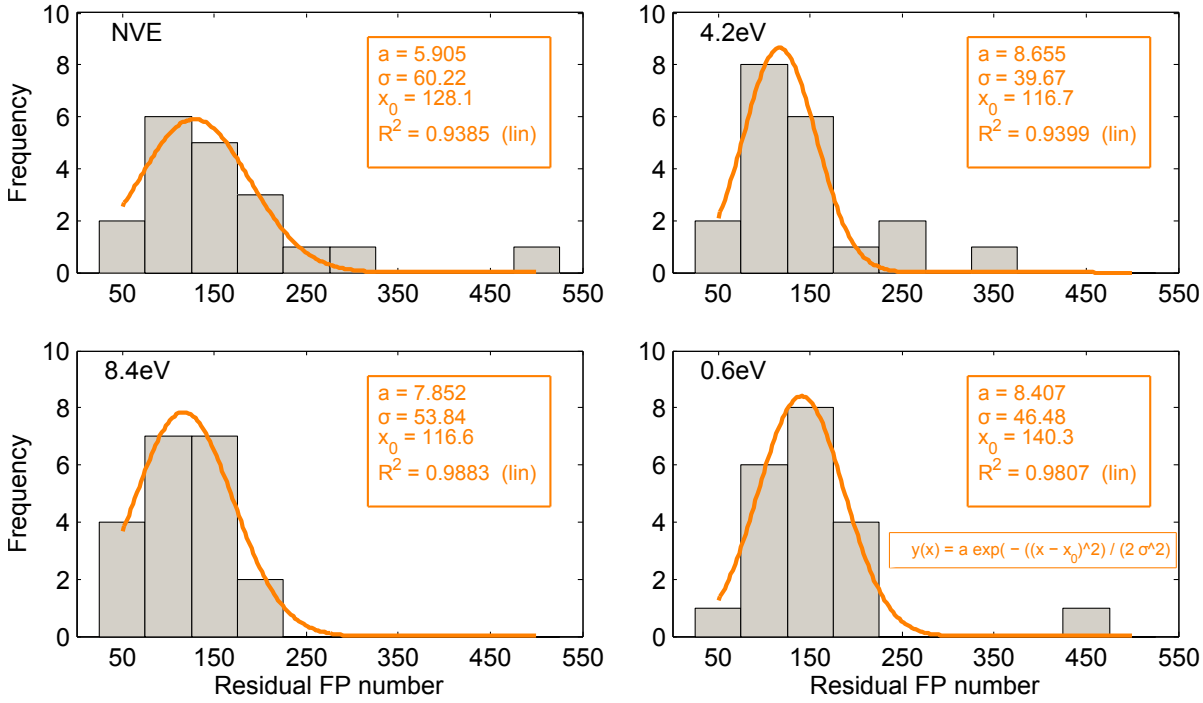

Figure 5.8: Histograms of residual FP distributions for NVE and three different friction cutoffs in 50 keV cascades. Gaussian fits are indicated by solid lines.

Figure 5.6 reveals another interesting feature, which is the high impact of outliers on the average defect count, as can be deduced by comparing mean, median and truncated mean. The most striking example is the $E_c = 0.6$ eV case, where both mean and median are far outside the error bars of the truncated mean. Firstly, this indicates that a statistically meaningful number of runs are required to make inferences about the impact of the individual parameters in the model. Secondly, it shows that when computing the primary radiation damage formation (as an input to kinetic Monte Carlo modelling, for instance), care must be taken to include

the impact of such outliers, as these can significantly distort the data. The $E_c = 0.6$ eV set contains a run that produced more than 450 FPs, as seen in Fig. 5.8, which is beyond 5σ from the mean value of 153. Such an outlier is generated because of an occasional large cluster production. Such clusters, which are typically composed of a parallel set of crowdions, are incorrectly identified by the sphere defect analysis criterion as a set of line defects. In fact, crowdions are composed of one net defect, as identified by Wigner-Seitz defect analysis - a point further discussed in Sec. 5.3.2.

Lastly, a consistently lower median than the (truncated) mean implies skewness in the distribution and perhaps the assumption of normally distributed defects needs to be readdressed. Nonetheless, for simplicity, we describe the residual FP defects distribution with a normal distribution ($R^2 > 0.93$ in all cases; see Fig. 5.8), usually around trimmed mean, which removes two outliers from each side of the distribution. This reduces non-normality in the data and hence is a somewhat more robust statistical tool.

Table 5.1: The FP recombination and electronic energy losses statistics for two simulation types: reduced pka damage energy (left side) and 50 keV pka cascades with varying friction cutoff E_c (right). The value in brackets represents the standard error in the mean for the 20 simulations. The energy losses in the pka set (NVE) represent the numerical accuracy in the energy evolution.

quantity		pka			E_c	
cascade set	34 keV	45 keV	50 keV	8.4 eV	4.2 eV	0.6 eV
Final FP	87(13)	120(14)	166(23)	119(11)	136(16)	153(17)
Recombined FP [$\cdot 10^4$]	6.2(0.4)	10.5(0.8)	11.2(1.1)	8.1(0.6)	7.6(0.5)	4.7(0.3)
Energy loss [keV]	0.2(0.05)	0.2(0.1)	0.1(0.02)	7.4(0.2)	8.4(0.2)	20.6(0.3)

5.4.1.3 The impact of electron-phonon coupling (50-100 keV)

The electron-phonon coupling, depending on the way it is handled in the model, can induce two competing effects in the cascade dynamics: (i) increased cascade quenching, when e-s is not effective, (ii) or increased recombination rate due to annealing of the defects with the energy coming from the hot electrons. The strength of these effects would depend on the dynamics of the e-s/e-p interplay, and the competition between the energy diffusion and the e-p coupling. The impact of the inclusion of the e-p coupling on the primary defect production in cascade simulations is examined. Firstly, the final N_{FP} discrepancy, when different methods of accounting for the electronic effects are included, is emphasised. Figure 5.9 presents the number of FPs produced when four different simulation methods are used: (i) NVE, 50 keV pka projectile, electronic effects are not included; (ii) NVE 34 keV, projectile has a reduced initial energy due to electronic effects; (iii) f (friction) MD runs with the electronic energy loss simulated as a damping term in MD; (iv) 2T-MD model, which includes both e-s and e-p

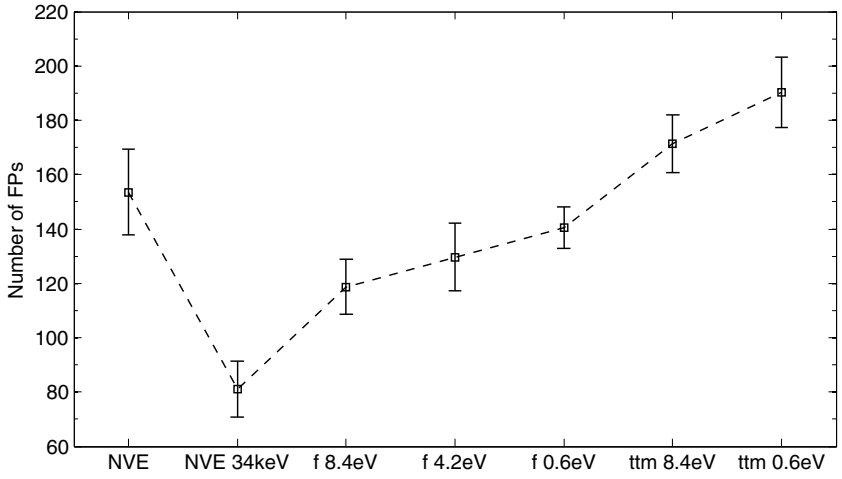

Figure 5.9: Average residual FP defect number versus the simulation type for 50 keV pka events. A particular set of 2T-MD runs can produce up to 3 times more defects than a cascade based on the reduced cascade energy assumption (34 keV pka set). Dashed line is a guide to the eye.

coupling effects. The discrepancy in the results for 50 keV pka is great, with the one of the models producing three times more defects than the lowest yield simulation set (see Fig. 5.9).

For a 50 keV pka, we have run a set of simulations with two e-s cutoffs: 8.4 eV and 0.6 eV, but with varying ways of handling the e-p coupling, i.e. different activation time t_{ep}. Our results indicate that the defect production yield peaks around $t_{ep} \sim 0.4$ ps, and that the inclusion of the e-p coupling increased defect production with t_{ep} tested up to 1.0 ps. This could be attributed to enhanced quenching of the cascade due to the additional energy loss channel to the electrons. The switch condition (denoted 'sw' in Fig. 5.10), which activates the e-p coupling only when e-s is deactivated in a particular temperature cell, gives a slightly smaller number of defects. This can be explained by the additional annealing coming from the e-p interaction at the end of the defect formation. However, it needs to be noted that this difference is not very significant. For the 8.4 eV cutoff (indicated by red line in Fig. 5.10), a similar effect happens - the e-p coupling activation at $t_{ep} = 0.2$ ps increases the defect yield. This, again, can be attributed to the enhanced quenching of the cascade. Interestingly, and contrary to the 0.6 eV case, the switch condition produces more defects. This is a manifestation of the increased cascade quenching under 8.4 eV cutoff. In the switch conditions we have used two different formulae for the electronic thermal conductivity: the ones derived in Eq. 5.8 and a constant one noting that the choice does not have an impact on the final results.

We move onto the comparison of 50 keV and 100 keV cascade runs in 2T-MD and friction-only setups. We find that the behaviour for the 100 keV pka is unchanged, as can be seen in Fig. 5.11, with the exception of the friction MD run with an 8.4 eV cutoff, for which no definitive conclusion can be drawn due to a large statistical uncertainty. We therefore conclude that similar trends as in the 50 keV pka case persist at 100 keV pka.

We note that for the 100 keV pka runs the LSS theory [24, 71] predicts a cascade energy of 62 keV, whilst SRIM gives a nuclear stopping power of 85.1 keV. The average energy losses

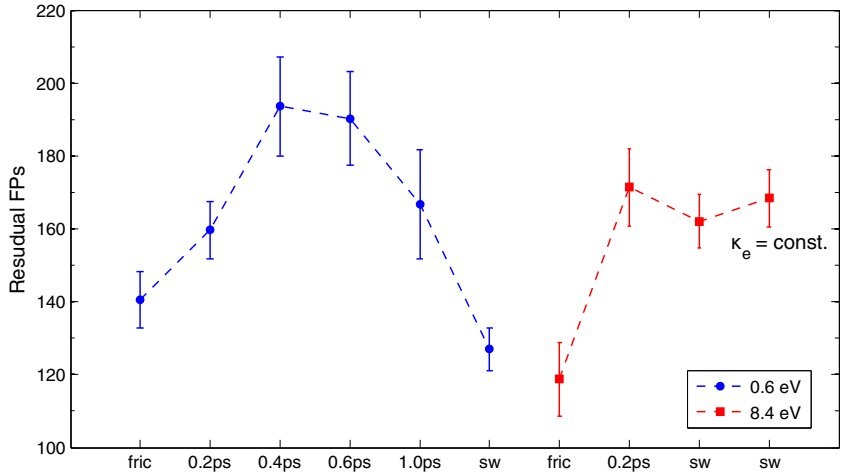

Figure 5.10: Average residual FP defect number versus the electron-phonon model type for 50 keV pka events with two friction cutoffs (E_c): 8.4 eV (left side) and 0.6 eV (right). Time on the x-axis denotes the e-p activation time, t_{ep}, and 'sw' denotes the 'switch' condition, where the e-p is activated only when the e-s is inactive. Dashed line is a guide to the eye.

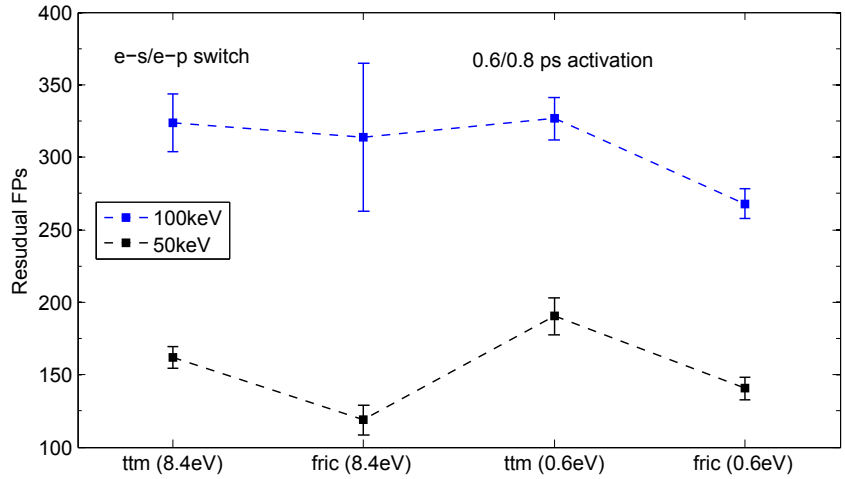

Figure 5.11: Comparison of FP defect number production in 50 keV and 100 keV pka cases for four different models types. Two E_c cutoffs: 8.4 eV (left side) and 0.6 eV (right) types are presented. The 2T-MD model was run either with the e-s/e-p switch condition ($E_c = 8.4$ eV) or with the activation time t_{ep} for e-p. The trends in N_{FP} production across model types are consistent between 50 keV and 100 keV pka cascades. Dashed line is a guide to the eye.

in our friction cascade for 8.4 and 0.6 eV cutoffs were 17.5(8) and 44.7(6) eV, respectively.

5.4.2 Cascade evolution and structure (50-100 keV)

By examining the defect time evolution during a collision cascade, the conclusions regarding increased defect quenching/annealing can be substantiated. In the case of the 50 keV pka events we see that the lower E_c indeed reduces the peak number of defects generated through increased quenching, as can be seen in Fig. 5.12. This process is visualised for an example collision cascade in Fig. 5.13, where it is apparent that the maximum size of the cascade is

lower at $t = 0.75$ ps in the 0.6 eV case. This increased quenching process from low E_c typically results in higher primary damage formation, as a colder ionic system leads to a lower defect recombination rate.

For 50 keV pka runs we have also compared the defect evolution at $E_c = 8.4$ eV and 0.6 eV, when the electron-phonon coupling was enabled once the electronic stopping was not effective. It can be seen from Fig. 5.14 that less peak defects are produced in the $E_c = 8.4$ eV 2T-MD case, which can be explained by the additional electronic energy loss coming from the e-p process from the atoms with the kinetic energy up 8.4 eV. This peak defect reduction is not so pronounced in the case of $E_c = 0.6$ eV, where the defect evolution differences between damped MD and 2T-MD are rather small. This is because the e-p coupling becomes effective relatively late in the cascade formation, when the primary radiation damage formation is almost stable.

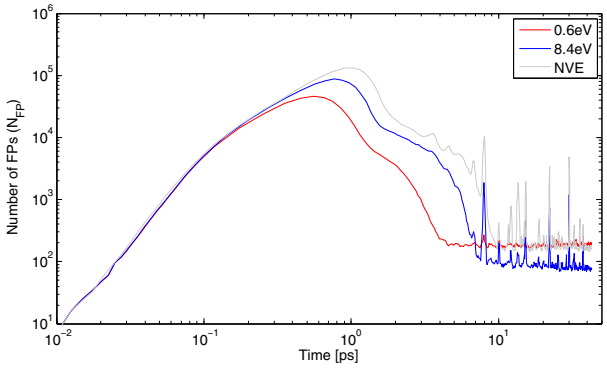

Figure 5.12: Defect evolution for an exemplar 50 keV pka cascade at three different electronic stopping cutoffs. Peak defect generation is significantly reduced with reduced cutoff and the cascade dynamics is the same until 0.5 ps. The spikes that are generated past $t = 10$ ps are due to a shock-wave reentering the simulation cell. Note that this does not happen for $E_c = 0.6$ eV, where the system is damped most heavily. Such shock-waves were a rare occurrence in the 2M atom simulations.

The maximum electronic and ionic temperatures (in a voxel) for 100 keV pka for the cases of $E_c = 8.4$ eV and 0.6 eV are presented in Fig. 5.15. The dynamics of these different sets is very similar, however only two exemplar runs are presented. There are very distinct features in the temperature behaviour. Namely, we see that the T_e and T_i relax around 5-10 ps and that the initially very high $T_i \sim 10^7$ decreases rapidly until 0.2 ps, after which it decreases at a much slower rate. The electronic temperature does not exceed 10,000 K implying that the approximation of a ground-state potential most likely still holds (this question is addressed in more detail in chapter 6).

5.5 Discussion

Let us begin the discussion with a few technical remarks on point defect analysis. Significant defect outliers occur in any defect sets presented here (see Fig. 5.8). It is difficult to establish whether these outliers are 'physical' (i.e. rare events), or just an artefact of the way the defects are measured. The 8M atom 50 keV pka set (not shown in Fig. 5.8) is a particularly good

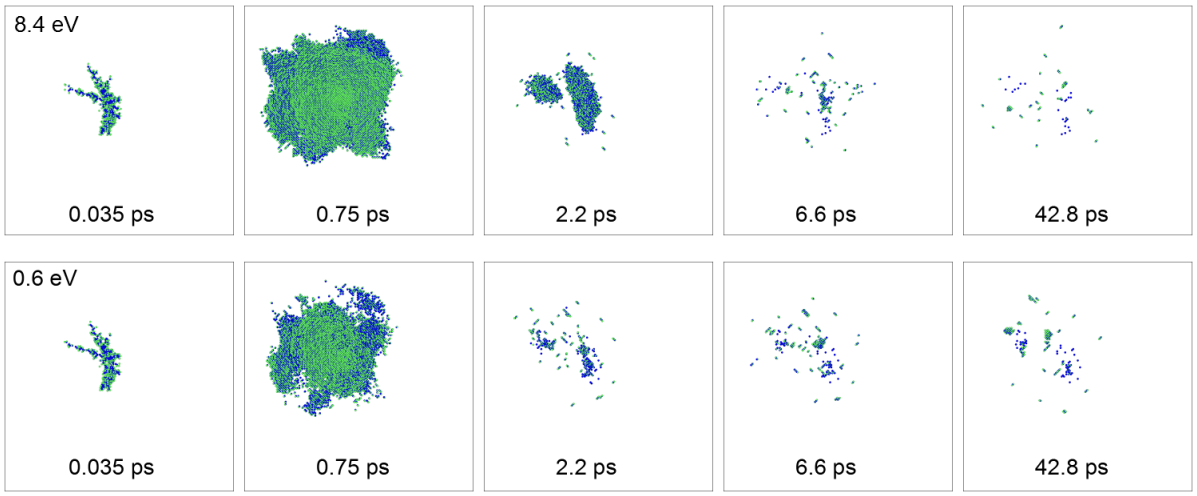

Figure 5.13: Comparison of defect evolution of an exemplar 50 keV pka cascade for two friction cutoffs. Increased damping manifests itself in smaller peak damage production ($t = 0.75$ ps), but larger residual damage ($t = 42.8$ ps).

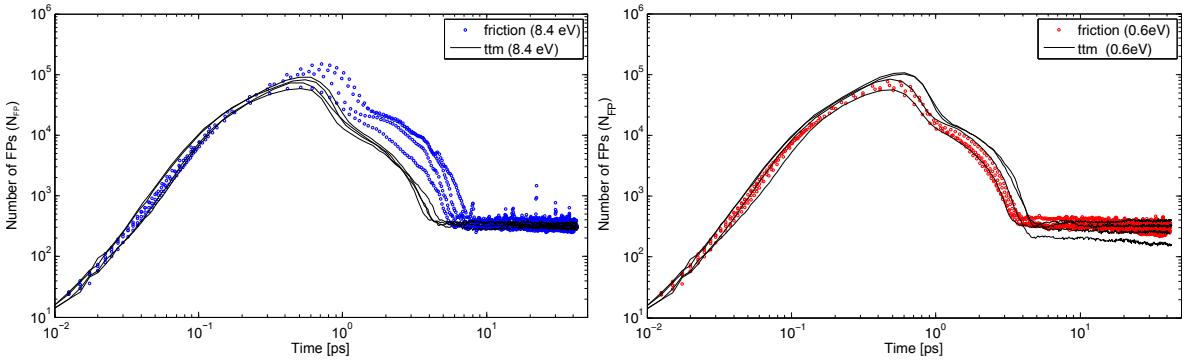

Figure 5.14: Defect evolution for an exemplar 100 keV pka cascades with $E_c = 8.4$ eV (left panel) and 0.6 eV (right), and varying e-p activation. The additional quenching from the 2T-MD model in the $E_c = 8.4$ eV case affects the peak defect generation and overall cascade dynamics, while the impact of the e-p in the $E_c = 0.6$ eV case is rather small.

example with an average $N_{FP} \sim 155 \pm 20$, and with one $N_{FP} = 825$ outlier produced. The Wigner-Seitz (W-S) method would be probably more consistent across runs, yet this remains to be validated. Fig. 5.3 shows the defect count difference when using a sphere model or the W-S method. An appeal of the W-S is that the method does depend on any adjustable parameters (such as the "sphere radius", d), which could make the literature comparison (with a scatter in the reported d) easier, and would therefore be preferred.

The number of defects in all simulation sets are not normally distributed - the median is typically smaller than the mean, and hence defects distribution is skewed to the right. This could be, again, an artefact of the way the defects are measured, or potentially imply a discovery of an important statistical feature of defects distributions.

In 50 keV pka (2M atoms) the lower the friction cutoff, the higher the defect yield; no cutoff (NVE 50 keV pka projectile) produces the highest defect yield, whereas NVE runs with

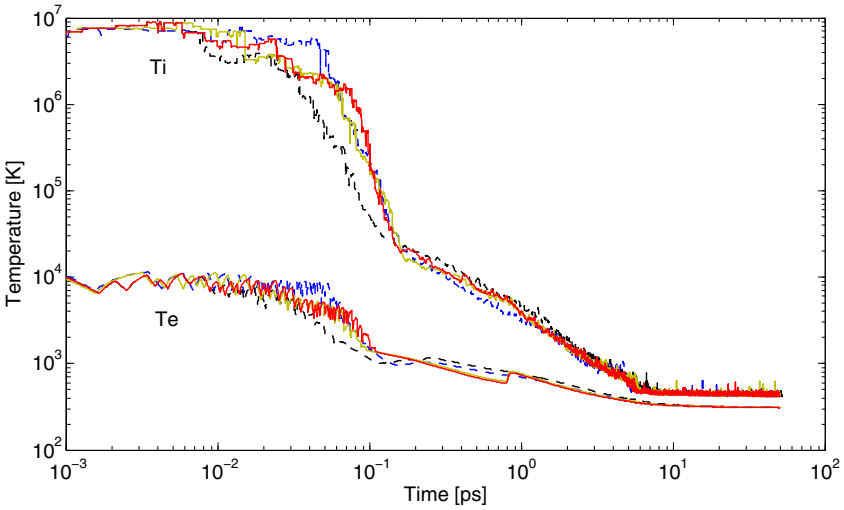

Figure 5.15: Time evolution of electronic and ionic temperatures for two sets of 100 keV pka cascades with different friction cutoffs; solid line: $E_c = 0.6$ eV, dashed line: $E_c = 8.4$ eV.

34 keV pka (the lower energy is supposed to correspond to the energy loss to electrons in the approximation to the LSS theory) produces much less defects than any of the friction MD simulation. For 100 keV (16M atoms), however, the trend seems to be reversed: higher cutoff corresponds to greater defect production, although the results are not statistically significant.

The number of FPs for 50 keV pka simulations has been rigorously tested. The runs are unaffected by neither the size of the cell (and hence the occasionally occurring reentering shock-wave as tested for 2M to 8M atom cells), nor the presence or size of the boundary thermostat (tested 0 Å, 2 Å, and 14.5 Å).

The conclusions regarding the electronic stopping cutoff are quite striking. Depending on the way we handle the energy loss (by subtracting the energy from the projectile, or changing the low velocity cutoff in the electronic friction term), statistically different results can be achieved. This implies that (i) more work needs to be done in understanding the behaviour of ion-matter interaction at low velocity to implement the correct physics in MD, (ii) because of the shown parameter sensitivity the collision cascade research should continue, as there exists a large scatter in the primary radiation damage results.

The effects of electron-phonon coupling are potentially as important, and yet significantly understudied. For the 50 keV pka simulations, the 2T-MD model with the activation time cutoff for the e-p coupling at (or before) the peak damage, produces significantly more damage than the friction MD runs (for both $E_c = 8.4$ eV and 0.6 eV). This can be attributed to the additional quenching at the radiation damage production stage. However, in the 0.6 eV cutoff case when the e-p is enabled only when e-s is not active in a given ionic temperature voxel, the resultant defect number is actually slightly smaller, but not in a statistically significant way. This is perhaps because of the extra defect annealing from e-p scattering. In the 8.4 eV cutoff scenario, the e-p coupling only contributes to the increased defect quenching and hence greater defect production. This is independent of the electronic thermal conductivity model used (a constant one or Eq. 5.8). This study, therefore, shows that when the e-p scattering

is included, care should be taken on how to handle its activation, as it may affect the results significantly. Probably the "switch" method (i.e. either the e-p or the e-s process) is the most physical, but in such case determining the projectile energy, when this switch occurs, can have an effect on the results too.

There are obvious simulation limitations, which may impact the conclusions that were drawn here. In particular, the use of the ground state interatomic potential at high local electronic temperatures (particularly for cascades with pka greater than 100 keV that most likely produce $T_e > 10,000$ K) could lead to different number of defects and most likely slight changes to the cascade dynamics. This is because the changes in the interatomic potential surface would provide the atoms with more kinetic energy, which could in turn (depending on the excitation relaxation time) lead to greater defect generation and/or greater recombination. The lack of magnetism is another, and potentially a more significant, downside of the simulations in Fe. The collision cascade simulation could excite spins selectively and affect the ionic dynamics. However preliminary static *ab initio* calculations in Fe show that all magnetisation disappears at an electronic temperature of $T_e \sim 0.5$ eV [2]. Input from advanced models based on the Ehrenfest dynamics (such as RT TD-DFT) could allow us to examine the complicated interplay between the e-s and e-p processes in the future, and hence to point to an energy cutoff between these, which would thus improve the 2T-MD simulations presented here. (An application of RT TD-DFT method to study cascades is presented in [91]). Future work should include an analysis if the different cascade dynamics models (2T-MD versus friction MD runs) produce different defects clusters.

5.6 Summary

In summary, we have performed a series of collision cascade simulations in α-Fe for pka energies of 50-100 keV. We have compared the standard cascade simulations with the ones that implement the electronic stopping as a damping term in MD and ones, which also include the e-p coupling effects in the two-temperature model formalism. We have also analysed very high energy friction MD cascades of 200-500 keV pka, which represent one of the highest pka energies reported to date.

While we cannot make a recommendation, from a theoretical standpoint, on the exact model of the electronic stopping or electron-phonon coupling, we have proven that the resultant primary radiation damage is very sensitive to the choice of the electronic effects treatment - particularly to the value of electronic stopping energy cutoff and the activation method of the electron-phonon coupling. This represents the first rigorous study of such type, which clearly shows that there are still open questions in collision cascades studies, which need to be addressed in order to build a comprehensive and predictive radiation damage simulation model.

[2] This is higher than and distinct from the Curie temperature at electron-ion equilibrium.

Chapter 6

Laser photo-excitation

☐ **Attribution:** This project has been undertaken in collaboration with Y. Giret, A. Shluger (UCL) and the experimental group at the Institute of Scientific and Industrial Research (ISIR) in Japan. All of the experimental work has been carried out by our collaborators. The *ab initio* parameterisation of the 2T-MD model has been performed by Y. Giret. The 2T-MD code development essential for this study, the subsequent simulation setup and the atomistic theoretical analysis have been carried out by the present author.

Substantial parts of the research (including the results) presented here are published in [3, 4].

6.1 Introduction

The aim of this chapter is to deliver a combined theoretical and experimental description of the melting processes of laser-excited gold nano-films on a picosecond timescale. As observed in the literature review (chapter 3), the recent results on ultrafast dynamics of such relatively simple system of gold films [60, 170, 172, 182, 184, 218, 237–242] are quite controversial. In fact, the atomistic and electronic dynamics following excitation are still unclear and the questions of photo-induced non-thermal melting or bond character change (and the excitation limits within which these occur) remain open. The results presented in this chapter focus on the detailed atomistic information for gold nano-films under different absorbed laser fluences obtained from the two-temperature molecular dynamics (2T-MD) method. We achieve an excellent quantitative theory-experiment agreement for the time-resolved ultrafast electron diffraction (UED) Bragg peak data and the 2T-MD model without any adjustable parameters. As a result, this direct comparison enables us to directly "observe" the ultrafast dynamics as it happens. In other words, we have effectively solved the inverse problem of structure determination of a laser irradiated metal from the UED measurements. In addition, because of the available experimental comparison, we also investigate the limits of the ground-state potential approximation as a function of the electronic temperature.

We start with a brief description of the UED experimental setup (Sec. 6.2). We later discuss the rigourous *ab initio* parameterisation of the 2T-MD model (Sec. 6.3). The results section focuses on the detailed analysis of the structural wealth of information from 2T-MD, which enables us to elucidate the ultrafast melting mechanism in gold (Sec. 6.4).

6.2 Experimental setup

The 10±2 nm thick monocrystaline free-standing gold films (placed on a gold mesh) were excited with the incident fluences (F_{inc}) of 1, 27 and 41 mJcm^{-2}. In this chapter we do not consider the 1 mJcm^{-2} case, as the absorbed energy is too low to cause any phase transformation - only some lattice heating[1]. We also analyse the data for the 35±5 nm thick sample illuminated with $F_{inc} = 108$ mJcm^{-2} pulse.

High-resolution ultrafast electron diffraction (UED) experiments were achieved with relativistic 3.0 MeV electrons. The UED temporal resolution was determined to be 180 fs (which includes timing jitter between laser and electron pulses) and the probe beam was 0.2 mm in diameter of almost top-hat transverse shape. The samples were photo-excited with photons of 3.1 eV energy. The pump pulse was 90 fs at full width at half maximum (FWHM) and of nearly Gaussian transverse shape (0.8 mm FWHM). The incident angle of the pump-laser light was 14° from the surface normal and the transmission-mode UED was measured along the (001) direction of the thin films. The pump and probe beam shape schematic is shown in Fig. 6.1. It is important to note that we are probing an almost perfectly homogeneously excited region in the lateral directions to the probe axis. More technical details of the experimental setup can be found in [3, 243, 244].

The relativistic energies of the UED have significant advantages over the conventional setups, such as the one used in [172]. First, using relativistic energies enables us to minimise the so-called space-charge effect and achieve higher densities of electrons per bunch. In this case, it was limited to $6 \cdot 10^4$ electrons per pulse, due to the dynamic range of the detection system[2]. This allows for high-quality single-shot diffraction measurements (as shown in Fig. 6.1) with sub-picosecond time resolution (180 fs) - a feature that is cardinal for studying ultrafast and irreversible processes. Furthermore, the UED setup provides structural information almost free from any multiple diffraction and possible inelastic effects, which would manifest themselves as (000)-order attenuation [172, 217]. We can safely neglect the multiple diffraction effects [245, 246], as the (001) thicknesses of the samples ($L \leq 35$ nm) are much smaller than the extinction distances (which characterise the efficiency of generating a diffracted beam by a sample) for the measured peaks. For 3.0 MeV electrons in Au the extinction distance for a (200)-order peak is 186 nm [3]. This UED setup feature is crucial for the theoretical analysis to calculate the structure function - it allows us to employ the kinematic theory assuming a single scattering event. The (000)-order attenuation is a clear breakdown of the kinematic regime.

[1] The data for 1 mJcm^{-2} can be found in [4].

[2] Nonetheless, due to the electron density per pulse constrained by the detector system, the liquid features could not be detected clearly to enable a quantitative analysis. The electron density per pulse was two-orders of magnitude less than in [218], where liquid structures of Au were detected.

In such case, a dynamical theory of diffraction needs to be applied, where the incident beam (i.e. the 0^{th} order) and the diffracted beams become correlated. This is in contrast with the previous results obtained by conventional UED, where the multiple scattering processes were not accounted for [172, 217].

Figure removed due to third party copyright restriction

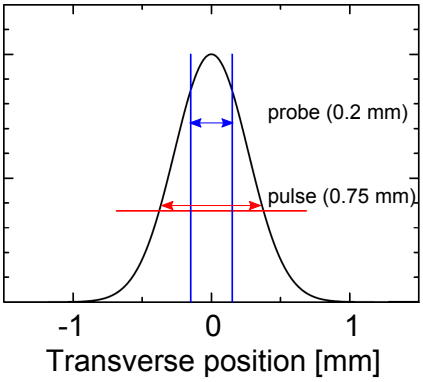

Figure 6.1: (Left panel) Single-shot UED image measured in a high-resolution mode at the delay time, $t = -0.5$ ps. The scattering vectors of (200) and (220) peaks are 0.490 and 0.693 Å^{-1}, respectively; (right panel) schematic depiction of the pump and probe transverse shapes. *Parts of the figure reproduced from [4].*

6.3 Model details for Au

6.3.1 Electronic system

6.3.1.1 Model parameterisation

The values of electronic specific heat $C_e(T_e)$, electron-phonon coupling $G(T_e)$ (see Fig. B.4) and the modified lattice parameter $a(T_e)$ (see Fig. 6.3) were calculated *ab initio* using density functional theory (DFT) and the high electronic temperature generalisation of DFT [247, 248] by Mermin [249] using the ABINIT code [250, 251]). We use the following approximations/setup in the *ab initio* calculations for Au: local density approximation (LDA) [252], norm-conserving pseudo-potential method [253] (with 5d and 6s electrons as valence electrons), wave-functions cutoff: 60 Ha and a $16 \times 16 \times 16$ Monkhorst-Pack k-points mesh.

The electronic specific heat is evaluated from the internal energy E_e derivative with respect to the electronic temperature: $C_e(T_e) = \partial E_e / \partial T_e$. In the calculations, we account both for the electronic density of states (DOS) change and its modification at elevated electronic temperatures [184]. The value of C_e used here is very similar to the one obtained in [29].

The electron-phonon pre-factor G_0 (i.e. $G(T_e)$ at room temperature) is obtained from an experimental measurement in [183], $G_0 = 2.1 \cdot 10^{16}$ Wm^{-3}K^{-1}. The electronic temperature dependence of the e-p coupling is calculated *ab initio*, using a T_e dependence proposed in [29, 30], which is appropriated for metals [254] as

$$G(T_e) = \frac{G_0}{g^2(\varepsilon_F)} \int_{-\infty}^{+\infty} g^2(\varepsilon) \left(-\frac{\partial f}{\partial \varepsilon} \right) d\varepsilon, \tag{6.1}$$

where ε_F is the Fermi energy, $g(\varepsilon)$ the electronic DOS, and f the Fermi-Dirac distribution. Again, the $G(T_e)$ function used here is very similar to the one published in [29]. We neglect any ionic temperature or structural change dependencies, such as defects or phase transitions, in $G(T_e)$ as these are unknown in Au [255].

For simplicity, the electronic thermal conductivity κ_e is assumed to be infinite (i.e. $\nabla^2 T_e = 0$), leaving the sample homogeneously excited throughout the simulation time with no thermal conduction into the bulk (i.e. zero-flux boundary conditions are used in the T_e system).

6.3.1.2 The initial conditions

Due to the rapid thermalisation time of electrons after photo-excitation ($t \sim 100$ fs [218]) we can assume a well-defined electronic temperature T_e at all times and hence apply the 2T formalism. Furthermore, as presented in Fig. 6.1, the laser spot diameter is much larger than the probed area and therefore we neglect any lateral energy redistribution and dissipation during the time of the UED experiment ($t < 30$ ps). As it has been experimentally confirmed that gold films up to 100 nm are homogeneously excited [183] due to ballistic electron transfer, initial homogeneous excitation is a reasonable assumption for our 10 nm and 35 nm films. Recent experiments have shown that the ballistic electronic range can be reduced at very high fluences [182]; however it is still larger than the films thicknesses used here. We also neglect the blast force [239], which results from a gradient of electronic temperature.

The above T_e homogeneity condition implies that for the laser source $S(z,t)$, which is of Gaussian shape in time t and an exponential decreasing amplitude in the direction into the film z [178], the z-dependencies disappear from the laser source term in Eq. 2.15, i.e.:

$$S(z,t) = \frac{2F}{Lt_p}\sqrt{\frac{\ln 2}{\pi}}\exp\left[\frac{(-4\ln 2)\cdot(t-t_0)^2}{t_p^2}\right], \tag{6.2}$$

where F is the absorbed fluence, L is the sample thickness (since we assume homogeneous excitation), t_p the duration of the pulse taken at the FWHM, and t_0 is the time zero, which is defined as the time when the laser pulse maximum arrives on the sample surface.

6.3.1.3 Absorbed fluence

In order to directly compare the model with the experiment, we require the knowledge of the adsorbed fluence, F, which is determined from the incident fluence (F_{inc}) as well as reflectivity (R), transmission (T) coefficients of the film and a coefficient η_{exp} dependent on the particular experimental setup [4]:

$$F = \eta_{\text{exp}} \cdot \overbrace{[1 - R(L) - T(L)]}^{A(L)} \cdot F_{\text{inc}}, \tag{6.3}$$

where L is the film thickness. The coefficient η_{exp} describes losses due to the energy dissipation into the supporting grid (most likely via ballistic electrons [239]) and/or electron ejection [238][3]. The independent time-resolved optical absorption study arrived at $\eta_{\text{exp}} = 0.5$ [4].

[3] Although the fluences used here induce temperatures significantly less than the Au work function, $W_{Au} = 5.1$ eV.

With absorption $A(L)$ measured to be 0.22 (0.46) for a 10 nm (35 nm) film, we relate the three incident fluences $F_{\text{inc}} = 27$, 41 (10 nm films) and 108 mJcm^{-2} (35 nm film) to the corresponding absorbed fluences of $F = 3.0$, 4.5 and 25.0 mJcm^{-2}.

6.3.2 Atomistic system

6.3.2.1 Ground-state interatomic potential

To simulate the ionic system of Au we have used a recent embedded atom model (EAM) ground-state potential developed by Sheng *et al.* [256]. It is highly optimised to correctly reproduce the thermal (melting point and latent heat of melting) and structural properties of Au; see Tab. 6.1. Ensuring correct thermal parameters in the model is crucial to correctly describe the melting dynamics as a function of the energy delivered by the electron-phonon coupling. Overall, the potential performs much better than the previously developed EAMs for Au, such as the commonly used ones developed by Johnson [257], Foiles *et al.* [258], Lee *et al.* [259] and Gronchola *et al.* [260].

Table 6.1: The performance of the EAM Au potential by Sheng *et al.*. Data obtained from [256, 261].

Property	Symbol	Unit	Sheng *et al.*	exp.
Melting point	T_m	K	1281	1337
Latent heat of melting	H_m	kJ/mol	11.1	12.55
Crystalline specific heat capacity	C_c	J/(kg K)	122	129

6.3.2.2 Electronic temperature dependent potential

Our *ab initio* calculations show a significant shift in the interatomic potential minima (a_0) with electronic temperature (i.e. Δa_0 >1% at $T_e' \gtrsim 9,000$ K, or $T_e' \gtrsim 0.8$ eV). This implies that in the high absorbed fluence regime, where $T_e \gtrsim 9,000$ K is expected, the ground-state potential will not capture the additional forces coming from such a shift and therefore it will no longer be a good approximation. An electronic temperature dependent (ETD) potential could in principle capture such additional "non-thermal" effects.

We use the only available electronic temperature dependent (ETD) potential for Au recently developed by Norman *et al.* [87], which was parameterised with respect to three T_e points (0.1, 3.0 and 6.0 eV) by the force-matching technique [86] and interpolated (originally) in T_e with a second order polynomial. It correctly reproduces the thermal ($T_m \sim 1200$ K) and mechanical properties of gold. We interpolate this potential (specifically its pair interaction and density parts, while keeping the embedding part unchanged) with cubic splines in 0.05 eV increments; see Fig. 6.2. We examine if it reproduces the increase of the *ab initio* results of lattice spacing shift with T_e.

In Fig. 6.3 we present the mismatch between the EDT potential and the *ab initio* calculations of $a(T_e)$. Such a discrepancy can be attributed to the fact that the EDT was not

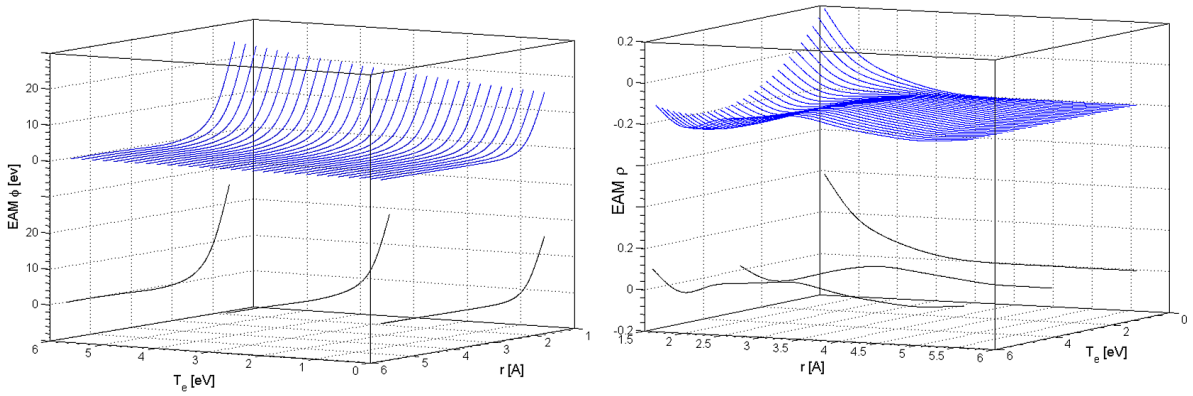

Figure 6.2: Selected cubic spline interpolation T_e points of the pair interaction (left panel) and the charge density (right panel) of the EDT EAM Au potential.

explicitly fitted to this property and the limited number of T_e points in the potential (we only extrapolate within the 0.1-0.3 eV range, while the "closest" T_e points available are 0.1 eV and 3.0 eV). We make the assumption that the shift of the potential minima is the most important non-thermal change in the interatomic interaction. Therefore to ensure that the potential used in the model accurately reproduces the *ab initio* modified parameter at high T_e, we match the T_e values obtained from the 2T-MD simulations with the *ab initio* $a(T_e)$ values, and subsequently map these onto the interpolated ETD potential T_e increment. For instance, in the $F = 25$ mJcm^{-2} simulation we choose an ETD potential at the 0.2 eV increment, which corresponds to the T_e averaged over the first 3 ps of the 2T-MD simulation. For simplicity, the ETD potential was changed in 0.05 eV steps, where 0.1 eV represents the ground-state.

Figure removed due to third party copyright restriction

Figure 6.3: Lattice parameter change as function of electronic temperature in Au: (blue) cubic-spline interpolated EDT, (red) *ab initio* data. The maximum electronic temperatures reached in the three different simulations are represented by vertical dashed lines. *Parts of the figure reproduced from [3].*

6.3.3 Simulation setup

To represent the experimental setup, we model a 10 nm <001>-orientated Au film with an MD simulation cell containing 250k atoms ($20.4 \times 20.4 \times 10.2$ nm); and a 35 nm <001>-orientated Au film with a simulation cell containing 860k atoms ($20.5 \times 20.5 \times 35.9$ nm). The overlaying T_e and T_i temperature cells are cubes with a side length of ~ 1.4 nm. The simulation setup is schematically presented in Fig. 4.5. To allow for uniaxial expansion of the free standing film, the MD simulation cell has two free (001) surfaces and periodic boundary conditions are applied in the lateral directions. When the MD system expands in the (001) directions, the ionic temperature cells become activated once populated with a certain number of atoms (usually around ten atoms per cell in order not to activate them when sputtering occurs).

We used a constant time-step of 1 fs for the MD part of the calculations. Since we consider a homogeneous excitation at each time-step, the finite difference solver time-step was equal to the MD time-step. We have checked for the conservation of the total energy (electrons and ions) for $\Delta t = 1$ fs. The atomistic configurations were pre-equilibrated in an NPT ensemble (1 atm, 300 K) and subsequently in an NVT ensemble at 300 K. When calculating the local ionic temperature, we consider the "thermal" velocities only (Eq. 4.34), discounting for the centre of mass motion due to uniaxial expansion.

6.4 Results for 10 and 35 nm Au thin-films

6.4.1 Comparison with experiment

Figure 6.4 shows a very strong dependence of the measured Bragg characteristic decay time on the absorbed fluence. At $F = 1$ mJcm^{-2}, about half of the normalised signal is detected at 30 ps, while at $F' = 7.1$ mJcm^{-2} ($F = 25$ mJcm^{-2} normalised to the 10 nm film thickness) the signal is half of the original intensity already at 2 ps.

The 2T-MD model gives an excellent agreement between the measured and the calculated Bragg peak evolution for the whole time domain of the experiment for the two lowest absorbed fluences without any adjustable parameters. Notably, the model reproduces the short time behaviour (i.e. the quick initial drop of the signal at $t \lesssim 3$ ps) and the longer-time behaviour for all Bragg peaks.

At high fluence, however, the ground-state EAM potential predicts a slower Bragg decay time than the one measured. Given the excellent theory-experiment agreement at lower fluences, this implies that other physical effects must be more significant in this absorbed energy regime. Indeed, such rapid loss of the Bragg peak intensities cannot be explained with a thermal model, i.e. one which assumes the electron-phonon coupling as the sole energy transfer channel. We infer that the modified interatomic interaction (i.e. a non-thermal effect), manifesting itself as an increase of the lattice parameter and hence an electronic pressure on the ions, will be non-negligible at this fluence. To capture this effect, we have used the electronic-temperature dependent (ETD) EAM potential in 2T-MD for the highest fluence and accurately reproduced the experimental UED results (see Fig. 6.4).

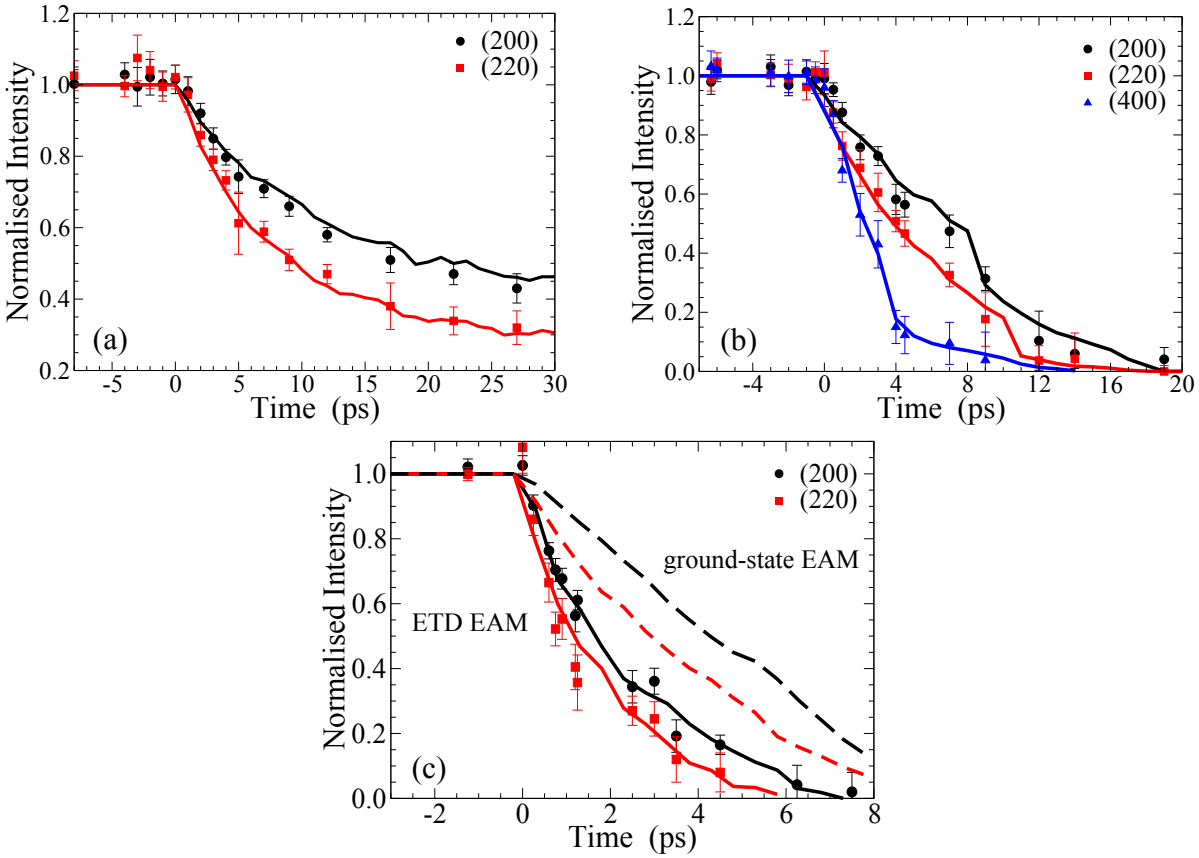

Figure 6.4: Direct comparison between experimental (data points) UED Bragg peaks and the theoretical peaks (solid lines). (a) $F = 3.0$, (b) $F = 4.5$, (c) $F = 25.0$ mJcm^{-2}. The dashed lines represent the results obtained with a ground-state potential, while the solid lines represent the ETD EAM potential. *Parts of the figure reproduced from [3, 4].*

The structure factor $S(Q)$ calculation scheme presented in Sec. 4.4.1 is based on a scattering equation for a random sample orientation[4], which is applicable in the case of a crystalline powder [216]. However, we are analysing the experimental UED scattering patterns of a mono-crystalline sample taken from a particular beam axis direction. The UED beam axis was placed normal to the (001) film surface (i.e. on the [001] zone axis) and therefore any peak splitting or shifts, which result from the uniaxial sample expansion in the (001) directions, are not detectable in the experimental setup. However, these effects and additional reflections not seen due to the particular beam axis direction, can be seen in the calculated pattern. For this reason, any visible peak splitting in the structure function $S(Q)$ is neglected and we compare only the areas under the main Bragg peaks. Figure 6.5 shows the temporal evolution of the computed $S(Q)$ pattern for the $F = 4.5$ mJcm^2 (10 nm) case. In the early stages, when only one peak is visible, we integrate the whole peak (subtracting the background) and we neglect the secondary peak when it was well separated from the original one, in effect integrating over the experimentally allowed Bragg reflections only.

[4] $S(Q)$ is obtained from a one-dimensional sine Fourier transform of the pair density function.

Figure removed due to third party copyright restriction

Figure 6.5: Time evolution of the pair density function (left panel) and the corresponding structure factor (right) computed for $F = 4.5$ mJcm^2 (10 nm). In the 2T-MD model peak splitting is caused by the uniaxial expansion of the sample. Peak splitting is not detected in the experimental setup due to the beam axis direction. *Figure reproduced from [3].*

6.4.2 Characterising the melting processes

Given the excellent agreement between the experimentally measured Bragg peaks with the computed ones, we can use the wealth of structural information from the 2T-MD model to describe the melting dynamics behind the Bragg peak evolution. We have identified three types of melting: heterogeneous, homogeneous and ultrafast "non-thermally" driven melting, which we discuss in turn.

The low absorbed fluence ($F = 3.0$ mJcm^{-2}) delivers just enough energy to the sample to melt it entirely. The melting process starts with the pre-melting of the free surfaces and continues as heterogeneous thermal melting by melt front propagation (see Fig. 6.6). The speed of the melting front propagation is about 0.3% of the speed of sound in Au, which is consistent with previous simulations for photo-excited Ni films [188]. Two melt fronts connect a thin filament at 400 ps, which subsequently grows. At 1.5 ns only a small pocket of crystalline gold remains in the middle and the film melts almost entirely. This is consistent with experiment - the film cannot be found on the UED sample holder seconds after the measurement. During melting the local temperature never exceeds the so-called limit of crystal stability ($\sim 1.25 \cdot T_m$ [60]), but exceeds T_m (see Fig. 6.9). This maximum superheating temperature $1.25 \cdot T_m$ criterion is an upper kinetic limit of crystal stability, above which homogeneous melting occurs throughout the system [263]. The crystalline gold remains slightly superheated until it is overrun by the cooler melt front. As expected, the solid to liquid phase transition is accompanied by the decrease in density. Throughout the melting processes, the sample oscillates to a very good approximation with a frequency of $2L/v_c$, where L and v_c are the sample thickness and the sound velocity in Au at equilibrium conditions. Such oscillations can be identified in the time evolution of the sample density and pressure presented in Fig. 6.11 and Fig. 6.12, respectively.

At medium absorbed fluence ($F = 4.5$ mJcm^{-2}) the ionic temperature reaches the melting

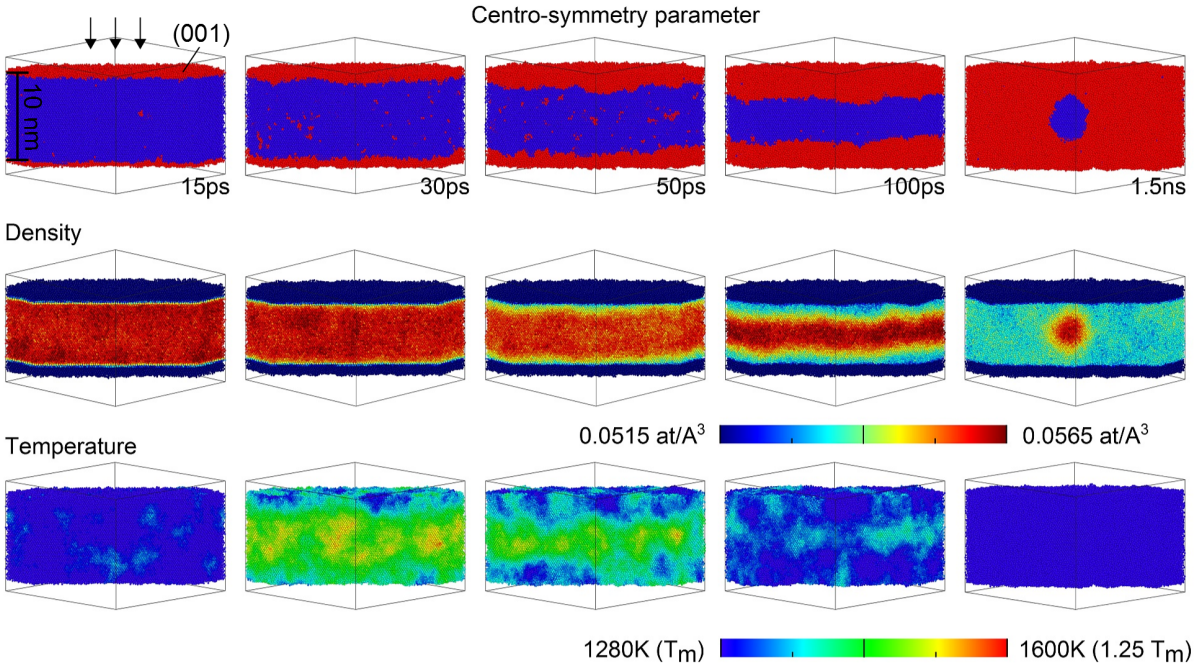

Figure 6.6: 2T-MD simulation ($F = 3.0$ mJcm^{-2}, $L = 10$ nm) cross-section showing centro-symmetry (top), density (middle) and lattice temperature (bottom). At this fluence heterogeneous melting is the dominant processes with the melt fronts propagating from the free surfaces. These liquid fronts are typically undercooled. The local temperature exceeds the melting point (T_m), but not the crystal stability criterion ($1.25 \cdot T_m$). The atoms in the top panel are coloured according to their nearest-neighbour averaged centro-symmetry parameter, red with $\Phi > 0.45$ and blue with $\Phi \leq 0.45$. The local atomic densities and temperatures are averaged over the neighbouring atoms over distances of 19 Å and 12 Å, respectively. Data visualisation performed with [262]. Arrows indicate the direction of the pump laser. *Parts of the figure reproduced from [3].*

point quicker (at 6 ps) and remains superheated between 6-12 ps ($T_m < T_i < 1.25 \cdot T_m$), see Fig. 6.7. During this time, the homogeneously distributed seeds of molten phase in the sample are created and destroyed. After 12 ps, the temperature increases beyond the crystal stability limit ($1.25 \cdot T_m$) locally and the molten seeds, which serve as nucleation sites, grow and coalesce until the sample melts entirely at around 20 ps. Interestingly, the average sample temperature does not exceed the $1.25 \cdot T_m$ limit and therefore the crystal structure does not collapse immediately. Such a collapse, which completes in ~ 3 ps, was reported in [60] in the 2T-MD model for a higher fluence. Heterogeneous melting, as in the case of lower fluence, is also observed, but it is much slower than the homogeneous counterpart. This complex melting processes is accompanied by oscillations in temperature and the film thickness (see Fig. 6.9 and Fig. 6.11). The overall dynamics is consistent with the recent theoretical predictions [192, 194]. The liquid radial distribution function of the molten sample ($t > 20$ ps) and the larger molten pockets that form during the melting process are equivalent to the equilibrium liquid gold at the same pressure and temperature (Fig. 6.13). The 2T-MD simulation shows that the disordered state of gold nano-films is equivalent to equilibrium liquid gold, in contrast to "exotic" highly

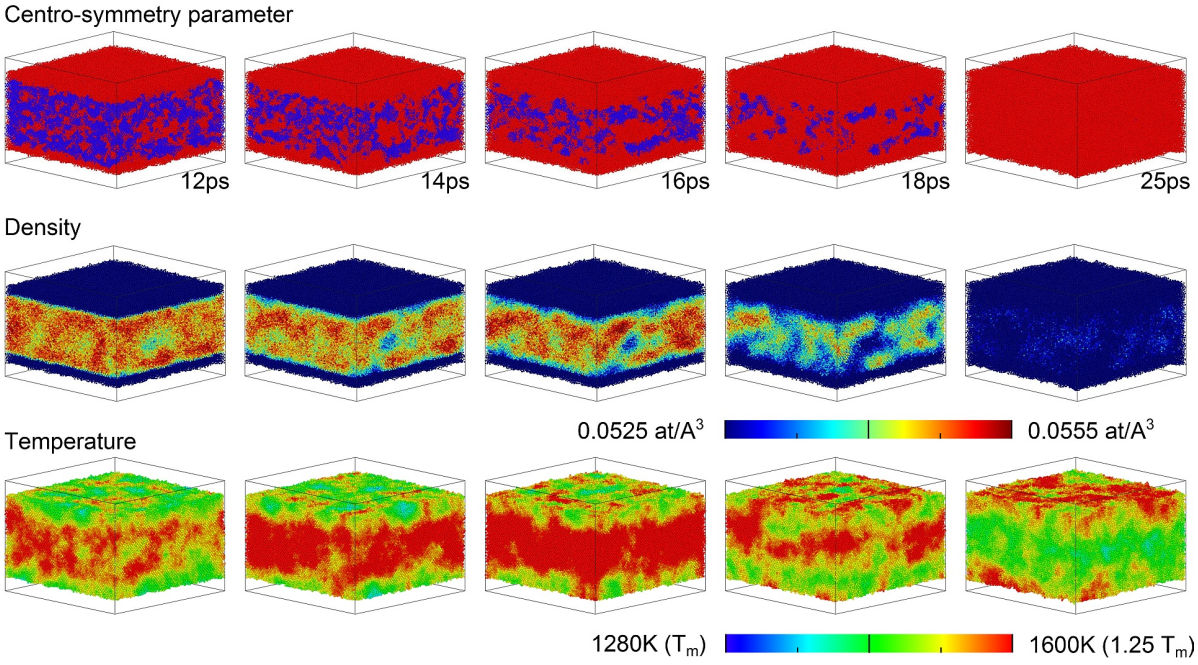

Figure 6.7: 2T-MD simulation ($F = 4.5$ mJcm^{-2}, $L = 10$ nm) side-view showing centro-symmetry (top), density (middle) and lattice temperature (bottom). At this fluence homogeneous melting occurs by nucleation site growth. The ionic temperature reaches beyond the $1.25 \cdot T_m$ threshold locally before 12 ps and the melting completes at 20 ps. Colour-coding the same as in Fig. 6.6. *Parts of the figure reproduced from [3].*

coordinated liquid states, which have been proposed for photo-excited semiconductors [264].

At the highest fluence ($F' = 7.1$ mJcm^{-2}) due to the significant change of the interaction potential, the core of the sample becomes initially compressed. The global electronic pressure change resulting from the high T_e modified forced interactions is 3 GPa. The pressure reaches a maximum of 5.5 GPa at 3 ps with the additional pressure coming from the heating induced by electron-phonon coupling, as seen in Fig. 6.12. For comparison, a maximum of 1.5 GPa is reached in the case of the 4.5 mJcm^{-2} fluence due to the electron-phonon coupling. For this absorbed fluence, the expansion is very rapid and the fronts of lower density propagate from the free surfaces and are followed by the melt fronts (Fig. 6.8). The melting therefore can be described as heterogeneous , but it completes much quicker than in the "thermal" case of $F = 3.0$ mJcm^{-2}. In fact, melting at this fluence involves thermal (electron-phonon coupling) and non-thermal (T_e-dependent forces) effects. The former dominates within the first ps and is responsible for the initial rapid drop of Bragg peak intensity. Due to this complex interplay of thermal and non-thermal processes this melting behaviour can be therefore referred to as "non-thermally accelerated melting". It is not purely non-thermal, as it occurs above the melting temperature and has a strong thermal (i.e. electron-phonon coupling induced heating) component, unlike the photo-excitation induced melting processes proposed for Si [265]. Similarly to the previous two cases, we did not see any significant difference in the laser-induced disordered state self-diffusion coefficient (Fig. 6.10) and pair density function (Fig. 6.13) from equilibrium liquid gold. Notably, the density of the non-equilibrium liquid

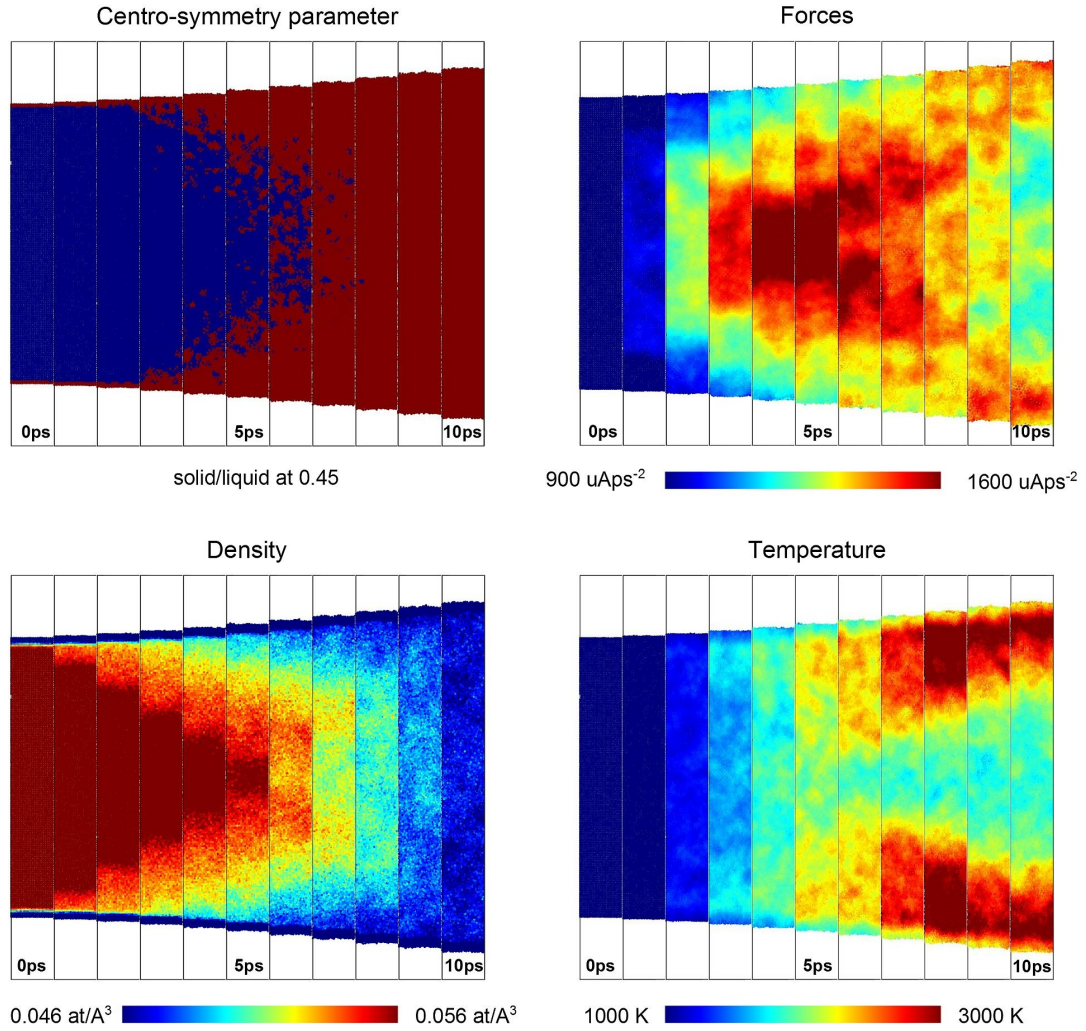

Figure 6.8: 2T-MD simulation ($F = 25.0$ mJcm^{-2}, $L = 35$ nm) cross-section showing centro-symmetry, density, forces and the local lattice temperature. The melting process is inhomogeneous, while the sample rapidly expands. Build-up of forces in the middle of the sample at around 3 ps is apparent. These result from both the T_e potential and electron-phonon coupling effects. Colour-coding the same as in Fig. 6.6. *Parts of the figure reproduced from [3].*

gold at 9 ps (1800 K, 2 GPa) is 0.051 atoms/Å^3, which is approximately that of an equilibrium (i.e. $T_e = T_i$) liquid at 2000 K and 2 GPa. This temperature difference can be attributed to the modified lattice parameter at high T_e. The diffusion coefficients of $3.5 \cdot 10^{-9}$ m^2/s (calculated with ETD potential) for the non-equilibrium gold and $4.1 \cdot 10^{-9}$ m^2/s (ground-state potential) for equilibrium gold are also very similar.

6.4.3 Ablation

In the highest fluence case ($F = 25$ mJcm^{-2}) once the system is entirely melted (after 8 ps), it continues to expand until small voids are created in the middle at around 20 ps (see Fig. 6.14). These voids subsequently coalesce (around 30 ps) and the film is held together only by a small filament (100 ps), at which point the expansion stops. We can make a reasonable assumption

Figure removed due to third party copyright restriction

Figure 6.9: Time evolution of global averaged electronic and ionic temperatures for: (green line) $F = 3.0$ mJcm^{-2}, (red) $F = 3.0$ mJcm^{-2} and (blue) 25 mJcm^{-2}. The horizontal lines represent the melting point of the ground state EAM potential ($T_m = 1281$ K) and the crystal stability limit ($1.25 \cdot T_m$). *Parts of the figure reproduced from [3].*

Figure removed due to third party copyright restriction

Figure 6.10: Time evolution of the self-diffusion coefficient (D) for three fluences as calculated from the mean-square displacements in the lateral directions only for the whole sample (circles) and molted pockets only (squares), which were identified by the centro-symmetry parameter at $\Phi > 0.55$ and $t = 16$ ps. The horizontal lines indicate the self-diffusion for equilibrium bulk gold at 1300 K and and 1400 K (both at 1 atm). *Parts of the figure reproduced from [3].*

Figure removed due to third party copyright restriction

Figure 6.11: Time evolution of the density and the surface expansion velocities (inset) for three fluences. The cases of $F = 3.0$ mJcm^{-2} and $F = 4.5$ mJcm^{-2} show periodic oscillations, while the sample at $F = 25$ mJcm^{-2} becomes continuously less dense in the time frame presented here. *Parts of the figure reproduced from [3].*

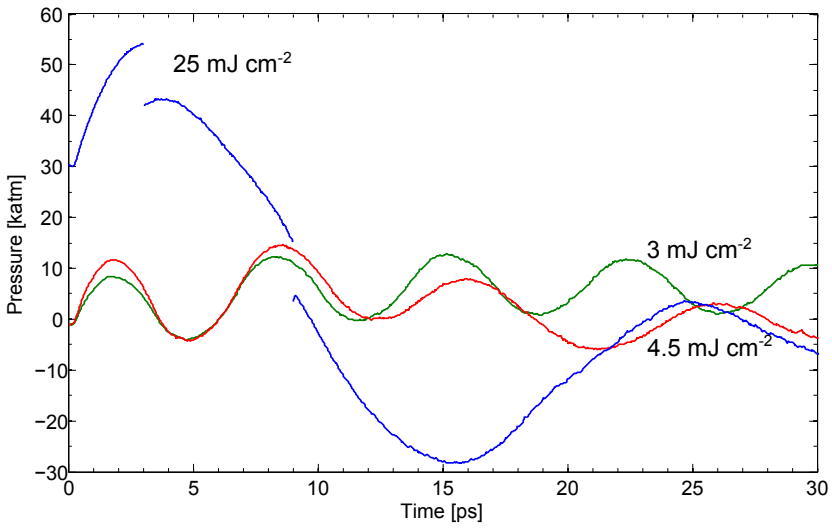

Figure 6.12: Time evolution of the global pressure for three fluences. The pressure for the two smaller fluences oscillates with the same frequency as the densities. In the case of $F = 25$ mJcm^{-2} due to the change of the potential the initial pressure is at 3 GPa. It reaches a peak of 5.5 GPa at 3 ps due to the electron-phonon coupling. The pressure relaxes at around 30 ps. The discontinuities in the pressure stem from the change in the EDT EAM potential in $T_e = 0.05$ eV steps.

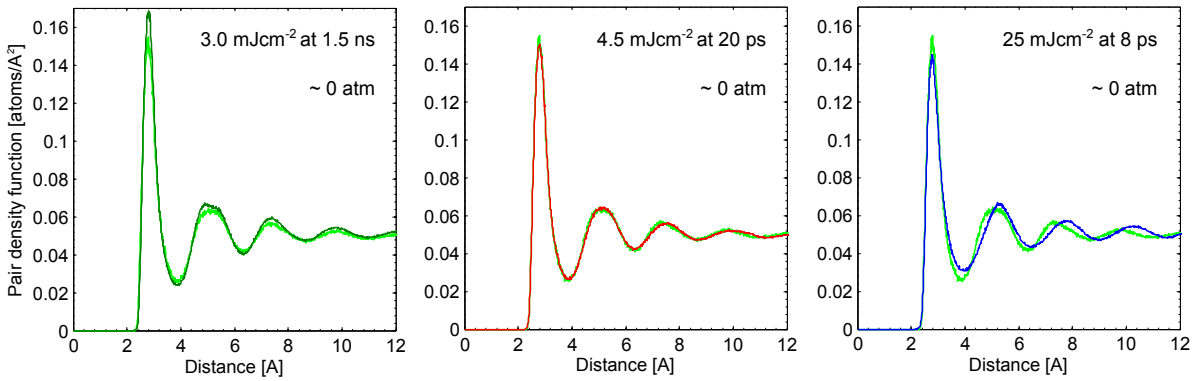

Figure 6.13: Pair density snapshots for the liquid structure produced by the three fluences. The green background represents a pair density function of equilibrium bulk gold (1400 K and 1 atm). No significant structural difference between the non-equilibrium disordered gold and "ordinary" equilibrium gold can be seen.

Figure removed due to third party copyright restriction

Figure 6.14: The 2T-MD simulation (variable ETD EAM potential) of $F = 25$ mJcm^{-2} at 15-100 ps. Colour-coding represents the density. At this fluence the 35 nm sample almost ablates with two parts being help by a thin filament at 100 ps. *Parts of the figure reproduced from [3].*

that slightly above the fluence used here the sample would most likely break into two in a mechanism similar to a "short-term" laser ablation described in [87]. It needs to be noted that we neglect here the blast force [191], which results from the T_e gradients. It typically occurs when a laser interacts with thicker samples and can enhance this ablation-like process. The experimental minimum absorbed fluence ablation thresholds for single pico- or sub-picosecond pulses in gold (10 mJcm^{-2} [266], 20 mJcm^{-2} [267]) are difficult to compare to, as ablation is typically studied in bulk samples. Nonetheless, $F = 25$ mJcm^{-2} for near-ablation, compares reasonably well.

6.5 Discussion and summary

We have achieved an excellent agreement between the rigorously *ab initio* parameterised 2T-MD simulations and the state-of-the-art ultrafast electron diffraction experiments of photo-excited thin-film gold. The quantitative theory-experiment agreement on Bragg peak evolution, which we have achieved across all fluences and within the whole measured time domains, enables us to describe the lattice heating effects and structural changes. The 2T-MD model has enabled us to identify three types of melting processes in Au: heterogeneous , homogeneous and non-thermally accelerated melting.

We have additionally tested whether we were able to reproduce the experimental results by a different combination of the electron-phonon coupling and the absorbed fluence. We have found that, for the first two fluences, the short-term behaviour of the Bragg peak is sensitive to the choice of the electron-phonon coupling at 300 K (G_0), while the long term behaviour is dependent on the absorbed fluence. We are, therefore, confident that the experiment and theory mapping we have achieved is unique. This implies that the 2T-MD model, which works on the same spatiotemporal scale as the experiment, captures the essential physics of melting of thin-films and, therefore, the atomistic description obtained from the MD part provides an accurate description of the melting processes. It is not too bold to assert that we have therefore observed the melting processes of gold on a picosecond timescale, not as the dynamics of the individual atoms, but as a "statistically averaged" movie of a phase transition. This is also akin to providing the solution to the inverse problem of structure determination from the diffraction pattern in time. The 2T-MD method is highly transferable, as most of the parameters are available for other metals, and therefore it can be potentially applied to describe photo-induced phase transitions in different materials.

The excellent experiment and model agreement without any fitting parameters has in effect experimentally validated the two-temperature approach for the first time - a theory which has been first proposed in the early sixties in [35]. We have also provided an electronic temperature threshold for the applicability of the ground-state interatomic potential approximation for Au, $T_e' \leq 0.8$ eV. The conclusion regarding the electronic temperature dependent lattice spacing and hence enhanced sample expansion can be verified by further experiments measuring surface expansions speeds, such as ultrafast Fourier domain interferometry (as used in [182]). Lastly, the 2T-MD model enabled us to predict the expansion speed velocities and therefore tackle the isochoric warm dense matter notion for free-standing films prevalent in literature [172].

Chapter 7

Swift heavy ion tracks

□ **Attribution:** Parts of the research presented here are published in [6]. Some of the ideas, but not results, developed in this section are published in [2, 7, 8].

7.1 Introduction

This chapter analyses the physics behind the latent track formation using the inelastic thermal spike (iTS) model and its band-gap extension (eiTS). The iTS scheme is based on the two-temperature (2T) approach, while eiTS solves a Boltzmann transport equation for carriers (electron-hole pairs) and their energies, rather than for the electronic temperature explicitly. We apply these schemes to study two exemplar semiconductors, namely Si and Ge. We start by analysing the latent track formation in silicon, where we describe in detail the continuum solution to eiTS (Sec. 7.4.1) and then compare it to the MD-coupled version of both iTS (Sec. 7.4.2.1) and eiTS (Sec. 7.4.2.2). We sample the free parameter space of the iTS-MD in Si and discuss the model's limitations. For germanium, we present the results from the eiTS (continuum and MD-coupled) model only (Sec. 7.5). The eiTS model results reported here provide us with the evolution of the electronic and ionic temperatures, and carrier density. In addition, the MD-coupled versions of both models offer an insight into the track evolution and morphology, which is important for a precise experimental comparison.

We concentrate our analysis on Si and Ge, as these are band-gap materials and hence are complex to simulate effectively in the thermal spike formalism. Owing to this fact, the modelling effort of swift heavy ion (SHI) impacts in band-gap materials remains quite controversial. However, we have selected Si and Ge for this study, as the electronic transport properties of both are very well characterised and therefore modelling these could form a starting point for a general model for band-gap materials. The long-term goal of this study is to build a predictive and transferable modelling scheme, which will enable us to accurately and precisely determine the latent track radii cross-sections for any SHI impact. We have made some progress towards this goal - we test the eiTS model by reproducing the tracks measured in Si and Ge using only one fitted parameter, namely the electron-phonon relaxation time, with some success.

The chapter concludes with a brief note on the results that can be obtained from *ab initio*

DFT modelling in the context of applicability of the thermal models, such as iTS and eiTS, to high electronic excitations produced by swift heavy ions. It also gives recommendations for future research avenues.

7.2 Model parameters for Si and Ge

7.2.1 Parameters for iTS

Here we present only the electronic parameters of Si, as we discuss the iTS results only in the context of iTS-MD. In the MD-coupled scheme the ionic system parameters are handled at the level of interatomic potentials, which are discussed in Sec. 7.2.3. One of the main criticisms of the iTS model is the requirement for a small set of electronic system parameters, many of which are poorly characterised or not known. These are namely, the electronic specific heat capacity C_e, electronic diffusivity D_e and electron-phonon relaxation time τ_{ep}, which we discuss in turn.

The electronic specific heat capacity's linear dependence on the electronic temperature $C_e(T_e) = \Gamma\ T_e$ is the most prevalent form in the literature. In Si, the scale factor Γ is usually set to $5.925 \cdot 10^{-5}$ J/(cm^3 K^2) [150], which derives from the free electron gas model that is applicable to metals only[1]. The heat capacity is also typically assumed to become constant, $C_e(T_e) = \frac{3}{2} n_e k_B$ for $T_e > T_F$ with $T_F = 12000$ K being the Fermi temperature of Si. Such a formulation has severe limitations. First of all, the electronic specific heat capacity is approximately zero and increases slowly for temperatures $T_e << E_g$, where E_g is the band-gap, due the presence of the gap between the conduction and valence bands. Secondly, there is no justification to cap C_e at any particular temperature and to a particular number of carriers. During SHI irradiation, the local temperatures can be in excess of several or even tens of eV. This is enough to excite also the core electrons, which can then contribute to the specific heat capacity. A comparison of a crude free electron gas model (due to [150]) and an *ab initio* calculation is shown in Fig. 7.1.

An accurate determination of the electronic diffusivity $D_e(T_e)$ at high electronic temperatures has not been achieved to date. This is because at very high excitations it is true to some extent that "hot electrons in the conduction band of an insulator behave like hot electrons in metals" [150, 157], and therefore the ground-state value of D_e, if measured, can be orders of magnitude different to the high T_e one. Typically, the predictions of the $D_e(T_e)$ evolution are made by comparing the results of models to track radii. Toulemonde *et al.* [268] stated a maximum value of the order of 2 cm^2/s in highly excited insulators, which was then used for fits in [150]. These arguments are based on a relationship of diffusivity to the electron-phonon mean free path, λ, and by arguing that λ cannot be significantly less than the interatomic distance. However, it needs to be noted that a rigourous theoretical consideration is still missing. Also, in the iTS model for band-gap materials, the diffusivity relates to electronic temperature

[1]The scaling factor is also written as $\Gamma = n_e(\pi^2 k_B^2/2\epsilon_F)$, where n_e is the number of valence electrons, k_B the Boltzmann constant and ϵ_F is the Fermi energy; $\epsilon_F = (\hbar^2/2m_e)(3\pi^2 n_e)^{2/3}$, where $\hbar$ is Planck's constant and m_e is the electron mass; see also Sec. 5.2.

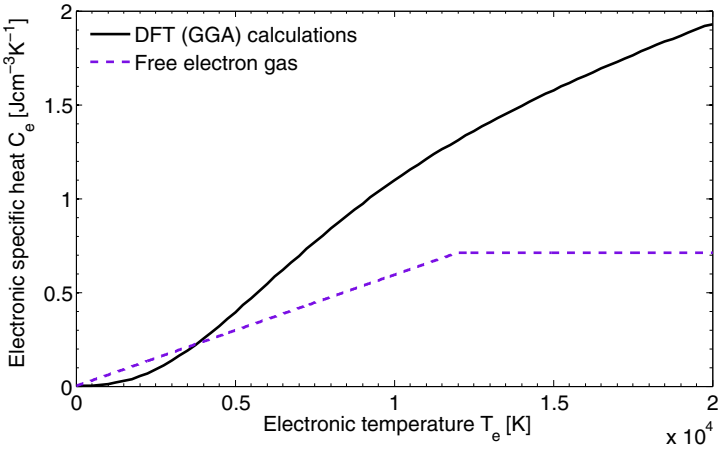

Figure 7.1: The electronic specific heat of Si. Mismatch between the *ab initio* DFT calculation and the crude free electron gas model (due to [150]) is very pronounced, particularly at low and high electronic temperatures. Such discrepancy will lead to large errors in the initial electronic temperature evaluation after a SHI impact. *DFT data: courtesy of Y. Giret.*

diffusion, rather than ambipolar carrier diffusion only. It is hence an "effective" parameter, as it encompasses both carrier diffusion and their kinetic energy conductivity.

The electron-phonon relaxation time (τ_{ep}) dependence on other parameters is still a subject of an ongoing debate. Here, $\tau_{ep} = C_e/G$, where G is the electron-phonon coupling strength. The simplest approach to modelling is to use a constant value for τ_{ep}; typical values for bulk Si are in the 0.3-0.5 ps range, yet values of 0.08-0.68 ps have also been reported [41]. Different electronic temperature dependencies have been published in literature (listed in [50]). However all of these approaches assume that τ_{ep} can be related to the energy exchange in the electronic system, such as the mean free path of electrons, and therefore to the electron transport properties. This is not true, because the electron-electron interactions are governed by the exchange of momentum, while the electron-phonon ones by the rate of exchange of energy and hence they must be described by two separate timescales [230].

All in all, the value of the electron specific heat capacity can, at least in principle, be obtained with very high accuracy. However, this cannot be said about the electron-phonon relaxation time and its dependence on electronic temperature, which are poorly known from both theoretical and experimental viewpoints. Likewise, the behaviour of the diffusivity at high electronic temperatures is not known. Therefore, in practice we have two adjustable parameters, namely a constant τ_{ep} and the diffusivity D_e. When using the iTS model, we treat τ_{ep} and D_0 as constant adjustable parameters, however we use the $D_e(T_e) = D_0 \cdot T_e^{-1}$ relationship due to [150].

7.2.2 Parameters for extended iTS

The electronic structure parameters required in the extended iTS are: Auger recombination, impact ionisation, band-gap and electron/hole thermal conductivities, in addition to τ_{ep}. However, the knowledge of C_e is not explicitly required, because in eiTS it can be obtained from

the carrier density via $C_{e-h} = 3Nk_B + N\frac{\partial E_g}{\partial T_e}$. This expression, combined with the DFT knowledge of C_{e-h}, puts a constraint on the initial carrier number generated by a SHI impact [51]. Note that we are using electron-hole $_{e-h}$, and electron $_e$ subscripts in relation to the iTS and eiTS models, respectively. The first three parameters can be relatively easily obtained from measured values for both Si and Ge and used under the assumption that they are applicable under heavy SHI-induced non-equilibrium conditions. However, carrier thermal conductivities are more difficult to estimate. A starting point is to relate these to the experimentally measured carrier mobility values. The Wiedemann-Franz law states that the ratio of the electronic contribution to the thermal conductivity (κ) and the electrical conductivity (σ) is proportional to the temperature (T). The generalised Wiedemann-Franz law [50] states that:

$$\kappa_{e-h}(T_e) = \left(\frac{5}{2} - p\right)\left(\frac{k_B}{q}\right)^2 q\mu_{e-h}NT_e \tag{7.1}$$

where p is the correction factor, q is the elementary charge and μ_{e-h} is the electron-hole mobility. Note that in the current simulations we are imposing a local charge neutrality condition, which implies that $\mu_{e-h} = \frac{1}{2}(\mu_e + \mu_h)$. The Wiedemann-Franz law was initially formulated empirically for metals and should be applied to insulators with great care, in particular the mobility values (μ_{e-h}) need typically to be adjusted for lattice and electronic temperatures. This can be done in two ways (adapted from [50]): (i) using the model after Baccarani *et al.* [269], i.e.

$$\frac{\mu(T_e)}{\mu_0} = \frac{T_i}{T_e}, \tag{7.2}$$

where μ_0 denotes the equilibrium mobility at $T = 300$ K; (ii) or alternatively the model after Hänsch [270]:

$$\frac{\mu(T_e)}{\mu_0} = \left(1 + \frac{3}{2}\frac{\mu_0 k_B}{q\tau_{ep}v_s^2}(T_e - T_i)\right)^{-1}, \tag{7.3}$$

where v_s is the velocity of the electron (taken as 10^5 m/s) and τ_{ep} is the electron-phonon relaxation time. This expression was derived under homogeneous conditions, where the energy flux is proportional to the particle current, which is not the case in the eiTS model and therefore the former and simpler formulation is subsequently used giving $\kappa_{e-h} \propto N \cdot T_i$. In similar studies, high density of carriers impact on the mobility and on screening of electron-ion interaction is sometimes also taken into account [271]. Finally, experimentally measured expressions for κ_e and κ_h can also be used at relatively low temperatures (as in [45]).

The parameters relating to the atomistic lattice, such as thermal conductivity $\kappa_i(T_i)$, specific heat $C_i(T_i)$ and latent heats of melting and vaporisation (H_m and H_v, respectively) are well-known from experimental measurements at equilibrium; see Tab. 7.2.

7.2.3 Interatomic potentials for Si and Ge

In order for the hybrid MD method to accurately describe the physics behind the SHI track formation and improve on the continuum description, the choice of an accurate interatomic potential is critical. In particular, the primary selection criteria for a "good" potential for this

Table 7.1: Electronic system parameters for Si and Ge used in eiTS.

Quantity	Symbol	Si	Ge	unit
Ambipolar diffusivity [272]	D	$18 \cdot (300\ \mathrm{K}/T_i)$	$65 \cdot (T_i/300\ \mathrm{K})^{-1.5}$	cm^2/s
Impact ionisation [272]	γ	$3.6 \cdot 10^{10} \exp(1.5E_g/k_B T_e)$	neglected	s^{-1}
Band gap [273]	E_g	$1.16 - 1.5 \cdot 10^{-8} N^{1/3}$ $-7.02 \cdot 10^{-4}\ T_i^2/(T_i + 1108\ \mathrm{K})$	$0.803 - 3.9 \cdot 10^{-4}\ T_i$	eV
Auger recombination [274]	δ	$3.8 \cdot 10^{-31}$	$\sim 1 \cdot 10^{-30}$	cm^6/s
Electron mobility [275, 276]	μ_e	≤ 1400	≤ 3900	$\mathrm{cm}^2/(\mathrm{Vs})$
Hole mobility [275, 276]	μ_h	≤ 450	≤ 1900	$\mathrm{cm}^2/(\mathrm{Vs})$

Table 7.2: Model lattice parameters for Si (used in continuum eiTS).

Property	Symbol	Value
Melting temperature	T_m	1683 K
Vaporisation temperature	T_v	2954 K
Solid density at T_m	ρ_s	$2.32\ \mathrm{g/cm}^3$
Liquid density at T_m	ρ_l	$2.50\ \mathrm{g/cm}^3$
Latent heat of melting at T_m	H_m	1797 J/g
Latent heat of vaporisation at T_v	H_V	13, 722 J/g
Specific heat capacity C_i [J/(g K)]		
$C_i = -0.1354 + 4.486 \cdot 10^{-3}\ T - 5.207 \cdot 10^{-6}\ T^2$		$(60\ \mathrm{K} \leq T < 300\ \mathrm{K})$
$C_i = 0.7007 + 1.469 \cdot 10^{-4}\ T + 3.183 \cdot 10^{-8}\ T^2$		$(300\ \mathrm{K} \leq T \leq T_m)$
$C_i = 1.045$		$(T > T_m)$
Thermal conductivity κ_i [W/(cm K)]		
$\kappa_i = 1042\ T^{-1.158}$		$(60\ \mathrm{K} \leq T \leq T_m)$
$\kappa_i = 0.14$		$(T_m < T \leq T_v)$
$\kappa_i = 8.76 \cdot 10^{-5}\ T^{1/2}$		$(T > T_v)$

purpose are its ability to reproduce the following properties: melting temperature (T_m), latent heat of melting (H_m), solid (crystalline) to liquid density change ($\Delta\rho_{c-l}$) and amorphous structure from quenched melt. The first two are critical to ensure that the potential reproduces the correct melting energetics; the remaining two are to ensure the correct latent track formation dynamics and final track morphology.

For Si, the modified Tersoff potential (MOD) performs very well. It correctly describes the crystalline, liquid and amorphous phases of Si (see [277] for a review) and reproduces the thermal properties (T_m, H_m, $\Delta\rho_{c-l}$) and amorphous structure from quenched melt correctly. On the other hand, the potential has too high density increase at melting and thermal expansion. We also note that it is one of the very few potentials that has been very recently parameterised with respect to electronic temperature (T_e) [278]. This is an additional reason why it is preferable, since it is anticipated that non-thermal effects in irradiated silicon will be studied using a T_e-dependent potential in the future. The MOD potential key properties compared against Tersoff T3 (third revision of the Tersoff potential for Si) and Stillinger and Weber (SW) [203] are shown in Tab. 7.3 (after [277]). In this chapter, we are reporting the results obtained using the T3 potential, which reproduces the amorphous structure and crystalline-to-

Table 7.3: Interatomic potential comparison for Si (after [277, 279]). The best fits to the experimental data for a particular property are in bold.

Property	Symbol	Unit	SW [203]	T3 [201]	MOD [202]	exp. [277]
Melting point	T_m	K	1691	2547	**1681**	1683
Latent heat of melting	H_m	kJ/mol	30.9	41.8	**33.7**	50.6
Density change	$\Delta\rho_{c-l}$	$\frac{\rho_l}{\rho_c}$ [%]	**7.7%**	2%	14%	10%
Liquid coordination			4.89	4.6-5.0	**5.6**	6.4
Amorphous density	ρ_a	g/cm^3	2.341	2.291	2.311	2.05-2.52
Latent heat of amorphisation	H_{c-a}	kJ/mol	30.9	**41.8**	33.7	50.6
Crystalline specific heat capacity	C_c	J/(g K)	0.999	1.00	**1.02**	1.04
Liquid specific heat capacity	C_l	J/(g K)	1.256	1.3	**1.17**	1.04

liquid density change, however it does not reproduce the melting point well. We chose T3 due to technical constraints, i.e. the initial lack of the MOD implementation in DL_POLY (which was later fixed with the help of the present author).

For Ge, we will be using a Tersoff potential form too with the parameters from [280]. Similarly to the Si case, this potential reproduces the solid and amorphous phases well, however it overestimates the melting point by about 1000 K.

7.3 Simulation considerations

7.3.1 Continuum-only

The continuum-only eiTS model is solved with a custom code using the algorithms described in Sec. 4.3.4. For Si the electronic and ionic parameters are listed in Tab. 7.1 and Tab. 7.2, respectively. We simulate Si over $100 \times 100 \times 1$ with a grid point volume of $\Delta V = 10$ Å. We use a constant time-step of $\Delta t_{FD} = 2.5$ as, which conserves the total energy of the system (sum of the lattice and carriers systems). The initial energy deposition in the lateral directions is Gaussian of $\sigma = r'_{ion} = 0.75$ Å (see Tab. 2.1) corresponding to a specific ion energy of $E' = 0.07$ MeV/u, while the time deposition is a decaying exponential with a characteristic time of $\tau_d = 1$ fs. The boundary conditions (Neumann) confine the evolved quantities (i.e. T_i, N and U) in the direction normal to the SHI impact. In the lateral directions Robin's boundary conditions are applied, to reflect energy dissipation into the bulk, which converge to the following values:

$$N_\perp \to N_{eq} \simeq 10^{-9} \text{ nm}^{-3}$$
$$U_\perp \to 1.19 \cdot 10^{-9} \text{ eV}$$
$$T_{i\perp} \to 300 \text{ K}.$$

7.3.2 MD-coupled

For iTS-MD swift heavy ion simulations in Si, the ionic system is subdivided into temperature cells, typically ~ 10 Å^3 in size or coarser. This, for a relatively small system of $50 \times 50 \times 10$

unit Si cells (200k atoms), corresponds to $25 \times 25 \times 5$ coarse grained ionic temperature cells (CIT) and a larger $75 \times 75 \times 5$ grid of electronic temperature cells (CET). Since the swift heavy ion travels at a normal incidence through the centre of the simulation cell we use Neumann boundary condition to confine the electronic energy in the z-direction. Therefore, only 5 (plus the additional 2 on each side for the 'halo' region) CETs are used in the z-direction. Additional CETs simulate the infinite bulk in the x,y-directions. Here the 'halo' regions are governed by Robin's boundary conditions with T_e converging to 300 K representing the electrons in the 'rest of the system'. The ionic system is not thermostated at the boundaries. The total simulation time is typically 80 ps. The iTS-MD model is run with a constant MD time-step of $\Delta t_{MD} = 1$ fs and a variable time-step for the (iTS) finite difference scheme, Δt_{FD}, having checked that it conserves energy under such strong non-equilibrium conditions. The initial energy deposition by an SHI is the same as in the continuum eiTS model.

For the eiTS simulations of Si, the same setup of 200k atoms is used, but divided into $25 \times 25 \times 5$ CITs and a slightly smaller $50 \times 50 \times 5$ CET grid due to the computational overhead associated with the grid size. We use the same boundary conditions as in the continuum case. We evolve the system over 50 ps with a constant MD time-step and a constant continuum part time-step of $\Delta t_{FD} = 1$ as.

For eiTS simulations of Ge we also use 200k atoms (simulation cell size: $28.36 \times 28.36 \times 5.67$ nm) with same number of grid points as for Si (CIT: $25 \times 25 \times 5$, CET: $50 \times 50 \times 5$). We additionally use stochastic boundary conditions in the ionic part of the system in the lateral direction (thickness of 1 nm at 300 K). The main difference to the eiTS Si setup is the initial lateral energy deposition, which was taken as a Gaussian with $\sigma = r'_{ion} = 1.24$ Å corresponding to $E' = 0.07$ MeV/u (Eq. 2.13).

7.3.3 Miscellaneous considerations

Optimal use of computational resources is paramount in sub-femtosecond time-step simulations, which are aimed to run for tens of picoseconds. A typical eiTS continuum solver simulation time-step (Δt_{FD}) for a grid of size $\Delta V = 10$ Å^3 is $\Delta_{FD} < 10$ as, which is equivalent to $> 100 \cdot \Delta t_{MD} = 1$ fs. In both model types (the continuum and the MD-coupled one), when most of the energy from the electronic system is transferred to the ionic one, they become decoupled and only the atomistic system is subsequently evolved. The minimum time-step required to evolve a heat equation in Si for the atomistic system is $\Delta t_{FD} \sim 2.5$ as (cf. $\Delta t_{MD} = 1$ fs), and so decoupling can speed up both simulation types significantly. Earlier simulations (which neglected the terms in $\nabla^2 E_g$) show that after a 60 keV/nm event in Si ($\tau_{ep} = 0.5$ ps) 99.9%, 99.95% and 99.99% of the energy is transferred to the atomistic system in 2.1 ps, 2.4 ps and 3.2 ps, respectively. Note that the errors carried in the discretisation of the initial Gaussian spike, both in time and space, for a narrow mean deposition radius in Si are of the order of $\sim 0.5\%$. Therefore it would be reasonable to decouple the electronic and ionic systems, once most of the energy transfer is complete, by a simple order of an uncertainty argument. For the continuum and MD-coupled eiTS models we thus decouple electronic system from the ionic systems at around $t \sim 2.0$ ps.

Initial eiTS model simulations, which allowed for a two-way energy exchange (from carriers to ions and vice-versa) indicated that much less than 1% of the total transferred energy goes back from the ionic system to the carriers. This allows us to simplify the simulations by considering a one-way energy exchange only. This is also a physical effect, the so-called cooling inhibition [150]. At a point when the electronic temperature falls locally below the ionic one, as the electronic energy diffuses away, there is insufficient carrier density for an effective energy transfer from ions to electron-hole pairs to occur. This shows a difference in physics, and hence the modelling requirements, of band-gap and metallic materials. In the latter case the energy from the hot ions can be transferred back to the colder electrons and subsequently diffused away out of the hot region.

7.4 Results for Si

7.4.1 The continuum eiTS model

7.4.1.1 Carrier confinement

In silicon the band-gap depends, to some degree, on the lattice temperature and carrier density and can be expressed as [273]:

$$E_g = E_g(T_i, N) = 1.16 - 7.02 \cdot 10^{-4}\ T_i^2/(T_i + 1108\ \text{K}) - 1.5 \cdot 10^{-8} N^{1/3}\ \text{eV}. \tag{7.4}$$

The terms in the J and W currents that depend on the gradients in E_g inhibit diffusivity [43]. Following a swift heavy ion irradiation event the lattice temperature can be constant in some regions for up to several picoseconds due to latent heat of melting or vaporisation. However, since the variation of the band-gap in silicon is dominated by the lattice temperature, rather than the number of carriers, the band-gap becomes nearly constant in the regions where phase transitions occur. On a picosecond timescale the carrier diffusivity inhibition is quite strong relative to the terms governed by $\nabla^2 T_e$ and $\nabla^2 N$, thus carrier confinement occurs around constant band-gap regions.

Carrier confinement can potentially have an impact the resultant molten region size, as more localised carriers enhance the electron-phonon coupling strength. It can affect impact on the numerical stabilities of the equations. Since the carriers are building up around regions where the band-gap is constant, in turn the spatial gradients in N increase. For the numerical solution to be stable, such high gradients require smaller mesh sizes (recall the Fourier condition $F = \alpha \frac{\Delta t}{\Delta x^2}$ from Sec. 4.3.2), i.e. smaller time-steps. As shown in the simulations, adequate time-stepping requires $\Delta t < 10$ as, which becomes quite computationally expensive.

The expression for the band-gap gradient can be rewritten as [43]:

$$\nabla E_g = \frac{\partial Eg}{\partial T_i} \nabla T_i + \frac{\partial Eg}{\partial N} \nabla N \tag{7.5}$$

where $\frac{\partial Eg}{\partial T_i}$ and $\frac{\partial Eg}{\partial N}$ terms can be obtained analytically from the expression for band-gap, Eq. 7.4. Since N varies in space (i.e. no regions where band-gap is constant), thus the $\frac{\partial Eg}{\partial N} \nabla N$

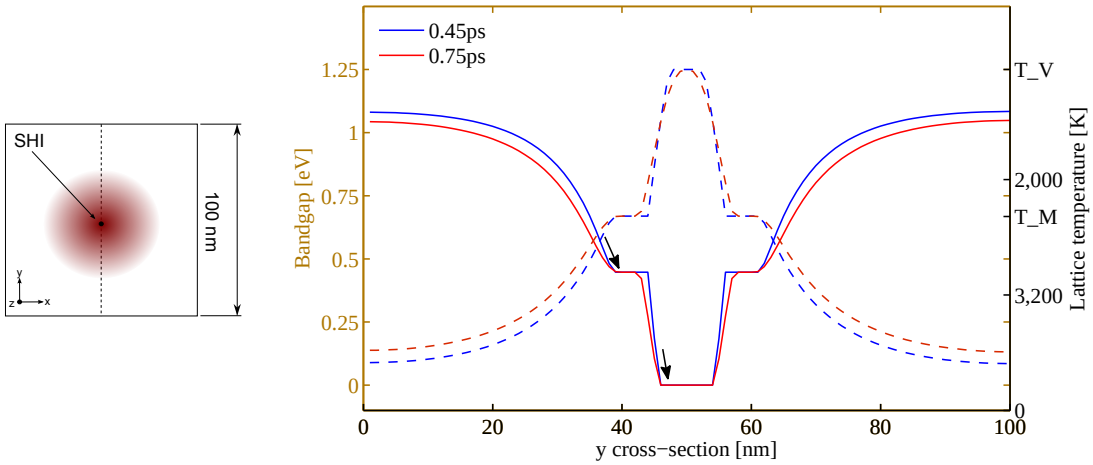

Figure 7.2: (Left panel) SHI impact simulation setup; (right panel) cross-section of lattice temperature (right y-axis, dashed line) and band-gap response to lattice temperature changes (left y-axis, solid lines) in Si at 0.45 ps and 0.75 ps following a 60 keV/nm irradiation event. It is apparent that the band-gap in silicon depends strongly on the lattice temperature; it becomes constant, where a phase transition occurs in the atomistic lattice. Since the band-gap can be thought of as potential for carrier diffusion inhibition, carriers would build up in the regions indicated by the arrows.

term above does not confine the carriers, while some carrier confinement can still occur due to the $\frac{\partial Eg}{\partial T_i}\nabla T_i$ term.

The diffusivity inhibition term (through $\nabla^2 E_g$) dominates over the carrier density currents coming from the $\nabla^2 N$ and $\nabla^2 T_e$ terms at $\sim$ 1-3 ps of the simulation time. This causes the spike in carrier density (in the centre of the simulation cell) to increase within that time frame, which is followed by non-inhibited diffusion. In semiconductors, the carrier confinement process has been confirmed by both theory and experiments [33]. This effect is illustrated in Fig. 7.2 and Fig. 7.3.

In silicon, the band-gap disappears, when the atomistic lattice melts. However, to avoid discontinuities in the band-gap function in the continuum finite difference solution, it is assumed that the E_g follows Eq. 7.4 analytically, until it reaches $E_g = 0$. This occurs at $T_i = 2411$ K, neglecting the contribution from the carrier density, which is mid-way between melting (T_m) and vaporisation (T_v) points for Si. This implies that in the continuum model we are allowing the material properties to superheat until that temperature is reached. An alternative approach is to cap the band-gap to a minimum value, for instance equivalent to a band-gap at the melting point, effectively disallowing silicon to become metal-like even transiently. Such approach has been applied in [7]. Note that significant changes in the band-gap (leading to a collapse) cannot occur at the sub-picosecond timescale, because of insufficient atomistic movement at such short times. When the melting or vaporisation temperatures are exceeded, melting or vaporisation cannot occur instantaneously, but both require picoseconds for the regions of liquid (or gas) to nucleate. Until this happens, the region remains solid, or liquid, respectively. This and other limitations, based on the lack of atomistic information in

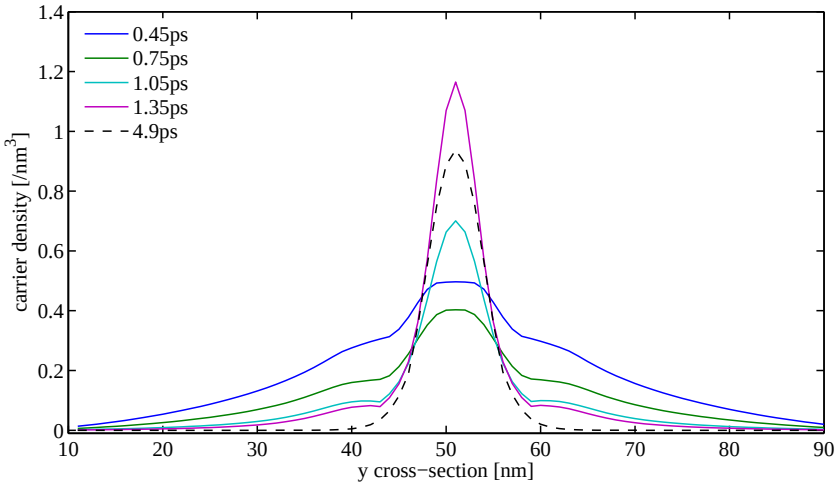

Figure 7.3: Cross-section of carrier densities at various simulation times (from 0.45 to 4.90 ps) in Si. Due to diffusion inhibition (from carrier confinement) the peak of carrier density increases after ~ 1 ps and returns to uninhibited diffusion at ~ 3 ps.

the continuum model, cannot be tackled within this scheme.

7.4.1.2 System dynamics

The time evolution of the local electronic and lattice temperature, and carrier density at the centre of a track for Si during a $S_e = 50$ keV/nm event ($\tau_{ep} = 0.5$ ps) is shown in Fig. 7.4. The rising carrier density and electronic temperature illustrate the time-dependent deposition of the electronic energy $A(r[v_{ion}], t)$ over the first 5 fs of the simulation. At later stages, up to $\sim$ 200 fs, the electronic temperature is still rising. This is because the band-gap decreases with the increasing lattice temperature and therefore the potential energy of carriers is transferred to the kinetic one. Moreover, the Auger recombination process, which is dominant over the impact ionisation, reduces the number of carriers without feeding the energy back to the lattice and, in effect, increases the electronic temperature. The computed values of the maximum electronic temperature for Si compare reasonably well with experiment; electronic temperatures of $T_e > 5 \cdot 10^4$ K obtained from Auger electron spectroscopy [149] were reported. After 200 fs, the local electronic temperature starts to decrease due to open boundary conditions in U and N and the energy exchange with the lattice. At $\sim$ 10 ps it equilibrates with the lattice. Both T_e and T_i cool down past that point due to open boundary conditions in all evolved quantities. The centre of the track exceeded the melting temperature between 0.2-2.0 ps, and hence a track is assumed to be formed. The higher the initial stopping power, the higher the resulting average peak in the electronic and lattice systems temperature.

For a different SHI event in Si ($S_e = 60$ keV/nm, $\tau_{ep} = 0.3$ ps), the local lattice temperature exceeds the melting point as far as 8 nm from the centre (see Fig. 7.5). Flat regions in maximum lattice temperature correspond to melting and vaporisation points. The lattice temperature reaches a peak of vaporisation temperature, T_v, very quickly at ~ 0.1 ps and the most excited part of the lattice cools down to below T_v as late as ~ 1.5 ps. The subsequent resolidification

Figure removed due to third party copyright restriction

Figure 7.4: Evolution of the lattice temperature (dot-dashed line), the electronic temperature (solid line) and the carrier density (dashed line) at the centre of a 50 keV/nm ion track in Si. The carrier confinement effects is responsible for the small carrier density peak at ~ 6 ps. *Figure reproduced from [7].*

starts at ~ 3 ps and finishes at about 10 ps when the temperature drops below the melting point presumably forming an amorphised region. Since typically 99% of the energy is deposited in the lattice at ~ 1 ps and most of the carriers have already diffused making the electron-lattice energy exchange rate very low at that point, the ionic thermal diffusion becomes the dominant process driving the T_i drop to the equilibrium 300 K.

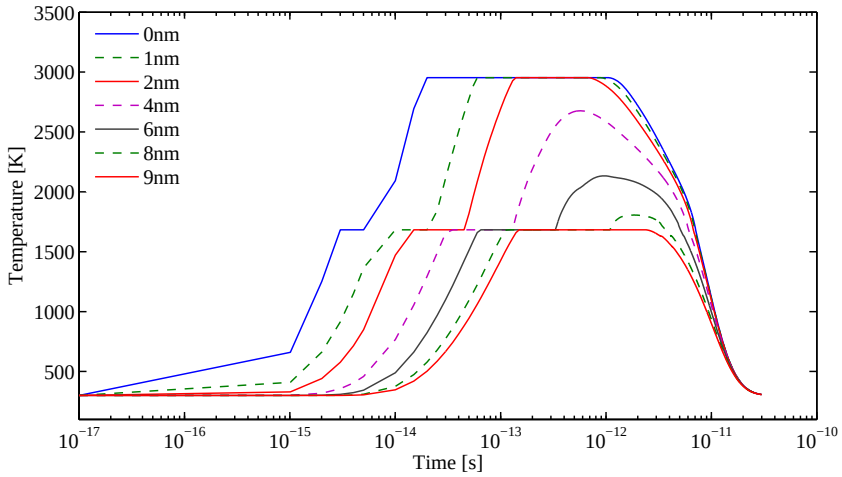

Figure 7.5: Time evolution of the lattice temperature at various radial distances from the centre of the energy deposition in Si ($S_e = 60$ keV/nm). The amorphised track radius (melting point T_m condition) can be read off from the figure easily - it is 8.5 ± 0.5 nm.

7.4.1.3 Fitting to track radii

The most important aspect of the simulation and one that can be verified experimentally is the amorphised track radii versus stopping power dependence. One criterion of track formation for

Si, corresponding to a molten phase transitions, for stopping powers in the range 20-90 keV/nm is plotted in Fig. 7.6. The latent track radii results compare reasonable well with experiment (carbon cluster C_{60} irradiation with $E' = 0.07$ MeV/u [281, 282]) for $\tau_{ep} = 0.4$ ps. Note that the vaporisation was not found to be occurring at relaxation times as low as 0.3 ps and stopping powers as high as 90 keV/nm, unlike in other models [150].

In addition, we compare the eiTS solution (denoted "full model") with its slightly simplified, but more computationally efficient version presented in [8]. The simplified solution assumed infinite κ_{e-h} and neglected the band-gap terms. The "full model", which introduces band-gap terms and finite conductivity, produces slightly greater melt radii for Si for the same values of the fitting parameter τ_{ep}, as expected.

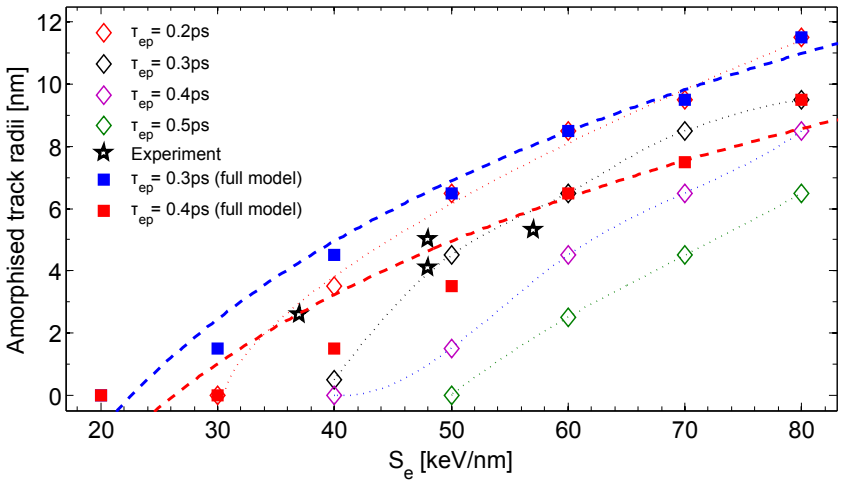

Figure 7.6: eiTS continuum model fit of the relaxation time τ_{ep} to the experimental data [281, 282] of track radii versus electronic stopping power in Si. The current eiTS model results (indicated as 'full model') is contrasted with the simplified eiTS solution presented in [8]. Only the molten phase is presented as an amorphisation criterion. The "full model" dashed lines are of the $a \cdot \log(x) + b$ form.

7.4.2 MD-coupled models

7.4.2.1 iTS-MD - parameter sweep

We now turn to the iTS model, which is based on the two-temperature formalism and on theoretical grounds applicable to metals only. Treating it is an effective theory, as applied to semiconductors, we examine if it can reproduce the experimental trends, nonetheless. We perform an extensive parameter sweep of D_e and τ_{ep} to match the experimental result of track radii resulting from C_{60} (carbon cluster) SHI irradiation in Si. We examine the impact of the electron-phonon relaxation time on the resultant radii, keeping $D_e(T_e)$ fixed, and vice-versa. The main finding is that a unique (i.e. one-to-one) mapping between the parameter set $\{D_e, \tau_{ep}\}$ and the resultant radii does not exist. This can be seen clearly from Fig. 7.7, where by varying one parameter a good experimental agreement with track radii can be obtained within a still reasonable (on physics grounds) parameter set. For instance, two very different

parameter sets {80 cm^2/s, 2.0 ps} and {180 cm^2/s, 1.15 ps} reproduce the results fairly well. This result implies that further research needs to be performed to narrow down the parameter range required in iTS in order to draw definitive conclusions about the effectiveness of the iTS model for describing latent track radii formation.

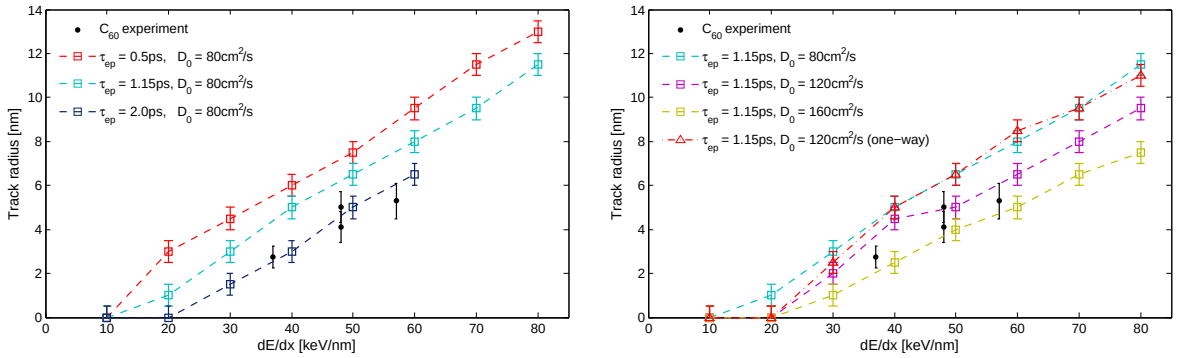

Figure 7.7: iTS-MD model $\{D_e, \tau_{ep}\}$ parameter set sweep in Si simulations. The black data points show the experimental data [281, 282] of track radii. "One-way" denotes cooling inhibition condition (i.e. no energy transfer from ions to electrons).

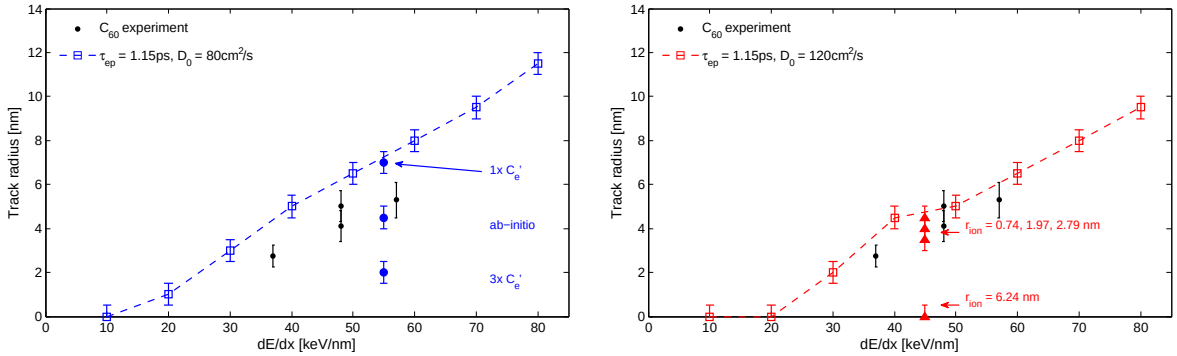

Figure 7.8: iTS-MD model C_e and r'_{ion} parameter sensitivity test in Si simulations. C'_e denotes the electronic specific heat capacity from the free electron gas model.

We also test for parameters sensitivity with respect to the electronic specific heat capacity, C_e, and the lateral size of the initial distribution function, r'_{ion}. First, the use of the incorrect free electron gas form of C_e [150] (even for wide band-gap materials in [59]) leads to incorrectly elevated electronic temperatures, and thus to greater track radii. We see in Fig. 7.8 that the use of the free electron gas calculation in effect severely overestimates the track radii for a particular simulation. Furthermore, Fig. 7.8 indicates that the choice of r'_{ion} is not that critical (at least for the chosen parameter set) and varying it in range of $0.7 - 2.8$ nm has a small impact on the track radii results.

The evolution of electronic and ionic temperatures for an exemplar iTS-MD simulation in Si is shown in Fig. 7.9. The equilibration of the ionic and electronic temperatures occurs quite quickly at time $t \sim 0.5$ ps. This is due to the electron-phonon coupling effect as well as high diffusivity. In fact, at around 0.5 ps the local T_e is slightly lower than T_i and at this point

the energy is transferred from the ions to the electrons and subsequently diffused away from the simulation cell. The ionic temperature falls down below the melting point at around 2 ps and quenching of the liquid phase occurs. The time evolution of an ion track is presented in Fig. 7.10. The main advantage of the MD modelling is the access to atomistic information. This structural data can be used for more precise comparison between the modelling work and the results from different experimental techniques [2].

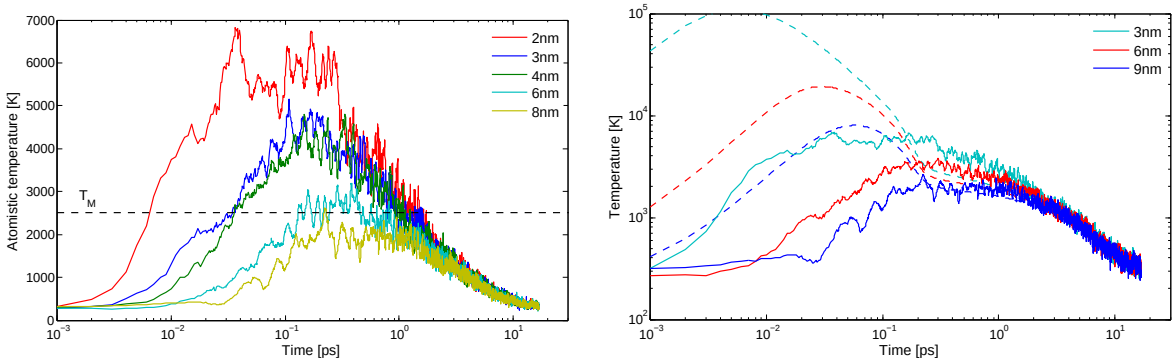

Figure 7.9: (Left panel) Ionic temperature profiles at different radial profiles from the ion impact centre; (right panel) Electronic (dashed line) and ionic (solid line) temperatures at three different radii from the centre. Resultant track radii is 3.5 nm. (Si, $S_e = 20$ keV/nm, $D_e = 80$ cm^2/s, $\tau_{ep} = 0.5$ ps).

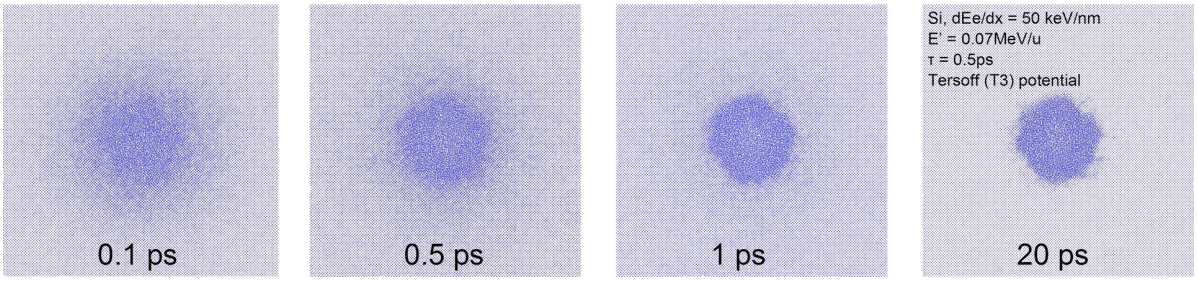

Figure 7.10: Snapshots (top view, projections down the [001] axis) of ion track evolution in Si simulated in the iTS-MD model ($S_e = 50$ keV/nm, $D_e = 80$ cm^2/s, $\tau_{ep} = 0.5$ ps). Due to the scale the individual atoms are not visible and thus the amorphous regions appear as darker areas in the figure.

7.4.2.2 eiTS-MD - fitting the e-p coupling

The coupled eiTS-MD model incorporates an additional continuity equation for carrier density and can hence account for some the effects associated with a finite band-gap. The eiTS-MD simulations give a good fit to the experimental results for $\tau_{ep} = 0.15$-0.20 ps; see Fig. 7.11. This is slightly lower than the continuum-only result with $\tau_{ep} = 0.3$-0.4 ps, which could be attributed to three effects. First, in the MD simulations superheating of the lattice can occur without formation of a latent track. This effect can be particularly strong when the temperature rises above the melting point T_m (or even the lattice stability point of $1.25 \cdot T_m$) for a very short

period of time: typically less than a picosecond, which is too short for an atom to move far enough and become a nucleation point for a phase transition. Therefore, unlike in the continuum model, T_m is not the criterion for latent track formation. A transient superheating effects is demonstrated in Fig. 7.12. The second, more technical, reason is due to the non-physically high melting point of the T3 potential used. The T3 potential gives higher energies of melting of Si, compared to experimental values, and a lower value of τ_{ep} compensates for this effect. Thirdly, the MD-coupled scheme does not consider the band-gap term (due to associated model complexity, the band-gap should depend in a non-trivial way on the local atomistic structure), which increases the diffusion of the carriers and their energy. Preliminary continuum-only results for Si indicate that including the $\nabla^2 E_g$ terms could lead to $10-20\%$ increase in track sizes. In short, the MD-coupled scheme provides a more physical description of the latent track formation processes by including superheating. However, the imperfections of the interatomic potential introduce another source of uncertainty to the model. The eiTS-MD fits are quite far off the $\tau_{ep} = 1.0 - 2.0$ ps values reported for iTS (for a range of diffusivities). This is probably due to the high electronic thermal conductivity (we take $\kappa_{e-h} \propto T_i \cdot N$), which is included in the eiTS model, and this hence efficiently diffuses the carriers' kinetic energy out of the excited region.

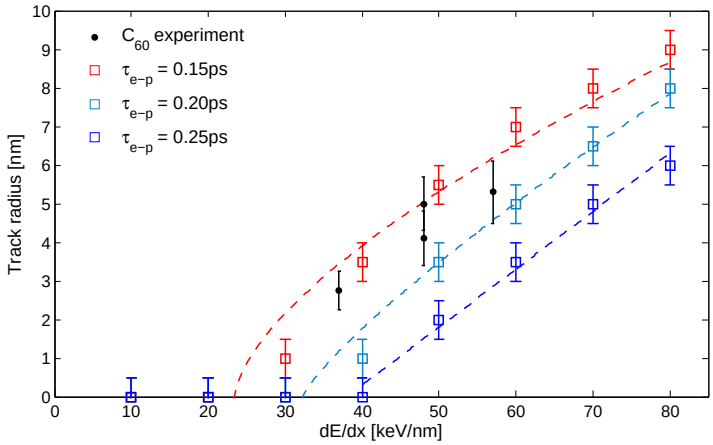

Figure 7.11: eiTS-MD model τ_{ep} fit to carbon cluster SHI latent tracks in Si.

The main difference between the eiTS and the iTS models is that carrier dynamics dominates the resultant track radii in eiTS, while T_e evolution dominates track formation in iTS. In Fig. 7.13 different radial profiles of carrier density and temperatures evolution are shown. The electronic temperature quickly equilibrates spatially, while there is a significant gradient in carrier number, at least up to 1 ps. Because of this strong electron-phonon coupling required in the model to reproduce the ion tracks, most of the energy gets transferred to the lattice at around 0.1 ps. The electronic temperature gets below the ionic one around 1 ps and the energy transfer from electrons to ions ceases. The energy transfer from ions to electrons is inhibited due to the lack of carriers.

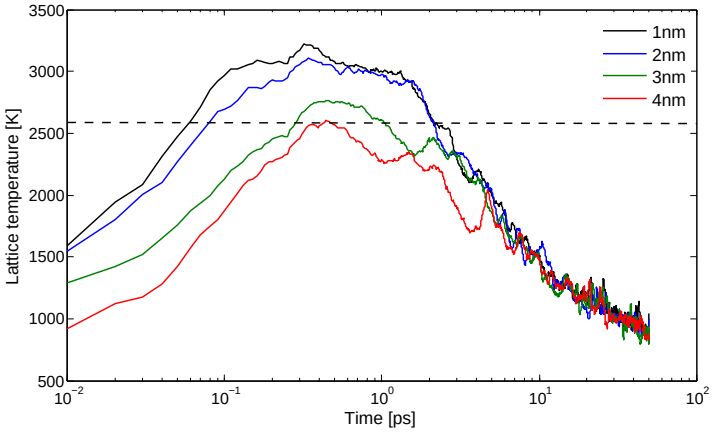

Figure 7.12: eiTS-MD model ionic temperature evolution profiles in Si. Despite the fact that superheating persisting up to 2 ps, no latent track was formed in this simulation (i.e. Si maintained crystallinity). The dashed line indicates the melting point of Si as reproduced by the T3 potential; the experimental value ($T_m = 1683$ K) is much lower. The ionic temperature plot is a 51-point moving average of the temperature data. ($S_e = 30$ keV/nm, $\tau_{ep} = 0.2$ ps, $E' = 0.07$ MeV/u).

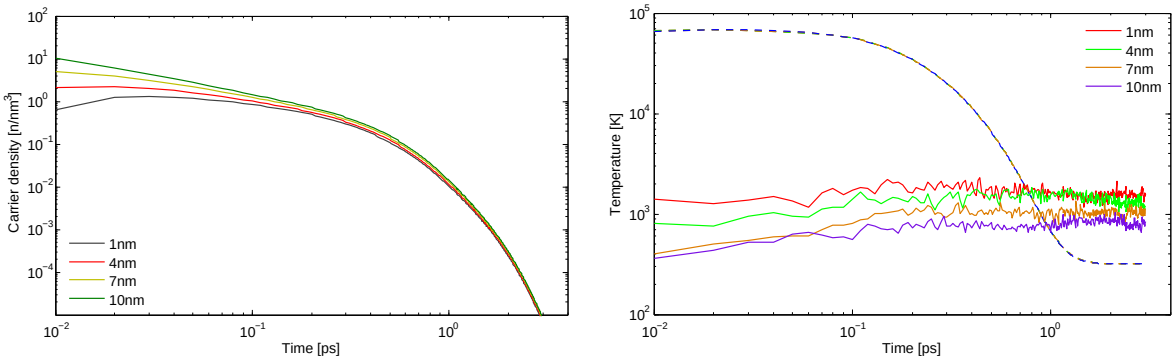

Figure 7.13: eiTS-MD radial profiles of carrier density (left panel) and ionic/electronic temperatures evolution (right) in Si. No latent track formed in this scenario. ($S_e = 40$ keV/nm, $\tau_{ep} = 0.5$ ps, $E' = 0.07$ MeV/u).

7.5 Results for Ge

The results from the continuum and MD-coupled fits to the ion track radii experimental data in Ge (carbon cluster C_{60} irradiation [283]) are shown in Fig. 7.14 and Fig. 7.15, respectively. Similarly to the case of Si, the continuum model ($\tau_{ep} = 0.15$ ps) gives greater electron-phonon relaxation times than the MD-coupled model ($\tau_{ep} = 0.05$ ps). As in Si, this is expected because of the superheating effects captured in the MD-coupled scheme and the imperfections of the interatomic potential - the Tersoff potential for Ge also overestimates its melting point. The results show a smaller τ_{ep} required for a good fit than in the Si case. This can be simply attributed to the greater ambipolar diffusivity and carrier mobility in Ge. Therefore, as carriers diffuse away quicker, a stronger electron-phonon coupling is required to produce a latent track. Another model feature can be inferred from the figure inset in Fig. 7.15 - the track radii

are exponentially sensitive to the value of τ_{ep}. Carrier density and energy show similar spatial trends to Si, as expected (Fig. 7.16), with carrier density having a stronger spatial gradient than carrier energy. Note that since the electron-phonon coupling is so strong, the ionic temperature reaches a peak very quickly (Fig. 7.16) at ~ 0.1 ps. The ionic system temperature equilibrates spatially at around 30 ps and subsequently slowly cools down, mainly due to the ionic thermal conductivity, with the energy being lost at the MD boundaries at 300 K.

In addition, we have performed basic parameter eiTS model sensitivity analysis in Ge. The model is sensitive to the choice of the ambipolar diffusivity (a factor of 0.5 decrease in D, results in an 1.5 factor increase in ion track radii). The model has been shown to be relatively insensitive to the variations in the remaining input parameters, such as Auger recombination and carrier mobility. Since, the carrier density diffusion is slower than the energy conduction, which has minimal spatial gradients on the nm scale within the first 1 ps, the carrier density evolution is a determinant of the resultant track radii.

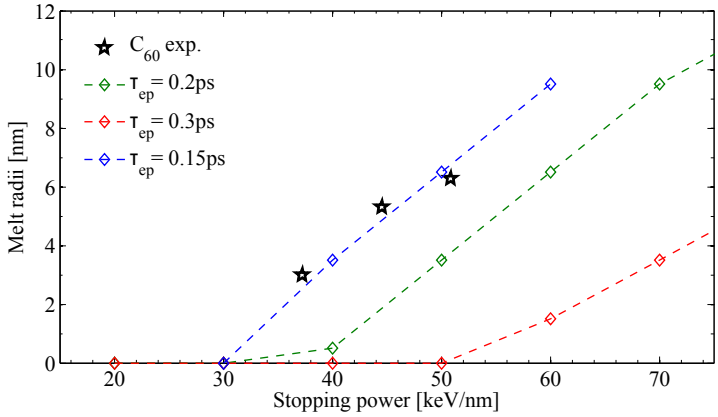

Figure 7.14: eiTS continuum model τ_{ep} fit to latent tracks in Ge. A value of $\tau_{ep} = 0.15$ ps (which corresponds to a very strong electron-phonon coupling) gives a reasonable fit to the sparse experimental data (carbon cluster C_{60} irradiation).

7.6 Model criticism

The best fit electron-phonon coupling strengths from the eiTS models in the case of Si and Ge are very strong, leading to an almost instantaneous deposition of electronic energy into ions. The relaxation times are lower than the ones reported in literature (cf. $\tau_{ep} = 0.3$ ps in Ge [284]), however there is a huge error typically associated with these. Such short deposition time is problematic, because of the thermalisation assumption for both ionic and electronic systems, which the two-temperature formalism is based on. During the time of $\tau_{ep} = 50$ fs, which the eiTS-MD model provides as the best fit in Ge, the electrons might not have enough time to thermalise and therefore transfer the energy to ions. The typical thermalisation times are of the order of 10-100 fs, potentially violating the 2T assumption.

The electronic temperatures at the centre of a track are reasonable given the huge electronic stopping power and a highly localised deposition. For example, in Si carrier temperatures of

Figure removed due to third party copyright restriction

Figure 7.15: (a) eiTS-MD model τ_{ep} fit to latent tracks in Ge. The inset shows the track size sensitivity on τ_{ep} for a particular value of S_e; (b) an exemplar latent track at $\tau_{ep} = 0.05$ ps and $S_e = 35$ keV/nm. *Parts of the figure reproduced from [6].*

Figure removed due to third party copyright restriction

Figure 7.16: eiTS-MD model radial profiles (at $r = 1$, 6, 10 nm) of ionic temperature and carrier density/energy in Ge. This SHI impact produced a 2 nm radius latent track. ($S_e = 50$ keV/nm, $\tau_{ep} = 0.10$ ps, $E' = 0.07$ MeV/u). *Parts of the figure reproduced from [6].*

several eV are expected (see Fig. 7.13). In the 2T scheme, we are neglecting the effects of the electronic excitations on the interatomic interactions, which are approximated to be of that of a ground state. However, while this has been shown to be a good approximation until about $T_e' = 0.8$ eV for metals (see Sec. 6.3.2.2), we expect it to hold for Si until about $T_e' < (0.8 \text{ eV} + \frac{1}{2}E_g) \sim 1.5$ eV. Preliminary *ab initio* DFT calculations presented in Fig. 7.13 can confirm this crude estimate. At around $T_e = 0.5$ eV the electronic pressure induced by the change of the interatomic potential minimum starts building up linearly with T_e. At around $T_e = 1.5$ eV it is greater than the tensile strength of Si and at around $T_e = 2.5$ eV, the Si-Si interactions are no longer bonding and the electronic pressure increases to a level equivalent to threefold the tensile strength of the material (see Fig. 7.17). This leads to the conclusion

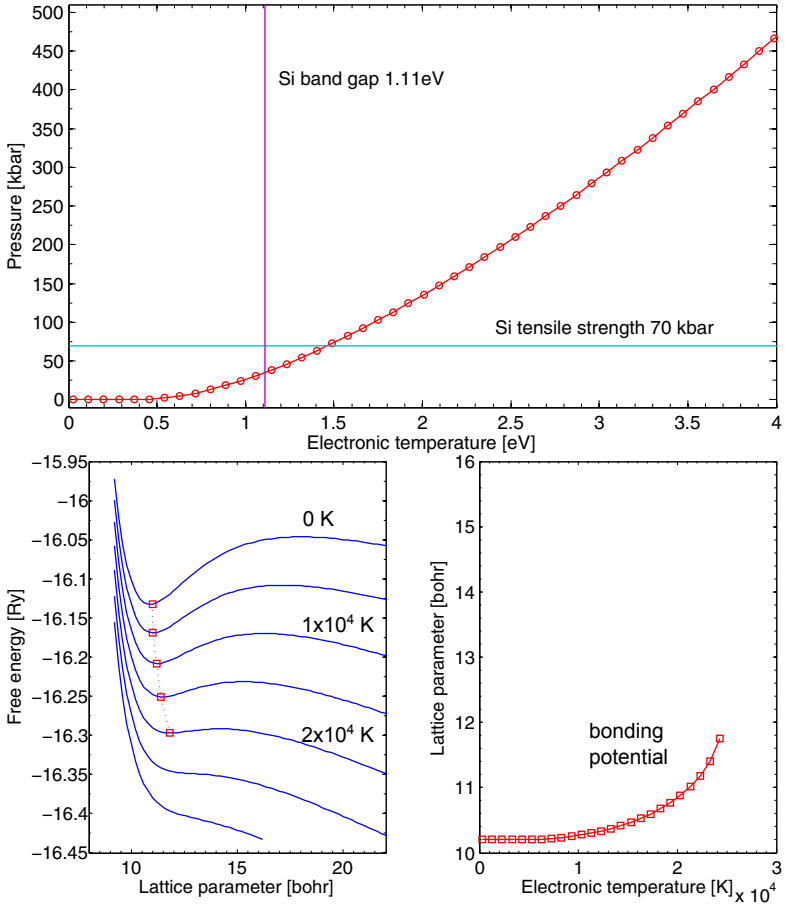

Figure 7.17: (top) Electronic pressure as a function of electronic temperature in Si; (bottom-left) Free energy versus lattice parameter at different electronic temperatures; (bottom-right) lattice parameter versus electronic temperature. Technical details: DFT data obtained with Quantum Espresso, $4\times4\times4$ ($1\times1\times1$ shifted) k-point mesh, local density approximation, norm conserving pseudo-potential (`Si.pz-vbc.UPF`), 120 bands, plane-wave energy cutoff 25.0 Ry.

that the non-thermal effects of a drastic change in the interatomic potential, can have a strong effect on the latent track formation. Thus, these effects have to be taken into account in the future comprehensive studies of swift heavy ion irradiation.

7.7 Discussion and summary

In summary, we have performed a series of ion track simulations in Si and Ge, using two models: iTS and eiTS, with the latter being specifically designed for band-gap materials by including band-gap effects and carrier dynamics explicitly. We have used both continuum and the more sophisticated MD-coupled version of the models. The MD-based versions provide the atomistic details of the latent track evolution and the resultant track morphology, which can be directly compared with experiments measuring defect-rich channels (Rutherford backscattering spectrometry) or local density changes (small angle X-ray scattering) [2].

The main appeal of iTS-MD model is that it has only two parameters (τ_{ep}, D_e) to be

fitted to the experimental track radii, assuming that C_e is obtained through first principles calculations. It follows that, if one of the remaining parameters is fixed, we could easily find the remaining one fitting it to the measured SHI track radii. We note that there is no unique mapping between the resultant track radii and the two parameters, as shown in the parameter sweep test. In addition, the exact correlation between the electronic diffusivity and electron-phonon coupling is unknown, although some models regarding this question have been put forward for metals.

The eiTS-MD model contains more parameters and provides a more physical description of the SHI track formation process. In particular, it is assumed to reveal the correct electronic system dynamics, such as carrier confinement and cooling inhibition (minimal energy transfer from ions to the electrons). The former process is due to the band-gap changes as a result of ionic temperature increase. The latter effect is a result of the dynamics of carriers and their kinetic energies. Furthermore, due to the correct sink/source terms in the carrier density continuity equation, the model can provide a more faithful local T_e, neglecting the uncertainty associated with the electron-phonon coupling and the electronic system diffusivity. The main criticism stems from the model complexity. The behaviour of "known" additional parameters under the conditions of high electronic excitations is poorly known. In particular, the carrier mobility rescaling (with N and T_i, also possibly with T_e) via the extended Wiedemann-Franz law can be problematic and may have led to orders of magnitude uncertainty in κ_{e-h}. Furthermore, the expression for C_{e-h} should be matched with the *ab initio* data to provide the correct number of carriers to start the simulation with. Lastly, the model is more computationally expensive and the physical effects added by the variable E_g are difficult to implement in the MD-based version.

The purpose of modelling, in general, is twofold. A "good model" should enable one to reveal the physical processes by including the relevant theory components and examining which of these are important and which are not. Secondly, a "good model" is transferable and predictive, and should therefore be based on a minimal set of parameters required, not to overfit to the available data. The eiTS-MD model does a good job on providing the first requirement, but bad on the latter. It includes the relevant physical properties and provided a valuable insight into non-equilibrium carrier dynamics, however due to its complexity and the number of parameters required, it is not immediately transferable and can be over-fitting the sparse experimental data. The iTS model does the opposite; for band-gap materials it scores poorly on physics grounds, however due to its simplicity and effectively capturing the main physics of diffusion versus electron-phonon coupling, it can be made transferable to other materials more easily.

MD-coupled schemes are more sophisticated and more accurate versions of the thermal spike models, as they naturally include the effects of superheating and potentially recrystallisation. They also enable direct comparison with experimental measurements of track radii. Nonetheless, in order not to introduce any unwanted additional uncertainties, the interatomic potentials must correctly reproduce the thermal properties of the studied materials - in particular the melting point and any solid-to-solid phase transitions.

Finally, we have shown that local electronic pressure due to the changes of the potential energy surface at high T_e cannot be neglected. In the case of Si (and very likely also in Ge), given the somewhat unrealistic high electron-phonon coupling required for the eiTS model to be fitted to existing data and the *ab initio* data which shows a non-bonding potential already at $T_e \sim 2.5$ eV, the electronic effects are likely to be the dominant in the SHI formation. Further investigation into the impact of the change of the bonding character (a non-thermal effect) and electron-phonon coupling (thermal) is required. However, it is conditional on the progress in the T_e-potentials development as *ab initio* methods cannot access spatiotemporal scales of SHI track formation.

Chapter 8

Concluding remarks

8.1 Research aims (revisited)

As discussed in the general introduction (chapter 1), the ability to understand and ultimately predict radiation damage and ultrafast dynamics processes will have huge implications for both fundamental science and technology. Knowledge of atomistic and electron dynamics at high electronic excitations will most likely help in the design of radiation-resistant materials. In particular, it will have a strong impact on materials technology for both fission and fusion reactors, and for space applications. Additionally, it is envisaged that the progress in the broader field of ultrafast science will eventually enable us to control the electronically excited state of matter and hence its macroscopic properties leading to, for instance, light-switching materials functionality. Modelling advancements are highly sought for and particularly timely not only for metals, but also for band-gap materials. For instance, predicting the exact structural changes in quartz under swift heavy ion irradiation will advance the nano-fabrication process of optical devices, as the refractive index of quartz can be tuned by irradiation.

The progress in gaining insight or even observing ultrafast dynamics and radiation damage at the atomic scale is conditional upon developing transferable, large-scale, predictive and rigorously justified models, which are ideally free of adjustable parameters. As presented in the theory (chapter 2) and the literature review (chapter 3) sections, the "standard" modelling options currently available are unfit to tackle the problems of primary radiation damage yield or photo-induced phase-transitions. Indeed, a simultaneous physical description of the electronic excitations (such as electron dynamics and electron-ion interaction) and almost a mesoscopic scale to simulate microstructural evolution is required in order to capture such processes. These have been for a long time mutually exclusive modelling requirements due to a trade off between models accuracy and their computational expense.

The modelling method presented and applied in this thesis is a variant of the augmented molecular dynamics (MD) model, which incorporates a mechanism for the electronic energy storage and redistribution at a level of an electron fluid coupled with the ionic motions represented by MD. The model uses a concurrent physical description of an effective electron-ion dynamics via a non-equilibrium Langevin thermostat. Its relatively simple electron fluid de-

scription was applied in metals and extended to account for the finite band-gap effects in semiconductors. The technical details of the model are outlined in the simulation techniques section (chapter 4). In this thesis, the coupled continuum-MD method has been successfully applied to tackle three classes of challenges: ultrashort laser pulse excitation of nano-films (Au), swift heavy ion irradiation of semiconductors (Si, Ge) and primary radiation damage production from collision cascades (Fe). This augmented MD model has provided us with a large-scale atomistic description of the effects of electronic excitations, which represents a major step in building a predictive and transferable direct simulation model for radiation damage and ultrafast dynamics.

8.2 Summary and conclusions

In brief, we have adapted the augmented molecular dynamics method to investigate a wide range of non-equilibrium processes. We have designed and implemented two versions of the method extensively advancing the capabilities of the DL_POLY molecular dynamics code. The one for metallic systems is based on the original two-temperature formalism, while the one for band-gap materials solves a Boltzmann transport equation and accounts for the variable carrier density. This thesis presents the versatility of the augmented molecular dynamics method as applied to different classes of physics problems. Each of these scenarios has led to different key results and conclusions.

In chapter 5 we have investigated the impact of the electronic stopping and the electron phonon-coupling effects on the primary radiation damage yield in bcc iron generated with 50-100 keV primary knock-on atoms. First, depending on the way the electronic stopping losses are handled (for instance by changing the low velocity cutoff in the electronic friction term), different results of the residual Frenkel pair defects are obtained. Second, the electronic-phonon coupling effects are also sensitive to the details of the model implementation and in particular to the thermalisation time at which the electron-phonon coupling is presumed to be effective. An analysis of the defect dynamics enabled us to identify competing effects, namely defect creation and defect annealing, depending on the details of the electron-ion interaction. In general, the inclusion of the electron-phonon coupling increases quenching (i.e. decreases defect annealing) and consequently increases the residual defect number, with one exception[1]. We note that all of the results are statistically significant, as we have employed twenty cascades for each simulation type. While we do not make a recommendation on the exact parameterisation of the electronic effects in the collision cascades, we have proven that the resultant primary radiation damage is quite sensitive to the choice of the electronic effects treatment. This represents the first rigorous and systematic study of this type, which clearly shows that there are still open questions in collision cascades studies, which need to be addressed in order to build a comprehensive and predictive radiation damage model. The results presented will have

[1]The exception is the low friction cutoff condition, where electron-phonon act in a mutually exclusive way to electronic stopping. Here, a minimal annealing effect was observed.

great practical implications, as these will serve as input to other modelling strategies, which are higher up in the multi-scale radiation damage modelling hierarchy.

In chapter 6 we have investigated the melting dynamics of photo-excited nano-films. First, by combining the ultrafast electronic diffraction experiment with atomistic modelling we were able to validate the two-temperature model directly and for the first time on a sub-picosecond timescale. An excellent agreement between the calculated and measured diffraction patterns implies that we have effectively achieved the goal of observing the photo-induced phase transitions as they happen at the atomistic level. We have identified three types of melting occurring in gold nanofilms (in the order of increasing absorbed energy): heterogeneous (by melt front propagation), homogeneous (uniform melt nucleation) and non-thermally accelerated melting, where the electronic pressure leads to violent expansion of the sample aiding heterogeneous melting propagation from the surfaces. Lastly, by analysing the high absorbed fluence data, we have accurately determined an upper T_e limit for the ground-state potential approximation to be valid and hence the limit of the "standard" two-temperature model applicability.

In chapter 7 we have analysed the results of two augmented MD methods for swift heavy ion simulations in Si and Ge, namely the inelastic thermal spike (based on two-temperature model) and its more complex band-gap extension (based on a Boltzmann transport equation). Very good agreement with experimental latent track radii has been achieved provided that we adjust the electron-phonon relaxation time in the eiTS model and additionally the diffusivity in iTS. We have contrasted the iTS and eiTS methods in detail in Sec. 7.7 and concluded that eiTS reproduces the system dynamics more accurately, while the simpler iTS is potentially more transferable. We have outlined the different technical and physics limitations of both. A further insight was provided by preliminary *ab initio* results, which indicated that in Si under huge excitations induced by swift heavy ions, the electronic pressure (coming from the modified lattice parameter, most likely from the reduced charge screening at high T_e) can be very significant. We concluded that in order to build a comprehensive and predictive framework for SHI radiation damage, interatomic potentials that depend on the level of electronic excitations are required.

8.3 Future outlook

In this thesis we have recognised that the ground-state interatomic potential approximation is accurate up to $T_e' = 0.8$ eV for gold, which puts an obvious limitation on the augmented MD modelling. This threshold will most likely be very similar in most metals and slightly larger for insulators increasing with the size of the band-gap. The changes in the potential energy surface can be captured by constructing the interatomic potentials at different values of the electronic temperature. This can be achieved using a force-matching method [86], or the one presented in [84]. We envisage that there will be more progress in this area, which will enable us to capture more physics of the highly non-equilibrium ionic dynamics by including non-thermal effects. There are only three excitation-dependent potentials that are currently available (for Si [278], Au [87], W [84]). Therefore, some additional simulations, which would

include T_e-dependent forces, are within reach with the current computational technology and are, in addition, of great interest in the radiation damage community. These are namely: collision cascade simulations in tungsten and laser-excitation and swift heavy ion irradiation of silicon.

We think that we will be able to address some of the model deficiencies in the near future. In particular, more augmented MD integration with the input from *ab initio* is required to make the method as free of adjustable parameters as possible. This is already the case for the electronic specific heat capacity and increasingly for the electron-phonon coupling strength, following the theoretical developments in the field. The remaining unsolved question, from the theoretical standpoint, is the behaviour of the electron transport as a function of both ionic and electronic temperatures in a non-equilibrium scenario with hot electrons and cold ions.

Because of the spatiotemporal scales that the augmented MD method can access, it will not be overtaken by the *ab initio* strategies for some years to come (at least to simulate the ion-electron effects at the nm scale). However, there is a clear need to build on the success of the augmented MD model and include further non-adiabatic effects, such as selective excitations in phonons and electrons. The current model includes an effective electron-phonon coupling mechanism and thus can only account for thermal lattice disordering. In order to simulate a range of scenarios predictively (such as speculated non-thermal solid-to-solid phase transitions), the physics of selective phonon excitations and the excitation-induced changes in the bonding character needs to be incorporated.

To bring forward a modelling scheme for non-equilibrium scenarios, which is free of adjustable parameters, the existing, *ab initio* MD codes can be amended by including an effective electron-phonon coupling as a random driving force on the ions. This will be a useful and almost parameter-free scheme to disentangle coherent (non-thermal) dynamics from thermal ultrafast dynamics. It could be used as a complementary validation tool to the larger-scale augmented MD. In the context of ultrafast dynamics, it will enable to investigate "hidden" macroscopic phases at high T_e from first principles.

The augmented MD model with further corrections coming from *ab initio* will accurately resolve the atomistic dynamics in the case of strong electron-ion non-equilibrium. Such development will bring us a step closer to a new generation of MD models capable of tackling the problems of electron-ion dynamics at a mesoscopic scale - a theoretical tool that is necessary to understand ultrafast, radiation damage and other non-equilibrium processes.

References

[1] E. Zarkadoula et al., 'Electronic effects in high-energy radiation damage in iron', J. Phys.: Condens. Mat. **26**, 085401 (2014) (see pp. 4, 79)

[2] A. A. Leino et al., 'Structural analysis of simulated swift heavy ion tracks in quartz', Nucl. Instr. Meth. Phys. Res. B, REI 2013 conference paper, accepted for publication (2013) (see pp. 4, 51, 52, 117, 130, 135)

[3] S. L. Daraszewicz et al., 'Structural dynamics of laser-irradiated gold nanofilms', Phys. Rev. B **88**, 184101 (2013) (see pp. 4, 28, 37, 55, 56, 73, 101, 102, 106, 108–115)

[4] Y. Giret et al., 'Transient atomic structure determination of laser-excited materials from time-resolved diffraction data', Appl. Phys. Lett., accepted for publication (2013) (see pp. 4, 101–104, 108)

[5] E. Zarkadoula et al., 'The nature of high-energy radiation damage in iron', J. Phys.: Condens. Mat. **25**, 125402 (2013) (see pp. 4, 79, 166)

[6] S. L. Daraszewicz and D. M. Duffy, 'Hybrid continuum–atomistic modelling of swift heavy ion radiation damage in germanium', Nucl. Instr. Meth. Phys. Res. B **303**, 112–115 (2013) (see pp. 4, 117, 134)

[7] D. M. Duffy, S. L. Daraszewicz and J Mulroue, 'Modelling the effects of electronic excitations in ionic-covalent materials', Nucl. Instr. Meth. Phys. Res. B **277**, 21–27 (2012) (see pp. 4, 28, 31, 117, 125, 127)

[8] S. L. Daraszewicz and D. M. Duffy, 'Extending the inelastic thermal spike model for semiconductors and insulators', Nucl. Instr. Meth. Phys. Res. B **269**, 1646–1649 (2011) (see pp. 4, 28, 117, 128)

[9] E. R. Hodgson, 'Challenges for insulating materials in fusion applications', Nucl. Instr. Meth. Phys. Res. B **191**, 744–751 (2002) (see pp. 18, 39, 48)

[10] A. Ibarra and E. R. Hodgson, 'The ITER project: the role of insulators', Nucl. Instr. Meth. Phys. Res. B **218**, 29–35 (2004) (see pp. 18, 39)

[11] A. M. Stoneham, J. R. Matthews and I. J. Ford, 'Innovative materials for fusion power plant structures: separating functions', J. Phys.: Condens. Mat. **16**, S2597–S2621 (2004) (see pp. 18, 39)

[12] D. J. Ward and S. L. Dudarev, 'Economically competitive fusion', Mater. Today **11**, 46–53 (2008) (see pp. 18, 39)

[13] D. M. Duffy, 'Modelling materials for fusion power', Inter. Mat. Rev. **56**, 324–340 (2011) (see pp. 18, 39)

[14] M. Toulemonde, C. Trautmann, E. Balanzat, K. Hjort and A. Weidinger, 'Track formation and fabrication of nanostructures with MeV-ion beams', Nucl. Instr. Meth. Phys. Res. B **216**, Proceedings of the E-MRS 2003 Symposium E on Ion Beams for Nanoscale Surface Modifications, 1–8 (2004) (see pp. 18, 48)

[15] P. Apel, 'Swift ion effects in polymers: industrial applications', Nucl. Instr. Meth. Phys. Res. B **208**, 11–20 (2003) (see pp. 18, 48)

[16] P. I. Gaiduk, A. N. Larsen, C. Trautmann and M. Toulemonde, 'Discontinuous tracks in arsenic-doped crystalline $Si_{0.5}Ge_{0.5}$ alloy layers', Phys. Rev. B **66**, 045316 (2002) (see pp. 18, 48)

[17] C. L. Claeys, *Radiation Effects In Advanced Semiconductor Materials And Devices*, Springer Series in Materials Science 57 (Springer, Berlin; New York, 2002) (see p. 18)

[18] A. Wambersie, T. Auberger, R. A. Gahbauer, D. T. L. Jones and R. Pötter, 'A challenge for high-precision radiation therapy: the case for hadrons', Strahlentherapie und Onkologie **175**, 122–128 (1999) (see p. 18)

[19] P. J. Chandler, F. L. Lama, P. D. Townsend and L. Zhang, 'Buried double waveguide by ion implantation in quartz', Appl. Phys. Lett. **53**, 89 (1988) (see pp. 18, 48)

[20] K.-M. Wang et al., 'Refractive index profiles in LiNbO3 waveguide formed by 3.2 MeV he ions', Surface and Coatings Technology **128-129**, 465–469 (2000) (see pp. 18, 48)

[21] C. P. Race, 'The modelling of radiation damage in metals using ehrenfest dynamics', PhD thesis (Imperial College London, 2010) (see pp. 23, 35, 47)

[22] O. B. Firsov, 'A qualitative interpretation of the mean electron excitation energy in atomic collisions', Sov. Phys.-JETP **9**, 1076–1080 (1959) (see pp. 24, 35, 63, 84)

[23] J. Lindhard and M. Scharff, 'Energy dissipation by ions in the keV region', Phys. Rev. **124**, 128–130 (1961) (see pp. 24, 35, 63, 84)

[24] J. Lindhard, M. Scharff and H. E. Schiott, 'Range concepts and heavy ion ranges', in *Kongelige Danske Videnskabernes Selskab: Matematisk-Fysiske Meddelelser*, Vol. 33 (1963) (see pp. 24, 90, 94)

[25] C. P. Race et al., 'The treatment of electronic excitations in atomistic models of radiation damage in metals', Rep. Prog. Phys. **73**, 116501 (2010) (see pp. 25, 47)

[26] J. Ziman, *Electrons and phonons*, UK (Oxford University Press, 2001) (see p. 25)

[27] P. B. Allen, 'Theory of thermal relaxation of electrons in metals', Phys. Rev. Lett. **59**, 1460–1463 (1987) (see p. 25)

[28] T. Qiu and C. Tien, 'Short-pulse laser heating on metals', Int. J. Heat Meas Tran. **35**, 719–726 (1992) (see p. 25)

[29] Z. Lin, L. V. Zhigilei and V. Celli, 'Electron-phonon coupling and electron heat capacity of metals under conditions of strong electron-phonon nonequilibrium', Phys. Rev. B **77**, 075133 (2008) (see pp. 25, 56, 80–82, 84, 103, 104, 165, 167)

[30] X. Wang, D. Riffe, Y.-S. Lee and M. Downer, 'Time-resolved electron-temperature measurement in a highly excited gold target using femtosecond thermionic emission', Phys. Rev. B **50**, 8016–8019 (1994) (see pp. 25, 103)

[31] B. Arnaud and Y. Giret, 'Electron cooling and Debye-Waller effect in photoexcited bismuth', Phys. Rev. Lett. **110**, 016405 (2013) (see p. 25)

[32] E. G. Gamaly and A. V. Rode, 'Electron-phonon energy relaxation in bismuth excited by ultrashort laser pulse: temperature and fluence dependence', Appl. Phys. A-Mater. **110**, 529–535 (2012) (see p. 25)

[33] S. K. Sundaram and E. Mazur, 'Inducing and probing non-thermal transitions in semiconductors using femtosecond laser pulses', Nature Mat. **1**, 217–224 (2002) (see pp. 26, 31, 54, 125)

[34] F. Desauer, Z. Physik **38**, 12 (1923) (see p. 27)

[35] I. M Lifshitz, M. I. Kaganov and L. V. Tanatarov, J. Nucl. Energy A **12**, 69 (1960) (see pp. 27, 116)

[36] M. I. Kaganov, I. M. Lifshitz and L. V. Tanatarov, 'Relaxation between electrons and the crystalline lattice', Sov. Phys.-JETP **4**, 173–178 (1957) (see p. 27)

[37] F. Seitz and J. S. Köhler, Solid State Phys. 2, 305 (1956) (see p. 27)

[38] J. Fujimoto, J. Liu, E. Ippen and N. Bloembergen, 'Femtosecond laser interaction with metallic tungsten and nonequilibrium electron and lattice temperatures', Phys. Rev. Lett. **53**, 1837–1840 (1984) (see p. 28)

[39] S. Brorson, J. Fujimoto and E. Ippen, 'Femtosecond electronic heat-transport dynamics in thin gold films', Phys. Rev. Lett. **59**, 1962–1965 (1987) (see p. 28)

[40] S. L. Daraszewicz, 'Modelling radiation damage in band-gap materials: extending the inelastic thermal spike model', MRes Thesis (University College London, 2010) (see p. 28)

[41] S. Klaumänzer, 'Thermal-spike models for ion track physics: a critical examination', in *Ion Beam Science: Solved and Unsolved Problems, Pts 1 and 2*, Vol. 52, edited by P Sigmund, Kongelige Danske Videnskabernes Selskab: Matematisk-Fysiske Meddelelser, Symposium on Ion Beam Science - Solved and Unsolved Problems, Copenhagen, Denmark, May 01-05, 2006 (2006), pp. 293–328 (see pp. 28, 29, 31, 33, 50, 119)

[42] J. Drabble and H. Goldsmid, *Thermal Conduction in Semiconductors* (Pergamon, New York, 1961) (see p. 28)

[43] H. M. van Driel, 'Kinetics of high-density plasmas generated in Si by 1.06- and 0.53-μm picosecond laser pulses', Phys. Rev. B **35**, 8166–8176 (1987) (see pp. 28, 29, 69, 124)

[44] S. S. Mao, X.-L. Mao, R. Greif and R. E. Russo, 'Simulation of infrared picosecond laser-induced electron emission from semiconductors', Appl. Surf. Sci. **127–129**, 4th International Conference on Laser Ablation (COLA 97), Monterey Bay, CA, Jul 21-25, 1997, 206–211 (1998) (see p. 28)

[45] J. Chen, D. Tzou and J. Beraun, 'Numerical investigation of ultrashort laser damage in semiconductors', Int. J. Heat Meas Tran. **48**, 501–509 (2005) (see pp. 28, 29, 67, 120)

[46] J. Chen, D. Tzou and J. Beraun, 'A semiclassical two-temperature model for ultrafast laser heating', Int. J. Heat Meas Tran. **49**, 307–316 (2006) (see p. 28)

[47] J. Thorstensen and S. Erik Foss, 'Temperature dependent ablation threshold in silicon using ultrashort laser pulses', J. Appl. Phys. **112**, 103514 (2012) (see p. 28)

[48] T. Q. Qiu and C. L. Tien, 'Heat transfer mechanisms during short-pulse laser heating of metals', J. Heat Tranf. **115**, 835 (1993) (see p. 28)

[49] Y. Gan and J. K. Chen, 'Combined continuum-atomistic modeling of ultrashort-pulsed laser irradiation of silicon', Appl. Phys. A-Mater. **105**, 427–437 (2011) (see p. 28)

[50] T. Grasser, T. W. Tang, H. Kosina and S. Selberherr, 'A review of hydrodynamic and energy-transport models for semiconductor device simulation', P. IEEE **91**, 251–274 (2003) (see pp. 29, 119, 120)

[51] L. Shokeen and P. K. Schelling, 'Role of electronic-excitation effects in the melting and ablation of laser-excited silicon', Comp. Mater. Sci. **67**, 316–328 (2013) (see pp. 30, 37, 120)

[52] B. Rethfeld, A. Rmer, N. Brouwer, N. Medvedev and O. Osmani, 'Electron dynamics and energy dissipation in highly excited dielectrics', Nucl. Instr. Meth. Phys. Res. B **327**, 78–88 (2014) (see p. 30)

[53] Y. Gan and J. K. Chen, 'A hybrid method for integrated atomistic-continuum simulation of ultrashort-pulsed laser interaction with semiconductors', Computer Physics Communications **183**, 278–284 (2012) (see pp. 30, 67)

[54] J. F. Ziegler, J. P. Biersack and M. D. Ziegler, *SRIM-2008.04*, (2008) `www.srim.org` (see pp. 32, 35, 46, 84)

[55] A. Meftah et al., 'Swift heavy ions in magnetic insulators: a damage-cross-section velocity effect', Phys. Rev. B **48**, 920–925 (1993) (see pp. 32, 33, 50)

[56] A. Mozumder, 'Track-core radius of charged particles at relativistic speed in condensed media', J. Chem. Phys. **60**, 1145 (1974) (see p. 33)

[57] B Gervais and S Bouffard, 'Simulation of the primary stage of the interaction of swift heavy-ions with condensed matter', Nucl. Instr. Meth. Phys. Res. Bs **88**, 355–364 (1994) (see p. 33)

[58] M. Waligórski, R. Hamm and R Katz, 'The radial-distribution of dose around the path of a heavy-ion in liquid water', International Journal of Radiation Applications and Instrumentation. Part D. Nuclear Tracks and Radiation Measurements **11**, 309–319 (1986) (see pp. 34, 53)

[59] C. Dufour, V. Khomenkov, G. Rizza and M. Toulemonde, 'Ion-matter interaction: the three-dimensional version of the thermal spike model. Application to nanoparticle irradiation with swift heavy ions', J. Phys. D **45**, 065302 (2012) (see pp. 34, 50, 129)

[60] D. Ivanov and L. V. Zhigilei, 'Combined atomistic-continuum modeling of short-pulse laser melting and disintegration of metal films', Phys. Rev. B **68** (2003) (see pp. 34, 56, 65, 70, 71, 82, 83, 101, 109, 110)

[61] J. Biersack and L. Haggmark, 'A Monte Carlo computer program for the transport of energetic ions in amorphous targets', Nucl. Instr. Meth. **174**, 257–269 (1980) (see p. 35)

[62] M. T. Robinson and I. M. Torrens, 'Computer simulation of atomic-displacement cascades in solids in the binary-collision approximation', Phys. Rev. B **9**, 5008–5024 (1974) (see p. 35)

[63] M. Yoshida, 'Distribution of interstitials and vacancies produced by an incident and fast neutron', J. Phys. Soc. Jpn. **16**, 44–50 (1961) (see p. 35)

[64] M. Robinson and O. Oen, 'Computer studies of the slowing down of energetic atoms in crystals', Phys. Rev. **132**, 2385–2398 (1963) (see p. 35)

[65] M. M. Jakas and D. E. Harrison, 'Dependence of atom ejection on electronic energy loss', Phys. Rev. B **32**, 2752–2760 (1985) (see pp. 35, 89)

[66] M. M. Jakas and D. E. Harrison, 'Influence of electronic energy losses on atom ejection processes', Phys. Rev. B **30**, 3573–3574 (1984) (see p. 35)

[67] M. Norgett, M. Robinson and I. Torrens, 'A proposed method of calculating displacement dose rates', Nucl. Eng. Des. **33**, 50–54 (1975) (see p. 35)

[68] G. H. Kinchin and R. S. Pease, 'The displacement of atoms in solids by radiation', Rep. Prog. Phys. **18**, 1–51 (1955) (see p. 35)

[69] J. B. Gibson, A. N. Goland, M. Milgram and G. H. Vineyard, 'Dynamics of radiation damage', Phys. Rev. **120**, 1229–1253 (1960) (see pp. 36, 41)

[70] B. J. Alder and T. E. Wainwright, 'Studies in Molecular Dynamics. I. General Method', J. Chem. Phys. **31**, 459 (1959) (see p. 36)

[71] R. E. Stoller, 'Primary radiation damage formation', in *Comprehensive Nuclear Materials* (Elsevier, 2012), pp. 293–332 (see pp. 36, 41–46, 88–90, 94)

[72] L. Malerba, 'Molecular dynamics simulation of displacement cascades in α-Fe: a critical review', J. Nucl. Mater. **351**, 28–38 (2006) (see pp. 36, 40, 41, 43, 62, 85, 87, 88)

[73] T. D. de la Rubia, 'Irradiation-induced defect production in elemental metals and semiconductors: a review of recent molecular dynamics studies', Annu. Rev. Mater. Sci. **26**, 613–649 (1996) (see p. 36)

[74] A. Caro and M. Victoria, 'Ion-electron interaction in molecular-dynamics cascades', Phys. Rev. A **40**, 2287–2291 (1989) (see pp. 36, 46, 63, 65)

[75] M. W. Finnis, P. Agnew and A. J. E. Foreman, 'Thermal excitation of electrons in energetic displacement cascades', Phys. Rev. B **44**, 567–574 (1991) (see p. 36)

[76] D. M. Duffy and A. M. Rutherford, 'Including the effects of electronic stopping and electron–ion interactions in radiation damage simulations', J. Phys.: Condens. Mat. **19**, 016207 (2007) (see pp. 36, 46, 63, 83, 84, 169)

[77] C. P. Flynn and R. S. Averback, 'Electron-phonon interactions in energetic displacement cascades', Phys. Rev. B **38**, 7118–7120 (1988) (see p. 36)

[78] F Gao, D. J. Bacon, P. E. J. Flewitt and T. A. Lewis, 'The effects of electron-phonon coupling on defect production by displacement cascades in α-iron', Model. Simul. Mater. Sc. **6**, 543–556 (1998) (see p. 36)

[79] V. G. Kapinos and D. J. Bacon, 'Influence of ion-electron interaction on the formation mechanism of depleted zones in displacement cascades in metals', Phys. Rev. B **50**, 13194–13203 (1994) (see p. 36)

[80] C. Zhang, F. Mao and F.-S. Zhang, 'Electron-ion coupling effects on radiation damage in cubic silicon carbide', J. Phys.-Condens. Mat. **25**, 235402 (2013) (see p. 36)

[81] A. M. Rutherford and D. M. Duffy, 'The effect of electron–ion interactions on radiation damage simulations', J. Phys.: Condens. Mat. **19**, 496201 (2007) (see pp. 36, 46, 64, 79, 169)

[82] J. Frantz, J. Tarus, K. Nordlund and J. Keinonen, 'Mechanism of electron-irradiation-induced recrystallization in Si', Phys. Rev. B **64**, 125313 (2001) (see pp. 37, 51, 52)

[83] L.-L. Wang, A. Perera and H.-P. Cheng, 'Molecular dynamics simulation of potential sputtering on a LiF surface by slow highly charged ions', Phys. Rev. B **68**, 115409 (2003) (see pp. 37, 52)

[84] S. Khakshouri, D. Alfè and D. M. Duffy, 'Development of an electron-temperature-dependent interatomic potential for molecular dynamics simulation of tungsten under electronic excitation', Phys. Rev. B **78**, 224304 (2008) (see pp. 37, 51, 141)

[85] L. Shokeen and P. K. Schelling, 'An empirical potential for silicon under conditions of strong electronic excitation', Appl. Phys. Lett. **97**, 151907 (2010) (see pp. 37, 51)

[86] F. Ercolessi and J. B Adams, 'Interatomic potentials from first-principles calculations: the force-matching method', Europhys. Lett. (EPL) **26**, 583–588 (1994) (see pp. 37, 105, 141)

[87] G. E. Norman, S. V. Starikov and V. V. Stegailov, 'Atomistic simulation of laser ablation of gold: effect of pressure relaxation', J. Exp. Theor. Phys. **114**, 792–800 (2012) (see pp. 37, 51, 56, 105, 115, 141)

[88] G. Norman et al., 'Nanomodification of gold surface by picosecond soft x-ray laser pulse', J. Appl. Phys. **112**, 013104 (2012) (see p. 37)

[89] D. R. Mason et al., 'Electronic damping of atomic dynamics in irradiation damage of metals', J. Phys.-Condens. Mat. **19**, 436209 (2007) (see p. 37)

[90] A. Schleife, E. W. Draeger, Y. Kanai and A. A. Correa, 'Plane-wave pseudopotential implementation of explicit integrators for time-dependent Kohn-Sham equations in large-scale simulations', J. Chem. Phys. **137**, 22A546 (2012) (see p. 37)

[91] M. A. Zeb, 'Electronic stopping power of slow ions in solids from first principles', PhD thesis (University of Cambridge, 2013) (see pp. 37, 47, 84, 99)

[92] A. A. Correa, J. Kohanoff, E. Artacho, D. Sánchez-Portal and A. Caro, 'Nonadiabatic forces in ion-solid interactions: the initial stages of radiation damage', Phys. Rev. Lett. **108**, 213201 (2012) (see pp. 37, 47)

[93] M. A. Zeb et al., 'Electronic stopping power in gold: the role of d electrons and the **H**/He anomaly', Phys. Rev. Lett. **108**, 225504 (2012) (see p. 37)

[94] C. P. Race, D. R. Mason and A. P. Sutton, 'A new directional model for the electronic frictional forces in molecular dynamics simulations of radiation damage in metals', J. Nucl. Mater. **425**, 33–40 (2012) (see p. 37)

[95] A. P. Horsfield et al., 'Correlated electron-ion dynamics in metallic systems', Comp. Mater. Sci. **44**, 16–20 (2008) (see p. 38)

[96] A. P. Horsfield et al., 'The transfer of energy between electrons and ions in solids', Rep. Prog. Phys. **69**, 1195–1234 (2006) (see p. 38)

[97] A. P. Horsfield, D. R. Bowler, A. J. Fisher, T. N. Todorov and C. G. Sánchez, 'Correlated electron-ion dynamics: the excitation of atomic motion by energetic electrons', J. Phys.-Condens. Mat. **17**, 4793–4812 (2005) (see p. 38)

[98] A. P. Horsfield, D. R. Bowler, A. J. Fisher, T. N. Todorov and C. G. Sánchez, 'Beyond ehrenfest: correlated non-adiabatic molecular dynamics', J. Phys.-Condens. Mat. **16**, 8251–8266 (2004) (see p. 38)

[99] K. Trachenko et al., 'Modeling high-energy radiation damage in nuclear and fusion applications', Nucl. Instr. Meth. Phys. Res. B **277**, 6–13 (2012) (see p. 40)

[100] A. Souidi et al., 'Dependence of radiation damage accumulation in iron on underlying models of displacement cascades and subsequent defect migration', J. Nucl. Mater. **355**, 89–103 (2006) (see p. 40)

[101] K. Morishita and T. Diaz de la Rubia, 'A molecular dynamics simulation study of displacement cascades in vanadium', J. Nucl. Mater. **271-272**, 35–40 (1999) (see p. 40)

[102] K. Nordlund, 'Computational materials science of ion irradiation', Nucl. Instr. Meth. Phys. Res. B **188**, 41–48 (2002) (see p. 40)

[103] A. F. Calder, D. J. Bacon, A. V. Barashev and Y. N. Osetsky, 'Computer simulation of cascade damage in α-iron with carbon in solution', J. Nucl. Mater. **382**, 91–95 (2008) (see p. 40)

[104] I. Farnan, H. Cho and W. J. Weber, 'Quantification of actinide α-radiation damage in minerals and ceramics', Nature **445**, 190–193 (2007) (see p. 40)

[105] C. Becquart et al., 'Effect of displacement cascade structure and defect mobility on the growth of point defect clusters under irradiation', J. Nucl. Mater. **351**, 39–46 (2006) (see p. 40)

[106] C. J. Ortiz and M. J. Caturla, 'Cascade damage evolution: rate theory versus kinetic monte carlo simulations', J. Comput.-Aided Mater. **14**, 171–181 (2008) (see p. 40)

[107] J. Dalla Torre, C.-C. Fu, F. Willaime, A. Barbu and J.-L. Bocquet, 'Resistivity recovery simulations of electron-irradiated iron: kinetic monte carlo versus cluster dynamics', J. Nucl. Mater. **352**, 42–49 (2006) (see p. 40)

[108] A. F. Calder and D. J. Bacon, 'A molecular dynamics study of displacement cascades in α-iron', J. Nucl. Mater. **207**, 25–45 (1993) (see p. 40)

[109] B. Domeij, F. Brown, J. Davies, G. Piercy and E. Kornelsen, 'Anomalous penetration of heavy ions of keV energies in monocrystalline tungsten', Phys. Rev. Lett. **12**, 363–366 (1964) (see p. 41)

[110] A. M. Rutherford, 'Electronic effects in radiation damage simulations in metals', PhD thesis (University College London, 2009) (see p. 41)

[111] M. Nastasi, J. Mayer and J. K. Hirvonen, *Ion-Solid Interactions: Fundamentals and Applications* (Cambridge University Press, 1996) (see pp. 41, 48)

[112] D. Terentyev et al., 'Effect of the interatomic potential on the features of displacement cascades in α-Fe: a molecular dynamics study', J. Nucl. Mater. **351**, 65–77 (2006) (see p. 43)

[113] N. Soneda, S. Ishino and T. D. de la Rubia, 'Vacancy loop formation by 'cascade collapse' in α-Fe: a molecular dynamics study of 50keV cascades', Phil. Mag. Lett. **81**, 649–659 (2001) (see p. 44)

[114] M. Warrier and M. C. Valsakumar, 'Large-scale molecular dynamics simulations of collision cascades caused by primary knock-on atoms in Fe', Radiat. Eff. Defect S. **168**, 615–619 (2013) (see p. 44)

[115] R. E. Stoller and L. R. Greenwood, 'Subcascade formation in displacement cascade simulations: implications for fusion reactor materials', J. Nucl. Mater. **271-272**, 57–62 (1999) (see pp. 44, 45)

[116] W. Weilu et al., 'Cascades damage in α-iron with high damage energy', arXiv:1101.0887 (2011) (see p. 44)

[117] K. Kadau, T. C. Germann and P. S. Lomdahl, 'Large-scale molecular-dynamics simulation of 19 billion particles', Int. J. Mod. Phys. C **15**, 193–201 (2004) (see p. 44)

[118] K. Kadau, T. C. Germann and P. S. Lomdahl, 'Molecular dynamics comes of age: 320 billion atom simulation on BlueGene/L', Int. J. Mod. Phys. C **17**, 1755–1761 (2006) (see p. 44)

[119] T. C. Germann and K. Kadau, 'Trillion-atom molecular dynamics becomes a reality', Int. J. Mod. Phys. C **19**, 1315–1319 (2008) (see p. 44)

[120] Available from: `http://www.hector.ac.uk/` (see p. 45)

[121] I. T. Todorov, W. Smith, K. Trachenko and M. T. Dove, 'DL_POLY_3: new dimensions in molecular dynamics simulations via massive parallelism', J. Mater. Chem. **16** (2006) (see pp. 45, 58)

[122] A. M. Stoneham and J. H. Harding, 'Not too big, not too small: the appropriate scale', Nature Mat. **2**, 77–83 (2003) (see p. 45)

[123] S. L. Dudarev and P. M. Derlet, 'A 'magnetic' interatomic potential for molecular dynamics simulations', J. Phys.: Condens. Mat. **17**, 7097–7118 (2005) (see p. 45)

[124] G. J. Ackland, 'Two-band second moment model for transition metals and alloys', J. Nucl. Mater. **351**, 20–27 (2006) (see p. 45)

[125] P.-W. Ma and S. L. Dudarev, 'Langevin spin dynamics', Phys. Rev. B **83** (2011) (see p. 45)

[126] P.-W. Ma, S. L. Dudarev and C. Woo, 'Spin-lattice-electron dynamics simulations of magnetic materials', Phys. Rev. B **85** (2012) (see p. 45)

[127] A. M. Stoneham, 'Energy transfer between electrons and ions in collision cascades in solids', Nucl. Instr. Meth. Phys. Res. B **48**, 389–398 (1990) (see p. 45)

[128] J le Page, D. R. Mason, C. P. Race and W. M. C. Foulkes, 'How good is damped molecular dynamics as a method to simulate radiation damage in metals?', New J. Phys. **11**, 013004 (2009) (see pp. 46, 84, 89)

[129] C. Björkas and K. Nordlund, 'Assessment of the relation between ion beam mixing, electron–phonon coupling and damage production in Fe', Nucl. Instr. Meth. Phys. Res. B **267**, 1830–1836 (2009) (see p. 46)

[130] Y. Zhong, K. Nordlund, M. Ghaly and R. Averback, 'Defect production in tungsten: a comparison between field-ion microscopy and molecular-dynamics simulations', Phys. Rev. B **58**, 2361–2364 (1998) (see p. 46)

[131] P. Kluth et al., 'Fine structure in swift heavy ion tracks in amorphous SiO_2', Phys. Rev. Lett. **101**, 175503 (2008) (see pp. 48, 52)

[132] K. Hjort, G. Thornell, J.-A. Schweitz and R. Spohr, 'Quartz micromachining by lithographic control of ion track etching', Appl. Phys. Lett. **69**, 3435–3436 (1996) (see p. 48)

[133] A. Dunlop et al., 'Phonon soft modes and damage production by high electronic excitations in pure metals', Europhys. Lett. (EPL) **15**, 765–770 (1991) (see p. 48)

[134] A. Barbu, A. Dunlop, D. Lesueur and R. S Averback, 'Latent tracks do exist in metallic materials', Europhys. Lett. (EPL) **15**, 37–42 (1991) (see p. 48)

[135] H. Dammak et al., 'Tracks in metals by MeV fullerenes', Phys. Rev. Lett. **74**, 1135–1138 (1995) (see p. 48)

[136] A. Dunlop, D. Lesueur, P. Legrand, H. Dammak and J. Dural, 'Effects induced by high electronic excitations in pure metals: a detailed study in iron', Nucl. Instr. Meth. Phys. Res. B **90**, 330–338 (1994) (see pp. 48, 50)

[137] C. Trautmann, S. Andler, W. Brüchle, R. Spohr and M. Toulemonde, 'Observation of etched tracks in an amorphous metal', Radiat. Eff. Defect S. **126**, 207–210 (1993) (see pp. 48, 50)

[138] F. Komarov, 'Track formation in germanium crystals irradiated with superhigh-energy ions', Vacuum **70**, 75–79 (2003) (see p. 48)

[139] P. Townsend, P. Chandler and L. Zhang, *Optical Effects of Ion Implantation* (Cambridge University Press, Cambridge, 1994) (see p. 48)

[140] A. Rivera et al., 'Giant enhancement of material damage associated to electronic excitation during ion irradiation: the case of $LiNbO_3$', Phys. Status Solidi (a) **206**, 1109–1116 (2009) (see pp. 48, 50)

[141] E. Silk and R. Barnes, 'The observation of dislocations in mica', Acta Metallurgica **9**, 558 –562 (1961) (see p. 49)

[142] D. A. Young, Nature **182**, 375 (1958) (see p. 49)

[143] R. L. Fleischer, P. B. Price and R. M. Walker, 'Ion explosion spike mechanism for formation of charged-particle tracks in solids', J. Appl. Phys. **36**, 3645 (1965) (see p. 49)

[144] Z. Insepov, A. Hassanein, D. Swenson and M. Terasawa, 'Computer simulation of surface modification with ion beams', Nucl. Instr. Meth. Phys. Res. B **241**, 496–500 (2005) (see p. 49)

[145] D. Avasthi and G. Mehta, *Swift heavy ions for materials engineering and nanostructuring*, Springer Series in Materials Science (Springer, 2011) (see p. 49)

[146] Z. Li, D. Chen, J. Wang and L. Shao, 'Molecular dynamics simulation of coulomb explosion, melting and shock wave creation in silicon after an ionization pulse', J. Appl. Phys. **115**, 143507 (2014) (see p. 49)

[147] R. Stoian, D. Ashkenasi, A. Rosenfeld and E. E. B. Campbell, 'Coulomb explosion in ultrashort pulsed laser ablation of Al_2O_3', Phys. Rev. B **62**, 13167–13173 (2000) (see p. 50)

[148] M. Famá, B. D. Teolis, D. A. Bahr and R. A. Baragiola, 'Role of electron capture in ion-induced electronic sputtering of insulators', Phys. Rev. B **75**, 100101 (2007) (see p. 50)

[149] F. Staufenbiel, G. Schiwietz, K. Czerski, M. Roth and P. Grande, 'Electronic energy-density effects in ion tracks of metals', Nucl. Instr. Meth. Phys. Res. B **230**, 426 –430 (2005) (see pp. 50, 126)

[150] A. Chettah et al., 'Behavior of crystalline silicon under huge electronic excitations: a transient thermal spike description', Nucl. Instr. Meth. Phys. Res. B **267**, 23rd International Conference on Atomic Collisions in Solids, Phalaborwa, South Africa, Aug 17-22, 2008, 2719–2724 (2009) (see pp. 50, 118, 119, 124, 128, 129)

[151] G. Szenes, Z. E. Horváth, B. Pécz, F. Pászti and L. Tóth, 'Tracks induced by swift heavy ions in semiconductors', Phys. Rev. B **65**, 045206 (2002) (see p. 50)

[152] A. Kamarou, W. Wesch, E. Wendler, A. Undisz and M. Rettenmayr, 'Swift heavy ion irradiation of InP: thermal spike modeling of track formation', Phys. Rev. B **73**, 184107 (2006) (see p. 50)

[153] S. Dhamodaran, A. Pathak, A. Dunlop, G. Jaskierowicz and S. Della-Negra, 'Energetic cluster irradiation of InP', Nucl. Instr. Meth. Phys. Res. B **256**, 229–232 (2007) (see p. 50)

[154] A. Meftah et al., 'Experimental determination of track cross-section in $Gd_3Ga_5O_{12}$ and comparison to the inelastic thermal spike model applied to several materials', Nucl. Instr. Meth. Phys. Res. B **237**, 563–574 (2005) (see p. 50)

[155] M. Toulemonde et al., 'Experimental phenomena and thermal spike model description of ion tracks in amorphisable inorganic insulators', in *Ion Beam Science: Solved and Unsolved Problems, Pts 1 and 2*, Vol. 52, edited by P Sigmund, Kongelige Danske Videnskabernes Selskab: Matematisk-Fysiske Meddelelser, Symposium on Ion Beam Science - Solved and Unsolved Problems, Copenhagen, Denmark, May 01-05, 2006 (2006), pp. 263–292 (see p. 50)

[156] C. J. O. Reichhardt, 'Coulomb explosion mechanism for ion damage', Theoretical Division Nuclear Weapons Program Hightlights 2005-2006 (2006) (see p. 50)

[157] I. A. Baranov, Y. V. Martynenko, S. O. Tsepelevich and Y. N. Yavlinski, 'Inelastic sputtering of solids by ions', Sov. Phys. Uspekhi **31**, 1015–1034 (1988) (see pp. 50, 118)

[158] N. A. Medvedev, A. E. Volkov, B. Rethfeld and N. S. Shcheblanov, 'Effect of interatomic Auger processes on relaxation of electronic vacancies at deep levels of highly ionized atoms in swift heavy ion tracks', Nucl. Instr. Meth. Phys. Res. B **268**, 15th International Conference of the Radiation Effects in Insulators, Italy, Aug 30–Sep 04, 2009, 2870–2873 (2010) (see pp. 50, 53)

[159] N. A. Medvedev, K. Schwartz, C. Trautmann and A. E. Volkov, 'Formation of the defect halo of swift heavy ion tracks in LiF due to spatial redistribution of valence holes', Phys. Status Solidi (b) **250**, 850–857 (2013) (see pp. 50, 53)

[160] N. A. Medvedev, A. E. Volkov, N. S. Shcheblanov and B. Rethfeld, 'Early stage of the electron kinetics in swift heavy ion tracks in dielectrics', Phys. Rev. B **82**, 125425 (2010) (see pp. 50, 53)

[161] N. A. Medvedev, A. E. Volkov, K. Schwartz and C. Trautmann, 'Effect of spatial redistribution of valence holes on the formation of a defect halo of swift heavy-ion tracks in lif', Phys. Rev. B **87**, 104103 (2013) (see pp. 50, 53)

[162] V. Lipp, A. Volkov, M. Sorokin and B. Rethfeld, 'Kinetics of propagation of the lattice excitation in a swift heavy ion track', Nucl. Instr. Meth. Phys. Res. B **269**, 865–868 (2011) (see p. 50)

[163] M. M. Jakas, E. M. Bringa and R. E. Johnson, 'Fluid dynamics calculation of sputtering from a cylindrical thermal spike', Phys. Rev. B **65**, 165425 (2002) (see p. 51)

[164] D. M. Duffy, N. Itoh, A. M. Rutherford and A. M. Stoneham, 'Making tracks in metals', J. Phys.: Condens. Mat. **20**, 082201 (2008) (see p. 51)

[165] P. A. F. P. Moreira, R. Devanathan and W. J. Weber, 'Atomistic simulation of track formation by energetic recoils in zircon', J. Phys.: Condens. Mat. **22**, 395008 (2010) (see p. 51)

[166] K. H. Bennemann, 'Ultrafast dynamics in solids', J. Phys.: Condens. Mat. **16**, R995–R1056 (2004) (see p. 51)

[167] O. Osmani, N. Medvedev, M. Schleberger and B. Rethfeld, 'Energy dissipation in dielectrics after swift heavy-ion impact: a hybrid model', Phys. Rev. B **84**, 214105 (2011) (see p. 53)

[168] H. Cailleau et al., 'Impacting materials by light and seeing their structural dynamics', Eur. Phys. J.: Special Topics **222**, 1077–1092 (2013) (see p. 54)

[169] H. Cailleau et al., 'PIPT from the Beginning to Future', Acta Physica Polonica A **121**, 4th International Conference on Photoinduced Phase Transitions and Cooperative Phenomena (PIPT), Wroclaw, Poland, Jun 28-Jul 02, 2011, 297–306 (2012) (see p. 54)

[170] G. Sciaini and R. J. D. Miller, 'Femtosecond electron diffraction: heralding the era of atomically resolved dynamics', Rep. Prog. Phys. **74**, 096101 (2011) (see pp. 54, 101)

[171] F. Schmitt et al., 'Transient electronic structure and melting of a charge density wave in TbTe3', Science **321**, 1649–1652 (2008) (see p. 54)

[172] R. Ernstorfer et al., 'The formation of warm dense matter: experimental evidence for electronic bond hardening in gold', Science **323**, 1033–1037 (2009) (see pp. 54, 55, 101–103, 116)

[173] K.-L. Yeh, M. C. Hoffmann, J. Hebling and K. A. Nelson, 'Generation of 10 μJ ultrashort terahertz pulses by optical rectification', Appl. Phys. Lett. **90**, 171121 (2007) (see p. 54)

[174] C.-Y. Ruan et al., 'The development and applications of ultrafast electron nanocrystallography', Microsc. Microanal. **15**, 323–337 (2009) (see p. 54)

[175] M. J. Cliffe, M. T. Dove, D. A. Drabold and A. L. Goodwin, 'Structure determination of disordered materials from diffraction data', Phys. Rev. Lett. **104**, 125501 (2010) (see p. 54)

[176] S. Koshihara, Y. Tokura, T. Mitani, G. Saito and T. Koda, 'Photoinduced valence instability in the organic molecular compound tetrathiafulvalene-*p*-chloranil (TTF-CA)', Phys. Rev. B **42**, 6853–6856 (1990) (see p. 54)

[177] P. Stampfli and K. H. Bennemann, 'Theory for the instability of the diamond structure of Si, Ge, and C induced by a dense electron-hole plasma', Phys. Rev. B **42**, 7163–7173 (1990) (see p. 54)

[178] Y. Giret, A. Gellé and B. Arnaud, 'Entropy driven atomic motion in laser-excited bismuth', Phys. Rev. Lett. **106**, 155503 (2011) (see pp. 54, 104)

[179] K. Onda et al., 'Photoinduced change in the charge order pattern in the quarter-filled organic conductor (EDO-TTF)2PF6 with a strong electron-phonon interaction', Phys. Rev. Lett. **101**, 067403 (2008) (see p. 54)

[180] D. M. Fritz et al., 'Ultrafast bond softening in bismuth: mapping a solid's interatomic potential with X-rays', Science **315**, 633–636 (2007) (see p. 54)

[181] K. S. Trainor, 'Construction of a wide-range tabular equation of state for copper', J. Appl. Phys. **54**, 2372 (1983) (see p. 55)

[182] T. Ogitsu et al., 'Ballistic electron transport in non-equilibrium warm dense gold', High Energy Density Physics **8**, 303–306 (2012) (see pp. 55, 101, 104, 116)

[183] J. Hohlfeld et al., 'Electron and lattice dynamics following optical excitation of metals', Chemical Physics **251**, 237–258 (2000) (see pp. 55, 103, 104)

[184] S. Mazevet, J. Clérouin, V. Recoules, P. Anglade and G. Zerah, 'Ab-initio simulations of the optical properties of warm dense gold', Phys. Rev. Lett. **95**, 085002 (2005) (see pp. 55, 70, 71, 101, 103)

[185] C. Schäfer, H. M. Urbassek and L. V. Zhigilei, 'Metal ablation by picosecond laser pulses: a hybrid simulation', Phys. Rev. B **66**, 115404 (2002) (see p. 56)

[186] D. S. Ivanov and L. V. Zhigilei, 'Effect of pressure relaxation on the mechanisms of short-pulse laser melting', Phys. Rev. Lett. **91**, 105701 (2003) (see p. 56)

[187] C. Wu, D. A. Thomas, Z. Lin and L. V. Zhigilei, 'Runaway lattice-mismatched interface in an atomistic simulation of femtosecond laser irradiation of Ag film-Cu substrate system', Appl. Phys. A **104**, 781–792 (2011) (see p. 56)

[188] Z. Lin and L. V. Zhigilei, 'Time-resolved diffraction profiles and structural dynamics of Ni film under short laser pulse irradiation', J. Phys.: Conference Series **59**, 11–15 (2007) (see pp. 56, 109)

[189] Z. Lin, R. A. Johnson and L. V. Zhigilei, 'Computational study of the generation of crystal defects in a bcc metal target irradiated by short laser pulses', Phys. Rev. B **77**, 214108 (2008) (see p. 56)

[190] H. Tang, M. Bai, Y. Dou, Q. Ran and G. V. Lo, 'Computer simulations of laser-induced melting of aluminum', Nucl. Instr. Meth. Phys. Res. B **301**, 36–40 (2013) (see p. 56)

[191] Y. Gan and J. K. Chen, 'Integrated continuum-atomistic modeling of nonthermal ablation of gold nanofilms by femtosecond lasers', Appl. Phys. Lett. **94**, 201116 (2009) (see pp. 56, 115)

[192] Z. Lin, E. Leveugle, E. M. Bringa and L. V. Zhigilei, 'Molecular dynamics simulation of laser melting of nanocrystalline Au', J. Phys. Chem. C **114**, 5686–5699 (2010) (see pp. 56, 77, 110)

[193] D. S. Ivanov and L. V. Zhigilei, 'Kinetic limit of heterogeneous melting in metals', Phys. Rev. Lett. **98**, 195701 (2007) (see p. 56)

[194] Z. Lin and L. V. Zhigilei, 'Time-resolved diffraction profiles and atomic dynamics in short-pulse laser-induced structural transformations: molecular dynamics study', Phys. Rev. B **73**, 184113 (2006) (see pp. 56, 73, 74, 76, 110)

[195] L. V. Zhigilei, Z. Lin and D. S. Ivanov, 'Atomistic modeling of short pulse laser ablation of metals: connections between melting, spallation, and phase explosion ', J. Phys. Chem. C **113**, 11892–11906 (2009) (see p. 56)

[196] D. S. Ivanov et al., 'Nanocrystalline structure of nanobump generated by localized photoexcitation of metal film', J. Appl. Phys. **107**, 013519 (2010) (see p. 56)

[197] M. Daw and M. Baskes, 'Embedded-atom method: derivation and application to impurities, surfaces, and other defects in metals', Phys. Rev. B **29**, 6443–6453 (1984) (see p. 60)

[198] J. Nørskov and N. Lang, 'Effective-medium theory of chemical binding: application to chemisorption', Phys. Rev. B **21**, 2131–2136 (1980) (see p. 60)

[199] J. Tersoff, 'New empirical model for the structural properties of silicon', Phys. Rev. Lett. **56**, 632–635 (1986) (see p. 60)

[200] J. Tersoff, 'New empirical approach for the structure and energy of covalent systems', Phys. Rev. B **37**, 6991–7000 (1988) (see p. 60)

[201] J. Tersoff, 'Empirical interatomic potential for silicon with improved elastic properties', Phys. Rev. B **38**, 9902–9905 (1988) (see pp. 60, 61, 122)

[202] T. Kumagai, S. Izumi, S. Hara and S. Sakai, 'Development of bond-order potentials that can reproduce the elastic constants and melting point of silicon for classical molecular dynamics simulation', Comp. Mater. Sci. **39**, 457–464 (2007) (see pp. 60, 61, 122)

[203] F. H. Stillinger and T. A. Weber, 'Computer simulation of local order in condensed phases of silicon', Phys. Rev. B **31**, 5262 (1985) (see pp. 61, 121, 122)

[204] I. T. Todorov and W Smith, *The DL_POLY_4 User Manual*, 4.05.1, `http://www.ccp5.ac.uk/DL_POLY/MANUALS/USRMAN4.pdf`, STFC Daresbury Laboratory (Sept. 2013) (see p. 62)

[205] M. V. Ramana Murty and H. A. Atwater, 'Empirical interatomic potential for Si-H interactions', Phys. Rev. B **51**, 4889–4893 (1995) (see p. 62)

[206] J. F. Ziegler, J. P. Biersack and U Littmark, *The Stopping and Range of Ions in Matter* (Pergamon, New York, 1985) (see pp. 62, 84)

[207] A. Duvenbeck and A. Wucher, 'Low-energy electronic excitation in atomic collision cascades: a nonlinear transport model', Phys. Rev. B **72**, 165408 (2005) (see pp. 65, 67)

[208] A. Duvenbeck, Z. Sroubek and A. Wucher, 'Electronic excitation in atomic collision cascades', Nucl. Instr. Meth. Phys. Res. B **228**, 325–329 (2005) (see p. 65)

[209] A. Duvenbeck, F. Sroubek, Z. Sroubek and A. Wucher, 'Computer simulation of low-energy electronic excitations in atomic collision cascades', Nucl. Instr. Meth. Phys. Res. B **225**, 464–477 (2004) (see p. 65)

[210] A. Powell, *Finite difference solution of the heat equation* (2002) (see p. 66)

[211] A. Tveito and R. Winther, *Introduction to Partial Differential Equations: A Computational Approach*, Texts in Applied Mathematics (Springer, 1998) (see p. 67)

[212] C. L. Phillips and P. S. Crozier, 'An energy-conserving two-temperature model of radiation damage in single-component and binary Lennard-Jones crystals', J. Chem. Phys. **131**, 074701 (2009) (see pp. 69, 70)

[213] K. Nordlund et al., 'Defect production in collision cascades in elemental semiconductors and fcc metals', Phys. Rev. B **57**, 7556–7570 (1998) (see p. 71)

[214] M. Ghaly, K. Nordlund and R. S. Averback, 'Molecular dynamics investigations of surface damage produced by keV self-bombardment of solids', Phil. Mag. A **79**, 795 (1999) (see p. 71)

[215] K. Nordlund, 'Molecular dynamics simulation of ion ranges in the 1 – 100 keV energy range', Comput. Mater. Sci. **3**, 448 (1995) (see p. 71)

[216] B. E. Warren, *X-Ray Diffraction* (Addison-Wesley, Reading, MA, 1969) (see pp. 74, 108)

[217] M. Ligges et al., 'Transient (000)-order attenuation effects in ultrafast transmission electron diffraction', J. Appl. Phys. **109**, 063519 (2011) (see pp. 75, 102, 103)

[218] P. Musumeci, J. T. Moody, C. M. Scoby, M. S. Gutierrez and M. Westfall, 'Laser-induced melting of a single crystal gold sample by time-resolved ultrafast relativistic electron diffraction', Appl. Phys. Lett. **97**, 063502 (2010) (see pp. 75, 101, 102, 104)

[219] T. O'Haver, *Peak fitter*, (2014) `http://terpconnect.umd.edu/~toh/spectrum/InteractivePeakFitter.htm` (see p. 76)

[220] C. Kittel, *Introduction to Solid State Physics*, 8th (John Wiley & Sons, Inc., New York, 2005) (see p. 76)

[221] C. Kelchner, S. Plimpton and J. Hamilton, 'Dislocation nucleation and defect structure during surface indentation', Phys. Rev. B **58**, 11085–11088 (1998) (see p. 77)

[222] LAMMPS centro-symmetry parameter implementation notes, `http://lammps.sandia.gov/doc/compute_centro_atom.html` (see p. 77)

[223] S. L. Daraszewicz and D. M. Duffy, 'The effects of electronic stopping and electron-phonon coupling on radition damage cascades in iron', Phys. Rev. B, submitted for publication (see p. 79)

[224] D. M. Duffy and A. M. Rutherford, 'Including electronic effects in damage cascade simulations', J. Nucl. Mater. **386-388**, 19–21 (2009) (see p. 79)

[225] N. W. Ashcroft and N. D. Mermin, *Solid State Physics* (Holt, Rinehart and Winston, New York, 1976) (see pp. 80, 81)

[226] E. G. Gamaly, 'The physics of ultra-short laser interaction with solids at non-relativistic intensities', Physics Reports **508**, 91–243 (2011) (see p. 81)

[227] L. V. Zhigilei, Additional data for electron-phonon couplings and electron heat capacities in metals at high electron temperatures, `http://www.faculty.virginia.edu/CompMat/electron-phonon-coupling/` (see pp. 81, 82, 84)

[228] P. L. Garrity, 'Spectroscopy of electronic thermal noise as a direct probe of absolute thermoelectric coefficients', J. Appl. Phys. **109**, 073701 (2011) (see p. 81)

[229] B. Hüttner, 'Thermodynamics and transport properties in the transient regime', J. Phys.: Condens. Mat. **11**, 6757 (1999) (see pp. 82, 83)

[230] S. I. Anisimov and B. Rethfeld, 'On the theory of ultrashort laser pulse interaction with a metal', in Nonresonant Laser-Matter Interaction (NLMI-9), Vol. 3093, edited by M. Libenson, Proceedings Of The Society Of Photo-Optical Instrumentation Engineers (SPIE), 9th International Conference On Nonresonant Laser-Matter Interaction (NLMI-9), St Petersburg, Russia, Jul 01-03, 1996 (Apr. 1997), pp. 192–203 (see pp. 83, 119)

[231] P. J. Antaki, 'Importance of nonequilibrium thermal conductivity during short-pulse laser-induced desorption from metals', Int. J. Heat Meas Tran. **45**, 4063–4067 (2002) (see p. 83)

[232] M. I. Mendelev et al., 'Development of new interatomic potentials appropriate for crystalline and liquid iron', Philosophical Magazine **83**, 3977–3994 (2003) (see p. 84)

[233] L. Malerba et al., 'Comparison of empirical interatomic potentials for iron applied to radiation damage studies', J. Nucl. Mater. **406**, 19–38 (2010) (see pp. 84, 85, 89)

[234] K. Nordlund, J. Wallenius and L. Malerba, 'Molecular dynamics simulations of threshold displacement energies in Fe', Nucl. Instr. Meth. Phys. Res. B **246**, 322–332 (2006) (see p. 85)

[235] C. Björkas, K. Nordlund and M. J. Caturla, 'Influence of the picosecond defect distribution on damage accumulation in irradiated α-Fe', Phys. Rev. B **85**, 024105 (2012) (see pp. 88, 90)

[236] E. E. Zhurkin and A. S. Kolesnikov, 'Atomic scale modelling of Al and Ni surface erosion under cluster impact', Nucl. Instr. Meth. Phys. Res. B **202**, 269–277 (2003) (see p. 89)

[237] B. Chimier, 'Solid-liquid phase transition induced by fast heating of a thin metal film', Europhys. Lett. (EPL) **92**, 15001 (2010) (see p. 101)

[238] Y. Ping et al., 'Warm dense matter created by isochoric laser heating', High Energy Density Physics **6**, 246–257 (2010) (see pp. 101, 104)

[239] J. Chen, W.-K. Chen and P. M. Rentzepis, 'Blast wave and contraction in Au(111) thin film induced by femtosecond laser pulses. A time resolved X-ray diffraction study.', J. Appl. Phys. **109**, 113522 (2011) (see pp. 101, 104)

[240] J. Chen, W.-K. Chen, J. Tang and P. M. Rentzepis, 'Time-resolved structural dynamics of thin metal films heated with femtosecond optical pulses', P. Natl. Acad. Sci. USA **108**, 18887–18892 (2011) (see p. 101)

[241] S. Schäfer, W. Liang and A. H. Zewail, 'Structural dynamics of nanoscale gold by ultrafast electron crystallography', Chemical Physics Letters **515**, 278–282 (2011) (see p. 101)

[242] M. Nicoul, U. Shymanovich, A. Tarasevitch, D. von der Linde and K. Sokolowski-Tinten, 'Picosecond acoustic response of a laser-heated gold-film studied with time-resolved X-ray diffraction', Appl. Phys. Lett. **98**, 191902 (2011) (see p. 101)

[243] Y. Murooka et al., 'Transmission-electron diffraction by MeV electron pulses', Appl. Phys. Lett. **98**, 251903 (2011) (see p. 102)

[244] J. Yang et al., '100-femtosecond MeV electron source for ultrafast electron diffraction', Rad. Phys. Chem. **78**, 1106–1111 (2009) (see p. 102)

[245] L. Reimer, *Transmission Electron Microscopy: Physics of Image Formation*, 5th ed, Springer Series in Optical Sciences 36 (Springer, New York, NY, 2008) (see p. 102)

[246] H. X. Gao and L.-M. Peng, 'Parameterization of the temperature dependence of the Debye-Waller factors', Acta Crystallogr. A **55**, 926–932 (1999) (see p. 102)

[247] P. Hohenberg, 'Inhomogeneous electron gas', Phys. Rev. **136**, B864–B871 (1964) (see p. 103)

[248] W. Kohn and L. J. Sham, 'Self-consistent equations including exchange and correlation effects', Phys. Rev. **140**, A1133–A1138 (1965) (see p. 103)

[249] N. Mermin, 'Thermal properties of the inhomogeneous electron gas', Phys. Rev. **137**, A1441–A1443 (1965) (see p. 103)

[250] X. Gonze et al., 'ABINIT: first-principles approach to material and nanosystem properties', Comp. Phys. Comm. **180**, 2582–2615 (2009) (see p. 103)

[251] X. Gonze, 'A brief introduction to the ABINIT software package', Z. Kristallogr **220**, 558–562 (2005) (see p. 103)

[252] D. M. Ceperley, 'Ground state of the electron gas by a stochastic method', Phys. Rev. Lett. **45**, 566–569 (1980) (see p. 103)

[253] N. Troullier and J. Martins, 'A straightforward method for generating soft transferable pseudopotentials', Solid State Commun. **74**, 613–616 (1990) (see p. 103)

[254] J. B. Lee, K. Kang and S. H. Lee, 'Comparison of theoretical models of electron-phonon coupling in thin gold films irradiated by femtosecond pulse lasers', Mater. Trans. **52**, 547–553 (2011) (see p. 103)

[255] E. G. Gamaly and A. V. Rode, 'Ultrafast electronic relaxation in superheated bismuth', New J. Phys. **15**, 013035 (2013) (see p. 104)

[256] H. Sheng, M. Kramer, A. Cadien, T. Fujita and M. Chen, 'Highly optimized embedded-atom-method potentials for fourteen fcc metals', Phys. Rev. B **83**, 134118 (2011) (see p. 105)

[257] R. Johnson, 'Alloy models with the embedded-atom method', Phys. Rev. B **39**, 12554–12559 (1989) (see p. 105)

[258] S. Foiles, M. Baskes and M. Daw, 'Embedded-atom-method functions for the fcc metals Cu, Ag, Au, Ni, Pd, Pt, and their alloys', Phys. Rev. B **33**, 7983–7991 (1986) (see p. 105)

[259] B.-J. Lee, J.-H. Shim and M. I. Baskes, 'Semiempirical atomic potentials for the fcc metals Cu, Ag, Au, Ni, Pd, Pt, Al, and Pb based on first and second nearest-neighbor modified embedded atom method', Phys. Rev. B **68**, 144112 (2003) (see p. 105)

[260] G. Grochola, S. P. Russo and I. K. Snook, 'On fitting a gold embedded atom method potential using the force matching method', J. Chem. Phys. **123**, 204719 (2005) (see p. 105)

[261] Additional Sheng *et al.* Au EAM potential performance data, `https://sites.google.com/site/eampotentials/` (see p. 105)

[262] A. Stukowski, 'Visualization and analysis of atomistic simulation data with OVITO - the Open Visualization Tool', Model. Simul. Mater. Sc. **18**, 015012 (2010) (see p. 110)

[263] K. Lu and Y. Li, 'Homogeneous nucleation catastrophe as a kinetic stability limit for superheated crystal', Phys. Rev. Lett. **80**, 4474–4477 (1998) (see p. 109)

[264] P. Silvestrelli, A. Alavi, M. Parrinello and D. Frenkel, 'Ab initio molecular dynamics simulation of laser melting of silicon', Phys. Rev. Lett. **77**, 3149–3152 (1996) (see p. 111)

[265] A. Rousse et al., 'Non-thermal melting in semiconductors measured at femtosecond resolution', Nature **410**, 65–68 (2001) (see p. 111)

[266] A. Y. Vorobyev and C. Guo, 'Enhanced absorptance of gold following multipulse femtosecond laser ablation', Phys. Rev. B **72**, 195422 (2005) (see p. 115)

[267] J. Krzywinski et al., 'Conductors, semiconductors, and insulators irradiated with short-wavelength free-electron laser', J. Appl. Phys. **101**, 043107 (2007) (see p. 115)

[268] M. Toulemonde, C. Dufour, A. Meftah and E. Paumier, 'Transient thermal processes in heavy ion irradiation of crystalline inorganic insulators', Nucl. Instr. Meth. Phys. Res. B **166-167**, 903–912 (2000) (see p. 118)

[269] G. Baccarani and M. Wordeman, 'An investigation of steady-state velocity overshoot in silicon', Solid State Electron. **28**, 407–416 (1985) (see p. 120)

[270] W. Hansch and M. Miura-Mattausch, 'The hot-electron problem in small semiconductor devices', J. Appl. Phys. **60**, 650 (1986) (see p. 120)

[271] N. M. Bulgakova et al., 'A general continuum approach to describe fast electronic transport in pulsed laser irradiated materials: the problem of coulomb explosion', Appl. Phys. A-Mater. **81**, 345–356 (2005) (see p. 120)

[272] J. Geist and W. Gladden, 'Transition rate for impact ionization in the approximation of a parabolic band structure', Phys. Rev. B **27**, 4833–4840 (1983) (see p. 121)

[273] Y. Varshni, 'Temperature dependence of the energy gap in semiconductors', Physica **34**, 149–154 (1967) (see pp. 121, 124)

[274] J. Dziewior and W. Schmid, 'Auger coefficients for highly doped and highly excited silicon', Appl. Phys. Lett. **31**, 346 (1977) (see p. 121)

[275] C. Jacoboni, F. Nava, C. Canali and G. Ottaviani, 'Electron drift velocity and diffusivity in germanium', Phys. Rev. B **24**, 1014–1026 (1981) (see p. 121)

[276] Collection of Ge and Si parameters, `http://www.ioffe.ru/SVA/NSM/Semicond/Ge/electric.html` (see p. 121)

[277] P. Schelling, 'Phase behavior and kinetics of a new bond-order potential for silicon', Comp. Mater. Sci. **44**, 274–279 (2008) (see pp. 121, 122)

[278] L. Shokeen and P. K. Schelling, 'Thermodynamics and kinetics of silicon under conditions of strong electronic excitation', J. Appl. Phys. **109**, 073503 (2011) (see pp. 121, 141)

[279] H. Balamane, T. Halicioglu and W. A Tiller, 'Comparative study of silicon empirical interatomic potentials', Phys. Rev. B **46**, 2250–2279 (1992) (see p. 122)

[280] J. Tersoff, 'Modeling solid-state chemistry: interatomic potentials for multicomponent systems', Phys. Rev. B **39**, 5566–5568 (1989) (see p. 122)

[281] B. Canut, N. Bonardi, S. Ramos and S. Della-Negra, 'Latent tracks formation in silicon single crystals irradiated with fullerenes in the electronic regime', Nucl. Instr. Meth. Phys. Res. B **146**, 296–301 (1998) (see pp. 128, 129)

[282] A. Dunlop, G. Jaskierowicz and S. Della-Negra, 'Latent track formation in silicon irradiated by 30 MeV fullerenes', Nucl. Instr. Meth. Phys. Res. B **146**, 302–308 (1998) (see pp. 128, 129)

[283] A. Colder et al., 'Latent track formation in germanium irradiated with 20, 30 and 40 MeV fullerenes in the electronic regime', Nucl. Instr. Meth. Phys. Res. B **174**, 491–498 (2001) (see p. 132)

[284] M. Gallant and H. van Driel, 'Infrared reflectivity probing of thermal and spatial properties of laser-generated carriers in germanium', Phys. Rev. B **26**, 2133–2146 (1982) (see p. 133)

[285] W. Humphrey, A. Dalke and K. Schulten, 'VMD: Visual molecular dynamics', J. Mol. Graphics **14**, 33–38 (1996) (see p. 166)

Appendices

Appendix A

Parallel structure factor code snippet

The following is a snippet of the Fortran95 (with OpenMP) code used for parallel pair density function computation. Very good parallelisation (almost linear with the number of cores) can be achieved with both static and dynamic schedulers with slightly better results for the former.

```
1  !$OMP PARALLEL DO SCHEDULE(runtime) DEFAULT(NONE)
2  SHARED (xyz, rho, nat, rstep, nr) PRIVATE (tmp, dist, ir, iat, jat)
3
4  do iat=1,nat
5      do jat=iat+1,nat
6          tmp(:)=xyz(iat,:)-xyz(jat,:)        ! xyz contains the coordinates
7          dist=sqrt(dot_product(tmp,tmp)) ! calculates distance
8          ir=nint(dist/rstep)+1
9          if (ir <= nr) then
10             !$OMP ATOMIC
11             rho(ir)=rho(ir)+1.0_wp
12         end if
13     end do
14 end do
15
16 !$OMP END PARALLEL DO
```

Appendix B

Additional figures

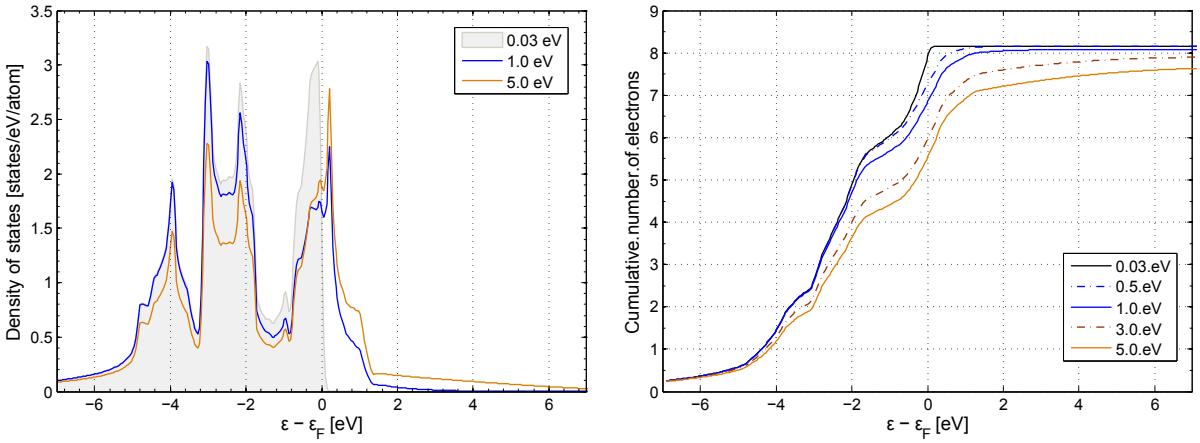

Figure B.1: Density of states (left) and cumulative electron number (right panel) for bcc iron based on the data from [29]. More than one electron is being excited above the Fermi level (ϵ_F) between 0.5-1.0 eV, while more than two electrons are excited above ϵ_F at 3.0 eV.

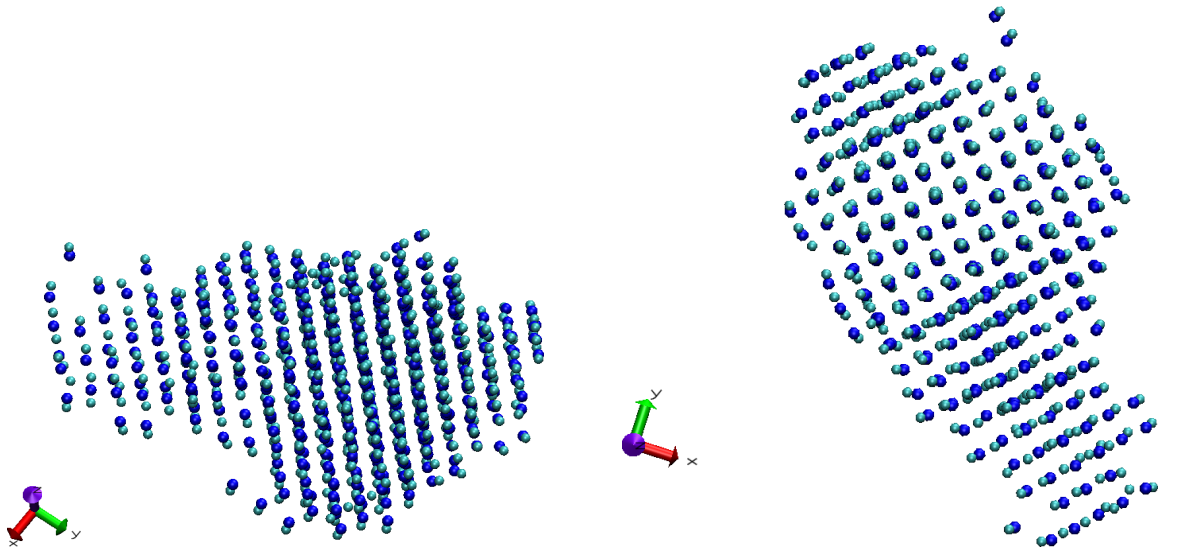

Figure B.2: The biggest cluster produced in the examined 200-500 keV pka energy range in Fe. It contains 1125 gross (and 89 net interstitial) defects, which makes it the biggest primary defect cluster reported in the literature resulting from a collision cascade. Formation of such a cluster occurred during a 200 keV event in <1.6,1.7,1.8> direction. The simulation was carried out with the electronic stopping friction term. Notice the highly symmetrical region at the top of the <110> projection, which can be potentially described as a dislocation plane. Green (blue) atoms depict interstitials (vacancies). Visualisation was performed with VMD package [285]. *Figure reproduced from [5].*

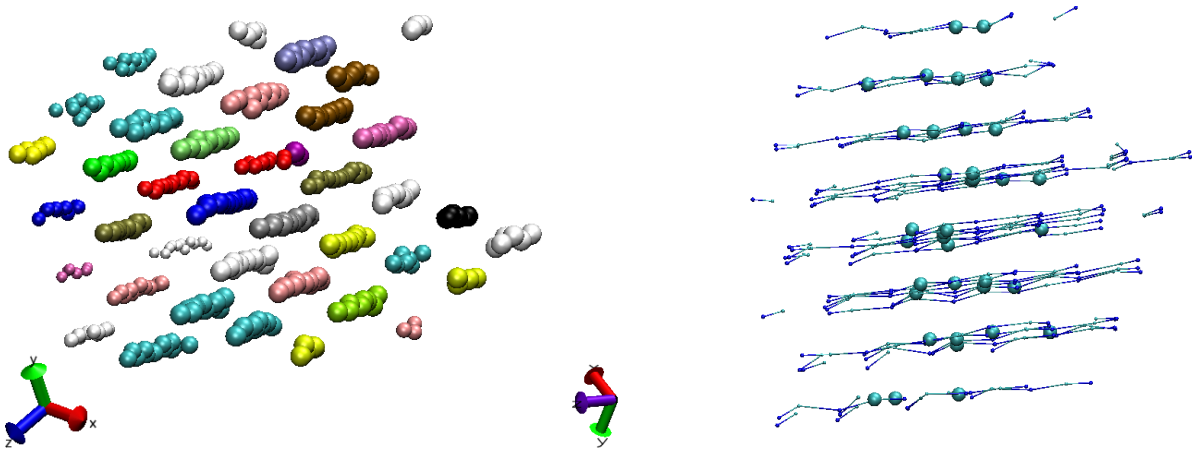

Figure B.3: Results of the automated crowdion analysis (200 keV pka event in Fe). Crowdions are line defects, aligned typically in <111> direction in α-Fe. (Left panel) Crowdions are identified with different colours. (Right panel) Centre of masses of these line defects (silver atoms) help to identify dislocation planes.

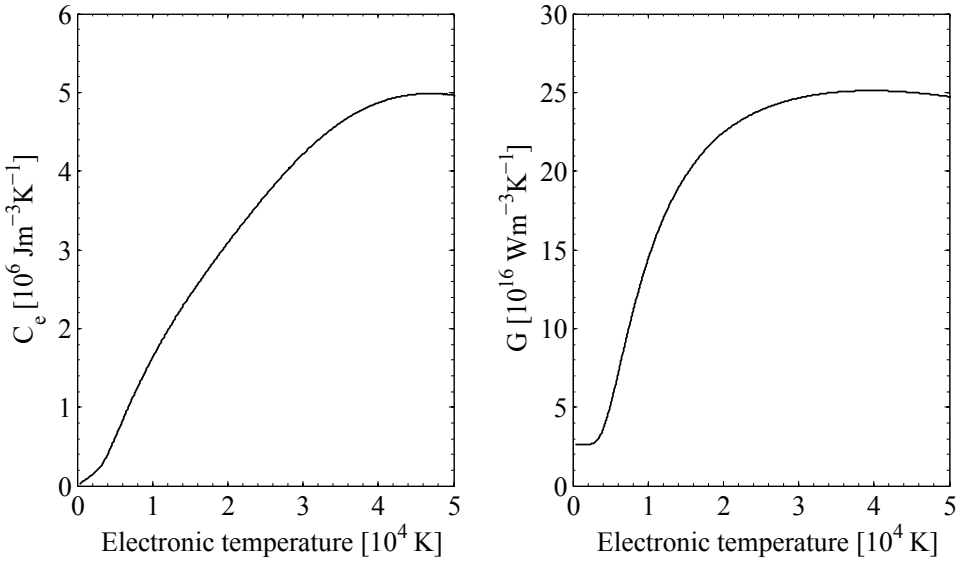

Figure B.4: Electronic temperature dependence of the specific heat capacity $C_e(T_e)$ and electron-phonon coupling $G(T_e)$ in Au [29].

Appendix C

2T-MD DL_POLY code

C.1 Overview of program structure

The following modules were added to incorporate the 2T model in DL_POLY (version 4.01):

- `twotemp_module.f90` - Module deals with array allocation and additional parameter declaration in the 2T model,
- `util_module.f90` - Module provides a set of utility subroutines and functions, dealing with: boundary conditions, parameter dependent materials properties and some i/o functionality,
- `track_module.f90` - Module implements the initial energy deposition in the electronic system.

Files inherited from D. M. Duffy and A. M. Rutherford [76, 81], now heavily modified:

- `md_lfv.f90` - Calls the inhomogeneous Langevin thermostat (`nvt_l2_lfv.f90`) - thermostat that uses the local electronic temperature (T_e) rather than the global target temperature (T_T). Includes calls to `iontemp` and `thermdiff`, which calculate ion temperatures and electronic temperatures, respectively,
- `nvt_l2_lfv.f90` - Modified version of the standard Langevin thermostat (changed forces scaling to local T_e instead of global T_T.),
- `iontemp.f90` - Calculates the local lattice temperature from the average kinetic energy of the atoms in coarse grained ion temperature cells (CITs). It also calculates the energy lost to electronic stopping that is added as a source in the electronic system,
- `thermdiff.f90` - Calculates the local electronic temperature by a finite difference solution to the heat diffusion equation. It includes source and sink terms that represent energy exchange with the ionic lattice.

Files which have undergone minor changes and additions:

- `DL_POLY.f90` - Added a few lines to call the initialisation subroutines from `twotemp_module.f90`,
- `read_control.f90` - Included new 2T-specific CONTROL file directives. Provided default values for the parameters required in the 2T model,
- `Makefile` - Included the new modules and subroutines required for the 2T model.

C.2 New directives in CONTROL

The new directives available for the 2T model are listed below. All of these are prefixed with **ttm**. The directives in blue are not yet tested. It is envisages that all of these will be available in the next major release of DL_POLY. CET/CIT denote coarse-grained electronic/ionic temperature cells, respectively.

ttm f_1 f_2 Inhomogeneous Langevin thermostat with electron-phonon friction of *f1* and electronic stopping friction of *f2*. Defaults to 2.0 ps^{-1} (i.e. $\tau_{ep} = 0.5$ ps) and 0.0 ps^{-1} (i.e. electronic stopping friction disabled).

ttmncit ***f*** Number of CITs in z-direction. The CITs in xy-directions would be calculated from the size of the simulation cell. Defaults to 10.

ttmncet ***i j k*** Number of CETs in x,y,z-directions. Note that the number of CETs cannot be smaller than CITs in any direction. Typically, for ion irradiation simulations the CIT would be equal to CET in z-direction and CETs in x,y would extend far beyond the simulation cell. For cascades, CETs would extend over CITs in all directions. Defaults to a minimum of 20, 20, 20.

ttmvcut ***f*** Velocity above which the electronic stopping is effective. Defaults to 50 Å/ps. Effective only if electronic stopping is enabled.

ttmnonmetal This specifies that the 2T model parameters for a non-metal would be used, i.e. **ttmdiff** would be required instead of electronic thermal conductivity.

ttmdiff ***f*** The diffusivity (D_e) of the electronic system at $T_e = 300$ K, which is assumed to follow a $D_e(T_e) \propto T_e^{-1}$ law. Above the temperature specified in **ttmcelin** it stays constant. Input values are in m^2/s. No default value - this parameter must be specified if **ttmnonmetal** was selected.

ttmceconst f_1 Specifies a constant electronic specific heat capacity (f_1 in kB/atom). Used as default when no **ce** directive is specified. The default value is 1 kB/atom.

ttmcelin f_1 f_2 Specifies the maximum electronic specific heat capacity (f_1 in kB/atom) at temperature f_2 K for a non-metal. The electronic specific heat capacity increases linearly up to that value, above which is stays constant. No default values.

ttmcetanh f_1 f_2 Specifies the electronic specific heat parameters of the following form $C_e(T_e) = f_1 \cdot \tanh(f_2 \cdot 10^{-4})$ [kB/atom] for a metal. Both parameters are required.

ttmcetab This directive would make the code to ask for an additional file (`Ce.dat`) containing two columns of data: $C_e(T_e)$ and T_e. The value of $C_e(T_e)$ would be obtained by linear interpolation. Input from `Ce.dat` is in $\mathrm{Jm^{-3}K^{-1}}$.

ttmgoffset f_1 Offsets the e-p coupling of the two systems by f_1 time-steps.

ttmoneway Electron-phonon coupling effective one-way only, i.e. from electrons to ions.

ttmamin f_1 An activation threshold for a minimum number of particles (f_1) in a CIT box.

ttmkecnst f Specifies the constant electronic thermal conductivity for metals in $\mathrm{Wm^{-1}K^{-1}}$. No default value and must be specified when **ttm** is used.

ttmkeinf Sets electronic thermal conductivity to infinity.

ttmvarg Specifies that the value of the electron-phonon coupling constant as a function of electronic temperature is read from a file (`g.dat`). This forces electron-phonon friction (χ) to change every time-step according to $\chi = G/(3Nk_B)$, where N is the number of atoms in a CIT.

ttmdedx f The electron stopping power of a projectile entering the electronic system. Default is 0 eV/nm, which means that the electronic lattice (CETs) is initialised to the thermostat temperature.

ttmsgauss f_1 f_2 Parameters pertaining to the spatial energy deposition in the electronic system. The first parameter (f_1) is the standard deviation σ of the Gaussian energy distribution in space. The default is 1 nm. The second parameter (f_2) is a dimensionless parameter that cuts the deposition at $f_2 \cdot \sigma$. Defaults to 3. Works only if **ttmdedx** is specified.

ttmsflat Specifies that the initial spatial deposition of energy is homogeneous. Works only if **ttmdedx** or **ttmlaser** are specified.

ttmlaser f_1 f_2 Specifies that the initial energy deposition results from a laser with f_1 absorbed fluence [mJ $\mathrm{cm^{-2}}$] and f_2 penetration depth [nm]. Cannot be used in conjunction with **ttmdedx**; forces **ttmsflat**.

ttmsread Specifies that the initial spatial deposition of energy on electron is to be read from a file (TETEMP). This would work only in combination with **ttmdelta** and when **ttmdedx** is not specified.

ttmgauss f_1 f_2 Parameters pertaining to the temporal energy deposition in the electronic system. The first parameter (f_1) is the standard deviation τ of the Gaussian energy distribution in time. The default is $1 \cdot 10^{-3}$ ps. The second parameter (f_2) is a dimensionless parameter that starts and stops the deposition around $\pm f_2 \cdot \tau$. Defaults to 3. Works only if **ttmdedx** or **ttmlaser** are selected.

ttmnexp f_1 f_2 Same as above with the same default parameters, however the shape of the temporal deposition is $\propto \exp(-t)$. Works only if **ttmdedx** or **ttmlaser** are selected.

ttmdelta Temporal deposition occurs during one MD time-step. Either **ttmdedx** or **ttmsread** must be given.

ttmthvelxyz Enable calculation of lattice temperature from the thermal velocities only, i.e. velocities discounting collective movements of atoms in a CIT cell in all directions.

ttmthvelz As above, but discounts the collective movements in the z-direction only.

ttmatomdens f_1 Manual input of atomic density in atoms/Å^3 to be used when vacuum is present in the simulation box, as it would give rise on an incorrect atomic density value.

ttmdyndens Recalculate atomic density at each time-step. Useful for simulations with a free-surface. To be used only in a combination with tabular specific heat capacity, i.e. **ttmcetab**.

ttmstats f Frequency of printing out of the 2T model basic statistics to `peak_e.txt` and `peak_i.txt` files, pertaining to electronic and ionic systems. By default it is disabled.

ttmtraj f Frequency of printing out of additional 2T model statistics to `lat_e.txt` and `lat_i.txt` files. These files represent a slice of the systems along the y-axis at constant x,z-directions. By default it is disabled.

ttmdebug1 Print debug files pertaining to the electron-phonon coupling strength.

ttmbcs ***(keyword)*** Specifies the boundary conditions (BCs) in the electronic system. The keyword options as follows:
dirich - Dirichlet BCs with the halo BC cells at the temperature specified in **temp**,
neumann - Zero-flux (Neumann) BCs,
robin f - Robin's boundary condition with fraction of the leaking flux of f (Default 0.96),
xydirich - Mixed case: Dirichlet BCs in the x,y-directions and zero-flux in the z-direction,
xyrobin f - Mixed case: Robin BCs in x,y-directions and zero-flux in z-direction.